Novel Composite Strategy to Optimize Thermoelectric Performance

by

Ruiming Lu

A dissertation submitted in partial fulfillment
of the requirements for the degree of
Doctor of Philosophy
(Materials Science and Engineering)
in the University of Michigan
2020

Doctoral Committee:

Professor Pierre F. P. Poudeu, Chair
Assistant Professor John Heron
Assistant Professor Liang Qi
Professor Ctirad Uher

Ruiming Lu

lurm@umich.edu

ORCID iD: 0000-0003-3180-9729

Dedication

To my friends and family.

Acknowledgements

At this moment of completing my PhD study, there are many people I would like to pay my gratitude to, including my family, my friends, my colleagues, my committee members and collaborators.

First and foremost, I would like to thank my advisor, Professor Pierre Ferdinand Poudeu Poudeu. From the very beginning to this moment, he has always been supportive and helpful, with exceptional patience and understanding. He is an excellent mentor who has constantly given me suggestions and taught me new knowledge whenever I needed them. I enjoyed the environment he created in our research group, everyone being a leader and a team player as well. It took so much more than just materials science expertise to succeed here. He is a true friend who has always been so understanding and willing to share his experience in life. I enjoyed our casual chats as much as our discussion about research work. For that, I am and will always be thankful.

I would like to pay special thanks to my committee members, Professor Ctirad Uher, John Heron and Liang Qi, for their valuable time and suggestions. Their help has made my progress of pursuing the PhD degree so much easier. It has been a pleasure to work with every one of them. I want to thank Professor Uher and his group. Not only has he served as my committee member, but he and his group also have been a solid collaborator, offering so much help and insights during my PhD studies. I enjoyed working and being friends with Dr. Trevor Bailey, Dr. Alexander Page, Dr. Hui Si, Dr. Si Wang, Dr. Pan Ren and Dr. Hang Chi.

I also want to thank the colleagues from my research group, Dr. Nick Moroz, Dr. Erica Chen, Dr. Alan Olvera, Dr. Juan Lopez, Dr. Changyu Meng, Brandon Buchanan, Yiqiao Huang, Yixuan Chen, Lamia Dawahre, Tyler Del Rose, Zhixiong Yin, Xin Qian, Dr. Chinwe Ikpo and Kayla Byrd. They have been really helpful and supportive, especially when I freshly joined the group. It's been a pleasure to work and to be friends with every one of them.

I would like to thank staff members in Materials Science and Engineering department, staff members at Michigan Center for Materials Characterization (MC2) and staff members at Mitchell Electron Microbeam Analysis Lab (EMAL), who have given so much help in my PhD program and research work.

Lastly, I want to thank my family, my beloved and my dearest friends. My family and my beloved have given me so much support and comfort that is far beyond what I could ask for, especially during the toughest period I ever had in life. I love you all.

Table of Contents

List of Tables

.

List of Figures

List of Appendices

Abstract

Thermoelectric (TE) technology is a promising strategy to recycle the waste heat. However, the major challenge of commercializing this technology is the poor performance of TE materials. Previously, there have been reported multiple strategies to optimize thermoelectric transport, such as doping, substitutional alloying and nanostructuring. So far, the best TE performance is mainly achieved by low thermal conductivity, either using materials with intrinsically low thermal conductivities or suppressing thermal transport by strategies like nanostructuring. However, it's difficult to achieve further improvement in TE performance by simply pushing the lower limit of thermal conductivity. High TE performance must rely on the optimization in electronic transport as well, which is also challenging due to the coupling relations between the transport parameters, for example, electrical conductivity and Seebeck coefficient coupled by carrier concentration. The coupling relations limit the possibility to simultaneously optimize multiple parameters. It is therefore urging to develop novel strategies that can break apart the coupling relations, such as modulation doping and band engineering.

This thesis is dedicated to exploring novel composite strategy for TE properties regulation. The advantage of making composite materials is the potentially high degree of freedom for properties tailoring. Instead of engineering single-phase materials, the composite strategy includes more aspects to be considered, for example, the choices of constituent components, the microstructures and interfaces to be developed. With different combinations of components and varied microstructures, various interactions will be expected. Nanocomposite strategy was originally applied to decrease thermal conductivity by introducing inert nano particles. The

traditional method of constructing composite materials is to mechanically mix the pre-synthesized components, which results in interfaces lack of chemical bonding or interaction.

Different from traditional method, novel composite strategy in this research focuses on developing highly interactive interfaces via the in-situ formations of secondary phases, which are chemically close relatives to the matrix materials. For example, full Heusler precipitates in half Heusler matrix and chalcopyrite compounds in Cu_2Se matrix. For half Heusler/ full Heusler composites, two phases are co-formed from the same elements through a solid-state reaction at high temperature. In contrast, the chalcopyrite/Cu_2Se composites are constructed by co-forming both phases from a common precursor, $CuSe_2$ through solid-state reactions. Due to the special consideration in selecting constituent components and unique routes to construct the composite materials, various interesting microstructures have been developed, leading to very different interactions between precipitates and the matrix, and thus various effects on TE transport properties. For example, by introducing magnetic full Heusler precipitates in half Heusler matrix, an even stronger modulation in electronic transport has been obtained, which was not observed in heavily doped half Heusler alloys with regular full Heusler precipitates. A two-step synthesis route enables the precise control over the ratio of room-temperature Cu_2Se to high-temperature Cu_2Se by simply adjusting the $CuGaSe_2$ content. $CuFeSe_2$ has a temperature-dependent solubility in Cu_2Se, which leads to the unique dendrite structure and further temperature-dependent doping effect in the composite materials. In contrast, $CuAlSe_2$ tends to agglomerate in Cu_2Se and extracts Cu ions from the matrix.

Above all, we demonstrate the capability of such composite strategy to achieve various modulations in TE properties, which can pave the path to future success of TE technology.

Chapter 1 : Introduction

1.1 Motivation and Outline of the Thesis

Undoubtedly, humankind has achieved a great success, prospering on this planet and even reaching out to outer space. One of the very fundamental conditions for such an unprecedented success and a continuous success in the coming future is and will always be the energy supply meeting the demand from our society. This is particularly true nowadays when we are advancing deeper into 21st century. It was estimated that a total amount of energy up to 1.575 x 10^{17} W h was consumed in the year of 2013, or 13.54 billion toe.[1] Yet, the surging demand for energy continues as it did in the past. Though various strategies or solutions have been come up to ease such an "Energy Crisis", the ugly truth is that our modern society relies heavily on fossil energy from ancient organisms. A recent report indicates that up to 81.3 percent of energy supply in 2017 was provided by fossil fuel (oil 32%, coal/peat/shale 27.1% and natural gas 22.2%).[2] The dominating status of fossil fuel as energy supply will hold true for a long time in the coming future. The major issue of using fossil energy, as we know, is that it is not sustainable and causes environmental issues, such as global warming due to the emission of greenhouse gases. Further, the energy efficiency is very low for fossil fuel, limited by the Carnot efficiency on the heat engine. For example, only ~30 percent of the total energy produced from fuel combustion is harnessed to support a vehicle, while the rest of energy up to 70 percent is all squandered in the form of waste heat in the exhaust.[3] Such low conversion efficiencies for heat engines suggests that billions of toe of fossil fuel has been wasted every year. It is therefore urgent and significantly important to improve its energy efficiency as long as we depend greatly on fossil fuel.

Semiconductors can potentially help to solve the energy problems as they brought us to the computer age, or information age. Thermoelectric (TE) technique based on proper semiconducting materials can realize the direct conversion between heat and electricity, acting as an electricity generator based on the Seebeck effect or as a refrigerator/ heater based on the Peltier effect.[4] In that case, the huge amount of wasted heat during the usage of fossil fuel becomes a great potential energy. Recycling this part of energy essentially, means improving the efficiency of fossil fuel. However, this task of developing TE technology is more difficult than expected, for it has taken decades already and yet many more to succeed. The current research on TE technology mainly focuses on improving the conversion efficiencies of thermoelectric materials, i.e. enhancing performance of current materials or searching for new materials with high performance. Being part of that, this thesis work is dedicated to developing novel strategies to optimize transport properties of TE materials. Particularly, a composite strategy via the in-situ formation of nano precipitates within a TE matrix has been studied in half Heusler-based and Cu_2Se-based TE materials.

The specific reason for this thesis work focusing on half Heusler-based and Cu_2Se-based materials is discussed as the following. The electricity generation efficiency via TE technology is determined by the temperature gradient across a TE module/device and the performance of the TE materials incorporated, which will be discussed in the following section of principles of thermoelectrics. For power generation, medium grade waste heat will be the main target. Among many materials for medium temperature TE generator, half Heusler and Cu_2Se based materials stand out due to their unique properties and receive tremendous research interest in recent years. For example, half-Heusler alloys are well known for their characteristics of high power factor (product of electrical conductivity and Seebeck coefficient), high chemical and mechanical robustness and being constituted of earth abundant, environmentally friendly elements. Cu_2Se

based materials, on the other hand, stand out because of their intrinsically low thermal conductivities and decent power factors. However, there are also challenges in developing these materials for TE application. This thesis work focuses on exploring the composite strategy of forming in-situ precipitates for optimizing thermal and electronic transport in half Heusler and Cu_2Se-based materials. The general content of this thesis includes introduction (Chapter 1), methods of research (Chapter 2), main research work (Chapter 3-6) and conclusion (Chapter 7). In the introduction (Chapter 1), it starts with the current section, i.e. motivation of the research and outline of the thesis. A brief discussion is given regarding general principles of thermoelectrics. The focuses of the introduction part are the recent development in thermoelectrics, particularly in half Heusler and Cu_2Se based materials, the general strategies to manipulate TE properties and challenges remaining to be solved. After that, a research plan is proposed, revealing the main research content. Chapter 3 discusses optimizing TE performance of $Ti_{0.25}Zr_{0.25}Hf_{0.5}(Ni,Fe_x)Sn_{0.975}Sb_{0.025}$ via incorporating in-situ formed full Heusler precipitates by introducing extra Fe atoms at Ni site during synthesis. Chapter 4-6 focus on exploring composites strategies for tuning TE performance of Cu_2Se based materials. In detail, the composites materials are constructed by forming ternary phases in Cu_2Se, including $CuGaSe_2$ (Chapter 4), $CuFeSe_2$ (Chapter 5), and $CuAlSe_2$ (Chapter 6) through varied synthesis routines. At last, conclusions are made in Chapter 7. Future work is also proposed based on the completed research projects with preliminary results presented.

1.2 General Principles of Thermoelectrics

1.2.1 Thermoelectric Effect

Thermoelectric effect generally includes the Seebeck effect, Peltier effect and Thompson effect.[4] The Seebeck effect describes the phenomenon that an electric voltage arises between the hot side

and the cold side when a temperature gradient is applied across a material. On the contrary, a temperature difference is generated when an electric voltage is applied across a material, the so-called Peltier effect. The Thompson effect is the heat absorption or generation when a current is applied to a conductor with temperature gradient. Conceptually, a thermoelectric generator works based on the Seebeck effect while a thermoelectric refrigerator works based on the Peltier effect. In the following, the general principles of thermoelectrics are presented in the case of Seebeck effect. The physical mechanism for the Seebeck effect can be illustrated in **Figure 1**. Initially, no electric potential exists between two ends of a metal/ semiconductor bar, because charge carriers (electrons for n-type materials) are homogeneously distributed over the entire body of the material, which is further attributed to the steady state achieved so that the average speed for electrons to drift from one side to another equals to that for the reverse, giving zero net charge migration. When a temperature gradient is applied, the initial steady state will be broken. The charge carrier at hot end, either electrons or holes, will get excited and gain much more kinetic energy compared to those at the cold end. As a result, more charge carriers drift from the hot end to the cold end, causing a charge separation in space and a corresponding electric potential across the materials bar macroscopically when steady state is achieved. Further, the resulted electric potential across the bar is proportional to the temperature gradient applied. The Seebeck coefficient was introduced to characterize the capability of generating electric voltage for a material, i.e. the voltage generated by unit temperature gradient:

$$S = \frac{\Delta V}{\Delta T} \tag{1}$$

or

$$S = \frac{\mathrm{d}V}{\mathrm{d}T} \tag{2}$$

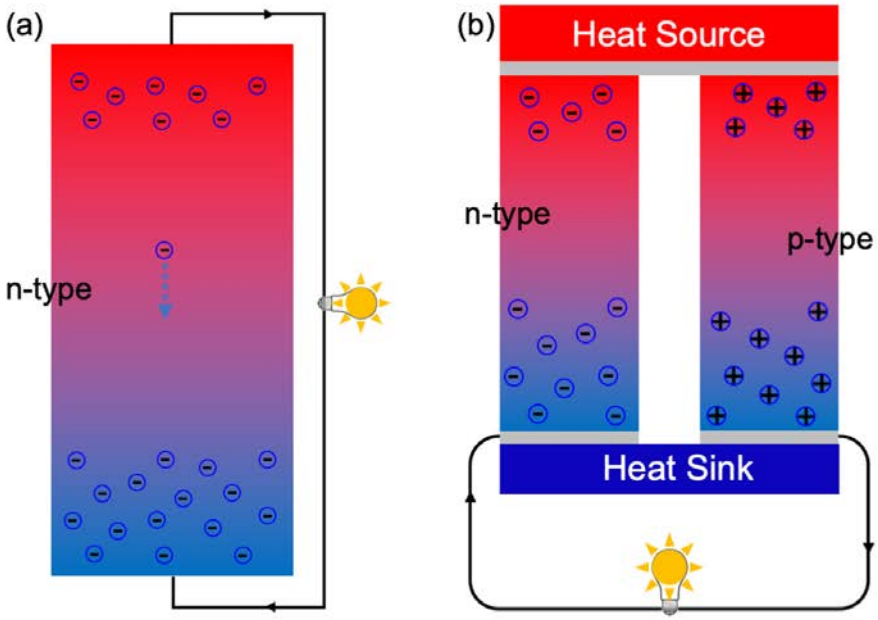

Figure 1-1. (a) A schematic diagram of Seebeck effect in a n-type material; (b) A schematic diagram of a dual-leg thermoelectric device.

1.2.2 Conversion Efficiency and Figure of Merit

However, a good thermoelectric generator asks for more than just a high Seebeck coefficient of a material. The efficiency of a TE generator, η, is given by[4]:

$$\eta = \left(1 - \frac{T_{\mathrm{C}}}{T_{\mathrm{H}}}\right) \cdot \frac{\sqrt{1+zT} - 1}{\sqrt{1+zT} + \frac{T_{\mathrm{C}}}{T_{\mathrm{H}}}} \tag{3}$$

where T_{H}, T_{C} are the temperature at hot and cold end, respectively while zT is the unit less figure of merit defined by:

$$zT = \frac{\sigma s^2}{\kappa} T \tag{4}$$

where σ, S and κ are the electrical conductivity, Seebeck coefficient and thermal conductivity of a material while T is the absolute temperature. According to **Equation** (3), the conversion

efficiency of a TE material is strongly related to the temperature gradient and to the material figure of merit, i.e. a high T_H/T_C ratio and a high zT lead to a high efficiency, η. Assuming zT approaches infinite, the efficiency, η, would end up being ($1-T_C/T_H$), which represents the efficiency of the Carnot heat engine. Given a defined environment (T_H and T_C), the conversion efficiency of a TE material, thus is only determined by its figure of merit. Looking at **Equation** (4), it may seem straightforward that a high figure of merit, zT, can be achieved by simultaneously increasing the electrical conductivity, Seebeck coefficient and lowering the thermal conductivity. However, it is often extremely difficult to optimize multiple parameters simultaneously due to the coupling relations between them, as discussed in the following.

1.2.3 Transport Parameters and Coupling Relationships

The electrical conductivity of a metal or degenerated semiconductor, σ, strongly depends on the charge carrier density, n, and charge carrier mobility, μ, via the **Equation** (5)[5]:

$$\sigma = ne\mu \tag{5}$$

where e is the elementary charge or electric charge. This relation implies that a high charge carrier density and a high carrier mobility lead to a high electrical conductivity. For intrinsic semiconductors, the electrical conductivity takes into account the contributions from both electrons and holes:

$$\sigma = (n_e\mu_e + n_h\mu_h)e \tag{6}$$

where subscript e and h denote electron and hole, respectively. However, intrinsic semiconductors are usually not good TE materials for two reasons: (1) poor electrical conductivity due to low carrier concentration, including both electrons and holes; (2) poor Seebeck coefficient due to comparable but counteracting contributions from electron and holes. In fact, an ideal intrinsic semiconductor is hard to find or to synthesize in the laboratory because of the difficulty to form

perfect crystals without introducing defects. In that sense, discussions will be focused on the degenerated semiconductors where only one type of charge carriers, either electron (n-type) or hole (p-type) is dominating the electrical conductivity. For a degenerated semiconductor, the Seebeck coefficient is also related to carrier concentration, n, via **Equation** (7)[4]:

$$\alpha = \frac{8\pi^2 k_B^2}{3eh^2} m^* T \left(\frac{\pi}{3n}\right)^{2/3} \quad (7)$$

where k_B and h are the Boltzmann constant ($1.38064852 \times 10^{-23}$ m^2 kg s^{-2} K^{-1}) and Plank constant ($6.62607004 \times 10^{-34}$ m^2 kg s^{-1}), respectively, while T is the absolute temperature. Besides carrier density, n, another material parameter in **Equation** (7) is the effective mass of charge carriers, m^*. Therefore, Seebeck coefficient is proportional to the effective mass of charge carriers, m^*, but inversely proportional to the carrier density term, $n^{2/3}$. Though it's highly desirable to have both high electrical conductivity and high Seebeck coefficient, for the sake of excellent figure of merit, zT, as shown in **Equation** (4), this can hardly be realized due to the coupling relation via carrier density. For example, increasing carrier density via doping can significantly enhance the electrical conductivity of TE materials, however, Seebeck coefficient degrades in response to a rising carrier density. In other words, tuning carrier concentration cannot improve one parameter without harming the other for electrical conductivity and Seebeck coefficient. As a result, an optimal carrier density is observed, usually between 10^{19} and 10^{21} cm^{-3}, where a peak power factor, PF (σS^2), happens.[6]

The coupling relation between electrical conductivity and Seebeck coefficient also happens via carrier mobility, which is buried in the effective mass of charge carrier in **Equation** (7). The effective mass of charge carriers, m^*, is related to carrier mobility, μ, by the following approximate relation:

$$\mu = \frac{e\tau}{m^*} \tag{8}$$

where τ is the average scattering time (average time between scattering events). **Equation** (8) suggests that carrier mobility is inversely proportional to the effective mass of charge carriers and so is the electrical conductivity. On the contrary, Seebeck coefficient is proportional to the effective mass of charge carriers. **Equation** (8) also implies that scattering events are critical in determining charge carrier mobility. Matthiessen's rule[5] gives an approximation to the carrier mobility in situations when multiple and independent scattering mechanisms are present:

$$\frac{1}{\mu} = \frac{1}{\mu_{\mathrm{i}}} + \frac{1}{\mu_{\mathrm{j}}} + \frac{1}{\mu_{\mathrm{k}}} + \cdots \tag{9}$$

Or

$$\frac{1}{\tau} = \frac{1}{\tau_{\mathrm{i}}} + \frac{1}{\tau_{\mathrm{j}}} + \frac{1}{\tau_{\mathrm{k}}} + \cdots \tag{10}$$

where i, j and k denote different scattering mechanisms, such as impurities, lattice (or phonon), boundaries scatterings etc.

Using the phonon gas model, the definition of thermal conductivity can be derived based on the kinetic theory of gases:

$$\kappa = \frac{1}{3} C_V v l \tag{11}$$

where C_v, v and l are the volumetric heat capacity, phonon velocity and phonon mean free path, which suggest the main factors determining the thermal conductivity of a material. Particularly, heat capacity is related to the phonon density, sound velocity to the distribution of phonon while phonon mean free path is affected by the scattering events. Realistically, the thermal conductivity of bulk materials κ can be measured based on the following equation:

$$\kappa = C_{\mathrm{p}} D \rho \tag{12}$$

where C_{p}, D and ρ are the heat capacity, thermal diffusivity and physical density of a material. It is worth mentioning that **Equation** (11) gives the estimation of thermal conductivity by only taking into account phonon contribution. To give a more accurate definition, it has to count in all heat carrying species including phonon and electrons (or charge carrier) so that the thermal conductivity will be the sum of terms similar to that in **Equation** (11) but from varied contributions. This is particularly true in metal and degenerated semiconductors, where the thermal conductivity, κ, has:

$$\kappa = \kappa_{\mathrm{ph}} + \kappa_{\mathrm{e}} \tag{13}$$

where ph and e denote phonon and electron (or charge carrier), respectively. The electronic thermal conductivity is coupled with the electrical conductivity via the empirical Wiedemann-Franz law:

$$\kappa_{\mathrm{e}} = L\sigma T \tag{14}$$

where L is the Lorenz number, which adopts the value of 2.44 x 10^{-8} W Ω K^{-2} for conductors with free electrons. **Equation** (14) implies that the electronic thermal conductivity is proportional to the electrical conductivity while high electrical conductivity and low thermal conductivity are desirable for high TE performance. Therefore, the electrical conductivity and total thermal conductivity are coupled by the electronic thermal conductivity.

1.3 Common Strategies to Improve TE Performance

According to **Equation** (4), it is obvious that all strategies to enhance TE performance should be about improving the electrical conductivity, increasing the Seebeck coefficient and/or suppressing the thermal conductivities. Because of the coupling relationships among these three parameters, it is better to discuss the common strategies individually instead of categorizing them into methods for tuning electrical conductivity, Seebeck coefficient or thermal conductivity.

1.3.1 Doping and Modulation Doping

So far, doping has been the most frequently used method for optimizing carrier density since most semiconductor materials of interest do not possess carrier densities optimal for TE performance, i.e. maximum power factors. Doping such materials can be realized by aniso-electronic substitutions. For instance, SiGe based alloys were doped into n-type semiconductors by phosphorus or arsenic and into p-type materials by boron.[7-10] Doping elements can be introduced by elemental form or compound, depending on the synthesis process, as long as atomic substitutions happen at target sites. Though it seems straightforward, special considerations should be taken to achieve effective doping, for example, the solubility of the doping element in a material. The solubility of elements determines their doping efficiency. In addition, it is worth evaluating whether the doping happens at the right site when the dopant dissolves into the matrix material. Another effective way to realize doping is to introduce vacancies by going off stoichiometry. For example, substantial enhancement in carrier concentration was obtained in SnSe by Sn vacancies.[11] Cu_2Se is usually found to be p-type semiconductor due to the formation of Cu vacancies and thus it was reported that engineering Cu vacancies can also optimize the carrier concentration, similar to extrinsic doping by exotic elements.[12-18]

The goal of doping is either to decrease or enhance the carrier concentration in under-doped or over-doped semiconducting materials. As a result, the electrical conductivity and Seebeck coefficient will be adjusted simultaneously towards an improved power factor. Further, the thermal conductivity can correspondingly increase or decrease due to the electronic contribution to thermal conductivity. A significant change in thermal conductivity is possible if the electronic thermal conductivity is comparable to or dominating over the lattice thermal conductivity, for instance in materials like Cu_2Se. Other effects of doping include enhanced electron scattering by ionized impurities, changed phonon scattering by charge carriers of varied density. All these effects arising

from doping have created various mechanisms of optimizing TE performance. For example, modulation doping, as a special form of doping, provides new opportunities to achieve high TE performance. Modulation doping essentially means heterogeneous doping in space. B Yu et al. have successfully achieved a high figure of merit zT by carrying out modulation doping in SiGe.[9] Similar success has also been reported in BiCuSeO[19] and half Heusler alloy[20]. High carrier mobility can be resulted from modulation doping when the dopant is only introduced to a limited area in a material such that ionized impurities are spatially restricted to the limited area. Therefore, modulation doping obtains a higher electrical conductivity at the same doping level compared to uniform doping, or a higher Seebeck coefficient at the same electrical conductivity, leading to an improved power factor. However, the challenge with modulation doping is to realize the spatially heterogeneous doping and later maintain it during service especially at high temperature.

Last but not the least, doping can also induce resonant states, which increases the charge carrier density of state and thus the Seebeck coefficient, according to Mahan-Sofo theory.[21] The enhancement in Seebeck coefficient via the increase in local density of state can be given in the Mott expression[22]:

$$\mathrm{S} = \frac{\pi^2}{3}\frac{k_B}{q}k_B T\left\{\frac{d\left[ln\left(\sigma(E)\right)\right]}{dE}\right\}_{E=E_F} = \frac{\pi^2}{3}\frac{k_B}{q}k_B T\left\{\frac{1}{n}\frac{dn(E)}{dE}+\frac{1}{\mu}\frac{d\mu(E)}{dE}\right\}_{E=E_F} \quad (15)$$

$$\sigma(E) = n(E)q\mu(E) \quad (16)$$

$$n(E) = g(E)f(E) \quad (17)$$

where $g(E)$ and $f(E)$ are the energy-dependent density of state and the Fermi-Dirac function. Comparing **Equation** (15) with **Equation** (7), the following relation can be derived:

$$(m_d^*)^{3/2} = \frac{g(E)}{\sqrt{2E}}\hbar^3\pi^2 \quad (18)$$

In other words, an increase in local density of state will enhance the effective mass of density of state and thus the Seebeck coefficient. J. Heremans et al. experimentally proved this strategy via Tl doping in PbTe.[23] Since high band effective mass leads to low carrier mobility, high density of state effective mass does not always mean high TE performance.[24-25] However, tuning effective mass through doping have been demonstrated as an effective strategy in optimizing power factors of TE materials, including PbTe[23, 26], FeNbSb[27-28], Mg_3Sb_2 [29]and BiCuSeO[30] etc.

1.3.2 Atomic Substitution/ Alloying

Atomic substitution/ alloying is another commonly adopted strategy to optimize electrical and/ or thermal properties of TE materials. This strategy is usually carried out by iso-electronic substitution of one or multiple elements in the compounds of interest. For example, both Si and Ge crystallize in the diamond-type structure and they can form complete solid solutions with each other, enabling a continuous change in bandgap of SiGe alloys by adjusting the Si/Ge ratio from zero to one.[31] Special attention should be paid to the solubility of the substitutional element since solid solution is the target. For example, Ti was reported to have a limited solubility in either ZrNiSn or HfNiSn while the latter two can form complete solid solutions.[32-33] Consequently, it will be impractical to synthesize single-phase half Heusler alloys with compositions like $Ti_{0.33}Zr_{0.33}Hf_{0.33}NiSn$, which will end up being composites of multiple half Heusler phases. It is therefore reasonable to choose substitutional elements from the same column where the targeted element sits in the periodic table, for relative compounds with similar structures are possible and so are the solid solutions. For example, S and Se can be chosen to alloy with PbTe at Te site[34] while Sn at Pb site[35].

One of the benefits from alloying is decreasing lattice thermal conductivity. When alloying, the exotic atoms are taken as point defects, which create mass and strain field fluctuations around the host atoms. The mass difference and strain field fluctuation can induce enhanced phonon scattering compared to the pristine materials with more ordered or perfect structures. According to Callaway's theory, the effect of point defects on thermal conductivity can be quantified by the following equation[36]:

$$\frac{\kappa}{\kappa_p} = \frac{1}{u} tan^{-1} u \tag{19}$$

where κ and κ_{p} are the lattice thermal conductivity of the defected and non-defected materials, respectively, while u is related to defect scaling factor Γ by:

$$u = \left(\frac{\pi^2 \theta_{\mathrm{D}} \Omega}{h v^2} \kappa_{\mathrm{P}} \Gamma \right)^{1/2} \tag{20}$$

where θ_{D}, Ω, h, υ are the Debye temperature, average volume per atom, Planck's constant and lattice sound velocity, respectively. Detailed calculation of defect scaling factor Γ can be found in literatures.[36-38] In the case of alloying, the point defect scaling factor is contributed by mass fluctuation Γ_{M} and strain field fluctuation Γ_{S}. According to **Equation** (20), a larger defect scaling factor will lead to more significant decrease in thermal conductivity in defected materials compared to that of non-defected materials. In the case of alloying, the defect scaling factor can be maximized by tuning the relative concentration of substitutional species.[36] Taking SiGe alloy for example, $Si_{50}Ge_{50}$ will have the maximum scaling factor and thus the lowest thermal conductivity, physically meaning the disorder or imperfection is maximized. Callaway's theory has been successfully proved experimentally in many materials. For example, an U-shaped thermal conductivity was observed for SiGe alloys with respect to the Si/Ge ratio, where the minimum

thermal conductivity always happened at compositions near $Si_{50}Ge_{50}$.[39] Similar phenomenon was also reported for $Ga_xIn_{1-x}As$.[40]

Another advantage of alloying is the capability of engineering the band structure of a material. The electronic structures of materials are determined by such factors as crystal structure, chemical species and interatomic bonding. Any changes to these factors will give rise to perturbations in the electronic structure. For example, the unit cell often expands or shrinks with alloying, leading to continuous broadening or narrowing of the bandgap. This again can be manifested in $Si_{1-x}Ge_x$ alloys.[31] However, band structure engineering includes not only the broadening or narrowing of a bandgap, but also the changes in the feature near the edge of conduction band or valence band that critically affects charge carrier transport, for example, band convergence to achieve high degeneracy. Y. Pei et al. reported a significant enhancement in *zT* for $PbTe_{1-x}Se_x$ via achieving high band degeneracy through Se alloying at Te sites.[41] It is noteworthy that temperature plays an important role in the band variation and degeneration as well. After Y Pei's work, many more similar success have been achieved in PbTe-based materials[42] and other TE materials, such as $Mg_2Si_{1-x}Sn_x$,[43-44] $Sn_{1-x}M_xTe$,[45-48] Mg_3Sb_2-Mg_3Bi_2,[49] $FeV_{1-x}Nb_xSb$,[50] $Ge_{1-x}M_xTe$[51] etc.

1.3.3 Nanostructuring

Nanostructuring is the most successful strategy so far to achieve improvement in thermoelectric performance. Nanostructuring strategy generally means strategies of introducing nanostructures into TE materials, including making nano-grained materials, making low-dimensional materials and making nanocomposites. For commercial application, bulk materials are still the major interest of research. Therefore, this section will mainly focus on making nano-grained bulk materials while nano composites will be covered in the following section. To achieve nano grains in bulk materials, non-equilibrium strategies are usually adopted, for example, ball milling (or mechanical alloying).

Successful synthesis of nanostructured bulk materials have been reported via mechanical alloying in many TE materials, such as Bi_2Te_3-based alloys,[52] SiGe alloys,[8, 10] SnTe,[53] AgPbSbTe[54] and MgAgSb[55] etc. Recently, X. F. Tang et al reported extensive research on making nanostructured TE materials using melt spinning technology, including BiSbTe,[56-58] skutterudites,[59-60] Zn_4Sb_3,[61] and $AgSbTe_2$ [62] etc. It is also common to use chemical synthesis methods to make nanostructured materials. For example, G. Zhang et al. reported ultrathin Bi_2Te_3 nanowires using a solution method.[63] The major concern about the nanostructured materials is the stability of the microstructures. Since most nanostructured materials are achieved by non-equilibrium methods, the structure will probably suffer great change during service especially at elevated temperatures, where atomic diffusion is sufficient to cause grain coarsening.

The major benefit arising from nanostructure is the depression of thermal conductivity, which is due to the decreased mean free path by the significantly increased grain boundaries. The phonons scattering is significantly enhanced at grain boundaries when the grains are refined to dimensions comparable to or below the mean free path of phonons. For instance, W. Xie et al. reported a dramatic decrease in thermal conductivity in nanostructured BiSbTe alloy, i.e. < 0.7 W m^{-1} K^{-1} compared to 1.4 W m^{-1} K^{-1} for materials by traditional method (zone melting).[56] G Joshi et al. have also successfully cut the thermal conductivity for SiGe alloys into almost half, from > 4.5 W m^{-1} K^{-1} for traditional SiGe alloys used on radioisotope thermoelectric generator (RTG) to ~2.5 W m^{-1} K^{-1}.[10] Similar success has been obtained in many other materials. It is the application of nanostructuring that boosts the figure of merit, zT, from sub unit to above one. Besides the stability of the nanostructure, another limitation of this strategy is that the electronic transport will be jeopardized when the crystal grains are refined to a few nano meters, which is comparable to the mean free path of charge carrier.

1.3.4 Compositing

It is very important to make materials of high purity to uncover their true properties, for example nearly perfect single crystals. On the contrary, it is critical to include and make use of defects when high material performance is targeted, for example, point defects created by doping or alloying. Composite materials essentially are mixtures of multiple phases, which are chemically and/ or structurally different from each other. The simplest way to make composite materials is to physically mix multiple phases together. More advanced method is to incorporate the formations of constituent phases into one synthesis recipe. The composite strategy is commonly used in thermoelectric materials. For example, many compounds were introduced into PbTe for better TE performance, such as Ag_2Te,[64] CdTe,[65] PbS/PbSe,[34] MgTe[66] etc. Similarly, full Heusler,[67-68] InSb,[69] ZrO_2,[70] WO_3[71] etc., were introduced in half Heusler and SiC, carbon nanotubes (CNT)[72-73], graphene[29, 74], nano boron[74], TiO_2 [75], SnSe[76], Ag_2Se[77], Cu_2S[78], $CuGaSe_2$[79] in Cu_2Se.

Originally, composite strategy in thermoelectric materials was about introducing nano particles to reduce the thermal conductivity.[80] The reduced thermal conductivity is attributed to the enhanced phonon scattering at vast phase boundaries. K. Biswas et al. reported high TE performance in PbTe by achieving an all-scale hierarchical structure, which leads to an enhanced phonon scattering at the full spectrum of phonon wavelength.[81] However, the advantage of composite strategy is far more than suppressing thermal conductivity. The action of including multiple components in one material system enables more degrees of freedom to manipulate material properties, particularly TE properties. This includes the choice of a secondary phase, the distribution of the secondary phase and the interaction between the secondary phase and the matrix. Further, the choice of a secondary phase and the material processing condition are the main factors that influence the distribution of the secondary phase and the interaction between the secondary

phase and matrix. Due to a high degree of freedom, it can be also challenging to untangle the effects of all acting factors. Generally speaking, evenly dispersed precipitates at nanoscale will lead to the decrease in thermal conductivity due to enhanced phonon scattering regardless of the nature of interfaces,[82-88] either coherent, semi-coherent or incoherent, which, however, does matter for electronic transport and coherent interfaces usually minimize the scattering of electron at the interfaces.

1.4 Thermoelectric Materials and Recent Development

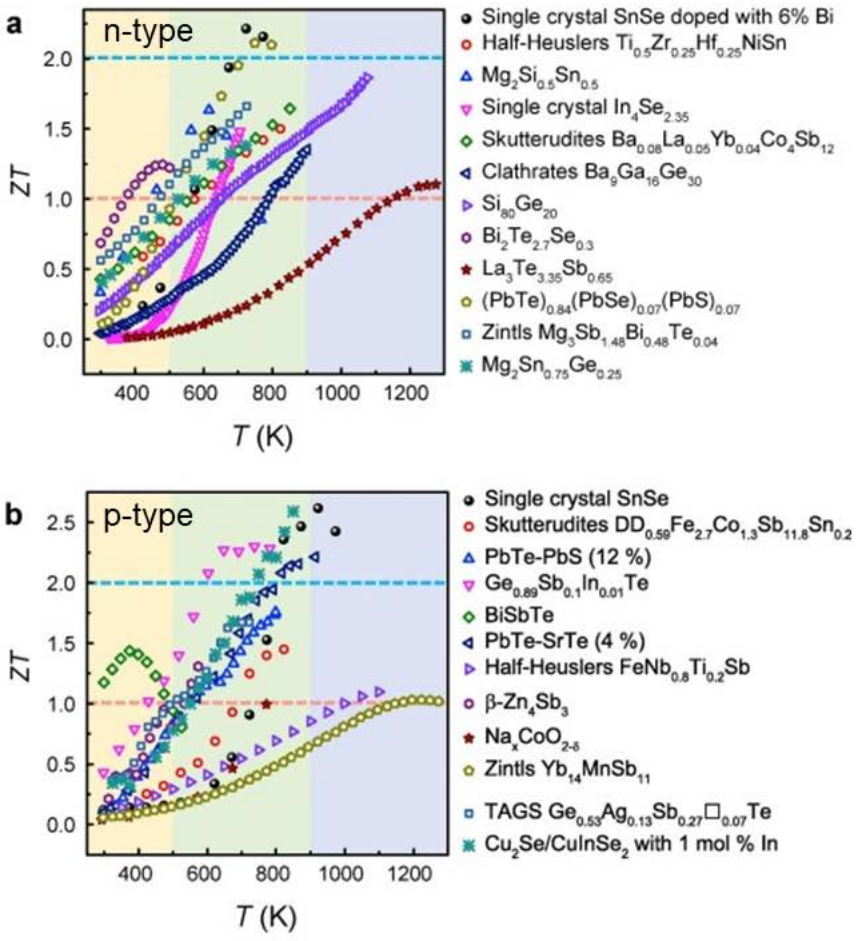

Figure 1-2. Typical thermoelectric materials in varied temperature ranges. (Reprinted with permission. © 2018 Elsevier Ltd)[89].

There are many TE materials reported so far despite of their very different performance. Based on the peak performance and stability of materials, they are categorized into three kinds, i.e. low-temperature (< 500 K), medium-temperature (500-900 K) and high-temperature (>900 K) TE materials. **Figure 2** shows the major TE materials and their figure of merits at varied temperatures. Among them, the low-temperature TE materials, such as Bi-Sb-Te alloys, are mainly for such applications as low-temperature thermoelectricity generation and thermoelectric refrigeration.

Recently, M. Kanatzidis et al. discovered more derivatives of Bi_2Se_3 and Bi_2Te_3, such as $K_2Bi_8Se_{13}$[90-91], $CsBi_4Te_6$[92-93], which show competitive TE performance near room temperature. The most well-known high-temperature thermoelectric materials are Si-Ge alloys, which are characterized by their high chemical stability and mechanical robustness. The Jet Propulsion Laboratory has done a lot research on SiGe alloys for the application of Radioisotope Thermoelectric Generators (RTGs).[94-97] Besides SiGe alloys, Zintl materials like $Yb_{14}MnSb_{11}$ are also reported as high-temperature TE materials.[98] As shown in **Figure 2**, many TE materials are clustering in medium-temperature range, among which are PbTe-based materials, Skutterudites, Clathrates, half Heusler alloys and copper chalcogenides etc. Recently, SnSe has attracted intensive research interest since L.D. Zhao et al. reported a high TE performance in single-crystalline SnSe.[99-100] Besides the materials shown in **Figure 2**, there have been many new materials reported as promising candidates for TE application, representing one of the major research activities in TE field. In addition to searching for new materials and strategies for making TE devices, most research is focusing on exploring effective strategies to optimize TE performance of the current TE materials, such as PbTe, half Heusler alloys, Copper chalcogenides etc.

1.4.1 Half Heusler Alloys

The half-Heusler (HH) alloys represent a fascinatingly large class of intermetallic phases with the

general composition TMX (T and M are transition metals or rare-earth metals and X is a main-group element) that crystallize in the MgAgAs-type structure (space group: *F*-43*m*). Their structure can be described as consisting of four interpenetrating *fcc* (face-centered cubic) sublattices of T, M and X atoms occupying respectively the crystallographic positions (0,0,0), (1/4, 1/4, 1/4), and (1/2, 1/2,1/2), whereas the fourth (3/4, 3/4, 3/4) position is vacant.[101-102] Materials parameters such as the type of crystal structure, the stoichiometry, the nature of the constituent elements and the valence electron concentration (VEC) dictate the physical and chemical properties of HH compounds. With careful selection of T, M and X atoms to satisfy a VEC = 18, HH phases with semiconducting behavior suitable for thermoelectric applications can be fabricated. Upon varying the chemical composition, one can tune the electrical band gaps (E_g ~0-4 eV) as well as the electronic and thermal properties of HH compounds.[103-110] This unique feature has led to a surge of research interest for the discovery of new physics and the development of multifunctional materials and devices for various important technological applications. For example, HH compounds have attracted tremendous attention as potential candidates for thermoelectrics,[67, 69, 71, 103-106, 108-109, 111-120] half-metallic dilute magnetic semiconductors (spintronics),[121-124] and topological insulators.[125-127]

Among HH phases, (Ti,Hf,Zr)NiSn and (Ti,Hf,Zr)CoSb are the most popular compositions investigated so far for high temperature power generation. These compositions attracted tremendous attention not only because the elements involved are cheap, abundant, lightweight and environmentally friendly, but also due to the combination of high Seebeck coefficients with moderately low electrical resistivities,[105, 107, 109, 112, 119-120, 128-130] which gives rise to intrinsically high power factors. However, high thermal conductivities associated with these HH compositions limit our ability to synthesize materials with decent figures of merit (zT>1). Therefore, significant

research efforts have been invested in the optimization of the thermoelectric figure of merit of HH alloys. For carrier density optimization, substitutional doping at the Sn (Sb) sites is the most effective method, as observed in (Ti,Hf,Zr)$NiSn_{1-x}M_x$ (M = Sb, Bi)[115-116, 128] and (Ti,Hf,Zr)$CoSb_{1-x}M_x$ (M = Sn, Ge).[112, 131] Alloying is also one of the most common strategies adopted for performance optimization in half Heusler alloys. The isoelectronic substitution can be carried out at various atomic sites in the structure, for example, the mixed occupation by Ti, Zr and Hf at T site in TMX[132], the substitution of Ni by Pd[129] and Co by Rh[110]. However, there has been rarely report about alloying at X site such as the substitution of Sn by Ge.[131] As mentioned earlier, special attention should be paid to the solubility of substituting elements in target half Heusler alloys. It is known that Ti has a very limited solubility (≤ 10 atm%) in either ZrNiSn or HfNiSn while ZrNiSn can have complete solid solutions with HfNiSn.[33] Therefore, synthesis of half Heusler alloys with compositions such as $Ti_{0.33}Zr_{0.33}Hf_{0.33}NiSn$ will most likely end up having composite materials including Ti-rich and Ti-poor half Heusler phases. The major effect of alloying is the reduction in thermal conductivity due to enhanced phonon scattering by mass fluctuation and/or strain fluctuation.[107, 128-129] However, other beneficial effects can also be expected in half Heusler alloys, for example, a variable bandgap can be achieved by alloying TiNiSn, ZrNiSn and HfNiSn, leading to the adjustable electrical conductivity and Seebeck coefficient.[103-104] Besides alloying, making nanometer-sized polycrystalline samples is another way to suppress the high thermal conductivity of half Heusler alloys by enhancing phonon scattering at grain boundaries[107, 113, 133-134].

Making composite materials seem particularly popular in the studies of half Heusler alloys. The easiest way to construct composite materials is the ex-situ approach, i.e. physically mixing the constituent phases together, which are pre-synthesized. So far, multiple oxides have been introduced as secondary phases at nanoscale in varied half Heusler matrices, including ZrO_2,[70, 133,

[135] HfO_2[136]and γ-Al_2O_3[137]. These metal oxides mainly act as phonon scattering centers to decrease the lattice thermal conductivity. However, the electronic transport was often degraded as well due to enhanced electron scattering. As a result, improved TE performance has been rarely reported in such composites. L. D. Chen et al. found that an improved power factor was achieved in $Zr_{0.5}Hf_{0.5}Ni_{0.8}Pd_{0.2}Sn_{0.99}Sb_{0.01}$ matrix by introducing a few molar percent of ZrO_2, due to the enhanced Seebeck coefficient, which is further attributed to the charge carrier scattering by the potential barrier formed at the hetero interfaces. However, the enhanced TE performance was mainly contributed by the suppressed thermal conductivity.[133] It implies that the effect of such inert oxides on electronic transport relies strongly on the matrix. Introducing other metal oxides such as WO_3,[71] NiO[108] and ZnO[138] leads chemical reactions with matrices, which usually leads to the degradation in TE performance. Such reaction with the half Heusler matrix leads to the formation of ZrO_2/HfO_2 and metallic compounds. It is therefore common to see a large increase in electrical conductivity but a severe depression in Seebeck coefficient, resulting in a poor power factor and figure of merit. Similar effect was also reported in half Heusler/C_{60} composites.[139] As a contrast, in-situ formed precipitates seem to have more effects than just lowering the thermal conductivity, for example, positive effect on electronic transport. W. Xie et al. reported a decrease in thermal conductivity and a simultaneous increase in both electrical conductivity and Seebeck coefficient for (Ti,Zr,Hf)(Co,Ni)Sb/InSb composites, where InSb and the half Heusler matrix were formed together during the synthesis.[69] The simultaneous increase in electrical conductivity and Seebeck coefficient is attributed to the fact that InSb, on one hand, acts as an electron dumper and, on the other hand, forms hetero interfaces with half Heusler matrix and therefore potential barriers, which scatters low-energy electrons.

The construction of composite materials for half Heusler alloys can be achieved based on the following two mechanisms as well, which will lead to a high similarity in both chemical composition and structure between the secondary phase and the matrix. The first method is based on the very limited solubility (≤ 10 atm%) of TiNiSn in ZrNiSn and/or HfNiSn.[33] When synthesizing material $Ti_{0.5}Zr_{0.5}NiSn$, composite materials will be achieved due to the incomplete solid solution between TiNiSn and ZrNiSn. The composite materials include Ti-rich and Ti-poor half Heusler phases, which are comparable in quantity, in contrast to composite materials with nano precipitates embedded in the half Heusler matrices. The other method is forming full Heusler precipitates in the half Heusler matrix by adding extra metal during the synthesis, for example extra Ni to form $TiNiSn/TiNi_2Sn$ composites. By controlling the amount of extra metal, the full Heusler precipitates can be formed at various scales, for example, nanoscale at low concentration of extra metal.[140] The advantage of this method is the possible coherent interfaces due to the chemical and structural similarities between half Heusler and corresponding full Heusler compounds. Previously, P. F. P. Poudeu et al. developed the strategy of "atomic-scale structural engineering of thermoelectric" (ASSET), i.e. constructing composite materials by in-situ forming nanoscale full Heusler precipitates within a half Heusler matrix. By taking advantage of the band offset at the interfaces, a strong modulation in electronic transport is expected. This is experimentally proved in non-doped half Heusler matrices, where a beneficial increase in both carrier mobility and Seebeck coefficient secures a high power factor, together with a decreased thermal conductivity, leading to the significant enhancement in figure of merit.[67-68] However, the performance is still low because the matrix was not doped to the optimized carrier density. Further, negligible effect on electronic transport was observed in the heavily doped half Heusler matrix when applying the ASSET strategy.[141] Similar issue has also been mentioned by Xie et al. when

introducing InSb as in-situ precipiates.[142] Therefore, further adjustment is needed to achieve similar effect in heavily doped systems.

1.4.2 Cu_2Se Based Materials

Cu_2Se has received tremendous research interest due to its intrinsically low thermal conductivity, the so-called "phonon-liquid-electron-crystal" (PLEC) material.[143] Cu_2Se adopts two different crystal structures in varied temperature ranges. At high temperature (> 400 K), Cu_2Se crystallizes in a cubic structure with space group Fm-3m, known as β-Cu_2Se, where Se atoms build the fcc framework with copper atoms randomly distributed over the 8 tetrahedral and 4 octahedral sites.[144-146] This leads to high diffusivities (of the order of 10^{-5} cm^2 s^{-1}) of Cu ions within the Se fcc sublattice, the so-called liquid-like state.[147] As a result, the ionic conductivity of Cu ions represents a non-negligible portion of the total electrical conductivity. For instance, an ionic conductivity was reported to be as high as 1000 S m^{-1} at 410 K for Cu_2Se.[148] Another consequence of the liquid-like behavior of Cu ions is the intrinsically low thermal conductivity of Cu_2Se, which is attributed to (i) a significant reduction of phonon mean free path and also (ii) a drop in the specific heat (C_v) due to the lowered density of phonon.[143] Below 400 K, the room-temperature phase, α-Cu_2Se, is thermodynamically favored. Unlike β-Cu_2Se, the α-Cu_2Se phase does not have a well-determined crystal structure. Several structures have been proposed for α-Cu_2Se, such as tetragonal[149], orthorhombic[149] and monoclinic[150-151] structures. Some research work also suggested that the room-temperature phase of Cu_2Se shows characteristics of a lamellar structure.[152-153] Lu et al pointed out that Cu ions adopt ordering in various ways with little energy difference, i.e. multiformity of Cu ordering in the Se lattice, which makes it hard to clarify the exact structure by diffractometry methods like X-ray diffraction.[153] Although stoichiometric Cu_2Se is expected to be an intrinsic semiconductor (bandgaps of ~1.23 eV reported for β-Cu_2Se),[154] freshly synthesized

Cu_2Se usually exhibits a p-type semiconducting behavior,[155] which is generally attributed to the Cu vacancies produced during the synthesis process. Because the crystal structure of β-Cu_2Se displays a high degree of tolerance to off-stoichiometry (Cu vacancies), the hole concentration and hence the electronic transport of freshly synthesized β-Cu_2Se can vary significantly with the synthesis conditions.[12, 156-159]

In fact, tuning Cu vacancies was used as an effective doping strategy to optimize the electrical properties.[12-13, 78, 156] Besides Cu vacancies, researchers have also been exploring chemical species for doping in Cu_2Se. For example, R. Bhardwaj et al. reported a complicated doping effect from Mg, i.e. increasing the hole concentration though it is expected to be n-type dopant.[160] T. Bailey et al. tried Sn doping in Cu_2Se while the secondary phase SnSe was developed even at low concentration of Sn.[161] P. Peng explored the doping effects from multiple metallic elements, including Al, Zn, Ni, Fe, Mn, In, Sm,[14, 18, 162] and found that all metallic elements except In acted as p-type dopants while In as a n-type dopant. Halogens like Cl, Br and I were observed to be n-type dopants, which simply compensates the hole concentration by dumping electrons.[15-17] Other elements include Bi[163], Hg[164]. Besides, there were also research work on iso-electronic "doping" at Cu site using elements like Li[165], Na[166], K[164] and Ag[167]. Further, Li, Na and K "doping" at Cu site all lead to a decrease in hole concentration, though they were iso-electronic substitutions, which hints at a possible anchoring effect on mobile Cu ions, leading to the improved chemical stability and lower Cu vacancies. Similarly, Ag substitution at Cu sites tends to decrease the electrical conductivity.[167-168] Although the electrical properties show good trends with the amount of doping elements, it is worth mentioning that secondary phases often form above a certain concentration, for example, CuAgSe in Ag doped Cu_2Se.[167] The iso-electronic substitution strategy has also been applied at Se site as well, i.e. alloying with Tellurium and/ or Sulphur. L. Yang et al.

reported an increasing electrical conductivity with low concentration Te ($\leqslant$ 10 at%) alloying at Se site.[169] K. Zhao et al. expanded the alloying to a broader range from pure Cu_2Se to pure Cu_2Te, in which pure phases were reported for various compositions but with varied crystal structures.[159] Consistent with Yang's work, alloying Te at Se sites, overall, increased the carrier concentration, which was attributed to the enhanced Cu deficiencies. Similarly, L. Zhao et al. conducted an extensive study on S alloying at Se sites in Cu_2Se in a broad range from pure Cu_2Se to pure Cu_2S, where single phases formed at the end compositions with S concentration either $\leqslant$ 16 at% or $\geqslant$ 80 at% while composites formed at compositions in between.[170] Contrary to Te alloying, S alloying decreases the electrical conductivity. In that case, the alloying with chalcogens like S and Te may affect the electrical properties by changing the bandgap. K. Zhao et al. further optimized the electrical properties and thermoelectric performance by co-engineering Cu deficiency and S alloying at Se site.[170]

In addition to atomic engineering at Cu and Se sites, making composites materials has been the most common strategy to tune TE properties via introducing secondary phases in Cu_2Se. For example, high S content in Cu_2Se leads to phase separation so that a hierarchical structure forms at compositions like $Cu_2Se_{0.5}S_{0.5}$.[170] S. Ballikaya et al. reported an enhanced TE performance via the incorporation of 4 mol% nano Ag_2Se particles, mainly due to the suppressed thermal conductivity.[77] Unfortunately, no further explanation was given regarding how the microstructure decreased the thermal conductivity and also how the introduced phase affected the electrical properties. F. Liu et al. reported an increase in resistivity for Cu_2Se with the introduction of SnSe and a significant enhancement in zT was resulted from an improved power factor and a decreased thermal conductivity.[76] Carbon materials have received special interest as secondary phases for making composite materials. For example, X. Wang et al. studied TE properties of Cu_2Se-based

composites with various carbon materials, including carbon nanotubes, graphite, hard carbon, graphene etc., and high TE performances were achieved attributed to the decreased thermal conductivity.[72, 74] However, it is interesting for them to report two optimal concentrations of graphene in Cu_2Se for the best TE performance. Similarly, ultrahigh TE performance was reported by R. Nunna et al. in Cu_2Se/CNTs composites, in which an organic/inorganic hybridization occurs and significantly lowers the thermal conductivity from ~1.2 W m^{-1} K^{-1} for the pristine Cu_2Se to 0.4 W m^{-1} K^{-1} for sample Cu_2Se/0.75 wt% CNTs.[73] Recently, F. Liu et al. have successfully synthesized $(Cu_2Se)_{1-x}(CuGaSe_2)_x$ composites by the traditional melting process and reported the TE properties of the $CuGaSe_2$-incorporated Cu_2Se.[79] The secondary $CuGaSe_2$ did not appear until x = 0.01 (1 mol% $CuGaSe_2$) from the XRD observations and $CuGaSe_2$ particles were seen, in the sample with x = 0.025, on the scale of a few hundred nanometers, which tended to agglomerate together. The resulted figure of merit, *zT*, was marginally improved due to the little enhancement in power factor and the increased thermal conductivity with the introduction of $CuGaSe_2$. Recently, Olvera et al. achieved an improved chemical stability and high TE performance in Cu_2Se through the in-situ formation of $CuInSe_2$ nanoinclusions.[171] Contrary to $CuGaSe_2$, an increase in power factor simultaneous with a decrease in thermal conductivity leads to a ultrahigh figure of merit, *zT* when 1 mol% and 3 mol% $CuInSe_2$ were introduced in Cu_2Se matrix. It was suggested that $CuInSe_2$ has a very low solution limit (~ 1 mol%) in Cu_2Se and the partial solution together with the secondary $CuInSe_2$ happens at high concentration of $CuInSe_2$. There were other phases reported as secondary phases introduced in Cu_2Se, such as SiC nanoparticles[172], TiO_2 nanoparticles[75] and amorphous Boron[74].

Over the years, there have been many works on Cu_2Se reporting ultrahigh TE performance with *zTs* > 2.0. Careful examining them implies that all the achievements are due to the extremely

low thermal conductivities. However, it is important to view the reported values in a critical manner. There are substantial errors in measuring thermal conductivity of TE materials[173] and other nonmaterial factors also affect the conductivity to a great extent, such as porosity. Instead, it is more meaningful to analyze the evolution of TE properties within the same series of samples using the same internal standard[173], so as to evaluate the effectiveness of the strategies applied.

1.5 Current Challenge and Proposed Study

As discussed, the challenge in making high-performance thermoelectric materials is to break the coupling relationships between electrical conductivity, Seebeck coefficient and thermal conductivity. So far, the best TE performance is mainly reported in materials with intrinsically low thermal conductivities, for example, AgPbSbTe,[174] Cu_2Se[171] and SnSe[99]. Even so, the efficiencies of TE materials are not comparable to those of other energy technologies, for example, photovoltaics. For current TE materials, especially those with low thermal conductivities either inherently or achieved artificially, it is extremely challenging or even impossible to enhance the performance by further pushing the lower limit of thermal conductivity. Therefore, optimization of the electrical properties, i.e. electrical conductivity and Seebeck coefficient, will be an inevitable route to achieve high-performance TE materials, reaching efficiencies required for actual commercialization. Due to the coupling relation between electrical conductivity and Seebeck coefficient, it seems as challenging to optimize them as it is to push the lower limit of thermal conductivity. Recently, there have been reported many novel strategies for the optimization of electrical properties, such as band engineering[24] and modulation doping[9], which can decouple the electrical conductivity and Seebeck coefficient. For example, high carrier mobilities and large Seebeck coefficients were reported in PbTe through increasing band degeneracy.[24-25, 41] Exploring more strategies is of great significance and absolutely necessary.

Originally, composite strategy in thermoelectric materials was about introducing nano particles to reduce the thermal conductivity.[80] However, the advantage of composite strategy is far more than suppressing thermal conductivity. The action of including multiple components in one material enables more degrees of freedom to manipulate materials properties, particularly TE properties. This includes the choice of a secondary phases, the distribution of the secondary phase and the interaction between the secondary phase and the matrix. Most research about composite strategy has focused on the first factor, i.e. trying various impurity phases with rare attention to the latter two. For example, a lot of composites with ex situ precipitates have marginal effects on the electronic transport due to the lack of interaction between the precipitate and the matrix. However, these three factors can be equally important, and the choice of an impurity phase will significantly affect its distribution and interaction with the matrix. The distribution of precipitates and microstructures also heavily rely on materials processing conditions. It is the chemical species and the microstructure, especially the interfaces, which determine the interactions. With such a high degree of freedom, it is possible to break apart the coupling relations between thermoelectric parameters and to give rise to strong modulations in electronic transport, as well as in thermal transport. This thesis is dedicated to exploring novel composite strategies for making high-performance TE materials. Different from the traditional method, we design special synthesis routes to make composite materials via the in-situ formations of secondary phases in target matrices, intending to achieve unique interfaces between the impurity and the TE matrix and thus beneficial interaction between them. Generally, high density of interfaces of excellent coherency will be beneficial for ensuring good electronic transport and suppressing thermal transport. However, we have to keep an open mind to other interfaces where complicated interactions

happen, which may lead to positive effects on TE performance as well. Particularly, the research content will include:

1. Using magnetic full Heusler precipitates to optimize the TE properties of half Heusler alloys;
2. Exploring novel ternary compounds as the secondary phase for the optimization of TE properties in Cu_2Se, including $CuGaSe_2$, $CuFeSe_2$, and $CuAlSe_2$, which are chemically close relatives to Cu_2Se.

The first part will be the content of Chapter 3. For the second part, the studies of Cu_2Se-based composites with $CuGaSe_2$, $CuFeSe_2$ and $CuAlSe_2$ will be the contents of Chapter 4, Chapter 5 and Chapter 6, respectively. All these ternary compounds are chemically related to Cu_2Se and crystallized in the chalcopyrite structure, which make them possible to synthesize together with Cu_2Se from a common precursor, $CuSe_2$. However, every compound stands out from another due to their unique chemical nature and microstructure to be developed, and thus various interactions with Cu_2Se will be expected.

Chapter 2 : Experimental Methods

2.1 Introduction

In this chapter, the major methods related to this thesis research will be listed and briefly described. The experimental methods will include the synthesis, composition and microstructure characterizations and physical property measurements, including electrical conductivity, Seebeck coefficient, thermal conductivity and magnetism etc. Experimental details for each project can be found later in the corresponding chapter.

2.2 Materials Synthesis

The materials synthesis is carried out using solid-state reactions, which are chemical reactions in solid state. Two major techniques were utilized in this work: high-temperature solid-state reaction in tube furnaces and room-temperature mechanical alloying (ball milling). High temperature solid-state reaction has been adopted in the synthesis of half Heusler/full Heusler composites materials (Chapter 3), (1-x)Cu_2Se/(x)$CuFeSe_2$ composites (Chapter 5), (1-x)Cu_2Se/(x)$CuAlSe_2$ composites (Chapter 6), (1-x)Cu_2Se/(x)$CuCrSe_2$ composites (Chapter 7) and (1-2x)Cu_2Se/(x)Cu_3SbSe_3 composites (Chapter 7). Room temperature mechanical alloying has been used in the synthesis of (1-x)Cu_2Se/(x)$CuGaSe_2$ composites (Chapter 4).

The general process of high temperature solid-state reaction includes the following steps: 1) weighing and mixing raw materials under Argon atmosphere; 2) vacuum sealing the well mixed materials in quartz tubes; 3) reacting at high temperature in tube furnace. For the first step, raw materials are usually elementary power or pre-synthesized compounds. For chemical reaction in furnace, specific temperature programs should be considered for different materials.

The general process of room temperature mechanical alloying includes: 1) weighing raw materials and loading them into agate jars with agate milling balls under Argon atmosphere; 2) ball milling to finish chemical reaction under Argon atmosphere. When transferring loaded agate jars out of glove box, it is necessary to conduct vacuuming to seal the jars under a low pressure of Ar atmosphere. The reaction is controlled by ball milling recipe, which includes sample to ball ratio in mass/volume, ball milling time and ball milling speed etc.

To carry out measurements of thermoelectric properties, bulk samples are usually required. In this work, all bulk samples have been made by condensing the synthesized powder samples using uni-axial hot press system. The pressing process was carried out under vacuum at a proper temperature with a pressure applied. Specific pressing conditions should be chosen accordingly for varied samples.

2.3 Materials Characterizations

Materials characterizations mainly include composition analysis and microstructure observations. After solid-state reaction, powder X-ray diffraction (PXRD) and/ or differential scanning calorimetry (DSC) are used to investigate the phase compositions, for example, the formation of secondary phase and matrix phase and the thermal events of the composite materials. XRD profiles are collected again after hot press to confirm the phase purity of the bulk samples, which represent the states where all the thermoelectrical properties and magnetic properties are measured later. It's important to choose proper pressing conditions so that only densification process happens without any undesirable reaction such as decomposition, which would change the phase composition. Besides doing qualitative analysis of what phases are present, quantifications of each phase can be obtained using either the relative intensity ratio (RIR) method or the whole profile pattern fitting

(WPPF) method. The latter can also extract the lattice parameters from XRD patterns based on Rietveld refinement.

The microstructure observations are first carried out under secondary electron microscope (SEM). Back scattered electron (BSE) images can give a good Z (atomic number) contrast, which is applied to investigate the distribution of secondary phase within matrix materials, for example, full Heusler precipitates in half Heusler matrix. Mirror finish polish is conducted on bulk samples to make sure the high quality of back scattered electron signal without much topographic information. Energy dispersive spectroscopy (EDS), integrated on SEM system, can further measure the compositions of different phases and/ or map the distributions of constituent elements within a sample. Sometimes, electron probe micro analysis (EPMA) is adopted to obtain the precise compositions at microscale.

Microstructure studies are continued at sub-micron scale under scanning transmission electron microscope (STEM), which enables observations of a very narrow area at nano or even atomic scale. The STEM samples are prepared by the lift-out method using focus ion beam (FIB) under SEM, which can precisely choose the area of interest, for example, phase boundaries.

In this work, the XRD patterns are mainly collected on Rigaku Smartlab operating at 40 kv and 44 mA using monochromated Cu-Kα radiation source. BSE images and EDS analysis are conducted on JEOL JSM-7800FLV SEM equipped with Oxford XMaxN 80 mm2 silicon-drift energy-dispersive X-ray spectrometer. TEM samples are made on Thermo Fisher Helios 650 Naonlab SEM/FIB. STEM observations are carried out on JEOL 2100F Probe-Corrected Electron Microscope and JEOL 3100R05 Double Cs Corrected TEM/STEM.

2.4 Thermoelectric and Magnetic Properties Measurement

The electrical conductivity and Seebeck coefficient are measured simultaneously based on four-probe method. The sample for such measurement is usually a rectangular bar (3 x 3 x 10 mm^3) cut out of a pressed pellet. Good polishing is necessary to achieve a good surface for an ohmic contact with the probes. A precise measure of the dimensions of a sample bar is important for the calculations of electrical conductivity and Seebeck coefficient. All measurements are conducted under a low pressure of Helium atmosphere. Charge carrier density is measured based on Hall Effect and together with electrical conductivity, charge carrier mobility can be calculated. High-temperature hall measurement usually uses a bar sample of 1 x 3 x 8 mm^3.

For thermal conductivity measurements, it's less straightforward compared to electrical conductivity and Seebeck coefficient. According the **Equation** (12), thermal conductivity can be calculated by multiplying the density, thermal diffusivity and heat capacity of a sample. The thermal diffusivity is measured based on the laser flash analysis (LFA) while the heat capacity is determined by the comparative method. The sample density is measured by a Helium gas pycnometer. The sample for such measurements is usually a flat pellet with diameter of 10 mm. Proper thickness should be chosen for varied sample to be measured, for example, thinner sample should be used for materials with low thermal conductivities to increase the accuracy and measurement efficiency. The lattice thermal conductivity is calculated by subtracting the electronic thermal conductivity from the total thermal conductivity, where electronic thermal conductivity is calculated based on the Wiedemann-Franz law (**Equation** 14). In calculating electronic thermal conductivity, Lorenz number is 2.44 x 10^{-8} W Ω K^{-2}, also known as degenerate limit. Lorenz number has a strong dependence on electronic density of state and doping level.[175-176] Using the degenerate limit to calculate electronic thermal conductivity may lead to a significant error, which will misevaluate the electronic and lattice thermal conductivities in total thermal

conductivity. This is particularly true in materials with low thermal conductivities, where electronic thermal conductivity accounts for a significant portion of the total thermal conductivity. Therefore, temperature dependent Lorenz constants were calculated using the following equations under the single band approximation[177]:

$$L = \left(\frac{k_B}{e}\right)^2 \left(\frac{\left(r+\frac{7}{2}\right)\left(r+\frac{3}{2}\right) F_{r+\frac{1}{2}} F_{r+\frac{5}{2}}(\xi) - \left(r+\frac{5}{2}\right)^2 F^2_{r+\frac{3}{2}}(\xi)}{\left(r+\frac{3}{2}\right)^2 F^2_{r+\frac{1}{2}}(\xi)} \right) \tag{21}$$

$$F_n(\xi) = \int_0^\infty \frac{x^n}{1+e^{x-\xi}}\, dx \tag{22}$$

$$\xi = E_f / k_B T \tag{23}$$

$$|S| = \frac{k_B}{e}\left(\frac{\left(r+\frac{5}{2}\right) F_{r+\frac{3}{2}}(\xi)}{\left(r+\frac{3}{2}\right) F_{r+\frac{1}{2}}(\xi)} - \xi\right) \tag{24}$$

where k_B, e, ξ and F_n are Boltzmann constant, elementary charge, reduced Fermi energy and Fermi integration respectively while r is the scattering parameter, which is -1/2 for acoustic phonon scattering and 3/2 for ionized impurity scattering and S the Seebeck coefficient of a material. Thermoelectric figure of merit zT is calculated according to **Equation** (4). It is worth mentioning that because electrical and thermal properties are collected separately on different instruments, it is necessary to fit the data as to calculate zT using values at the same temperature. Though measured along different directions, the electrical and thermal properties represent the properties

of the bulk samples if the materials studied are isotropic, for example, cubic half Heusler alloy and cubic Cu_2Se.

The magnetic properties are collected by the vibrating-sample magnetometer. The sample for such measurement is powder enclosed in a polypropylene sample holder. The measurement includes temperature scan of magnetic moment under field cooled (FC) and zero-field cooled (ZFC) conditions and field scan of magnetic moment at certain temperatures.

In this work, the electrical conductivity and Seebeck coefficient are collected simultaneously on ULVAC-RIKO ZEM-3 system. The thermal diffusivity and heat capacity data are measured on Linseis LFA-1000. Sample density is measured on Micromeritics Accupyc II 1340. Low-temperature and high-temperature hall measurements are carried out on home-built apparatuses. Magnetic properties measurements are conducted on either MPMS-CL SQUID or PPMS by Quantum Design.

Chapter 3 : Coherent Magnetic Nanoinclusions Induce Charge Localization in Half-Heusler Alloys leading to High-T_c and Enhanced Thermoelectric Performance

3.1 Introduction

Limited enhancements in the TE performance are expected through the application of the nanostructuring concept alone, due to the existence of lower limits to thermal conductivities of materials, the so-called glass limits κ_g.[6, 178-187] The thermal conductivities of some leading thermoelectric materials under investigation are already approaching their glass limits,[181-187] while their figure of merit *zT* still does not ensure efficiencies comparable to that of other energy conversion technologies, such as photovoltaics.[188-189] Additionally, electron scattering will become severe as grains are refined to sizes as small as few nanometers,[176, 190-191] comparable to the mean free path of electrons. Therefore, the benefit from the suppressed thermal conductivity may be counteracted by the degradation in electrical transport, giving marginal improvement in the figure of merit. As a result, further significant enhancements in the thermoelectric performance should include optimization of the electronic parameters, i.e., electrical conductivity σ and Seebeck coefficient *S*. However, it is challenging to improve both parameters simultaneously since they are adversely coupled by the carrier concentration.[6] Recently, band engineering,[6, 24, 41, 43, 192] modulation doping,[9, 19, 193-194] energy filtering,[67-68, 195-196] etc., have been reported as appropriate strategies to tailor the electronic properties of TE materials.

Making composite materials is a popular strategy to engineer thermoelectric properties of half Heusler. Chai *et al.* have systematically studied the structural evolution of HH by HRTEM when introducing extra Ni and concluded that the FH phases form because of clustering of extra Ni,

which confirms the results from theoretical calculations.[197-198]. Phase segregation has an important effect on the transport properties in the HH alloys as has already been demonstrated in HH/FH composites. Another important phase separation process occurring in the HH alloys with general composition $Ti_xZr_yHf_{1-x-y}NiSn$ is the formation of Ti-rich and Ti-poor phases with HH structure when the amount of Ti exceeds the solubility limit in the Zr(Hf)-based HH alloy.[32-33, 199-200] Previously, our group introduced the concept of atomic scale structural engineering of thermoelectrics (ASSET),[67-68] as an elegant approach to achieve simultaneous enhancement in the power factor and reduction in the thermal conductivity using suitable nanoinclusions that are coherently embedded within the matrix. We demonstrated the successful fabrications of nanocomposites consisting of a HH matrix with coherently embedded ultrafine full-Heusler (FH) inclusions.[67-68, 201] By taking advantage of the band offset at the interfaces, a strong modulation in electronic transport is expected. This is experimentally proved for non-doped half Heusler matrices, where a beneficial increase in both carrier mobility and Seebeck coefficient secure a high power factor and together with decreased thermal conductivity, lead to significant enhancement in figure of merit.[68, 201] However, the performance is still low because the matrices were not doped to optimized carrier density. Further, negligible effect on electronic transport was observed in heavily doped half Heusler matrix when applying the ASSET strategy. Therefore, an even stronger modulation is needed in heavily doped systems. Traditionally, it was thought that magnetism would not benefit thermoelectric performance and could even be detrimental due to localization effects and/or enhanced electron scattering by magnetic moments. However, Tsujii and Mori pointed out that strong interactions between extrinsic carriers and magnetic moments could potentially yield a large Seebeck coefficient, as they found in $CuFeS_2$, by enhancing charge carrier effective mass.[202-204] Recently, improved thermoelectric performance have been achieved through

suppression of intrinsic charge carrier excitations using the magnetic transition of embedded particles.[202-204]

In this study, we investigate the interplay between both types of phase segregation in $Ti_{0.25}Zr_{0.25}Hf_{0.5}NiFe_xSn_{0.975}Sb_{0.025}$ HH/FH composites obtained through incorporation of various amounts of elemental Fe into a HH matrix with optimized doping level.[199] It is anticipated that the added elemental Fe will fill in tetrahedral vacancies within the HH crystal lattice, enabling the formation of nanoscale inclusions with FH structure within the HH matrix via a similar reaction mechanism previously proposed for the Ni-incorporated HH systems.[67-68] By adjusting the Fe concentration, one can tune the density and average particle size of Fe-containing FH (Fe-FH) inclusions within the composites. Meanwhile, phase separation into Ti-rich and Ti-poor phases with HH structure is also anticipated in $Ti_{0.25}Zr_{0.25}Hf_{0.5}NiSn_{0.975}Sb_{0.025}$, given the high substitution level of Ti beyond the solubility limit of Ti in Zr(Hf)-based HH alloys.[32-33, 205-208] Here, we report that the incorporation of coherent magnetic nanoinclusions (Fe-FH) into half-Heusler (HH) alloys with optimized doping level ($Ti_{0.25}Zr_{0.25}Hf_{0.5}NiFe_xSn_{0.975}Sb_{0.025}$) induces charge localization and formation of overlapping bound magnetic polarons leading to (1) high-T_c ferromagnetism along with (2) enhanced thermoelectric figure of merit owing to the drastic reduction of the effective carrier density, large increase in the carrier mobility and Seebeck coefficient, as well as a significant decline in the electronic contribution to the thermal conductivity. We attempt to rationalize the interesting electronic transport and magnetic properties resulting from the multiscale engineering of the internal structure of heavily doped $Ti_{0.25}Zr_{0.25}Hf_{0.5}NiFe_xSn_{0.975}Sb_{0.025}$ HH/FH composites by integrating the concepts of the energy filtering effect at nanoscale FH/HH interfaces[67-68, 195-196] with charge carrier localization by nanoscale magnetic FH inclusions embedded within the HH matrix.

3.2 Experimental Details

Synthesis. To synthesize $Ti_{0.25}Zr_{0.25}Hf_{0.5}(Ni,Fe_x)Sn_{0.975}Sb_{0.025}$ (x = 0-0.15) composites, elemental powders of high purity were weighed and thoroughly mixed using agate pestle and mortar under Ar atmosphere in a glove box. The mixed powder was then loaded into a quartz tube and sealed under residual pressure of 10^{-3} Torr. The powder was heated at 673 K for 24 hours and subsequently heated at 1173 K for 300 hours. The resultant powder after solid-state reaction was ground, sealed in a quartz tube, and further annealed at 1173 K for another 168 hours to make sure the starting elements are thoroughly reacted. High-density pellets were obtained by sintering the powder from solid-state reaction at 1173 K for 1 hour under an applied pressure of 100 MPa using a uniaxial hot press.

Characterization. Composition and microstructure characterization are described in Chapter 2. The electrical conductivity and Seebeck coefficient were measured simultaneously from room temperature to 773 K using the four-probe method on a commercial ULVAC-RIKO ZEM-3 system under a low-pressure helium atmosphere. The specific heat capacity and thermal diffusivity were measured on a laser flash system (Linseis LFA-1000) from room temperature to 773 K. The density of the pressed pellets was measured using Helium gas pycnometry on Micromeritics Accupyc II 1340. Low temperature and high temperature Hall measurement were carried out under a magnetic field of 1 T on a home-built apparatus to evaluate the carrier concentration and mobility. The magnetic moment data were collected using a Quantum Design MPMS-CL SQUID magnetometer. DC magnetic moment under field cooled (FC) and zero-field cooled (ZFC) conditions were measured on powder of samples of selected $Ti_{0.25}Zr_{0.25}Hf_{0.5}(Ni,Fe_x)Sn_{0.975}Sb_{0.025}$ compositions over a temperature range of 2-800 K with an applied field of 100 Oe.

3.3 Result and Discussion

3.3.1 Structure and Composition

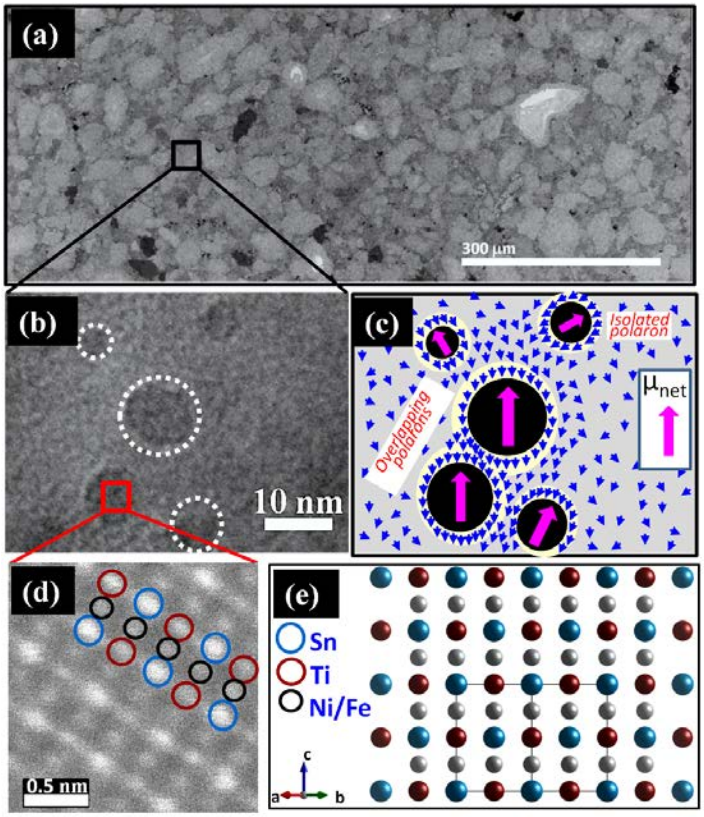

Figure 3-1. Microstructure of $Ti_{0.25}Zr_{0.25}Hf_{0.5}(Ni,Fe_{0.05})Sn_{0.975}Sb_{0.025}$ composites: (a) SEM image showing micron scale (Ti,Fe)-rich (black) and (Zr,Hf)–rich (grey) grains; (b) HRTEM image of a (Zr,Hf)-rich grain showing the presence of nanometer scale (Ti,Fe)-rich inclusions; (c) schematic illustration of bound magnetic polarons (BMPs) formed through magnetic interactions between magnetic (Ti,Fe)-rich inclusions in (b) and itinerant electrons; (d) atomic scale resolution image of one of the (Ti,Fe)-rich inclusions in (b) showing the FH structure; (e) a schematic representation of the (110) plane of a FH structure.

Several compositions of the $Ti_{0.25}Zr_{0.25}Hf_{0.5}(Ni,Fe_x)Sn_{0.975}Sb_{0.025}$ (x = 0-0.15) HH/(Fe-FH) composites were synthesized as described in the Experimental Section (Supporting Information). A combination of scanning electron microscopy (SEM), high-resolution transmission electron microscopy (HRTEM) and powder X-ray diffraction (PXRD) confirmed both the formation of nanoinclusions with FH structure (**Figure 3-1**) and phase separation of the HH matrix into Ti-rich and (Zr,Hf)-rich HH phases (**Figure A1-1** to **A1-3**). For instance, all major diffraction peaks on the XRD patterns of various compositions can be indexed to the cubic MgAgAs structure (**Figure**

A1-1). However, a close-up look at the 220 peak indicated splitting, suggesting the presence of multiple phases with closely related crystal structure and similar lattice parameters. For the samples with x = 0 and x = 0.02, three shoulder peaks can be identified that are associated with the formation of Ti-rich and Zr-rich phases embedded within an Hf-rich HH matrix (**Figure A1-2**).The PXRD analysis is also consistent with the back-scattered electron (BSE) images of these two samples (**Figure A1-3**), which show a random dispersion of the Ti-rich HH domains (black) within a (Zr, Hf)-rich (grey) HH matrix. Upon increasing the Fe content to 5 at%, the shoulder peaks disappear leading to a large single 220 peak. This suggests either a decrease in the fraction of the Ti-rich phase within the (Zr/Hf)-rich HH matrix, or the formation of the Ti-rich phase with very small sizes and/or the coexistence of multiple phases with very similar lattice parameters. Indeed, the SEM images of the sample with x = 0.05 revealed the presence of a small fraction of microscale Ti-rich phase (**Figure 3-1** and **A1-3**), and HRTEM images of the (Zr,Hf)-rich regions indicate the formation of nanometer scale Ti-rich inclusions. In addition, composition mapping and EPMA (electron probe microanalysis) point analysis (**Table A1-1**) revealed the coexistence in various $Ti_{0.25}Zr_{0.25}Hf_{0.5}(Ni,Fe_x)Sn_{0.975}Sb_{0.025}$ compositions of a Ti-rich FH phase with composition $Ti(Ni_{4/3}Fe_{2/3})Sn$ along with Zr-rich and Hf-rich HH phases. It is interesting to note from the EPMA result (**Table A1-1**) that while the $Ti_{0.25}Zr_{0.25}Hf_{0.5}NiSn_{0.975}Sb_{0.025}$ HH composition naturally phase separates into Ti-rich and (Zr,Hf)-rich phases, the added Fe tends to mix exclusively with the Ti phase to form (Ti,Fe)-rich nanoinclusions ($Ti(Ni_{4/3}Fe_{2/3})Sn$) with the FH structure embedded within the (Zr,Hf)-rich HH matrix. The lattice parameter of the $Ti(Ni_{4/3}Fe_{2/3})Sn$ phase in the cubic FH structure (Fm-3m) was estimated to be 6.073 Å assuming the formation of a $TiNi_{2-y}Fe_ySn$ solid solution (with y = 2/3) between $TiNi_2Sn$ (a = 6.076 Å),[209] and $TiFe_2Sn$.(a = 6.068 Å).[210-211] The similarity in the lattice parameters of the $Ti(Ni_{4/3}Fe_{2/3})Sn$ FH

phase and the solid solutions between the HH phases (F-43m) TiNiSn (a = 5.930 Å),[209] ZrNiSn (a = 6.123 Å),[212] and HfNiSn (a = 6.0756 Å),[213] helps explain the overlapping of their 220 peaks in the sample with x = 0.05 (**Figure A1-1**). As the Fe content in the starting mixture increases, the population density and average size of the (Ti,Fe)-rich FH phase, $Ti(Ni_{4/3}Fe_{2/3})Sn$, within the resulting composites increase (**Figure A1-3**, **Table A1-1** and **A1-2**) whereas the fraction of Ti within the matrix decreases according to the chemical **Equation** (26).

$$0.25\ Ti + 0.25\ Zr + 0.5\ Hf + Ni + Sn + x\ Fe \rightarrow 3x/2\ Ti(Ni_{4/3}Fe_{2/3})Sn\ (FH\ inclusion) + [Ti_{(0.25-1.5x)}Zr_{0.25}\ Hf_{0.5}]Ni_{(1-2x)}Sn_{(1-1.5x)}\ (HH\ matrix) \quad (26)$$

Therefore, as the Fe content increases, an increasingly larger fraction of the sample consists of the $Ti(Ni_{4/3}Fe_{2/3})Sn$ FH phase and Hf-rich HH phase with a smaller lattice parameter (6.073 Å) compared to ZrNiSn (6.123 Å). Accordingly, the magnitude of the 220 high angle shoulder peak increases for the samples with x = 0.1 and 0.15 (**Figure A1-1**), whereas the intensity of the low angle shoulder peak attributed to the Zr-rich HH phase remains essentially unchanged. The increased population density and average size of the (Ti, Fe)-rich FH phase are further confirmed by BSE observation (**Figure A1-3**) and element mapping (**Figure A1-4** to **A1-7**). An estimation of mole fraction (ν_{obs}) of the (Ti, Fe)-rich phase were extracted from BSE images processing (**Table A1-2**). The detail is thoroughly described in supporting information. According to chemical **Equation** (26), a theoretical fraction (ν_{calc}) of (Ti, Fe)-rich can be calculated (**Table A1-2**). It is interesting to notice the discrepancy between the observed mole fraction (ν_{obs}) and calculated mole fraction (ν_{calc}) of (Ti, Fe)-rich phase with the former lower than the latter. The discrepancy can be taken as an indirect measurement of the mole fraction of subnanometer scale (Ti,Fe)-rich phases within various samples, which was either not observed by BSE or missed during image processing. Remarkably, the discrepancy between the observed (ν_{obs}) and the predicted (ν_{calc}) mole fraction of

the (Ti,Fe)-rich phase drastically decreases with the increasing Fe content, suggesting that as the nominal Fe content increases, the population density of (Ti,Fe)-rich nanoinclusions within the sample rises, leading to agglomeration into larger particles. Within this picture, one can consider that ~78% of the (Ti,Fe)-rich phases formed in the sample with x = 0.05 are at the subnanometer scale (**Table A1-2**), whereas for the sample with x = 0.15 this number is only ~16%. The above described modulation of the microstructure and chemistry of various phases within the synthesized $Ti_{0.25}Zr_{0.25}Hf_{0.5}(Ni,Fe_x)Sn_{0.975}Sb_{0.025}$ composites upon incorporation of Fe is expected to profoundly influence their magnetic and thermoelectric properties.

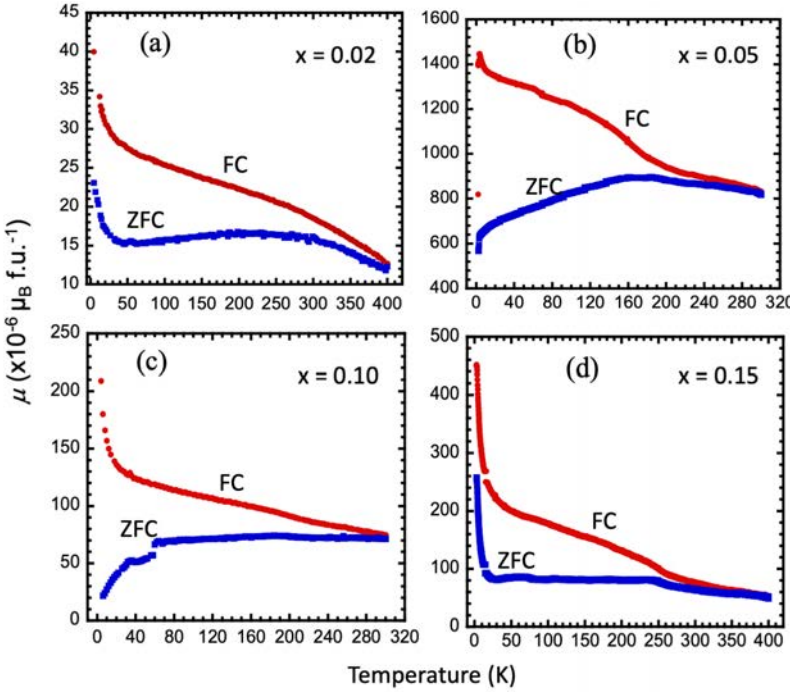

Figure 3-2. Temperature-dependent magnetic moment of $Ti_{0.25}Zr_{0.25}Hf_{0.5}(Ni,Fe_x)Sn_{0.975}Sb_{0.025}$ composites under Field-cooled (FC, red circles) and zero-field cooled (ZFC, blue squares) conditions: (a) x = 0.02; (b) 0.05; (c) x = 0.1; (d) x = 0.15.

3.3.2 Magnetic Properties

Field cooled (FC) and zero-field cooled (ZFC) magnetic moment data of selected $Ti_{0.25}Zr_{0.25}Hf_{0.5}(Ni,Fe_x)Sn_{0.975}Sb_{0.025}$ composites collected under an applied field of 100 Oe showed that all Fe-containing samples display various degrees of magnetic interactions (**Figure 3-2**).

Interestingly, the magnitude of the magnetic moment as well as the nature of magnetic ordering within various samples strongly depends on the Fe content, which, in turn, strongly affects the microstructure and chemistry of the resulting composites. For instance, the FC curve for the sample with x = 0.02 shows a gradual increase of the magnetic moment from ~12 x 10^{-6} μ_B/f.u. at 300 K to ~28 x 10^{-6} μ_B/f.u. at 40 K. Further dropping the temperature resulted in a drastic increase of the magnetic moment to ~40 x1 0^{-6} μ_B/f.u. at 5 K. A similar trend is observed in the magnetic moment curves of the samples with x = 0.1 and 0.15. However, the magnitude of the magnetic moment at 300 K is enhanced to ~80 x 10^{-6} μ_B/f.u. for the sample with x = 0.1 and to ~90 x 10^{-6} μ_B/f.u. for the sample with x = 0.15. The magnetic moment of the sample with x = 0.1 and 0.15 increases to ~120 x 10^{-6} μ_B/f.u. and ~200 x 10^{-6} μ_B/f.u., respectively, upon cooling to 40 K, then sharply rises to ~210 x 10^{-6} μ_B/f.u. and ~460 x 10^{-6} μ_B/f.u. at 5 K. The sample with x = 0.05 showed a unique trend with the largest value of the magnetic moment at 300 K, ~700 x 10^{-6} μ_B/f.u., which reaches ~1440 x 10^{-6} μ_B/f.u. upon cooling to 5 K.

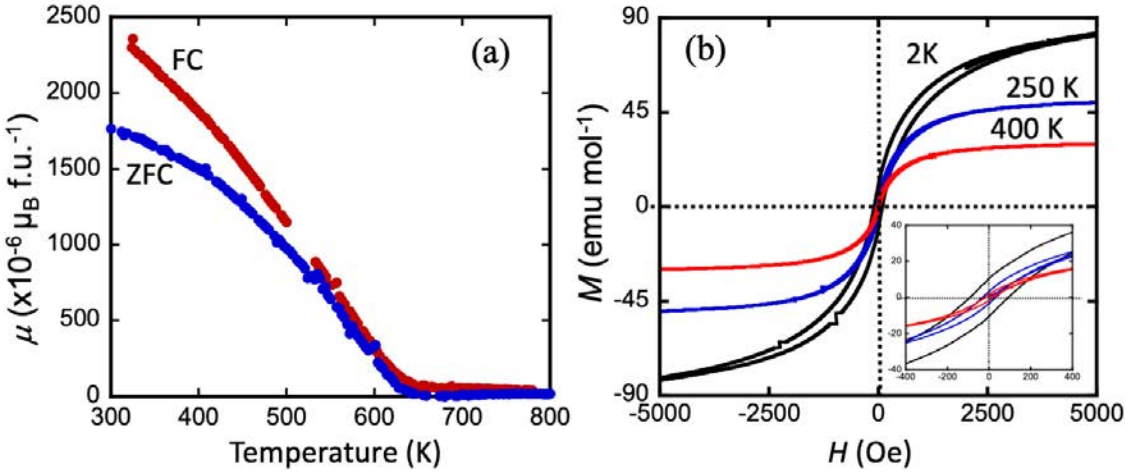

Figure 3-3. Magnetic behavior of $Ti_{0.25}Zr_{0.25}Hf_{0.5}(Ni,Fe_{0.05})Sn_{0.975}Sb_{0.025}$ composites: (a) temperature-dependent magnetic moment above 300 K showing the Curie transition temperature T_c ~650 K (FC: field cooled, red circles; ZFC: zero-field cooled, blue circles); (b) magnetization versus applied field at various temperatures between 2 K and 400 K. Inset of (b) is the enlarged detail of hysteresis near zero field to show the coercive force.

The presence of magnetic ordering within various samples can be associated with the formation of the magnetically active (Ti,Fe)-rich FH nanoinclusions within the (Zr,Hf)-rich HH matrix.

Indeed, a schematic illustration of the molecular orbital diagram for TiNiFeSn (**Figure A1-8**) reveals the presence of unpaired spins with a total spin value $S = 2$, suggesting some degree of magnetic ordering within the (Ti,Fe)-rich FH phase. However, the magnitude of the magnetic moment in the FH inclusion depends on the relative position of the bonding a_1 orbital with respect to the pair of degenerate bonding e_g (d_z^2, $d_{x^2-y^2}$) orbitals and the set of triple-degenerate bonding t_{2g} (d_{xy}, d_{yz}, d_{xz}) orbitals, which, in turn, can be altered by the change in the average size of the FH inclusions. For instance, in the bulk TiNiFeSn phase, one would anticipate the localization of the bonding a_1 orbital at energy levels below that of the bonding d-orbitals resulting in a total spin value $S = 1$.[214-216] Within this picture, one can rationalize the observed change in the magnitude of the magnetic moments of various samples by taking into account the average particle size as well as the distribution of (Ti,Fe)-rich FH within the HH matrix. The incorporation of low Fe content ($x \leq 0.05$) resulted in the formation of widely dispersed nanometer scale (Ti,Fe)-rich FH inclusions (**Figure 3-1b**) with high spin state ($S = 2$) within the HH matrix, yielding the large magnetic moments observed in the sample with $x = 0.05$ (**Figure 3-2b**). Further increasing the Fe content beyond $x > 0.05$ gives rise to the agglomeration of nanometer scale (Ti,Fe)-rich FH inclusions into microscale particles (**Figure A1-3**) with bulk-like properties. Accordingly, the magnetic moments for the samples with $x = 0.1$ and 0.15 are much reduced compared to that of $x = 0.05$. The observed increase in the magnitude of magnetic moment of samples with $x = 0.1$ and 0.15 compared to that of the sample with $x = 0.02$ can be associated with the increase in the population density of the (Ti,Fe)-rich phase within the samples, as suggested by the SEM images (**Figure A1-3** to **A1-7**).

The complex shape of the magnetic moment curves (ZFC and FC) for various samples points to frustrated magnetic ordering. For instance, the divergence between the ZFC and the FC magnetic moment curves at temperatures below 300 K suggests the coexistence of ferromagnetic (FM)

and/or anti-ferromagnetic (AFM) ordering in the samples, which leads to magnetic frustration.[214, 217-219] While the sharp increase of the magnetic moment below 40 K can be attributed to AFM ordering, the apparent saturation of the ZFC magnetic moment below 200 K for samples with x = 0.02, 0.05 and 0.15 points to FM ordering (**Figure 3-2**). Notably, the FC magnetic moment of the sample with x = 0.05 above 300 K gradually decreases with rising temperature up to 650 K, at which point the moment drops to nearly zero (**Figure 3-3a**) and thereafter, remains constant with further increase in the temperature. Thus, $Ti_{0.25}Zr_{0.25}Hf_{0.5}(NiFe_{0.05})Sn_{0.975}Sb_{0.025}$ hosts predominantly FM behavior with $T_c \sim 650$ K.

The FM character of the sample with x = 0.05 was further confirmed through field-dependent magnetization measurements at selected temperatures between 2 K and 400 K (**Figure 3-3b**). The characteristic S-shape of the magnetization curves up to 400 K is consistent with FM ordering with saturation values decreasing from 100 emu/mol at 2 K to 30 emu/mol at 400 K. We attribute the high-T_c FM behavior to long-range coupling of localized moments on adjacent (Ti,Fe)-rich magnetic nanoinclusions within the (Zr,Hf)-rich semiconducting HH matrix via formation of overlapping bound magnetic polarons (BMPs)[215-216, 220-227] and/or carrier-mediated mechanisms (**Figure 3-1c**). The above described magnetic ordering of (Ti,Fe)-rich inclusions within the (Zr,Hf)-rich HH matrix is expected to strongly influence atomic scale electronic transport behavior in the synthesized composites.

3.3.3 Thermoelectric Properties

One interesting unique characteristic of the synthesized $Ti_{0.25}Zr_{0.25}Hf_{0.5}(NiFe_x)Sn_{0.975}Sb_{0.025}$ composites is their multifunctional behavior, which is manifested by the coexistence of high T_c ferromagnetism and *n*-type heavily doped semiconductivity. As shown in **Figure 3-4**, the electrical conductivity at zero-field for all compositions gradually decreases with rising temperature, which

is a typical behavior for heavily doped semiconductors. The temperature-dependent electrical conductivity data are well fit by the power law $T^{-\alpha}$, as expected for acoustic phonon scattering of charge carriers. Interestingly, the power law exponent decreases with the increasing Fe content from $\alpha \approx 0.70$ for the sample with x = 0 to $\alpha \approx 0.41$ for the sample with x = 0.15, which suggests a transition of the transport mechanism from metallic-like to semi-metal-like behavior, possibly due to variations of the charge carrier concentration in different samples (**Figure 3-4c**).

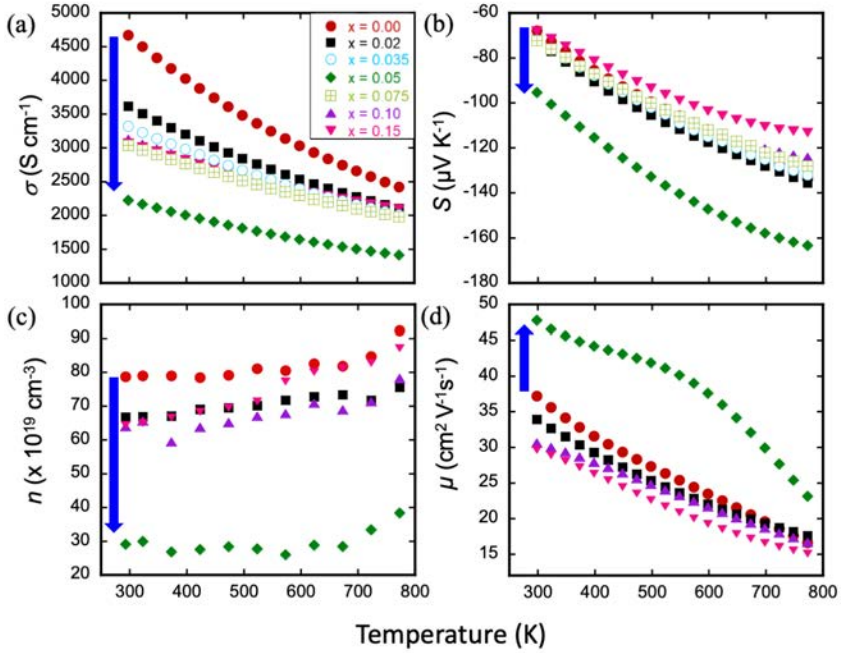

Figure 3-4. Electronic transport properties of $Ti_{0.25}Zr_{0.25}Hf_{0.5}(Ni,Fe_x)Sn_{0.975}Sb_{0.025}$ composites: (a) electrical conductivity; (b) Seebeck coefficient; (c) carrier concentration and (d) carrier mobility.

Regardless of the temperature, the magnitude of the electrical conductivity initially decreases with increasing Fe content, reaching minimum values for the composition with x = 0.05, then increases thereafter with further increase in the Fe content. However, the electrical conductivity of all Fe containing samples remains lower than that of the Fe-free HH matrix. For instance, the electrical conductivity at 300 K is ~4700 S cm^{-1} for the Fe-free sample (x = 0) and gradually decreases to ~3600 S cm^{-1} for the sample with x = 0.02 and further drop to ~3300 S cm^{-1} for the sample with x = 0.035 before reaching the minimum value of ~2200 S cm^{-1} for the sample with x

= 0.05. The electrical conductivity of samples with x= 0.075, x = 0.1 and 0.15 showed a slight increase (~3100 S cm^{-1} at 300 K) compared to the sample with x = 0.05. The observed drop in the electrical conductivity upon incorporation of Fe atoms is attributed to the decrease in the charge carrier density, which, in turn, can be associated with (1) the energy filtering of low-energy carriers at the atomic scale interfaces between the HH matrix and FH inclusions as discussed elsewhere,[67-68, 111, 201, 228] and/or (2) the localization of free carriers by magnetic (Ti,Fe)-rich FH inclusions embedded within the (Zr,Hf)-rich HH matrix. This analysis is consistent with the carrier density data (**Figure 3-4c**) extracted from the Hall coefficient data (**Figure A1-9a**), assuming a single carrier model ($R_H = 1/n \times q$, where q is the electron charge). All selected samples showed negative Hall coefficient values indicating *n*-type semiconducting behavior. The carrier density of the Fe-free sample remains nearly constant (~80 x 10^{19} cm^{-3}) with rising temperature, as anticipated for a heavily doped semiconductor. At temperatures above 600 K, thermal activation of carriers from the valence band (VB) to the conduction band (CB) leads to marginal increase in the overall carrier density. Intriguingly, the incorporation of Fe into the HH matrix to develop FH nanoinclusions results in a reduction of the overall effective carrier concentration (*n*) for all samples, which is consistent with the observed drop in the electrical conductivity. The observed drop in *n* values is quite a surprising result since one would anticipate larger carrier concentration upon doping a semiconductor with a metallic phase. However, the observation is in agreement with previous studies where diminished overall carrier densities were found upon embedding nanoscale inclusions with full-Heusler (FH) structure into a half-Heusler (HH) matrix using excess elemental Ni.[67-68] Such a change in the carrier density was rationalized using the concept of energy filtering of low-energy carriers at HH/FH interfaces, owing to the electronic energy band alignment offset between the neighboring phases. However, it was also found that the decrease in the carrier density

due to energy filtering at the HH/FH interfaces strongly depends on the doping level of materials.[228] Only a marginal drop in the carrier density was found for heavily doped HH/FH composites containing a small fraction of low-energy carriers, such as the HH compositions under consideration in the present study. Therefore, the large drop in the carrier density upon increasing the Fe content (up to ~63% for the sample with x = 0.05) (**Figure 3-4c**) suggests that there must be an additional mechanism for electron "trapping" at play in these samples. For example, the large population density of magnetic (Ti,Fe)-rich FH nanoinclusions in $Ti_{0.25}Zr_{0.25}Hf_{0.5}(NiFe_{0.05})Sn_{0.975}Sb_{0.025}$ may act as trapping centers for itinerant charge carriers through a combination of the energy filtering effect at the matrix/inclusion interfaces,[67-68, 111, 201, 228] and charge localization by the magnetic nanoinclusions (**Figure 3-1c**). The localization of charge carriers around such magnetic (Ti,Fe)-rich FH nanoinclusions presumably leads to the formation of overlapping bound magnetic polarons (BMPs), resulting in the observed long-range ferromagnetic ordering up to T_c = 650 K and the large drop in the effective carrier density. Importantly, the charge carrier density for the sample with x = 0.05 remains nearly constant with the rising temperature up to ~650 K, above which a gradual increase in the carrier density is observed. This suggests that the loss of the FM ordering at temperatures above 650 K triggers the release of a fraction of initially trapped carriers into the electronic conduction. Further increase of the Fe content to 0.1 and 0.15 resulted in an increase in the carrier density compared to that of the sample with x = 0.05 (**Figure 3-4c**), suggesting partial doping of these samples due to the observed agglomeration of a large fraction of (Ti,Fe)-rich nanoinclusions into micrometer scale particles with bulk metallic conductivity.

Remarkably, the drastic reduction in the carrier density of the sample with x = 0.05 resulted in a large increase in both the thermopower (**Figure 3-4b**) and the carrier mobility (**Figure 3-4d**).

All samples showed negative thermopower values in the whole measured temperature range, further confirming the *n*-type semiconducting behavior of the synthesized composites. At 300 K, a ~42% increase in the thermopower (from ~68 μV K^{-1} to ~96 μV K^{-1}) was observed for the sample with x = 0.05 when compared to that of the Fe-free sample, with a ~22% enhancement at 775 K. The observed large increase in the thermopower offsets the reduction in the electrical conductivity. In addition, the 27 % increase in the carrier mobility (**Figure 3-4d**) partially compensates for the 63% reduction in the carrier concentration, leading to only a marginal decrease (13 % at 800 K) in the power factor (*PF*) (**Figure 3-5a**) for the composition with x = 0.05. Further increasing the Fe concentration above x = 0.05 leads to a decreasing power factor, mainly due to the degradation of the Seebeck coefficient.

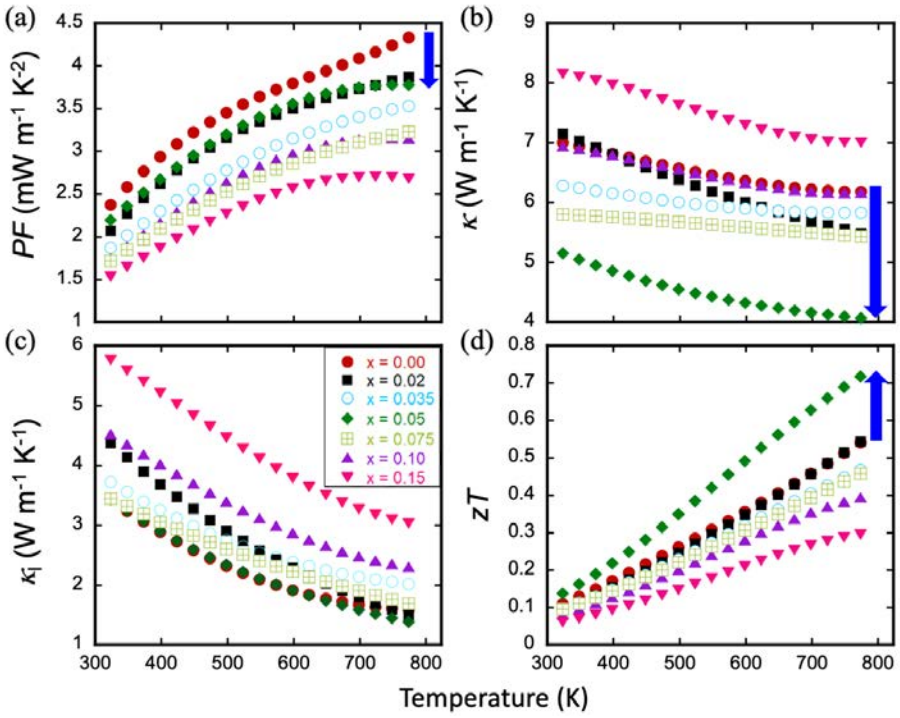

Figure 3-5. Thermoelectric properties of $Ti_{0.25}Zr_{0.25}Hf_{0.5}(Ni,Fe_x)Sn_{0.975}Sb_{0.025}$ composites: (a) power factor; (b) total thermal conductivity; (c) lattice thermal conductivity; and (d) thermoelectric figure of merit.

The total thermal conductivity of the Fe-containing samples initially decreases with the increasing Fe content reaching minimum values for the sample with x = 0.05. At 300 K, the thermal

conductivity of the Fe-free HH matrix is ~7 W m^{-1} K^{-1} and drops to ~5 W m^{-1} K^{-1} upon incorporation of 5 at% Fe. Additional Fe resulted in the total thermal conductivities larger than that of the Fe-free HH matrix. While the reduction in the total thermal conductivity of samples with x = 0.02, 0.035 and 0.05 is consistent with the observed trend in the electrical conductivity data, the measured larger total thermal conductivities for the samples with greater Fe contents are quite surprising. To fully understand the effect of nanostructuring on the total thermal conductivity of the synthesized samples, the electronic thermal conductivity (**Figure A1-9b**), calculated based on the Wiedemann–Franz law, was subtracted from the total thermal conductivity. The resulting lattice contribution to the total thermal conductivity shown in **Figure 3-5c** reveals that Fe incorporation into $Ti_{0.25}Zr_{0.25}Hf_{0.5}NiSn_{0.975}Sb_{0.025}$ leads to composites with larger lattice thermal conductivity, except for the sample with x = 0.05, which maintains similar lattice thermal conductivity to that of the Fe-free HH matrix. The observed increase in the lattice thermal conductivity with increasing Fe content is consistent with the formation of interconnected (Ti,Fe)-rich FH inclusions with large thermal conductivity within the resulting composites, as shown from the SEM images (**Figure A1-3**). In the samples with x = 0.05, the (Ti,Fe)-rich FH nanoinclusions are widely dispersed, diminishing their contributions to the lattice thermal conductivity of the HH matrix. Therefore, the observed large reduction (33% at 800 K) in the total thermal conductivity for the sample with x = 0.05 compared to the Fe-free sample arises from the combination of low electronic thermal conductivity due to the substantial drop in the electrical conductivity and low lattice thermal conductivity owing to the dispersion of (Ti,Fe)-rich FH nanoinclusions within the HH matrix. Overall, the marginal decrease (13% at 800K) in the *PF* and the large reduction (33%) in the total thermal conductivity for the sample with x = 0.05 resulted in a significant (29%) improvement in the thermoelectric performance. A thermoelectric figure of merit, *zT,* as high as

0.75, was obtained at 775 K for the sample with x = 0.05, which corresponds to a marked enhancement compared to results previously reported for similar compositions at the same doping level.[199] The sharp slope of the *zT* plot points to even higher values at higher temperatures.

3.4 Conclusion

In summary, we demonstrate that starting from a half-Heusler thermoelectric material with fully optimized doping level, $Ti_{0.25}Zr_{0.25}Hf_{0.5}NiSn_{0.975}Sb_{0.025}$, further enhancement of the figure of merit can be achieved through incorporation of widely dispersed coherent atomic scale magnetic nanoinclusions within the matrix. The incorporation of magnetic nanoinclusions within the HH matrix is achieved through preferential reactivity of the added elemental Fe atoms with Ti to form (Ti,Fe)-rich ($TiNi_{4/3}Fe_{2/3}Sn$) nanoinclusions with FH structure coherently embedded within the (Zr,Hf)-rich HH matrix. We found that such atomic scale magnetic FH inclusions regulate the electronic behavior of the existing ensembles of electrons by trapping a significant fraction of itinerant charge carriers via (1) energy filtering at the matrix/inclusion interfaces and, more importantly, through (2) magnetic coupling interactions between localized moments of embedded FH inclusions and the spins of the free carriers, resulting in a large reduction in the effective carrier density. The atomic scale engineering of electronic transport within the HH matrix using magnetic nanoinclusions has the following three major consequences. First, the localization of itinerant carriers by the magnetic nanoinclusions results in the formation of overlapping bound magnetic polarons (BMPs), inducing a high T_c ~650 K diluted ferromagnetic semiconductor. Secondly, the large reduction in the effective carrier density gives rise to a significant enhancement of both the carrier mobility and thermopower, which minimizes detriment to the overall power factor. Finally, the decreased electrical conductivity arising from the diminished effective carrier concentration causes a significant drop in the total thermal conductivity, owing to the reduction of the electronic

contribution to the thermal conductivity. The discovery of this novel approach to enhance the thermoelectric figure of merit using coherent magnetic nanoinclusions is expected to pave the way towards even larger figures of merit in leading thermoelectric materials.

Chapter 4 : Nanoscale Engineering of Polymorphism in Cu_2Se via $CuGaSe_2$ precipitates

4.1 Introduction

Cu_2Se is known as a phonon-liquid-electron-crystal (PLEC) material[143], which is an extending concept of phonon-glass-electron-crystal (PGEC)[4, 229]. Conceptually, Cu_2Se has decent electrical properties and intrinsically low thermal conductivity, which is directly related to its unique crystal structure. Cu_2Se crystallizes in Cubic structure (Fm-3m) at high temperature (> 400 K), known as β-Cu_2Se. In β -Cu_2Se, Se atoms form the FCC frame structure with copper atoms distributed over 8 (c) tetrahedral and 32 (f) trigonal sites.[144-146] Low occupation of these available sites and high diffusivity (10^{-5} cm^2 s^{-1}) enables Cu^+ ions to move from site to site easily, displaying a highly disordered state (liquid-like state).[147] As a result, ionic conductivity makes a decent contribution to the total electrical conductivity. Benefiting from the liquid-like state, Cu_2Se shows intrinsically low thermal conductivity due to (1) reduced phonon free path due to strong scattering by Cu ions and (2) lowered heat capacity.[143] The lowered heat capacity stems from the liquid-like behavior of Cu_2Se, which leads to truncated density of state of phonon. On the other hand, there is still controversy about the room-temperature Cu_2Se, also known as α-Cu_2Se.[149, 151-153] This may arise from the multiformity of Cu^+ ions ordering within Se lattice.[153] Cu_2Se has high tolerance of Cu vacancies, forming off-stoichiometric $Cu_{2-x}Se$. Large Cu vacancies (such as $Cu_{1.75}Se$) even lead to cubic-structured Cu_2Se at room temperature.[12, 144] It is the Cu vacancies that gives rise to the p-type transport in Cu_2Se. Cu vacancies seems to be thermodynamically favored, for it cannot be avoided even when materials are synthesized according to the stoichiometry. High tolerance of Cu vacancies leads to hole concentration changing in an extensive range. Therefore, the electrical

properties are sensitive to synthesis conditions, which lead to varied densities of Cu vacancies.[12, 156-158] H. Liu et al. reported a high TE performance for Cu_2Se due to the self-doping effect from Cu vacancies and ultra-low thermal conductivity from disordered Cu ions.[143]

It can be concluded that the thermoelectric properties of Cu_2Se are strongly related to the material structure and composition, for example, the Cu deficiency and the mobility of Cu ions in β-Cu_2Se. Developing strategies to gain more control over the change in structure and composition will be the key to achieve desirable modulation in electronic and thermal transport in Cu_2Se, targeting even higher TE performance upon its intrinsically low thermal conductivity. Among many different strategies, making composite materials has been commonly adopted to manipulate the TE properties in Cu_2Se. For example, nanoscale SiC[172], carbon nanotubes (CNT)[72-73], graphene[29, 74], nano boron[74], TiO_2 [75], SnSe[76], Ag_2Se[77], Cu_2S[78] and $CuGaSe_2$[79] etc. were studied as the secondary phases in Cu_2Se and their impacts on TE performance. Most of the composite materials were simply made by physically mixing the constituent components. Recently, A. Olvera et al. developed a novel strategy to synthesize pure $CuInSe_2$ and (1-x)Cu_2Se/(x)$CuInSe_2$ composites through a topochemical solid-state reaction starting from precursor, $CuSe_2$.[171] High TE performance has been reported for (1-x)Cu_2Se/(x)$CuInSe_2$ composites synthesized by this method. Meanwhile, an improved chemical stability was observed in such composite materials. Inspired by this, a major part of this thesis work is dedicated to further develop this strategy, including applying similar or adjusted methods to make more (1-x)Cu_2Se/(x)$CuMSe_2$ composites and studying the modulation effects on TE properties achieved by such strategy. Due to the fact that the composite materials are achieved by sequentially/ simultaneously forming $CuMSe_2$ precipitates and Cu_2Se matrix from the same precursor, Cu_2Se, very unique interfaces will be expected, for example forming chemically bonded instead of physical interface, potentially leading to various interactions

between precipitate and the matrix materials. Such interactions enable us the capability to manipulate the variation in structure, composition and thus TE properties. $CuGaSe_2$ is a close relative to $CuInSe_2$, both of which crystallize in chalcopyrite structure. Due to their wide band gaps, they have been known as absorber materials for solar cell.[230] Given the positive effect of $CuInSe_2$ on TE properties, it is expected that an introduction of $CuGaSe_2$ into Cu_2Se will also induce interesting interaction between the precipitate and the matrix, leading to modulation of TE properties.

In this chapter, we demonstrate a synthesis approach that enables control over nucleation, at the atomic scale, of β-Cu_2Se phase during the solid-state reaction. We show that starting from a $CuSe_2$ precursor, the incorporation of ultrafine (sub-10 nm) $CuGaSe_2$ nanoparticles into $CuSe_2$ matrix facilitates the nucleation and stabilization of β-Cu_2Se phase during a solid-state reaction of (x)$CuGaSe_2$/(1-x)$CuSe_2$ composites with elemental Cu. Moreover, increasing the fraction of $CuGaSe_2$ nanoparticles in the (x)$CuGaSe_2$/(1-x)$CuSe_2$ composites drastically increases the fraction of β-Cu_2Se phase formed at the expense of the α-Cu_2Se phase. Interestingly, the β-Cu_2Se phase within the resulting (x)$CuGaSe_2$/(1-x)Cu_2Se composites remains thermally stable upon annealing during hot pressing. This ability to tune the ratio between the α-Cu_2Se and the β-Cu_2Se in the synthesized (x)$CuGaSe_2$/(1-x)Cu_2Se composites results in a strong dependency of the electronic and thermal transport properties of (x)$CuGaSe_2$/(1-x)Cu_2Se composites on the $CuGaSe_2$ content.

4.2 Experimental Details

Synthesis. The synthesis of (x)$CuGaSe_2$/(1-x)Cu_2Se polycrystalline nanocomposites was carried out using the topo-chemical transformation approach developed in our group and implemented for the synthesis of (1-x)Cu_2Se/(x)$CuInSe_2$ composites.[171] Here, the metastable nanocomposites (y)$CuGaSe_2$/(1-y)$CuSe_2$ are first synthesized through the solid-state reaction of the $CuSe_2$

precursor with various amounts of elemental Ga using mechanical alloying, which results in partial transformation of the precursor into $CuGaSe_2$ nanoinclusions according to the chemical **Equation** (27).

$$CuSe_2 + (y)Ga \rightarrow (1\text{-}y)CuSe_2 + (y)CuGaSe_2 \quad (27)$$

In the subsequent reaction, the remaining $CuSe_2$ after the first step was further transformed into Cu_2Se through the reaction of the metastable $(y)CuGaSe_2/(1\text{-}y)CuSe_2$ composites with the appropriate amount of element Cu to form the desired $(y)CuGaSe_2/(2\text{-}2y)Cu_2Se$ composites following the chemical **Equation** (28).

$$(1\text{-}y)CuSe_2 + (y)CuGaSe_2 + 3(1\text{-}y)Cu \rightarrow 2(1\text{-}y)Cu_2Se + (y)CuGaSe_2 \quad (28)$$

Therefore, the percentage of $CuGaSe_2$ is $x = y/2(1\text{-}y)$. For each step of the synthesis process, the starting mixtures were loaded into agate jars together with agate balls and mechanically alloyed using planetary ball mill. The mass ratio of agate balls to reactants was maintained at 5:1. The $CuSe_2$ precursor was pre-synthesized via a solid-state reaction of elemental Cu and Se.

Characterization. Composition and microstructure characterizations are described in Chapter 2. The electrical conductivity and Seebeck coefficient were measured simultaneously from room temperature to 873 K using the four-probe method on a commercial ULVAC-RIKO ZEM-3 system under a low-pressure helium atmosphere. The specific heat capacity and thermal diffusivity were measured on a laser flash system (Linseis LFA-1000) from room temperature to 873 K. The density of the pressed pellets was measured using Helium gas pycnometry on Micromeritics Accupyc II 1340. Low temperature and high temperature Hall measurement were carried out under a magnetic field of 1 T on a home-built apparatus to evaluate the carrier concentration and mobility.

4.3 Result and Discussion

4.3.1 Phase Selection Strategy

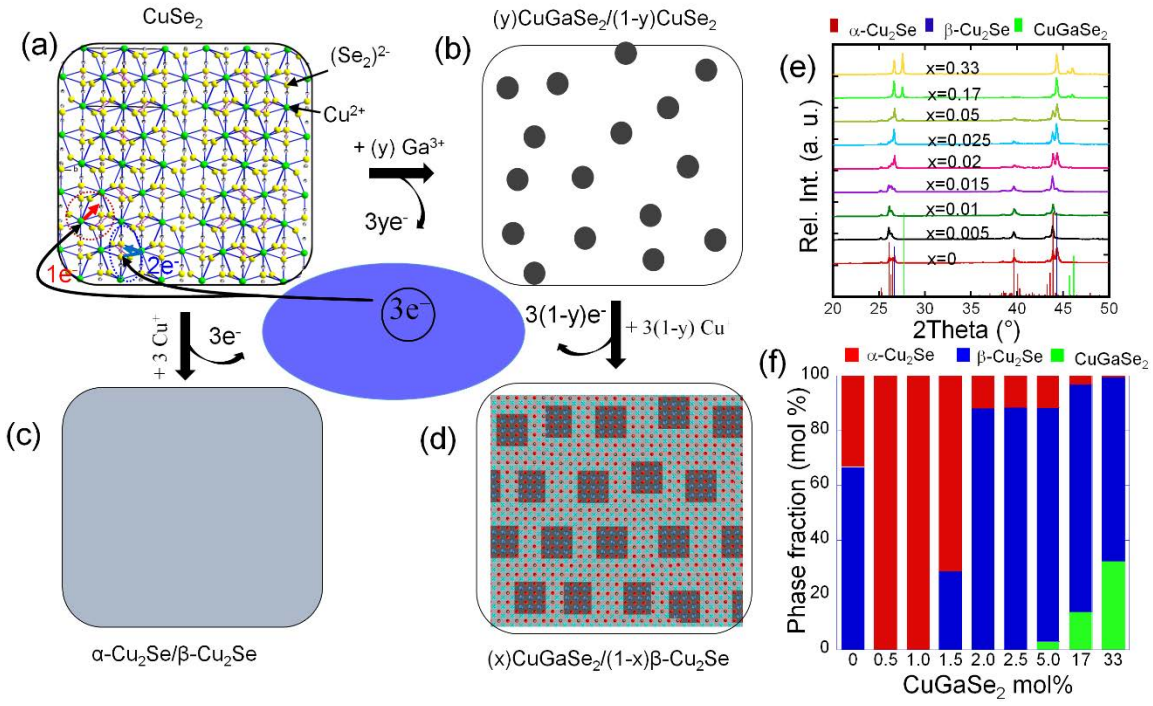

Figure 4-1. Directed solid-state formation of β-Cu_2Se in (x)$CuGaSe_2$/(1-x)Cu_2Se composites. (a) $CuSe_2$ precursor, which acts both as a reagent and as a reaction template to direct the solid-state nucleation of the desired phases; (b) formation of $CuGaSe_2$ nanocrystals within the $CuSe_2$ matrix; the $CuGaSe_2$ nanocrystals served as "seeds" catalyzing the preferential nucleation of β-Cu_2Se upon incorporation of elemental Cu. This leads to the formation of (x)$CuGaSe_2$/(1-x)β-Cu_2Se (d). In the absence of $CuGaSe_2$ nanocrystals, the solid-state reaction between $CuSe_2$ precursor and elemental Cu results in the formation of a mixture of α-Cu_2Se and β-Cu_2Se phases (c); (e) XRD patterns of various samples after consolidation using uniaxial hot-press. All diffraction peaks can be indexed with α-Cu_2Se (monoclinic), β-Cu_2Se and tetragonal $CuGaSe_2$ phases; (f) fraction of α-Cu_2Se, β-Cu_2Se and $CuGaSe_2$ phases in various composites, obtained from quantitative analysis using the reference intensity ratio (RIR) method.

To demonstrate the robustness of our synthesis approach, selected compositions of the (x)$CuGaSe_2$/(1-x)Cu_2Se ($0 \leq x \leq 1$) system were synthesized following a two-step solid-state transformation of $CuSe_2$ precursor using mechanical milling. The centerpiece of our synthesis approach relies on the use of $CuSe_2$ precursor, which serves both as a reagent and as a template to help guide the solid-state reaction towards the formation of compounds with the desired stoichiometry ($CuGaSe_2$ and Cu_2Se), as well as directing the atomic-scale alignment at the interfaces between the coexisting phases. A schematic illustration of the important features and results of our synthesis approach is shown in **Figure 4-1a** to **4-1d**. We begin with a partial reaction of the $CuSe_2$ precursor with incremental amounts of elemental Ga via mechanical milling, which results in the formation of $CuGaSe_2$ nanocrystals widely dispersed within the $CuSe_2$ matrix.

Subsequent reaction of the resulting metastable (y)$CuGaSe_2$/(1-y)$CuSe_2$ precursor with elemental Cu leads to the formation of (x)$CuGaSe_2$/(1-x)Cu_2Se nanocomposites. A systematic investigation of the structure and phase composition using X-ray diffraction (XRD) of the as-synthesized polycrystalline powders as well as samples annealed during hot press revealed successful formation of the targeted composites (**Figure 4-1e** and **Figure A2-1**). All diffraction peaks can be indexed using theoretical patterns of tetragonal $CuGaSe_2$ as well as both α-Cu_2Se (monoclinic) and β-Cu_2Se polymorphs. No additional diffraction peak from impurities such as unreacted precursor, $CuSe_2$, could be observed. The relatively broad diffraction peaks for the as-synthesized samples (**Figure A2-1**) indicates poor crystallinity and the formation of ultrafine grains after the mechanical milling process. The crystallinity of the synthesized composites was significantly improved during consolidation using uniaxial hot press, as indicated by the sharper and more resolved diffraction peaks on the XRD patterns of (x)$CuGaSe_2$/(1-x)Cu_2Se composites (**Figure 4-1e**). No major change in the phase composition during hot-pressing could be noticed from the XRD patterns. Upon increasing the amount of Ga in the starting mixture from x = 0.5% to x = 33% and finally to x = 100% (pure $CuGaSe_2$), diffraction peaks corresponding to the formation of $CuGaSe_2$ only begin to appear at the x = 5% composition. Thereafter, the $CuGaSe_2$ peak intensities continuously increase with increasing Ga content (**Figure 4-1e** and **A2-1c**) suggesting an increase in the fraction of $CuGaSe_2$ phase in the composites. It is also interesting to note the strong variation in the phase fraction of α-Cu_2Se and β-Cu_2Se polymorphs upon increasing the Ga content. An estimation of the phase fractions was obtained by refinements using the reference intensity ratio (RIR) method (**Figure 4-1f** and **Table A2-1**). It is interesting to see that the pristine Cu_2Se sample (x = 0) is actually a mixture of α-Cu_2Se (~33%) and β-Cu_2Se (67%) polymorphs. The formation at room temperature of a larger fraction of β-Cu_2Se, which is normally more stable at high

temperatures, in the pristine Cu_2Se sample is most likely a consequence of the ball milling process, which causes high density of Cu vacancies and anti-site defects. However, the introduction of a small amount of Ga ($x \leq 0.01$) into the reaction mixture clearly suppressed the formation of β-Cu_2Se, producing almost 100% α-Cu_2Se phase in these samples (**Figure 4-1f**). A plausible explanation for this behavior is that Ga atoms, at very low concentration, all dissolve into the Cu_2Se structure and inhibit the formation of Cu vacancies and anti-site defects, therefore stabilizing the α-Cu_2Se polymorph at room temperature. The solubility of Ga into α-Cu_2Se was evidenced by a marginal expansion of the unit cell parameters with increasing Ga content ($0 < x \leq 0.01$), as shown in **Figure A2-2a** and **A2-2b**. However, a close-up examination of the diffraction peak for the α-Cu_2Se polymorph around 26 degrees reveals no major systematic peak shift with increasing amount of Ga, suggesting a very limited solubility of Ga into the Cu_2Se crystal lattice (**Figure A2-1c**). Remarkably, such a low solubility of Ga into Cu_2Se not only enables an excellent control over the phase ratio in $(x)CuGaSe_2/(1-x)Cu_2Se$ composites, but also promotes the stabilization of β-Cu_2Se at the expense of the α-Cu_2Se polymorphs at higher Ga concentrations. For instance, upon increasing the Ga content to $x = 0.015$, one observes the reappearance of the β-Cu_2Se polymorph (~28%) along with α-Cu_2Se (~71%). The phase fraction of β-Cu_2Se then drastically increases with increasing Ga concentration while that of the α-Cu_2Se polymorph diminishes (**Figure 4-1f**). For example, the fraction of α-Cu_2Se phase decreases from 100% for the sample with $x = 0.01$ to 70% for $x = 0.015$, then drops to 12% for $x = 0.02$ and finally to just 0.5% in the sample with $x = 0.33$, while the fraction of β-Cu_2Se polymorph increases from 28% for the sample with $x = 0.015$ to 88% and 83% for the samples with $x = 0.02$ and 0.33, respectively. This trend can also be confirmed by tracking the diffraction peak of α-Cu_2Se around $2\theta = 13$ degrees, which diminishes in intensity for samples with increasing Ga content and vanishes for the

sample with x = 33% **(Figure A2-1b**). Evidently, the introduction of Ga facilitates the formation of the β-Cu_2Se polymorph during the solid-state reaction process. Surprisingly, the β-Cu_2Se polymorph remains stable at room temperature in samples with Ga concentration x > 0.01, even after consolidation under high pressure at high temperature (**Figure 4-1e**). The results are in sharp contrast with the Cu-Se phase diagram, which suggests α-Cu_2Se as the thermodynamically stable phase at room temperature.[231]

One rational explanation of the stabilization of the β-Cu_2Se phase in samples with Ga content x > 0.01 is that the excess Ga beyond the solubility limit (~1 mol%) in α-Cu_2Se, leads to the formation of nanoscale $CuGaSe_2$ particles during the first reaction step between the $CuSe_2$ precursor and elemental Ga (**Figure 4-2**). Such $CuGaSe_2$ nanoparticles randomly dispersed within the unreacted $CuSe_2$ matrix then serve as "nanoseed crystals" for the nucleation of the β-Cu_2Se phase during the second reaction step between elemental Cu and (y)$CuGaSe_2$/(1-y)$CuSe_2$ precursor, leading to the formation of (x)$CuGaSe_2$/(1-x)Cu_2Se nanocomposites with hierarchical microstructure (**Figure 4-2** and **4-3**). A underlying structural feature favorable for the formation of such microstructure is the close lattice matching ($\Delta a/a \approx 4\%$) between the basal plane (001) of tetragonal $CuGaSe_2$ (a = 5.60 Å) and the axial planes {100} of the β-Cu_2Se phase (a = 5.85 Å), as well as the similarity in the packing of Se atoms on both $CuGaSe_{2\{001\}}$ and β-$Cu_2Se_{\{100\}}$ planes, which presumably facilitates epitaxial nucleation of β-Cu_2Se crystals on the {001} planes of $CuGaSe_2$ nanoparticles (**Figure 4-2e**). Such coherent $CuGaSe_{2\{001\}}$/β-$Cu_2Se_{\{100\}}$ interfaces (**Figure 4-2d** and **4-2e**) guide the solid-state reaction towards the formation of the β-Cu_2Se polymorph at the expense of the α-Cu_2Se phase. The reaction mechanism triggers a small tensile strain (+0.4%) on the $CuGaSe_2$-{001} plane and a compression strain (~1.4%) on the β-Cu_2Se-{100} plane, as can be measured by the expansion in the *ab* plane of $CuGaSe_2$ (a = 5.62 Å) and

contraction in the unit cell parameter of β-Cu_2Se (a = 5.77 Å) (**Figure A2-2c, A2-2d** and **Table A2-1**). Such lattice distortions further lower the energy of the $CuGaSe_{2\{001\}}$/β-$Cu_2Se_{\{100\}}$ interfaces, providing sufficient "*chemical pressure*" for the stabilization of β-Cu_2Se polymorph within the nanocomposites.

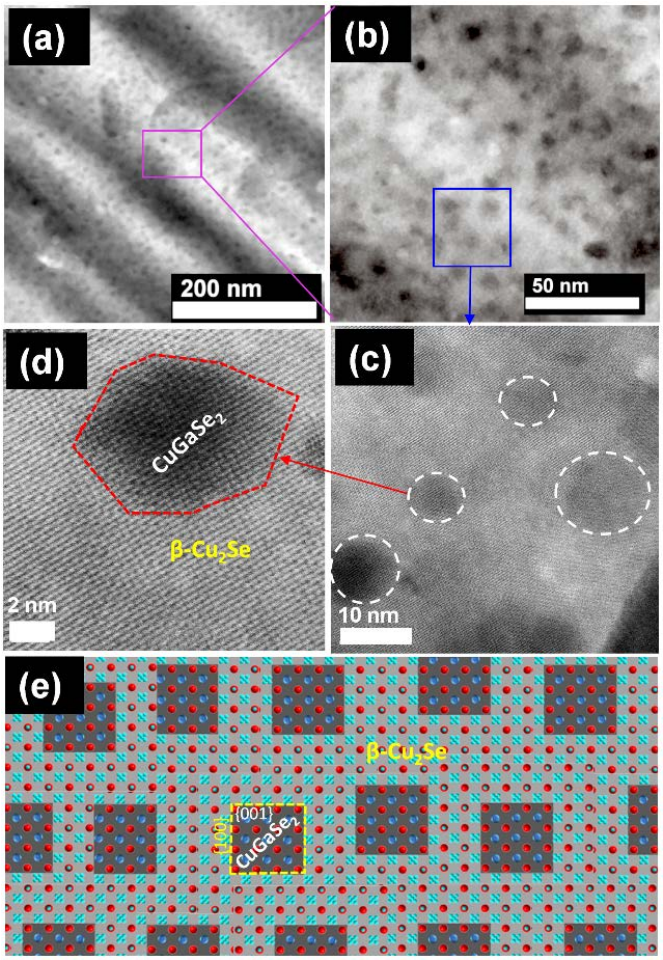

Figure 4-2. Microstructure of 0.05$CuGaSe_2$/0.95Cu_2Se composites. (a) and (b) Low magnification TEM images revealing a high density of sub-ten nanometer $CuGaSe_2$ particles widely dispersed within the β-Cu_2Se matrix. (c) and (d) High magnification TEM images revealing the high degree of coherency at the atomic scale interfaces between $CuGaSe_2$ inclusions and the β-Cu_2Se matrix. (e) Schematic illustration of the crystallography registry at the atomic-scale interfaces between $CuGaSe_2$ nanoinclusions and the β-Cu_2Se matrix.

While this mechanism explains well the preferential formation of β-Cu_2Se over the α-Cu_2Se polymorph at reaction fronts in the vicinity of $CuGaSe_2$ nanoseeds, it does not intuitively clarify why the incorporation of just a small amount of Ga above the solubility limit of ~1% drastically

swings the reaction from the formation of 100% α-Cu_2Se in the sample with x = 0.01 to the formation of predominantly β-Cu_2Se phase (>90%) in samples with x ≥ 0.02 (**Figure 4-1f**). To fully understand this trend, we carefully examine the microstructure of the sample with x = 0.05 using high-resolution transmission electron microscopy (HRTEM). As can be observed from **Figure 4-2a**, the incorporation of 5 mol% Ga in the first reaction leads to the formation within the unreacted $CuSe_2$ matrix of a high density of sub-10 nm $CuGaSe_2$ nanoparticles, which significantly increases the density of nucleation sites for the formation β-Cu_2Se phase during the second reaction step. Such microstructures clearly explain the substantial rise in the phase fraction of β-Cu_2Se with a marginal increment in Ga content above the solubility limit. Further increasing the Ga content to 17% and 33% leads to the clustering and percolation of sub-10 nm $CuGaSe_2$ nanoparticles into sub-10 micron networks (dark-grey) that are interwoven with another network formed by the β-Cu_2Se phase (light-grey) to form a microstructure with a complex hierarchical architecture that is only revealed at high magnification under scanning electron microscopy (SEM) (**Figure 4-3a** to **4-3d**). For instance, one can also observe on the high magnification SEM image (**Figure 4-3d**), that the β-Cu_2Se-rich region also contains widely dispersed nanometer scale particles of the $CuGaSe_2$ phase (dark grey particle in the bright-contrasted phase). Under such a high magnification, composition mapping displays a nearly homogeneous distribution of Cu, Ga, and Se in the samples (**Figure 4-3f** to **4-3h**). However, a line scan through the $CuGaSe_2$ particles (**Figure 4-3e**) and energy-dispersive X-ray spectroscopy (EDS) point analysis of the $CuGaSe_2$-rich region (**Figure 4-3i**) and the β-Cu_2Se-rich region (**Figure 4-3j**) clearly reveal a high concentration of Cu and very low concentration of Ga within the β-Cu_2Se-rich region, whereas a high concentration of Ga is found in the $CuGaSe_2$-rich region.

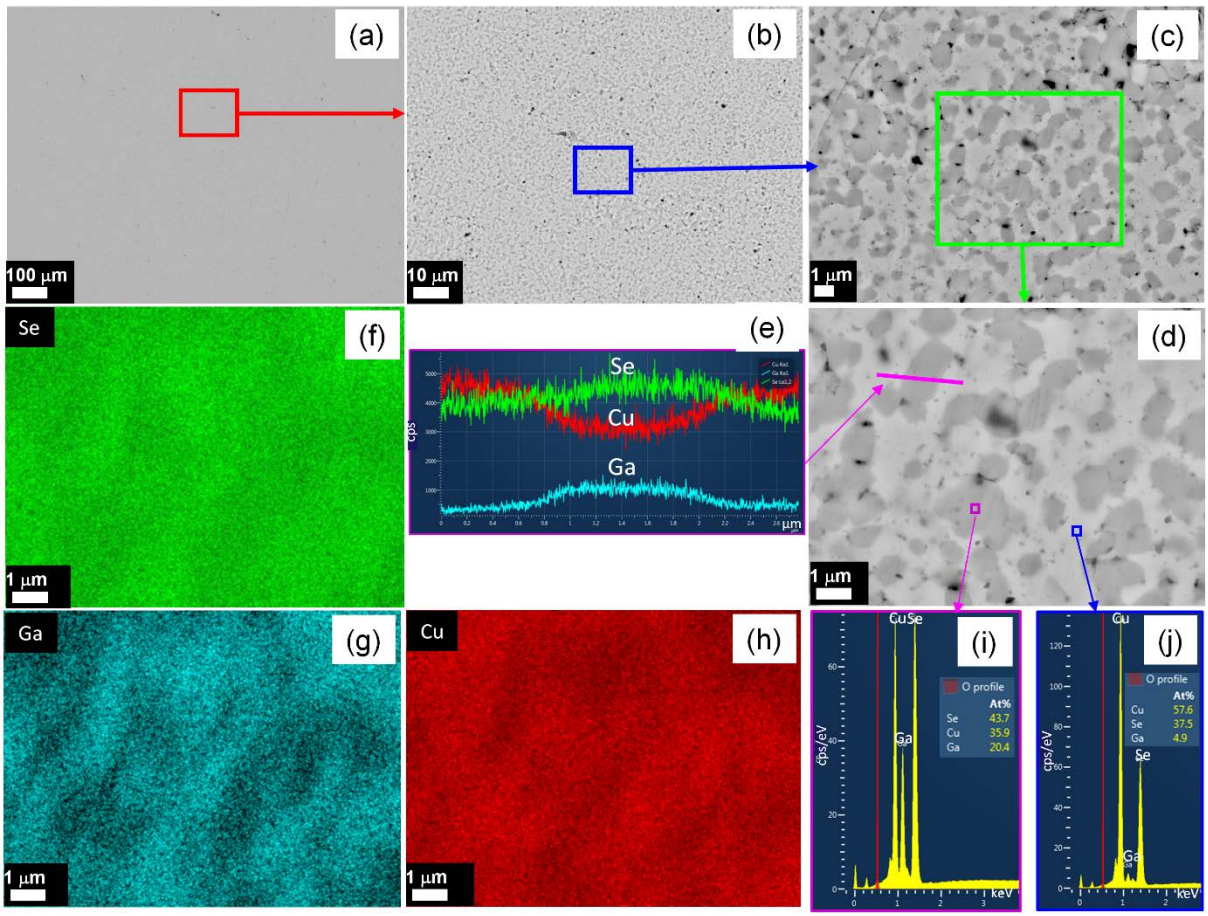

Figure 4-3. Microstructure of $0.33CuGaSe_2/0.67Cu_2Se$ composites. (a-d) BSE images at various magnifications. Despite the large fraction of $CuGaSe_2$ phase (~33 mol%) present in the composite, the SEM image surprisingly shows a uniform contrast at low magnification (a). The micron-scale particles of $CuGaSe_2$ within the β-Cu_2Se matrix are only revealed at high magnification (b-d). It can be seen that upon increasing the Ga content in the composites, the $CuGaSe_2$ nanoparticles clustered into sub-10 micron regions (dark-grey), which are interconnected to form a network that is interwoven with another network formed by the β-Cu_2Se phase (light-grey) (c-d). The composition mapping obtained from image (d) show a nearly uniform distribution of all elements (f-h). The line scan through the $CuGaSe_2$ particles (e) and energy-dispersive X-ray spectroscopy (EDS) point analysis of the $CuGaSe_2$-rich region (i) and the β-Cu_2Se-rich region (j) revealed a high concentration of Cu and very low concentration of Ga within the β-Cu_2Se-rich region, whereas a high concentration of Ga is found in the $CuGaSe_2$-rich region.

The successful synthesis of the targeted $(x)CuGaSe_2/(1-x)Cu_2Se$ composites was further confirmed by differential scanning calorimetry (DSC) measurements (**Figure A2-3**). The DSC heating curves of all composites (except for the sample with x = 33%) showed two endothermic peaks. The thermal event around 400 K can be associated with the phase transition from α-Cu_2Se to β-Cu_2Se, whereas the peak at higher temperature corresponds to the melting of the composites. The melting temperature of $(x)CuGaSe_2/(1-x)Cu_2Se$ composites gradually decreases with

increasing amount of Ga ($CuGaSe_2$) from ~1420 K for the pristine Cu_2Se to ~1243 K for the composition with x = 33% (**Figure A2-3c**), which despite the presence of a large fraction of both $CuGaSe_2$ and β-Cu_2Se phases, only showed a single endothermic peak of melting at a temperature lower than the melting temperature of either constituent phase. This trend is consistent with the Cu_2Se-$CuGaSe_2$ pseudo-binary phase diagram, which predicts an eutectic composition around 33 mol % $CuGaSe_2$ with a melting temperature lower than that of pristine $CuGaSe_2$ (~1313 K)[232]. Another interesting feature of the DSC heating curves of (x)$CuGaSe_2$/(1-x)Cu_2Se composites is the gradual reduction of the α- to β-Cu_2Se phase transition peak around 400 K with increasing $CuGaSe_2$ content, completely gone for the sample with x = 0.33. The trend is consistent with the results of the phase fractions calculated from the XRD powder patterns, which revealed the disappearance of diffraction peaks from α-Cu_2Se in favor of those from β-Cu_2Se for samples with increasing $CuGaSe_2$ content (**Figure A2-1** and **Figure 4-1f**). These results suggest some degrees of chemical and structural integration at the atomic scale and nanometer scale interfaces between the coexisting Cu_2Se and $CuGaSe_2$ phases as demonstrated by the detailed studies of the microstructure of various composites discussed above (**Figure 4-2** and **4-3**). The microstructures of the synthesized (x)$CuGaSe_2$/(1-x)Cu_2Se composites indicate that the $CuSe_2$-template solid-state synthesis technique used in this work not only enables a good control over the phase composition, but also facilitates control over the microstructure. Importantly, the crystallographic relationship at the $CuGaSe_2$/β-Cu_2Se interfaces is critical for tailoring the electronic and thermal transport properties. For instance, the smooth and coherent interfaces between nanoscale $CuGaSe_2$ inclusions and the micron-scale β-Cu_2Se matrix is expected to minimize the scattering of charge carriers across the interfaces, enabling high charge carrier mobility. Yet, the difference in lattice vibrations between $CuGaSe_2$ and β-Cu_2Se is expected to enhance phonon scattering in the

composites, leading to low thermal conductivity compared to pristine $CuGaSe_2$ and β-Cu_2Se phases.

4.3.2 Electronic and Thermal Transport Properties

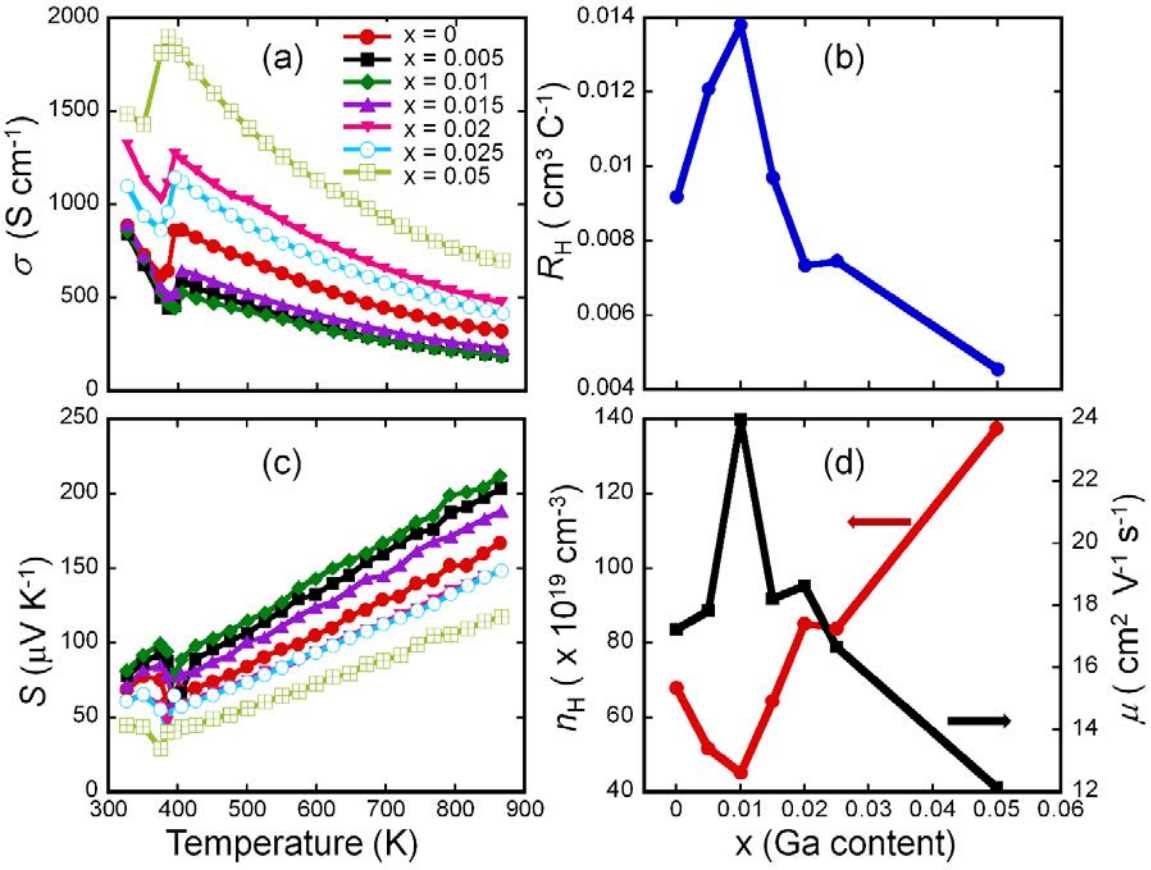

Figure 4-4. Electronic transport properties in (x)$CuGaSe_2$/(1-x)Cu_2Se composites: (a) temperature-dependent electrical conductivity; (b) room-temperature Hall coefficient as a function of Ga content; (c) temperature-dependent Seebeck coefficient and (d) carrier concentration and carrier mobility at 300 K as a function of Ga content.

The ability to control at the atomic scale the stability of α-Cu_2Se and β-Cu_2Se polymorphs in (x)$CuGaSe_2$/(1-x)Cu_2Se composites as well as the phase compositions upon tuning the Ga content (x value) paves the way for precise engineering of their electronic and thermal transport properties. For example, the electrical conductivity of the synthesized composites at 325 K initially decreases marginally from 895 S cm^{-1} for the pristine Cu_2Se (x = 0) to 830 S cm^{-1} for the composition with x = 0.01 (**Figure 4-4**). The slight change can be associated with the observed increase in the phase fraction of the α-Cu_2Se polymorph from

33% in the sample with x = 0 to 100% in the samples with x = 0.01 (**Figure 4-1f**). Interestingly, further increasing the Ga content above the solubility limit (x = 1 mol%) results in a rapid rise in the electrical conductivity value at 325 K to 880 S cm^{-1}, 1330 S cm^{-1} and 1485 S cm^{-1} for the samples with x = 0.015, 0.02 and 0.05, respectively. The observed enhancement in the electrical conductivity of (x)$CuGaSe_2$/(1-x)Cu_2Se composites is attributed to the large increase in the fraction of the β-Cu_2Se polymorph in the samples (**Figure 4-1f**). Similar trend in the alteration of electrical conductivity with increasing Ga content (x values) were observed at temperatures above the structural phase transition between α-Cu_2Se and β-Cu_2Se polymorphs ($T_{\alpha-\beta}$ = 375 K). For instance, the electrical conductivity of the pristine β-Cu_2Se (x = 0) at 400 K is 875 S cm^{-1}, drops to 590 S cm^{-1} for the sample with x = 0.005 and further decreases to 527 S cm^{-1} for the sample with x = 0.01. The trend is suddenly reversed for samples with larger Ga content (x > 0.01). For example, the electrical conductivity of the sample with x = 0.02 (~2 mol% $CuGaSe_2$) is 1250 S cm^{-1} at 400 K, which is more than two-fold that of the sample with x = 0.01 at the same temperature. The electrical conductivity at 400 K further increases to 1890 S cm^{-1} for the sample with x = 0.05 (~5 mol% $CuGaSe_2$). While it is reasonable to anticipate from a simple rule of mixture that the incorporation of a wide band-gap semiconductor (E_g($CuGaSe_2$) > 1.5 eV) as a second phase within a narrow band-gap semiconducting matrix (Cu_2Se) would lead to a reduction in the electrical conductivity as observed for the samples with x ≤ 0.1, the observed drastic increase of the electrical conductivity in samples with Ga content x > 0.01 strongly points to a more complex mechanism that takes into account the chemical and structural interaction between the incorporated $CuGaSe_2$ inclusions and the Cu_2Se matrix as discussed above. Regardless of the composition, the electrical conductivity of all

(x)$CuGaSe_2$/(1-x)Cu_2Se composites decreases with increasing temperature between 400 K and 875 K, which is consistent with degenerate semiconducting behavior (**Figure 4-4a**). To gain a better insight into the origin of the observed change in the electrical conductivity of (x)$CuGaSe_2$/(1-x)Cu_2Se composites with increasing x values, the carrier concentrations were extracted from the Hall measurements for various samples at room temperature (**Figure 4-4b** and **4-4d**) as well as from high-temperature Hall measurements of representative samples (**Figure A2-4**). All samples show positive Hall coefficient implying *p*-type semiconducting behavior. It can be noticed from **Figure A2-4b** that the magnitude of the carrier density of various samples at temperatures below the structural phase transition ($T_{\alpha\text{-}\beta}$ = 375 K) strongly depends on the fraction of the β-Cu_2Se polymorph in the sample. For instance, the carrier concentration at 300 K of the pristine Cu_2Se sample (x = 0), which contains 66.7% β-Cu_2Se and 33.3% α-Cu_2Se (**Table A2-1**), is ~69 × 10^{19} cm^{-3}. The carrier density decreases to ~46 × 10^{19} cm^{-3} for the sample with x = 0.01, which is essentially 100% α-Cu_2Se. The trend is consistent with the observed decrease in the electrical conductivity and strengthens our proposed dissolution of Ga into α-Cu_2Se as the likely mechanism leading to lower electrical conductivity. The carrier density at 300 K then increases to ~85 × 10^{19} cm^{-3} for the sample with x = 0.02, which contains 88.1% β-Cu_2Se and 11.9% α-Cu_2Se (**Table A2-1**). The results strongly point to the discrepancy in the phase composition (β-Cu_2Se/α-Cu_2Se) as the origin of the strong variability in the magnitude of the electrical conductivity for pristine Cu_2Se reported in the literature.[13, 143, 167, 171, 233-235] Upon increasing the temperature above the phase transition from the α-Cu_2Se to β-Cu_2Se polymorph, the hole density increases by nearly two-fold at 400 K and continues to increase with rising temperature (**Figure A2-4b**). This behavior can be understood by the enhanced

density of anti-site defects owing to the superionicity of Cu^+ ions in β-Cu_2Se, where the large atomic disorder arising from the diffusion of Cu^+ ions at high temperature leads to the formation of more Cu vacancies.

From the room-temperature values of the carrier density (**Figure 4-4d**), it can be observed that the initial decrease in the electrical conductivity for samples with $x \leq 0.01$ is consistent with a drop in the carrier density. The solubility of Ga into the Cu_2Se crystal lattice, as can be inferred from the initial expansion of the lattice parameters of α-Cu_2Se for compositions with $x \leq 0.01$ (**Figure A2-2a** and **A2-2b**), is expected to reduce the density of structural vacancies as well as serve as an n-type dopant. The resulting electron-hole compensation should lead to a reduction in hole density. In addition, it is anticipated that the intermixing of Cu and Ga at tetrahedral metal positions within the α-Cu_2Se crystal lattice should improve localization of Cu^+ ions, thereby increasing hole mobility due to the reduction in carrier-impurity scattering. Such a mechanism explains well the observed large increase in the carrier mobility in the sample with $x = 0.01$ (24 $cm^2\ V^{-1}\ s^{-1}$ at 300 K), which contains 100% α-Cu_2Se, compared to that of the pristine Cu_2Se (17 $cm^2\ V^{-1}\ s^{-1}$ at 300 K), which is a mixture of 66.7% β-Cu_2Se and 33.3% α-Cu_2Se (**Figure 4-4d** and **A2-4c**). A large increase in the carrier density and sharp drop in the charge carrier mobility are observed for samples with $x > 0.01$, which contain $CuGaSe_2$ nanoinclusions. The rule of mixture suggests that the incorporation of $CuGaSe_2$, which is a wide band-gap semiconductor with large electrical resistivity (50 mΩ cm around 300 K)[236], into Cu_2Se, a narrow band-gap semiconductor, should normally be detrimental to its electrical conductivity as the fraction of $CuGaSe_2$ inclusion increases. Therefore, the observed continuous increase in carrier density (and electrical conductivity) with increasing amount of $CuGaSe_2$ can only be understood by taking into consideration chemical and structural interactions between the coexisting $CuGaSe_2$ and Cu_2Se

phases at the atomic scale (i.e. chemical bonding between $CuGaSe_2$ and Cu_2Se instead of the physical interfaces in simple mixtures). Indeed, it was observed from the DSC measurements (**Figure A2-3a**) and structural characterization (XRD, SEM and HRTEM) data discussed above, that the formation of $CuGaSe_2$ nanoinclusions arising from excess Ga leads to the stabilization at room temperature of a larger fraction of β-Cu_2Se in the synthesized (x)$CuGaSe_2$/(1-x)Cu_2Se nanocomposites, which in turn strongly correlates with the increase in hole concentration and also electrical conductivity in samples with $x > 0.01$. Although all the α-Cu_2Se phase in (x)$CuGaSe_2$/(1-x)Cu_2Se nanocomposites will eventually transform into cubic structure (β-Cu_2Se) above 400 K, the fraction of β-Cu_2Se stabilized at room temperature in various (x)$CuGaSe_2$/(1-x)Cu_2Se nanocomposites increases with the incorporation of high density of $CuGaSe_2$ nanoinclusions. This results in an increase in the hole density and a drop in the carrier mobility for (x)$CuGaSe_2$/(1-x)Cu_2Se composites, at 300 K, with increasing $CuGaSe_2$ content as observed in **Figure 4-4d**.

All samples show positive Seebeck coefficients, which agrees with the positive sign of the Hall coefficients for all samples, indicating the p-type semiconducting behavior (**Figure 4-4c**). Regardless of the composition, the Seebeck coefficient above 400 K increases nearly linearly with rising temperature, once again suggesting that all samples are degenerate semiconductors. On the other hand, the Seebeck coefficient initially increases with Ga content, reaching maximum values for the sample with $x = 0.01$, then decreases with further increase in Ga content ($x > 0.01$), which is consistent with the observed dependence of the electrical conductivity and carrier density for (x)$CuGaSe_2$/(1-x)Cu_2Se composites on Ga content. At 400 K the Seebeck coefficient of the composites initially increases from 69 $\mu V K^{-1}$ for the pristine Cu_2Se ($x = 0$) to 90 $\mu V K^{-1}$ for the sample with $x = 0.01$, which consists essentially of 100% α-Cu_2Se polymorph. Further increasing the Ga content above the solubility limit leads to a drastic drop of the Seebeck to 58 $\mu V K^{-1}$ and

43 μV K^{-1} for the samples with x = 0.02 and 0.05, respectively. It follows from the above analysis that while the $CuGaSe_2$ inclusion is electronically inert, given its wide band gap (E_g ~1.66 eV)[237], it plays a pivotal role in the stabilization of β-Cu_2Se at ambient temperature owing to the high degree of crystallographic registry at the $CuGaSe_2$/Cu_2Se atomic-scale interfaces. Therefore, the fraction of β-Cu_2Se in (x)$CuGaSe_2$/(1-x)Cu_2Se composites and hence the observed electronic transport properties can be tuned by controlling the $CuGaSe_2$ content. As a result, enhanced power factors (**Figure A2-5a**) are observed in samples with $CuGaSe_2$ content x > 0.01, while samples with low fraction (x ≤ 0.01) of $CuGaSe_2$ exhibit degraded power factors due to poor electrical conductivities. For example, the power factor at 873 K initially decreases from 0.89 mW m^{-1} K^{-2} for the pristine Cu_2Se to 0.83 mW m^{-1} K^{-2} for the sample with x = 0.01, then increases to ~1.1 mW m^{-1} K^{-2} for the sample with x = 0.02 (2% $CuGaSe_2$), which represents an improvement of ~20% compared to the pristine Cu_2Se.

The thermal properties (thermal diffusivity, heat capacity and thermal conductivity) of (x)$CuGaSe_2$/(1-x)Cu_2Se composites are displayed in F**igure 4-5**. Similar to the trend observed in the electronic properties, the thermal diffusivity and hence the total thermal conductivity of Cu_2Se initially decrease upon the incorporation of a small fraction of Ga (x ≤ 0.01), reaching the minimum values for the sample with x = 0.01 (**Figure 4-5a** and **4-5c**). Further increasing the Ga content above the solubility limit (x > 0.01) results in a gradual increase in the thermal diffusivity and total thermal conductivity. For example, the thermal diffusivity of the pristine Cu_2Se at 400 K is 0.0046 cm^2 s^{-1} and drops to 0.0021 cm^2 s^{-1} for the sample with x = 0.01 (**Figure 4-5a**). Although the diffusivity at 400 K increases to 0.0038 cm^2 s^{-1} for the sample with x = 0.02, this value is still lower (17% reduction) than that of pristine Cu_2Se. This is a departure from the trend observed in the electrical conductivity and carrier concentration data, where higher carrier density and electrical

conductivity were found for the sample with x = 0.02 compared to the pristine Cu_2Se (**Figure 4-4a** and **4-4d**). Such a low value of the thermal diffusivity for the sample with x = 0.02 suggests either (i) a rather low lattice thermal conductivity or (ii) an "effective" electronic contribution to the thermal conductivity ($\kappa_{e\text{-}eff}$) lower than the value anticipated from the Wiedemann-Franz law ($\kappa_e = \sigma LT$, where L is the Lorenz number and T is the absolute temperature). The diffusivity further increases to 0.0051 $cm^2\ s^{-1}$ and 0.0063 $cm^2\ s^{-1}$ for the samples with x = 0.025 and x = 0.05, respectively. The total thermal conductivity at 400 K follows a similar trend with the lowest value of 0.61 $W\ m^{-1}\ K^{-1}$ obtained for the sample with x = 0.01, which is ~35% lower than the thermal conductivity of the pristine Cu_2Se (0.91 $W\ m^{-1}\ K^{-1}$). Upon increasing the Ga content above the solubility limit, the thermal conductivity at 400 K increases to 0.78 $W\ m^{-1}\ K^{-1}$ for the sample with x = 0.02, which is still 15% lower than that of pristine Cu_2Se (**Figure 4-5c**).

To understand the observed gradual increase in the thermal diffusivity and thermal conductivity for samples with high x values (x > 0.01), we must again consider the atomic scale structural interactions between the coexisting phases. Within the composition range 0.01 < x < 0.05, which is above the solubility limit of Ga in the crystal lattice of α-Cu_2Se, additional incorporation of Ga leads to the formation of $CuGaSe_2$ nanoprecipitates, as observed from XRD, SEM and HRTEM data (**Figure 4-2** and **4-3**). The population density of such nanometer scale $CuGaSe_2$ inclusions increases with the Ga content, leading to higher density of coherent $CuGaSe_2/Cu_2Se$ atomic-scale interfaces. While high density of phase boundaries in semiconducting composites typically results in enhanced phonon scattering and therefore reduced thermal conductivity, the high degree of crystallographic registry at the $CuGaSe_{2\{001\}}/\beta$-$Cu_2Se_{\{100\}}$ interfaces (**Figure 4-2d** and **4-2e**) seems to favor *synchronization* and amplification of lattice vibrations from both sides of the interfaces,

leading to a strong contribution from the lattice thermal conductivity of $CuGaSe_2$ to the total thermal conductivity of the composites. Considering that the room-temperature value of the thermal conductivity of pristine $CuGaSe_2$ is approximately 2.5 W m^{-1} K^{-1},[238] one can better understand the gradual increase in the total thermal conductivity of (x)$CuGaSe_2$/(1-x) Cu_2Se composites with increasing $CuGaSe_2$ content for compositions with x > 0.01. Both the thermal diffusivity and the thermal conductivity of various composites showed very weak temperature dependence between 400 K and 873 K.

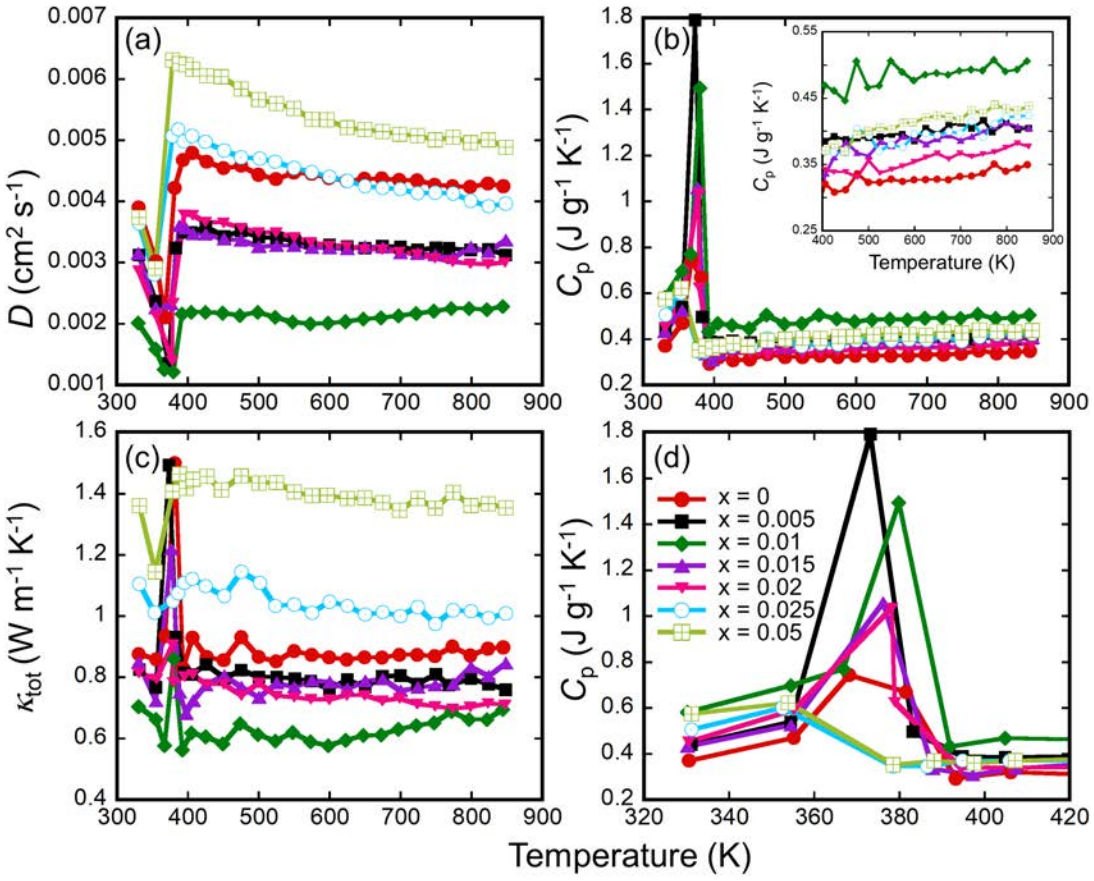

Figure 4-5. Thermal properties of (x)$CuGaSe_2$/(1-x)Cu_2Se composites. (a) Temperature-dependent thermal diffusivity; (b) temperature-dependent heat capacity with (d) a close-up view near the α-Cu_2Se to β-Cu_2Se phase transition and above the transition (inset); and (c) temperature-dependent thermal conductivity.

In contrast to the thermal diffusivity and thermal conductivity, which showed a strong compositional dependency, the heat capacity (C_p) of various (x)$CuGaSe_2$/(1-x)Cu_2Se composites (x > 0.01) above the phase transition temperature (400 K) seems to change

marginally upon increasing the $CuGaSe_2$ content (**Figure 4-5b**). However, a close-up look at the temperature-dependent C_p data (inset of **Figure 4-5b**) revealed that the C_p initially increases from ~0.32 J g^{-1} K^{-1} for the pristine Cu_2Se to ~0.48 J g^{-1} K^{-1} for the sample with x = 0.01, then decreases to values around ~0.4 J g^{-1} K^{-1} for the samples with higher Ga content (x > 0.01). The observed variation in the heat capacity can be attributed to changes in phonon modes resulted from the alteration of the relative proportion of α-Cu_2Se and β-Cu_2Se phases in the synthesized composites. Since β-Cu_2Se, owing to its truncated phonon density compared to α-Cu_2Se, behaves like a liquid, the alteration of its relative abundance in various samples leads to the observed composition-dependent heat capacity. In addition, the heat capacity shows very weak temperature dependence after the phase transition. Careful examination of the phase transition peak around 400 K suggests that the $CuGaSe_2$ inclusions play a significant role in the stability of the β-Cu_2Se phases. It can be observed from **Figure 4-5d** that starting from the sample with nearly 100% α-Cu_2Se (x = 0.005), the intensity of the phase transition peak from α-Cu_2Se to β-Cu_2Se decreases with increasing amount of $CuGaSe_2$, which is consistent with the drop in the relative abundance of the α-Cu_2Se in the samples (**Figure 4-1f**). This further supports our proposed acting mechanism that the incorporation of $CuGaSe_2$ inclusions into Cu_2Se matrix facilitates the formation of the β-Cu_2Se phase at the expense of the α-Cu_2Se phase. It follows from the above analysis that although the embedded $CuGaSe_2$ nanoinclusions do not directly contribute to the electronic properties of (x)$CuGaSe_2$/(1-x)Cu_2Se composites (x > 0.01), they dominate the observed thermal transport properties. This demonstrates a unique ability to decouple charge and heat transports in (x)$CuGaSe_2$/(1-x)Cu_2Se composites, which paves the way to independently tailor the power factor and the total thermal conductivity.

To further assess the degree of independence between the electronic and thermal transport properties in the synthesized composites, the electronic contribution to the thermal conductivity, κ_e, and the lattice thermal conductivity, κ_l, were calculated according to the **Equation** (13) and (14). These equations assume a strong coupling between the electronic and thermal transport in the composites through the Wiedemann-Franz law. To estimate the electronic contribution to the thermal conductivity, the temperature-dependent Lorenz constant was calculated (**Figure A2-6a**) for each composite using the measured Seebeck coefficient data. One can observe a strong dependence of the Lorenz number on both chemical composition ($CuGaSe_2$ content) and temperature. Regardless of the composition, the Lorenz number decreases monotonously with rising temperature. At room temperature, the Lorenz number initially decreases with increasing amount of Ga ($CuGaSe_2$) from 2.1×10^{-8} W Ω K^{-2} for the pristine Cu_2Se to 1.9×10^{-8} W Ω K^{-2} for the sample with x = 0.01, then suddenly increases to 2.15×10^{-8} W Ω K^{-2} and 2.25×10^{-8} W Ω K^{-2} for the composition with x = 0.02 and 0.05, respectively, which is consistent with the trend observed in the electrical conductivity data. Using these Lorenz numbers, the electronic contribution to the thermal conductivity (**Figure A2-6b**) was calculated according to the Wiedemann-Franz law. The resulting values of the electronic thermal conductivity for samples with high Ga content (x > 0.01) represent a large fraction of the measured total thermal conductivity. For compositions with high Ga content, x = 0.02 and x = 0.05, the electronic thermal conductivity is even higher than the total thermal conductivity, which results in negative values of the lattice thermal conductivity (**Figure A2-6c**). This result implies that the Wiedemann-Franz law is not valid for the (x)$CuGaSe_2$/(1-x)Cu_2Se (with x > 0.01). Such deviation from the Wiedemann-Franz law can be interpreted as a manifestation of an independent propagation of charge carriers and heat waves within the synthesized

composites. Such a decoupling can be beneficial in the optimization of the thermoelectric performance of (x)$CuGaSe_2$/(1-x)Cu_2Se composites, through independent tuning of the power factor and the total thermal conductivity. The optimal condition is realized for the sample with x = 0.02, which exhibits a ~48% enhancement in the electrical conductivity and ~22% reduction in the total thermal conductivity at 873 K compared to the pristine Cu_2Se. This leads to a thermoelectric figure of merit, zT ~0.85 at 873 K for the composite with x = 0.02, which corresponds to a 50% enhancement compared to the pristine Cu_2Se (**Figure A2-5b**).

4.4 Conclusion

In summary, we have demonstrated the ability to stabilize the superionic cubic phase of Cu_2Se (β-Cu_2Se) at ambient temperature using coherently embedded sub-ten nanometer scale inclusions of $CuGaSe_2$. Such a nanocomposite was successfully achieved using a two-step solid-state reaction by mechanical alloying. We found that in the first step, the reaction between elemental Ga and $CuSe_2$ results in the formation of the metastable composites (y)$CuGaSe_2$/(1-y)$CuSe_2$ in which nano-scale particles of $CuGaSe_2$ are widely dispersed within the $CuSe_2$ template matrix. In the second reaction step, which involves elemental Cu and the metastable (y)$CuGaSe_2$/(1-y)$CuSe_2$ composites obtained from the first step, the $CuGaSe_2$ nanoinclusions serve as preferential sites for the nucleation of the β-Cu_2Se phase and the formation of low-energy coherent $CuGaSe_2$/Cu_2Se atomic-scale interfaces. This is due to small lattice mismatch, $\Delta a/a$ ~4%, between the *ab* plane of the tetragonal structure of $CuGaSe_2$ and the cubic structure of β-Cu_2Se. Simultaneously, the reaction between elemental Cu and $CuSe_2$ at other reaction fronts far away from the $CuGaSe_2$ inclusions results in the formation of α-Cu_2Se. Therefore, the fraction of the β-Cu_2Se phase in the synthesized composites increases with the $CuGaSe_2$ content in samples with $x \geq 0.01$ and the α-Cu_2Se phase completely vanishes at x = 0.33. This suggests that within this composition range, the

competing reaction leading to the formation of α-Cu_2Se is inhibited by the percolation of $CuGaSe_2$ inclusions, which favors the nucleation of β-Cu_2Se throughout the reaction medium. The ability to tune the ratio between α-Cu_2Se and β-Cu_2Se polymorphs in (x)$CuGaSe_2$/(1-x)Cu_2Se composites by controlling the fraction of $CuGaSe_2$ inclusions, and in turn the formation of nano-scale coherent interfaces between the coexisting phases, leads to some degree of independence between charge and heat transports in the synthesized composites. While the β-Cu_2Se phase dominates the electronic transport, the thermal transport seems to be controlled by the embedded coherent $CuGaSe_2$ inclusions. As a result, a large improvement in the electrical conductivity and significant reduction in the thermal conductivity can be realized simultaneously in samples with optimized compositions, leading to drastic enhancement in the thermoelectric figure of merit. For example, the sample with x = 0.02 shows a ~48% enhancement in the electrical conductivity and ~22% reduction in the total thermal conductivity at 873 K, amounting to a 50% improvement in the thermoelectric figure of merit, zT ~0.85, compared to the pristine Cu_2Se. Our work puts forward an important strategy for the control of phase stability between polymorphs using suitable atomic-scale coherent inclusions, enabling regulations of their functional properties. In addition, it opens a new direction in the design of metamaterials with multifunctional properties, which is achievable by exploiting polymorphism in various phase change materials.

Chapter 5 : Temperature-Dependent Solubility of $CuFeSe_2$ Leads to Dendrite Structure and Temperature-Dependent Doping in Cu_2Se

5.1 Introduction

$CuFeSe_2$ was reported to be a p-type semi-metallic compound with paramagnetic behavior at room temperature.[239-242] In this chapter, we design and synthesize the composite materials $(1-x)Cu_2Se/(x)CuFeSe_2$ with $x = 0, 0.005, 0.01, 0.02, 0.03, 0.05$ and 0.10. We found that $CuFeSe_2$, similarly, has such a low solution limit ($x < 0.02$) in Cu_2Se structure at room temperature that $CuFeSe_2$ starts to form as precipitates when $x \geq 0.02$. A lamella/ dendrite structure is observed when $CuFeSe_2$ appears, which is due to the temperature-dependent solubility of $CuFeSe_2$ in Cu_2Se. The solution of $CuFeSe_2$ gives rise to a doping effect in Cu_2Se. Such temperature-dependent solubility also leads to a temperature-dependent doping effect. As a result, enhanced TE performance is achieved in the samples with low $CuFeSe_2$ content ($x = 0.005$ and 0.01) due to the improved power factors and the reserved low thermal conductivities. The temperature-dependent doping may serve as a promising strategy to achieve future success in thermoelectrics.

5.2 Experimental Details

The $(1-x)Cu_2Se/(x)CuFeSe_2$ composites were synthesized via a one-step solid-state reaction under vacuum following the chemical **Equation** (29).

$$CuSe_2 + 3(1-y)Cu + (y)Fe \rightarrow (1-y)Cu_4Se_2 + (y)CuFeSe_2 \quad (29)$$

Obviously, $x = y/(2-y)$ according the above equation. $CuSe_2$ was pre-synthesized as precursor via solid-state reaction of elemental Cu and Se powders weighed in the stoichiometric ratio. The as synthesized $CuSe_2$ polycrystalline powder was mixed with elemental Fe and Cu powders under

argon atmosphere in a glove box, then thoroughly mixed using mortar and pestle and subsequently sealed under vacuum in a quartz tube. The solid-state reaction was performed at 783 K for 72 hours using a tube furnace. High-density pellets of the synthesized materials were obtained through consolidation of the polycrystalline powder at 758 K under a uniaxial pressure of 100 MPa.

Characterization

The composition and microstructure characterizations are described in Chapter 2. The electrical conductivity and Seebeck coefficient were measured simultaneously from room temperature to 748 K using the four-probe method on a commercial ULVAC-RIKO ZEM-3 system under a low-pressure helium atmosphere. The specific heat capacity and thermal diffusivity were measured on a laser flash system (Linseis LFA-1000) from room temperature to 773 K. Low-temperature and high-temperature Hall measurements were carried out under a magnetic field of 1 T on a home-built apparatus to evaluate the carrier concentration and mobility. Low-temperature magnetic properties were measure on PPMS by Quantum Design.

5.3 Results and Discussion

5.3.1 Structure and Composition

A systematic investigation of phase composition and microstructure was performed on the synthesized (1-x)Cu_2Se/(x)$CuFeSe_2$ composites, which revealed a successful fabrication of the targeted phases. **Figure 5-1** shows the PXRD of (1-x)Cu_2Se/(x)$CuFeSe_2$ composites right after the solid-state reaction. All the samples have clean diffraction patterns, where all diffraction peaks can be indexed with the anticipated Cu_2Se and $CuFeSe_2$ phases. The diffraction peak of $CuFeSe_2$ starts to appear in the sample with x = 0.02 (2% $CuFeSe_2$) and continuously grows in intensity with increasing Fe content in the starting mixture. Most diffraction peaks can be

indexed to monoclinic Cu_2Se (α-Cu_2Se), which is the matrix of the designed composites samples.

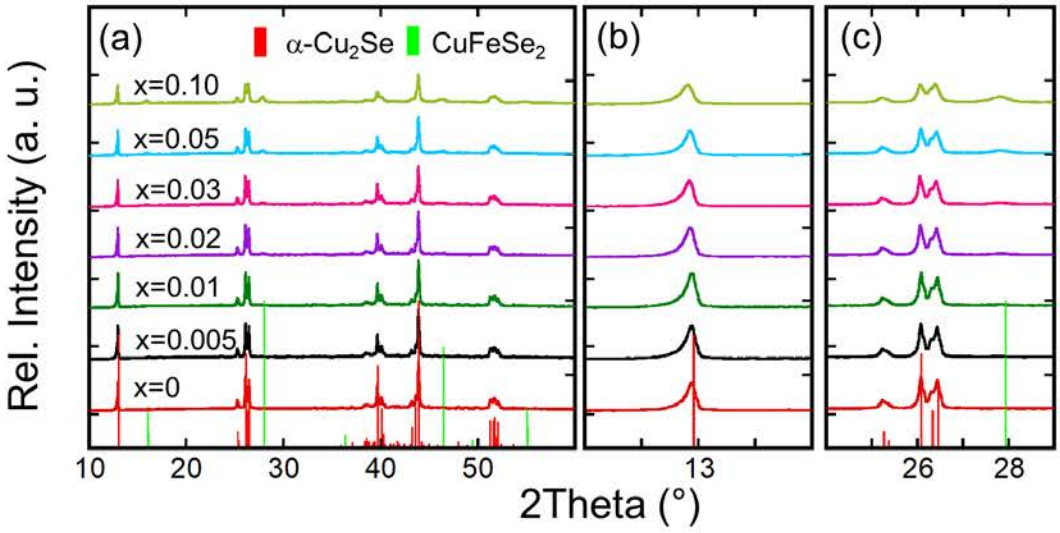

Figure 5-1. Powder X-Ray diffraction (PXRD) of (1-x)Cu_2Se/(x)$CuFeSe_2$ samples after the solid-state reaction (a). Enlarged views of the diffraction peaks around 13° (b) and 27° (c) imply excellent purity of the synthesized samples.

The lattice parameters of the constituent phases were extracted from the XRD patterns using Rietveld refinement (**Figure A3-1**).The variation in lattice parameters of the α-Cu_2Se matrix with increasing Fe content can be divided into 3 segments. The lattice parameters initially decrease with the incorporation of a small amount of Fe ($x \leq 0.01$), then marginally increase for samples with x = 0.02 and 0.03 and finally decrease rapidly with further increase in Fe content ($x > 0.03$). This trend suggests that for low Fe content ($x \leq 0.01$), the incorporated Fe atoms completely dissolve into the Cu_2Se structure, presumably through formation of $Cu_{4-3y}Fe_ySe_2$ solid solution according to the **Equation** (30).

$$(1\text{-}y)\ Cu_4Se_2 + (y)\ CuFeSe_2 \rightarrow Cu_{4-3y}Fe_ySe_2 \qquad (30)$$

Since Fe^{3+} has a smaller ionic radius than Cu^+,[243] the dissolution of Fe leads to a decrease in lattice parameters. Increasing the Fe content above its solubility limit in Cu_2Se ($x \leq 1$ mol%) leads to the precipitation of the ternary compound, $CuFeSe_2$, as nanoscale ribbons within the α-Cu_2Se

matrix, resulting in the expansion of the lattice parameter. At sufficiently high Fe content, the $CuFeSe_2$ nano-precipitates agglomerate into large ribbons that segregate from the Cu_2Se crystals to form incoherent $Cu_2Se/CuFeSe_2$ interfaces. The microstructuring of the composite results in the shrinkage of the lattice parameters of the α-Cu_2Se matrix due to compression strain arising from the smaller lattice parameters of $CuFeSe_2$ (P -4 2 c; a = 5.530 Å, c = 11.049 Å).

The successful synthesis of $(1-x)Cu_2Se/(x)CuFeSe_2$ composites were further confirmed by the DSC analysis, as shown in **Figure A3-2**. All samples have low content of $CuFeSe_2$ (<10 mol%) and only show two endothermic peaks during heating. The peak around 400 K is associated with the phase transition from monoclinic α-Cu_2Se to cubic β-Cu_2Se structure, and the peak around 1373 K corresponds to the melting of Cu_2Se-$CuFeSe_2$ composites. No phase transition or melting peaks anticipated at 819 K and 910 K, respectively, for $CuFeSe_2$ were detected due to its low concentration in the synthesized composites, which are clearly observed in pure $CuFeSe_2$ and $0.5Cu_2Se/0.5CuFeSe_2$, similar to the result reported in literature[244]. Further examination of the transition peaks around 400 K and 1373 K for low-Fe samples gives more information about how the introduction of $CuFeSe_2$ affects thermal stability of the phases in $(1-x)Cu_2Se/(x)CuFeSe_2$ composites. It can be seen that the phase transition peak and the melting peak of Cu_2Se shift towards lower temperature with increasing amount of $CuFeSe_2$. Interestingly, the α-Cu_2Se to β-Cu_2Se (cubic) phase transition peak completely vanishes for the $0.5Cu_2Se/0.5CuFeSe_2$ sample, while the melting peak of Cu_2Se is severely suppressed, decreasing to 1133 K. This is a quite surprising behavior given that the presence of the Cu_2Se phase in the sample is clearly evidenced from PXRD data, suggesting intricate interaction between Cu_2Se and $CuFeSe_2$ in the synthesized composites. The synthesized composites exhibited excellent phase stability after consolidation, as can be measured by the absence of impurity peaks in the XRD patterns (**Figure A3-3)**.

Additionally, no significant peak shift is observed with the increasing amount of Fe/$CuFeSe_2$, indicating a very limited solubility of Fe in Cu_2Se at room temperature which enables an excellent control over composition when forming $CuFeSe_2$ in situ within the Cu_2Se matrix.

The phase composition of the synthesized $Cu_2Se/CuFeSe_2$ composites was further confirmed by SEM observations. At low concentration of Fe/$CuFeSe_2$ ($x < 0.02$), BSE (backscattered) images show a uniform contrast (**Figure 5-2a**) indicating good homogeneity of $Cu_2Se/CuFeSe_2$ composites, with no distinguishable feature from the $CuFeSe_2$ phase. The homogeneity implies that the $CuFeSe_2$ phase is either well dispersed at sub-microscale within the Cu_2Se matrix or that the incorporated Fe is fully dissolved into the Cu_2Se structure to form a solid solution. However, considering the discontinuous decrease in the lattice parameter with increasing Fe content (**Figure A3-1a**), it is reasonable to assume that different mechanisms are at play for various ranges of Fe concentration. The nearly linear decrease in the lattice parameters upon increasing Fe content up to $x = 0.01$ hints at the solid solution of $CuFeSe_2$ in Cu_2Se. Further increase in Fe content to $x \geq 0.02$ resulted in the precipitation of a Fe-rich secondary phase within the Cu_2Se matrix. The phase separation is manifested by the peaks in XRD patterns (**Figure 5-1** and **A3-3**) and by the discontinuity of the lattice parameters versus composition (**Figure A3-1a**) as well as the observation from the BSE images (**Figure 5-2b** to **5-2f**) of fine dendritic features uniformly dispersed within the Cu_2Se matrix. The population density as well as the size of the dendrites increases continuously with increasing Fe content, resulting in the formation of a complex microstructure consisting of Cu_2Se-rich regions with embedded $CuFeSe_2$ fine structures interwoven with $CuFeSe_2$-rich regions containing Cu_2Se nanofibers, as can be observed in the $0.5Cu_2Se/0.5CuFeSe_2$ composite (**Figure 5-2e**). The formation of such hierarchical interweaving dendritic structure is believed to arise from the temperature-dependent partial solubility of

$CuFeSe_2$ into the Cu_2Se matrix.

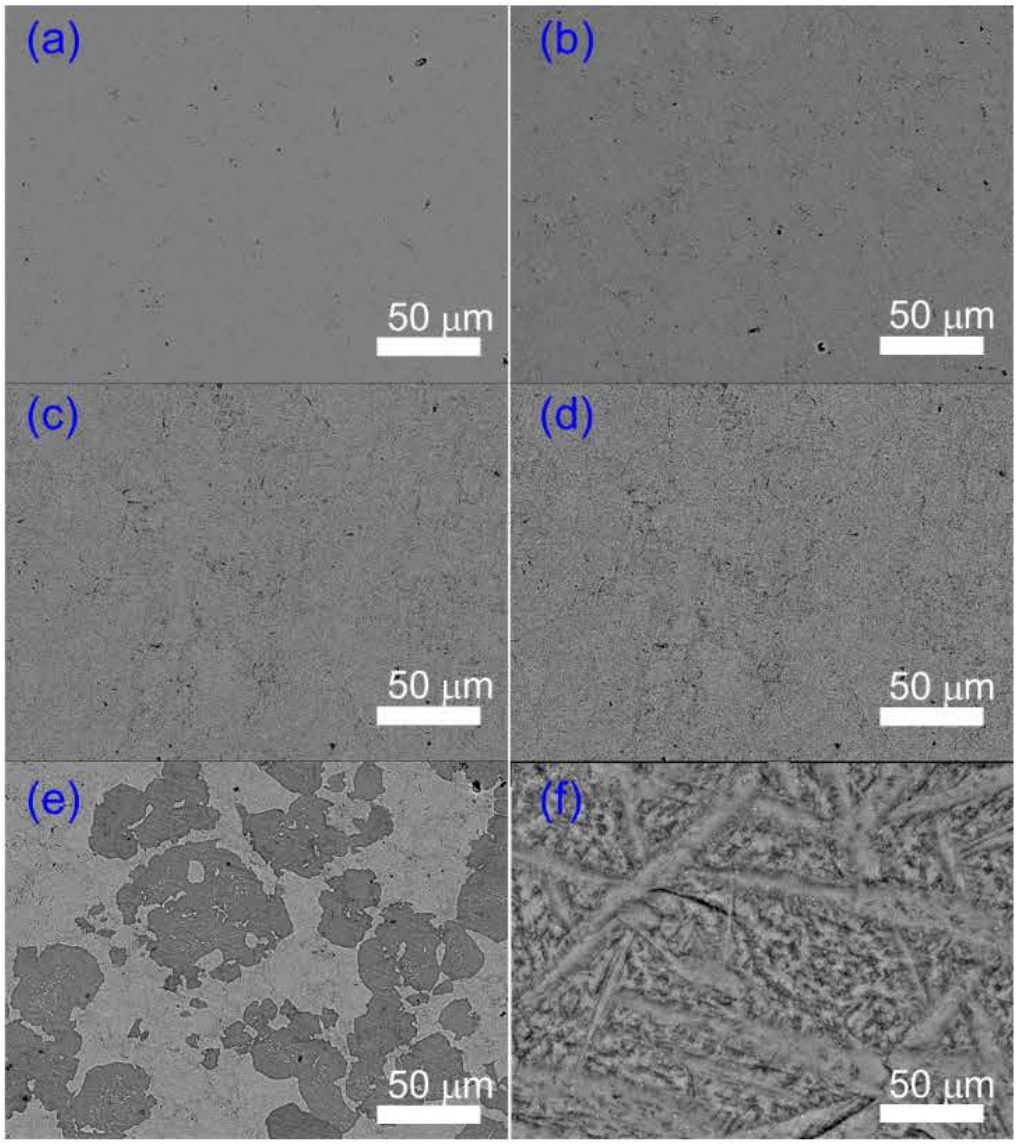

Figure 5-2. BSE images of $(1-x)Cu_2Se/(x)CuFeSe_2$ composite samples: (a) x = 0; (b) x = 0.02; (c) x = 0.05; (d) x = 0.10; (e) x = 0.50; (f) an enlarged view of sample x = 0.10.

Elemental mapping of the synthesized composites indicates a homogeneous distribution on the micron scale of Cu, Fe and Se across the whole sample (**Figure A3-4**, **A3-5**), except for the $0.5Cu_2Se/0.5CuFeSe_2$ sample, which showed a clear separation between Cu_2Se-rich and $CuFe_2Se$-rich regions **(Figure A3-6)**. Such homogeneity in element distribution even for the composite with 10% $CuFeSe_2$, which is far above the solubility limit and should be phase separated, points to a

high degree of integration between the Cu_2Se and the $CuFeSe_2$ phases from the atomic scale to the micrometer scale. Indeed, a careful examination of the high magnification BSE images of all composites with $CuFeSe_2$ mol% ≥ 2% show ultrafine lamella, or dendrite structure, across the entirety of the samples (**Figure 5-3a** to **5-3c**). A close look at the $CuFeSe_2$-rich region in the $0.5Cu_2Se/0.5CuFeSe_2$ composite revealed the presence of similar fine dendritic features presumably with Cu_2Se-rich composition (**Figure 5-3d**).

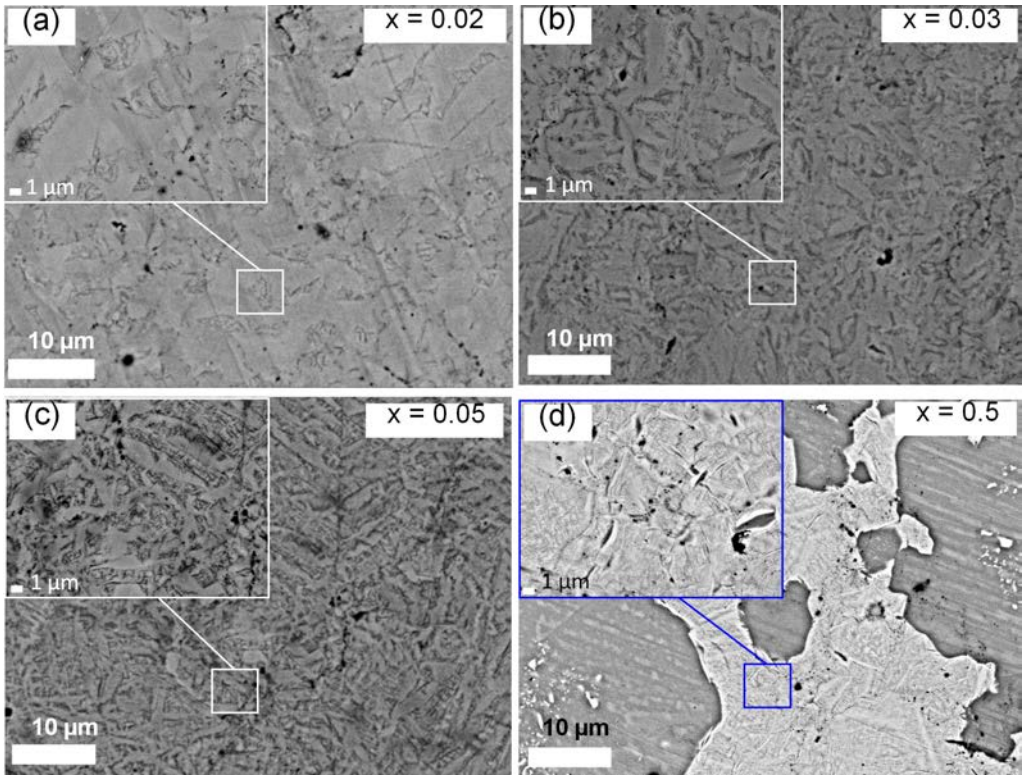

Figure 5-3. High magnification BSE images of $(1-x)Cu_2Se/(x)CuFeSe_2$ composite samples: (a) x = 0.02; (b) x = 0.03; (c) x = 0.05; (d) x = 0.50. Inset in each figure shows an enlarged view of local area.

Furthermore, TEM observations reveal that the black needle-like phase (dendrites) observed under SEM are actually chains of $CuFeSe_2$ particles with average particle size below 50 nm (**Figure 5-4a** to **5-4b**). Such chains of nano particles are randomly embedded in the α-Cu_2Se matrix, as shown by the atomic-resolved image of the matrix (**Figure 5-4c**), which revealed the stacking layers corresponding to the structure projected along the ***c***-axis in monoclinic Cu_2Se (**Figure 5-**

4d). The unique microstructure must stem from an intricate formation process. Specifically, the observed dendritic structure may originate from the enhanced solubility of $CuFeSe_2$ in Cu_2Se at high temperatures.[244-245] Therefore, it is reckoned that a homogeneous solid solution was formed at synthesis temperature, and $CuFeSe_2$ gradually precipitated out due to decreased solubility at lower temperature during cooling. This ex-solution process gives rise to the observed lamella/ dendrite structure. Such temperature-dependent solubility of $CuFeSe_2$ into Cu_2Se is expected to have critical impact on the transport properties of the synthesized $Cu_2Se/CuFeSe_2$ composites.

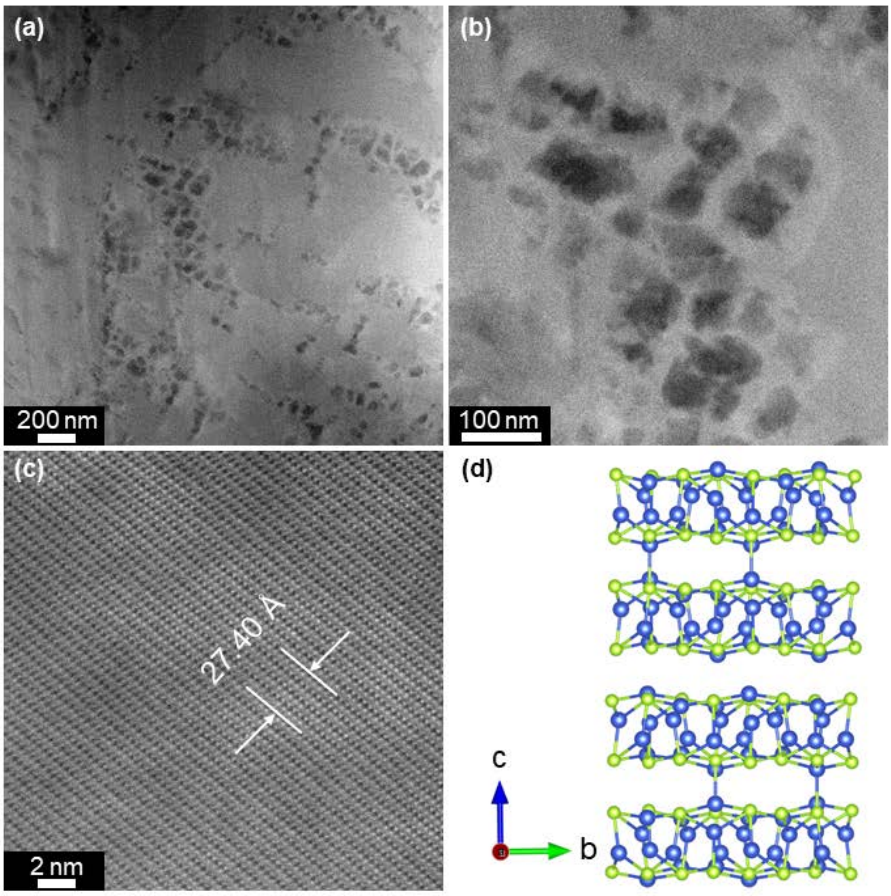

Figure 5-4. TEM images of $0.95Cu_2Se/0.05CuFeSe_2$ composites (a-b) showing chains of $CuFeSe_2$ particles below 50 nm embedded within monoclinic Cu_2Se matrix (c-d).

5.3.2 Thermoelectric Properties

To assess the effect of the observed hierarchical microstructure of the synthesized $Cu_2Se/CuFeSe_2$ composites on their thermal and electronic properties, temperature-dependent measurements of the

electrical conductivity, Seebeck coefficient, Hall effect and thermal conductivity were performed on selected samples. As shown in **Figure 5-5a**, all samples show decreasing electrical conductivity with increasing temperature, indicating the degenerate semiconducting behavior. The degenerate semiconducting behavior in pristine Cu_2Se stems from the formation of Cu vacancies, which seems to be thermodynamically favored in this material. The incorporation of just 0.5 mol% Fe into the Cu_2Se matrix resulted in a surge on the electrical conductivity, which rapidly increases to ~1000 S cm^{-1} at 300 K from ~400 S cm^{-1} for pristine Cu_2Se. The electrical conductivity further increases to ~1200 S cm^{-1} for the composition with 1 mol% Fe and saturates thereafter for all samples with $x \geq 1$ mol% Fe. The electrical conductivities for these samples ($x \geq 1$ mol%) remain clustered over the entire temperature range. Such rapid increase in the electrical conductivity upon Fe incorporation is consistent with a large increase in hole density (**Figure 5-5d**). This trend implies the formation of a solid solution between Cu_2Se and $CuFeSe_2$ at low Fe content ($x \leq 0.01$), which seems to be the solubility limit at 300 K. The clustering of the electrical conductivities for compositions with $x \geq 3$ mol% suggests contributions from p-type $CuFeSe_2$ inclusions to the electronic transport,[241] which is manifested by the marginal increase in the carrier density and gradual decrease in the carrier mobility (**Figure 5-5d**).

Another interesting consequence of the incorporation of $CuFeSe_2$ inclusions into the Cu_2Se matrix is the sharp decrease in the effect of temperature on the electrical conductivity. For example, the electrical conductivity drastically decreases with rising temperature for the sample with $x = 0.5$ mol% $CuFeSe_2$, whereas further increasing the $CuFeSe_2$ content leads to a suppressed degradation of the electrical conductivity at high temperatures. Such leveling off of the electrical conductivity at high temperatures is presumably another signature of the increased solubility of $CuFeSe_2$ in Cu_2Se at high temperatures.

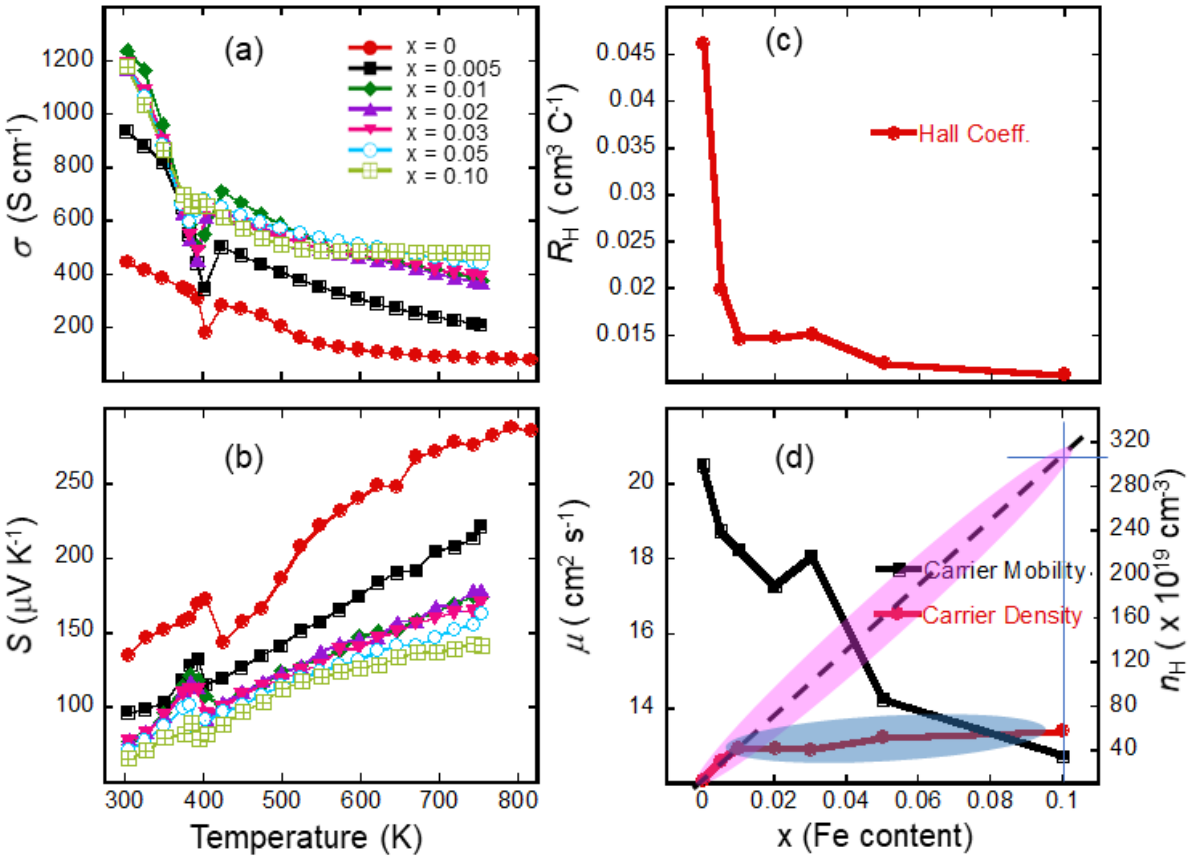

Figure 5-5. Electronic transport properties of (1-x)Cu_2Se/(x)$CuFeSe_2$ composites: (a) electrical conductivity; (b) Seebeck coefficient; (c) room-temperature Hall coefficient and (d) room-temperature carrier concentration, carrier mobility with increasing Fe content.

All samples show positive Seebeck coefficient implying p-type semiconducting behavior. The Seebeck coefficient for all samples, including pristine Cu_2Se continuously increases with increasing temperature, which again is indicative of degenerate semiconducting transport. Samples with 0.5 mol% and 1.0 mol% $CuFeSe_2$ showed a significant drop in Seebeck coefficient compared to pristine Cu_2Se, consistent with the observed increase in the electrical conductivity. Further increasing the amount of $CuFeSe_2$ leads to a continuous decrease in Seebeck coefficient but at a slower rate. The nearly constant Seebeck coefficients for the samples with 1 mol%, 2 mol% and 3 mol% $CuFeSe_2$ again demonstrates the limited solubility of $CuFeSe_2$ into Cu_2Se. The observed strong correlation between the electrical conductivity and Seebeck coefficient data for

$Cu_2Se/CuFeSe_2$ samples is directly linked to the carrier concentration upon incorporation of $CuFeSe_2$. To test this hypothesis, we performed room-temperature Hall measurement on all samples and high-temperature Hall measurement on selected samples. As shown in **Figure 5-5c**, all samples have positive Hall coefficient, indicative of the p-type transport observed from the Seebeck effect. The carrier concentration at 300 K (**Figure 5-5d**) increases rapidly from ~1.3 x 10^{20} cm^{-3} for pristine Cu_2Se to ~3.1 x 10^{20} cm^{-3} for the sample with 0.5 mol% $CuFeSe_2$, then jumps to ~4.3 x 10^{20} cm^{-3} for the sample with 1 mol% $CuFeSe_2$, after which it plateaus until the composition with 3.0 mol% $CuFeSe_2$ is reached. The carrier concentration further increases for samples with x > 3 mol% $CuFeSe_2$, although at a much slower rate. The sharp demarcation in the composition dependence of carrier density for samples with high $CuFeSe_2$ (x > 3 mol% $CuFeSe_2$) clearly points to low doping efficiency arising from the limited solubility of $CuFeSe_2$ into the Cu_2Se matrix at 300K. This result agrees well with the observed saturation of electrical conductivity for samples with x > 3 mol% $CuFeSe_2$ (**Figure 5-5a**). Notably, all composite samples show increasing carrier concentration with rising temperature (**Figure A3-7**), similar to the trend for pristine Cu_2Se and consistent with the semiconducting behavior of the materials. However, a stronger temperature dependence of the carrier concentration can be observed for compositions with high $CuFeSe_2$ content. For example, the carrier concentration for the sample with x = 0.005 shows only a marginal increase with rising temperature, whereas the samples with x = 0.05 and x = 0.10 exhibit a much faster increase in the carrier density with temperature, especially above 573 K. For instance, the carrier concentration for the sample with x = 0.10 increases from ~6.0 x 10^{20} cm^{-3} at 300 K to almost 2.00 x 10^{21} cm^{-3} at 773 K. This represents an enhancement of 230% and the trend is reminiscent of an “intrinsic-semiconducting” behavior, which is in sharp contrast with the degenerate semiconducting behavior observed in the electrical conductivity. Therefore, we can

conclude from the above data that the large increase in the carrier density at higher temperatures originates from the increased solubility of $CuFeSe_2$ into Cu_2Se matrix rather than the typical thermal activation of carriers across the band gap generally anticipated in semiconductors. The observed increase in the carrier concentration at high temperature also explains the plateauing of the electrical conductivity for samples with high $CuFeSe_2$ content (**Figure 5-5a**).

To better understand the effect of the introduced $CuFeSe_2$ it is beneficial to examine the electrical properties of pure $CuFeSe_2$. P-type semi-metallic behavior was reported for pristine $CuFeSe_2$.[240] Therefore, the various effects of $CuFeSe_2$ inclusions on the electrical properties of $Cu_2Se/CuFeSe_2$ composites can be rationalized by considering the intrinsic contribution from $CuFeSe_2$, in samples with large $CuFeSe_2$ content, and the contribution resulting from the temperature-dependent chemical interaction (solid solution) between Cu_2Se and $CuFeSe_2$ phases. In addition, $CuFeSe_2$ was also reported to be ferromagnetic at low temperature,[239-240] which potentially can lead to an interaction between localized magnetic moments and free charge carriers, and transform to paramagnetic at elevated temperature. To investigate the possible influence of the magnetic properties on transport behavior, we performed VSM measurements on selected samples, as shown in **Figure A3-8**. Pristine Cu_2Se is diamagnetic and a very weak field response was observed even at ~2 K. However, the introduction of a small fraction of Fe in the sample leads to various degrees of magnetic ordering at low temperatures. For instance, at a given temperature, the magnetic moment of the various samples increases with increasing Fe content (x values). Regardless of the composition, the magnetic moment gradually increases with decreasing temperature from 400 K to 120 K, and then rapidly increases with further drop in temperature. This behavior is consistent with parallel alignment of localized magnetic moments in the samples. Upon increasing the applied external magnetic field, the magnetic moment of various samples at

a given temperature also increases, which is consistent with ferromagnetic ordering of localized magnetic moments. All these magnetic signatures point to the fact that the magnetism within the $Cu_2Se/CuFeSe_2$ composites agrees well with previous results on the magnetic behavior of pristine $CuFeSe_2$, where ferromagnetism is observed at low temperatures while paramagnetism prevails at/above room temperatures. This magnetic data also confirms the presence of the $CuFeSe_2$ phase in various samples. In addition, given the paramagnetic behavior of $Cu_2Se/CuFeSe_2$ composites at and above room temperature, it is reasonable to rule out the interaction between localized magnetic moments and free charge carriers within the temperature range of thermoelectric interest.

Therefore, we can conclude that the electrical properties of $Cu_2Se/CuFeSe_2$ composites are dominated by the concentration of holes, which in turn is determined by the interaction between the incorporated $CuFeSe_2$ inclusions and the Cu_2Se matrix, as evidenced by the highly consistent correlation between composition, microstructure and electrical properties. At low Fe content, $CuFeSe_2$ dissolves into the Cu_2Se crystal lattice, which makes the overall composition $Cu_{4-3y}Fe_ySe_2$. In other words, the doping of Fe atoms at Cu sites in Cu_2Se together with the cation vacancies boosts the hole concentration significantly. Because of the very limited solubility of $CuFeSe_2$ in Cu_2Se at room temperature, $CuFeSe_2$ exists as a secondary phase when more Fe atoms are added. As a result, the carrier density enhancement from the dissolution of $CuFeSe_2$ gets saturated at room temperature. Although $CuFeSe_2$ was reported to be a p-type metallic phase with the electrical resistivity increasing with rising temperature, it actually has carrier concentrations lower than that in pristine Cu_2Se. Accordingly, there should only be a marginal doping effect from $CuFeSe_2$ precipitates compared to Fe doping at Cu sites in the solid solution. As a result, the electrical conductivity is fairly constant as a function of Fe content above 1 mol%. On the other hand, the temperature-dependent carrier concentration is strongly related to the temperature-

dependent interaction between Cu_2Se and $CuFeSe_2$. For pristine Cu_2Se, a relatively flat carrier concentration is observed until ~573 K above which thermal excitation kicks in, leading to an increase in carrier concentration. However, for $Cu_2Se/CuFeSe_2$ composites, some $CuFeSe_2$ precipitates likely dissolve back into the Cu_2Se matrix due to enhanced solubility at elevated temperature. Consequently, a significant increase in carrier concentration is observed for the sample with high Fe content. For example, the hole concentration increases from ~6.0 x 10^{20} cm^{-3} and 300 K to ~2.00 x 10^{21} cm^{-3} at 773 K for sample with 10 mol% $CuFeSe_2$, which is a much steeper temperature dependency compared to pristine Cu_2Se. Here again it proves that the Fe dissolution gives much higher doping efficiency than precipitate $CuFeSe_2$ itself. The surge in the density of holes in samples with high Fe content leads to a marginal drop of electrical conductivity at high temperatures.

Such careful modulation of the doping level through temperature-dependent solubility of $CuFeSe_2$ into Cu_2Se results in a significant enhancement of the powder factor of $Cu_2Se/CuFeSe_2$ composites at high temperatures compared to pristine Cu_2Se (**Figure 5-6a**). The power factor improvement arose from the ability of the sample to achieve a large electrical conductivity at high temperatures while maintaining a decently high Seebeck coefficient. For instance, pristine Cu_2Se shows a low power factor of ~0.7 mW m^{-1} K^{-2} around 773 K, which is mainly due to a rather low hole concentration and electrical conductivity. Owing to the temperature-dependent solubility of $CuFeSe_2$ into the Cu_2Se crystal lattice, a maximum power factor of ~1.2 mW m^{-1} K^{-2} has been achieved at 773 K for the sample with 1 mol% $CuFeSe_2$, representing an enhancement of ≥ 70% compared to pure Cu_2Se. For degenerate semiconductors, the electrical conductivity usually degrades significantly with rising temperature, which impairs the TE performance at high temperature. The temperature-dependent doping strategy presented here represents a promising

way to tackle this issue, dynamically striking a balance between electrical conductivity and Seebeck coefficient by adjusting the carrier density at elevated temperature.

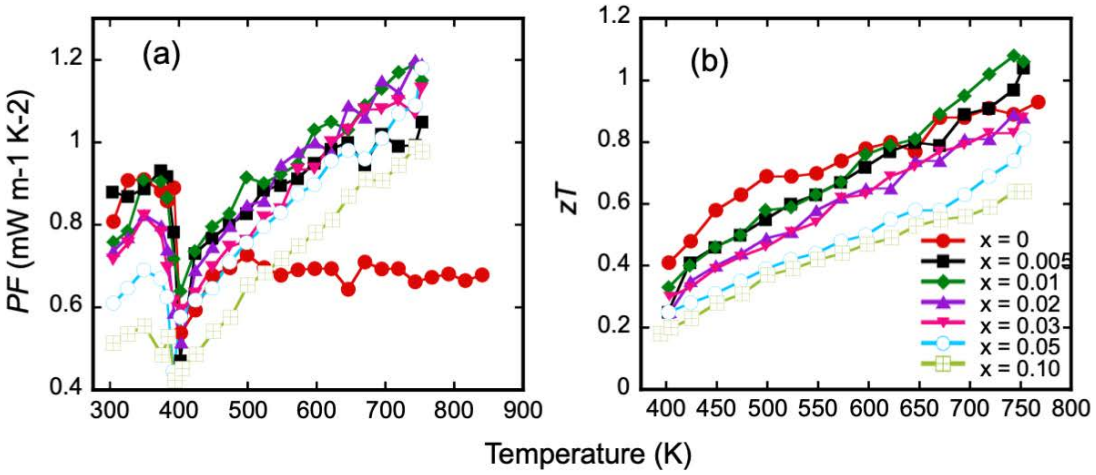

Figure 5-6. Power factor, *PF*, (a) and figure of merit, *zT*, (b) of (1-x)Cu_2Se/(x)$CuFeSe_2$ composites.

The thermal transport properties are presented in **Figure 5-7**. It can be clearly seen that the introduction of $CuFeSe_2$ into the Cu_2Se matrix strongly altered the thermal diffusivity and total thermal conductivity, while a marginal effect is observed on the heat capacity. For example, the thermal diffusivity at 300 K increases rapidly from 0.003 $cm^2\ s^{-1}$ for pristine Cu_2Se to 0.004 $cm^2\ s^{-1}$ and 0.005 $cm^2\ s^{-1}$ for the samples with 0.5 mol% and 1 mol% $CuFeSe_2$, respectively. With even greater content of $CuFeSe_2$, the samples possess essentially the same diffusivity. The temperature dependence of the thermal diffusivity is also strongly affected by the $CuFeSe_2$ content. While the thermal diffusivity of pristine Cu_2Se and that of samples with low Fe content ($x \leq 0.01$) slightly decreases with rising temperature, the samples with high $CuFeSe_2$ content ($x > 0.01$) exhibit a gradual increase in thermal diffusivity, especially at temperatures above 573 K. The trend is consistent with the measured electrical conductivity and further confirms the temperature-dependent doping of the Cu_2Se matrix through dissolution of Fe atoms into the Cu_2Se crystal lattice. The heat capacity of various samples is nearly independent of the $CuFeSe_2$ content, and the magnitude remains similar to that of pristine Cu_2Se in the whole measured temperature range. As

a result, the varying total thermal conductivity of the $Cu_2Se/CuFeSe_2$ composite samples is dominated by the change of thermal diffusivity, which in turn is strongly influenced by the electrical conductivity. The pristine Cu_2Se shows a relatively flat thermal conductivity over the entire temperature range with a value ~0.55 W m^{-1} K^{-1} at 300 K. The incorporation of 0.5 mol% $CuFeSe_2$ and 1.0 mol% $CuFeSe_2$ into the Cu_2Se matrix increases dramatically the total thermal conductivity at 300 K to 0.65 and 0.95 W m^{-1} K^{-1}, respectively. The total thermal conductivity then remains constant with further increase in Fe content. At high temperatures, a gradual increase in the total thermal conductivity is observed, which is consistent with the increase in the electrical conductivity due to temperature-dependent doping of Cu_2Se by $CuFeSe_2$ inclusions.

The observed similarity in the composition and temperature dependencies of the thermal diffusivity and total thermal conductivity to those of the electrical conductivity implies a significant contribution to heat conduction from the charge carriers. To assess this hypothesis, the electronic thermal conductivity, κ_e, and the lattice thermal conductivity, κ_l, were calculated within the temperature range above the phase transition according to the **Equation** (13) and (14). For free electrons, for example electrons in metal, L adopts the value of 2.44 x 10^{-8} W Ω K^{-2}, also knowns as the degenerate limit. However, for most thermoelectric materials, the actual Lorenz constant is lower than 2.44 x 10^{-8} W Ω K^{-2}. Using the degenerate limit to calculate electronic thermal conductivity may lead to a significant error, which will misevaluate the electronic and lattice thermal conductivities. This is particularly true in materials with low thermal conductivities, where electronic thermal conductivity can account for a significant portion of the total thermal conductivity. Therefore, temperature-dependent Lorenz constants were calculated using the temperature-dependent Seebeck coefficients based on **Equation (21-24)** under the single band approximation, as shown in **Figure A3-9a**. A dramatic change in the Lorenz number is observed

with respect to both temperature and composition. On one hand, the Lorenz number decreases monotonically with rising temperature regardless of the composition. On the other hand, it increases significantly with the incorporation of a small amount of Fe atoms into the Cu_2Se matrix up to $x \leq 0.01$, and then continues to increase at a much slower rate with further increase in Fe content ($x > 0.01$). The calculated electronic thermal conductivities are shown in **Figure A3-9b**, which indeed account for a decent portion of the total thermal conductivity. For instance, an electronic thermal conductivity of ~0.2 $W\ m^{-1}\ K^{-1}$ is observed at 426 K for pure Cu_2Se, representing ~36% of the total thermal conductivity. The electronic contribution gets even larger in samples with high $CuFeSe_2$ content. For example, the electronic thermal conductivity at 426 K for the sample with 3.0 mol% $CuFeSe_2$ represents ~62% of the total thermal conductivity. In general, the dependence of the electronic thermal conductivity and the electrical conductivity on both composition and temperature follows a similar trend. However, the calculated lattice thermal conductivities (**Figure A3-9c**) exhibit a more complex composition dependency, which is essential due to the prevalence of multiple phonon scattering mechanisms. Mass fluctuation arising from Fe alloying at Cu sites and the formation of secondary phases at nano/ micro scale are the two main scattering mechanisms we anticipate. More importantly, the variation of the relative importance of either scattering mechanism with the temperature is highly influential on the lattice thermal conductivity. Above all, the variation in thermal conductivity is dominated by the change in the electronic component, which accounts for a large portion of the total thermal conductivity. The change in electronic thermal conductivity is essentially due to the alteration of charge carrier density with respect to composition and temperature through the interaction between the Cu_2Se matrix and $CuFeSe_2$ inclusions.

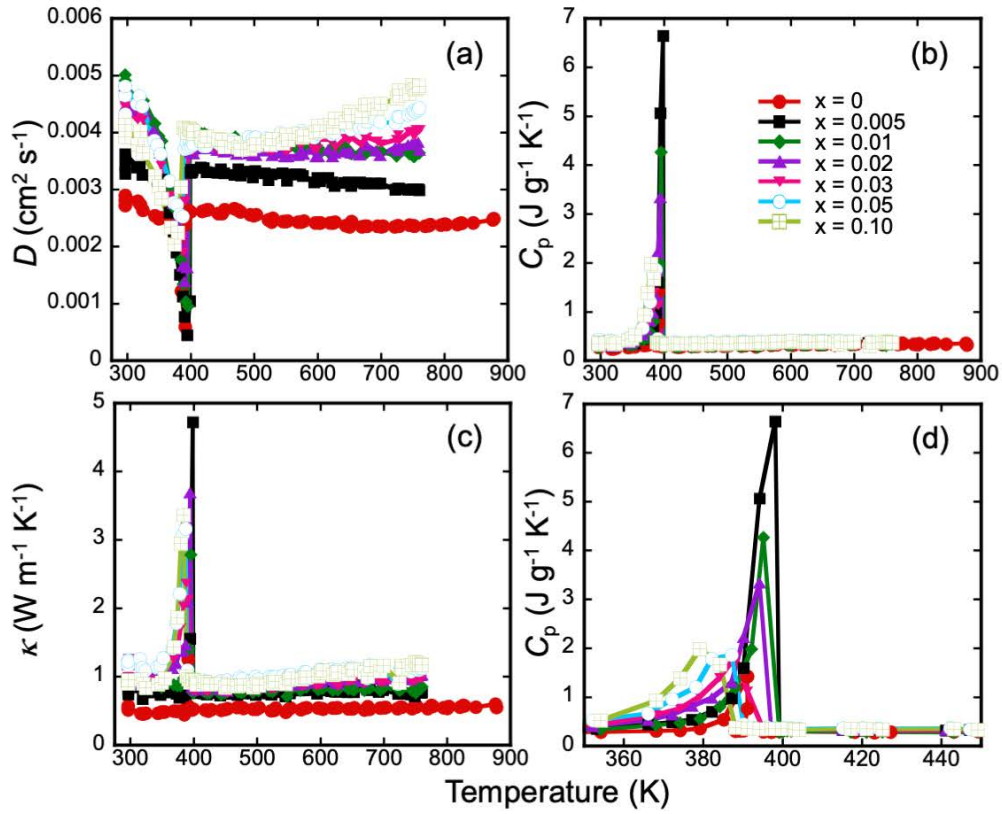

Figure 5-7. Thermal transport properties of (1-x)Cu_2Se/(x)$CuFeSe_2$ composites: (a) thermal diffusivity; (b) heat capacity; (c) thermal conductivity and (d) a close-up view of heat capacity around 400 K.

The thermoelectric figure of merit, *zT,* was calculated for all the samples, as shown in **Figure 5-6b**. Although improved power factor due to enhanced hole concentration at high temperatures was achieved for all composite samples, enhanced $zT \geq 1.1$ at 773 K was only observed for samples with 0.5 mol% and 1 mol% $CuFeSe_2$, while samples with high $CuFeSe_2$ content show degraded figure of merit. The improved figure of merit is due to both high power factors and relatively low thermal conductivity resulting from the modulation of chemical composition (doping level) and microstructure. Crucially, the composition modulation is temperature-dependent, which may help secure even higher TE performance, paving the way to successful application of TE technology.

5.4 Conclusion

(1-x)Cu_2Se/(x)$CuFeSe_2$ composites were successfully synthesized through one-step solid-state transformation of $CuSe_2$ precursor at 783 K using elemental Cu and Fe in the desired ratio. It was

found that at low concentration ($x \leq 0.01$), the incorporated Fe atoms completely dissolve into the Cu_2Se matrix to form $Cu_{4-3y}Fe_ySe_2$ solid solutions with significant increase in the hole density compared to pristine Cu_2Se. However, further increasing the Fe content beyond 1 mol% leads to the formation of $CuFeSe_2$ precipitates as a secondary phase, which contributes much fewer holes to the materials. The formation of $CuFeSe_2$ precipitates implies poor solubility between the Cu_2Se and $CuFeSe_2$ phases at room temperature. However, the solubility of $CuFeSe_2$ into the Cu_2Se matrix increases significantly at elevated temperature, which is evidenced by a rapid increase in hole concentration at temperatures 573 K for samples with high Fe content ($x > 0.01$). Such temperature-dependent solubility between $CuFeSe_2$ and Cu_2Se facilitates the formation, through solid-state reaction, of ultrafine dendrite structures upon cooling the sample to room temperature. In addition, the temperature-dependent solubility of $CuFeSe_2$ into Cu_2Se also enables a temperature dependent dopability of the Cu_2Se matrix, which compensates the degradation in carrier mobility at high temperatures, leading to enhanced electrical conductivity at elevated temperatures for $Cu_2Se/CuFeSe_2$ composites with high Fe content. Such temperature-dependent doping strategy, which is based on the dynamic solubility of the inclusion phase within the matrix, is a powerful tool for properties modulation in thermoelectric materials.

Chapter 6 : Cu Ions Extraction by $CuAlSe_2$ Leads to High Thermoelectric Performance in Cu_2Se

6.1 Introduction

In this chapter, we report a composite strategy via the in-situ formation of $CuAlSe_2$ precipitates as a secondary phase to tune the electrical and thermal properties in Cu_2Se. $CuAlSe_2$ is introduced to construct composite materials within Cu_2Se similarly through a one-step solid-state reaction at high temperature. However, different from $CuGaSe_2$ and especially $CuFeSe_2$, $CuAlSe_2$ as a secondary phase within Cu_2Se matrix leads to composite materials with a completely different microstructures, owning to the unique distribution of $CuAlSe_2$ within Cu_2Se matrix as well as the chemical interaction between them. It was found that the in-situ formed $CuAlSe_2$ extracts Cu ions from the Cu_2Se matrix, creating high Cu deficiency in the matrix and super saturation of Cu in the $CuAlSe_2$ inclusion near the interfaces. This enables an excellent control over the transport properties of Cu_2Se, which is achieved by adjusting the amount of $CuAlSe_2$ introduced. The effects of $CuAlSe_2$ can be traced back to the evolution in chemical composition and microstructure. Consequently, an increased power factor along with a suppressed lattice thermal conductivity is observed in the composite samples with low concentration of $CuAlSe_2$. A high figure of merit zT ~1.8 has been obtained for the sample with 1 mol% $CuAlSe_2$, representing an enhancement of ~80% compared to the pristine Cu_2Se. This improved TE performance in Cu_2Se implies another alternative strategy to achieve future success in thermoelectrics.

6.2 Experimental Details

Synthesis. The synthesis of (1-x)Cu_2Se/(x)$CuAlSe_2$ composites (x = 0, 0.005, 0.01, 0.02, 0.03, 0.05 and 0.10) was carried out in a one-step solid-state reaction starting from $CuSe_2$ as precursor, similar to the manner we synthesized (1-x)Cu_2Se/(x)$CuFeSe_2$. The composite samples were ground up and condensed into solid pellets by a uni-axial hot press system at 773 K under a pressure of 100 MPa for 3 hours. The as-prepared pellets were cut and polished up for various measurements.

Characterization. The composition and microstructure characterizations are described in Chapter 2. Thermoelectric properties were measured from room temperature to ~850 K.

6.3 Results and Discussion

6.3.1 Microstructure and Composition

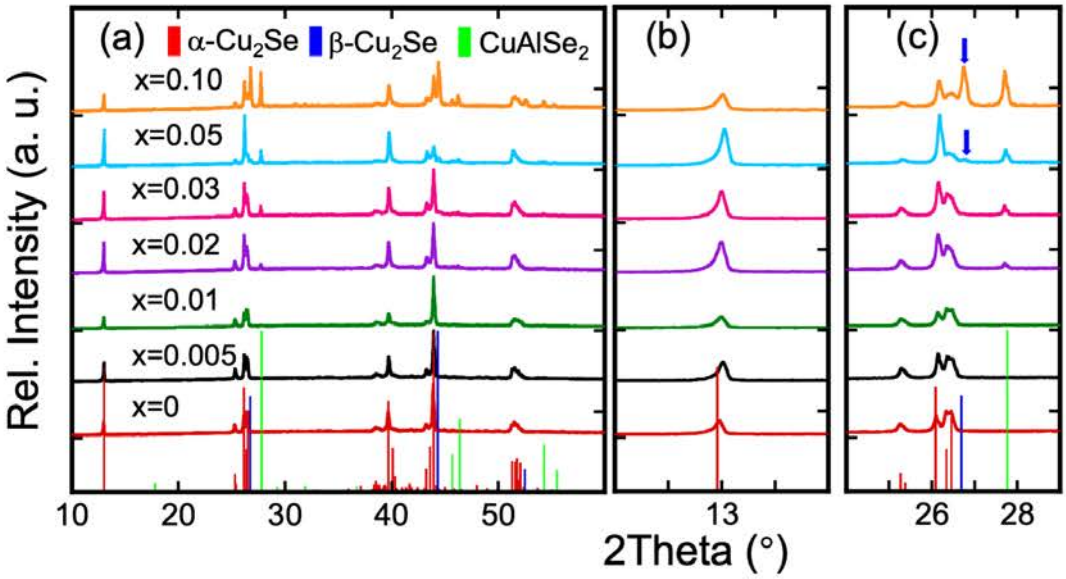

Figure 6-1. Bulk XRD of (1-x)Cu_2Se/(x)$CuAlSe_2$ composites.

Figure A4-1 presents the PXRD patterns of (1-x)Cu_2Se/(x)$CuAlSe_2$ samples. As can be observed, all the samples contain two phases (Cu_2Se and $CuAlSe_2$) with no impurity phase detected. The matrix is monoclinic Cu_2Se and the tetragonal $CuAlSe_2$ starts to appear in the sample with 1 mol% $CuAlSe_2$. With increasing amount of $CuAlSe_2$ introduced, the diffraction peaks from $CuAlSe_2$ significantly grow in intensity. Surprisingly, the diffraction peak around 28° from $CuAlSe_2$

becomes the strongest peak, even when compared to those from Cu_2Se, which may be due to the difference in the crystallinity between these two compounds. The successful synthesis of (1-x)Cu_2Se/(x)$CuAlSe_2$ composites materials is also evidenced by the DSC measurement, as shown in **Figure A4-2**. No extra phase transition peak is observed in the DSC scan. There are only two thermal events during each scan: one being the phase transition from monoclinic Cu_2Se to cubic Cu_2Se and the other being the melting of the composites. A close-up view of these peaks implies that the phase transition peak shifts to lower temperature with increasing amount of $CuAlSe_2$, and similarly, the melting temperature overall decreases with increasing $CuAlSe_2$ content from pure Cu_2Se to sample 0.9Cu_2Se/0.1$CuAlSe_2$. These thermal behavior can be well explained by the pseudo-binary phase diagram of Cu_2Se-$CuAlSe_2$, which is incorporated in Cu_2Se-Al_2Se_3 phase diagram[246]. However, the appearance of the $CuAlSe_2$ phase in these composite samples seems to contradict predictions from the Cu_2Se-$CuAlSe_2$ phase diagram, i.e. a complete solid solution should form with no more than 10 mol % $CuAlSe_2$. This is most likely due to the fact that the phase diagram was constructed based on twenty alloys prepared by mixing Cu_2Se and Al_2Se_3. The purity of the composite samples has been maintained during the hot pressing process (**Figure 6-1**). However, careful examination of the XRD of bulk samples implies that subtle changes happened during consolidation. In powder XRD, it was clearly observed that all diffraction peak can be perfectly indexed to monoclinic Cu_2Se and/ or tetragonal $CuAlSe_2$ with no extra peak for any other phase. By contrast, those peaks around 26-27^o and 42-44^o for monoclinic Cu_2Se change in relative intensity and a new peak (as marked by blue arrow in **Figure 6-1**) appears in the samples with 5 mol% and 10 mol% $CuAlSe_2$, which can be further indexed to cubic Cu_2Se with noticeable peak shifts. Taking those three peaks around 26-27^o from monoclinic Cu_2Se for example, the high-angle peaks gradually diminish with increasing amount of $CuAlSe_2$ after hot press, though the

relative intensity of these peaks looks similar across the whole series of samples in the powder right after solid state reaction. This implies that the pressure assisted consolidation further modulated the composition and microstructure and particularly, the introduced $CuAlSe_2$ plays a vital role in determining the final state of the material. It is quite interesting to see such a transition after hot press, producing cubic Cu_2Se at room temperature. Therefore, a quantitative evaluation of various phases in each sample was carried out using relative intensity ratio (RIR) method, as shown in **Figure A4-3**. Meanwhile, lattice constants were extracted from the Rietveld refinement (**Figure A4-3**). Consistent with the qualitative observation, the quantitative result shows a responsive increase in cubic Cu_2Se with increasing $CuAlSe_2$ and the percentage of $CuAlSe_2$ in each sample is close to the nominal composition considering a reasonable deviation. As a result, cubic Cu_2Se becomes a major phase in the sample with 10 mol% $CuAlSe_2$, accounting for more than 30 percent of the total.

The phase evolution with respect to $CuAlSe_2$ was further evidenced by a detailed study of the microstructure (**Figure 6-2** and **Figure A4-4** to **A4-8**). In the pristine Cu_2Se, the sample appears homogeneous with uniform contrast in the BSE image. EDS analysis indicates a composition of stoichiometric Cu_2Se. The crystal grains are at tens of microns, whose boundaries are marked by scattered mini pores (**Figure 6-2a**). The $CuAlSe_2$, confirmed by EDS analysis, segregates at the grain boundaries and appears as a secondary phase at sub-ten-micron scale in darker contrast even at low concentration (1 mol% $CuAlSe_2$). As its concentration increases, the $CuAlSe_2$ precipitates generally grow in size, but a broad size distribution is still observed in the sample with 10 mol% $CuAlSe_2$. Above all, the $CuAlSe_2$ is evenly dispersed in the Cu_2Se matrix, decorating the boundaries of Cu_2Se grains. Composition analysis near the $Cu_2Se/CuAlSe_2$ interfaces infers an interesting interaction between these two components. **Figure A4-8a** shows $CuAlSe_2$ precipitates

embedded in the Cu_2Se matrix. Point analysis via EDS was carried out at various positions relative to the interface. It is found that compositions are close to stoichiometric Cu_2Se and $CuAlSe_2$ at spots far away from the interface in the matrix and precipitate, respectively. However, a high concentration of Cu was detected in the precipitate near the interfaces, 50% higher than the Al concentration, while the Al: Se ratio is fixed at 1:2. On the other side of the interface, high cation deficiency (~25 mol%) was detected in the matrix compared to stoichiometric Cu_2Se, with a decent amount of Al (~7-10 mol%) in contrast to ~1-2 mol% in the matrix far away from the interface.

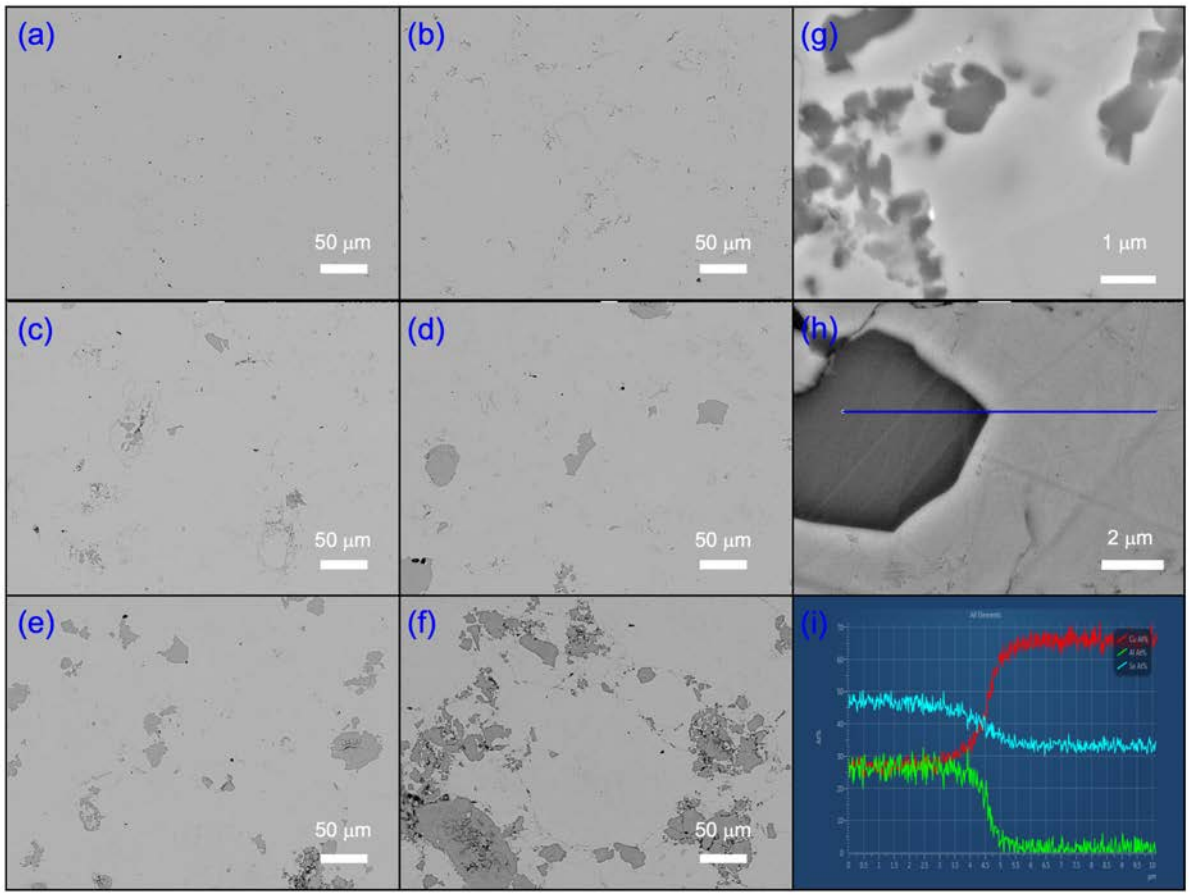

Figure 6-2. Microstructure of $(1-x)Cu_2Se/(x)CuAlSe_2$ composites: BSE image for (a) x = 0; (b) x = 0.01; (c) x = 0.02; (d) x = 0.03; (e) x = 0.05; (f) x = 0.10; (g) an enlarged view of x = 0.01; (h) EDS line scan in x = 0.02 and (i) EDS scanning profiles corresponding to (h).

The composition evolution is further evidenced by a line scan via EDS across the phase boundary, as shown in **Figure 6-2h** and **6-2i**. Continuous variations in Cu, Al and Se content are

observed from the core of the precipitate, across the interface, to the body of the matrix. At the core of the precipitate, a composition roughly of $CuAlSe_2$ is obtained while that in bulk matrix is roughly Cu_2Se. The concentration of individual elements changes significantly at the phase boundary region, which is estimated to be 3 μm in thickness. Such continuous variation in composition may be the result of a steady state achieved out of the diffusion process, where the concentration gradient for each individual element is the driving force.

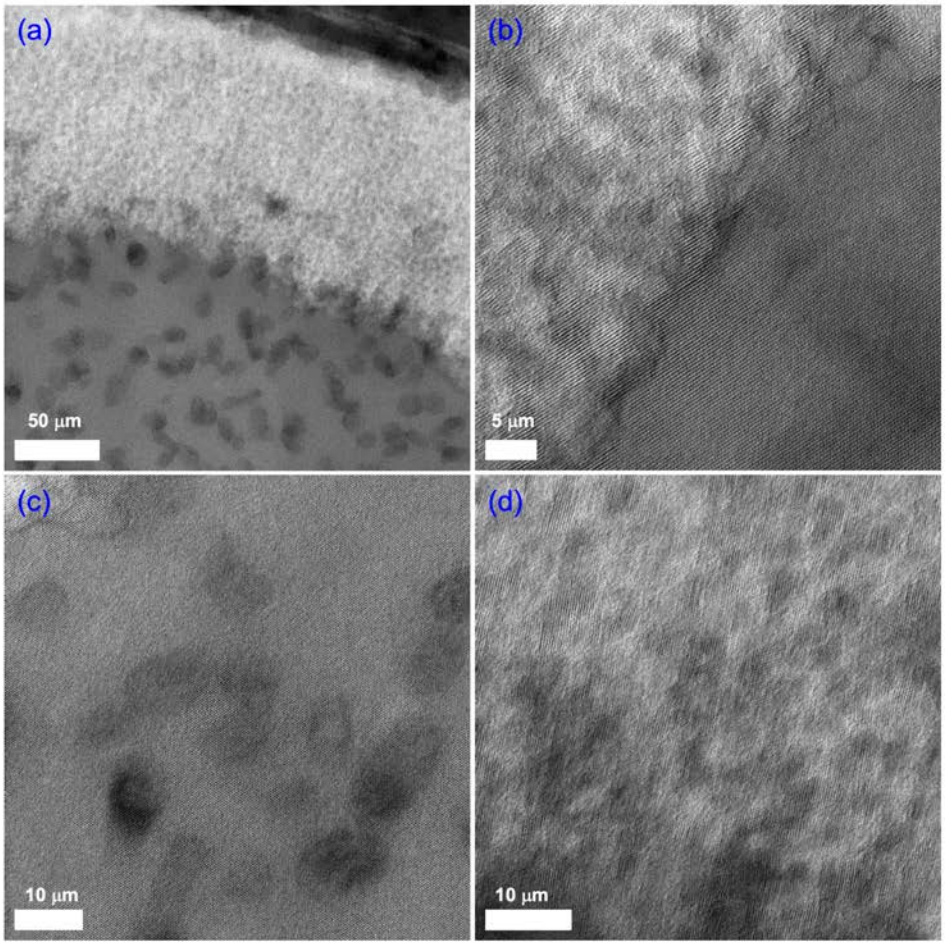

Figure 6-3. TEM images of the $0.95Cu_2Se/0.05CuAlSe_2$ composite: (a-b) low magnification images showing the nanostructures on both sides of the interface; (c) nanostructures around 10 nm in Cu_2Se matrix and (d) nanostructures below 10 nm in $CuAlSe_2$ precipitate.

The diffusion process is supported by the TEM observations. **Figure 6-3** features the microstructure near the $Cu_2Se/CuAlSe_2$ interface in the sample with 5 mol% $CuAlSe_2$, where the

dark side is Cu_2Se and the bright side is $CuAlSe_2$. As mentioned, the interface spans a few microns and therefore, the TEM observations really focus on the area close to the interface (within 150 nm on each side). In both phases, a large density of nano features are observed, which are the traces of the diffusion process. In the $CuAlSe_2$ area, fine dark particles below 5 nm are observed to penetrate from Cu_2Se into $CuAlSe_2$. In the Cu_2Se area, dark features ~10 nm are evenly dispersed within the matrix. Combining with the EDS analysis at microscale, we suspect that nano particles in $CuAlSe_2$ are the mark of Cu ions migrating through the $CuAlSe_2$, which is possible due to the high density of vacancies in its structure. On the other side, Cu deficient $Cu_{2-x}Se$ is created due to the migration of Cu ions, which is probably of cubic structure and appears to be darker in the regular Cu_2Se matrix. The unique microstructure and composition resulted from the interaction between $CuAlSe_2$ and Cu_2Se is expected to significantly affect the electrical and thermal transports.

6.3.2 Thermoelectric Properties

The effect of $CuAlSe_2$ inclusions on the electrical properties is straightforward. With a slight amount of $CuAlSe_2$, the electrical conductivity is significantly boosted and more $CuAlSe_2$ leads to a monotonic increase in the conductivity (**Figure 6-4a**). On the other hand, all samples, including the pristine Cu_2Se, behave as degenerated semiconductors, showing decreasing electrical conductivities with rising temperature. Again, the self-doping phenomenon is due to the formation of Cu vacancies. The conductivity of the pristine Cu_2Se is consistent with the result in our study of (1-x) Cu_2Se/(x)$CuFeSe_2$ composites. The Seebeck coefficient shows a completely opposite trend with respect to both $CuAlSe_2$ concentration and temperature (**Figure 6-4b**). The Seebeck coefficient seems to proportionally decrease with $CuAlSe_2$ concentration, while it increases with

rising temperature. All samples have a positive Seebeck coefficient, indicative of p-type semiconducting behavior.

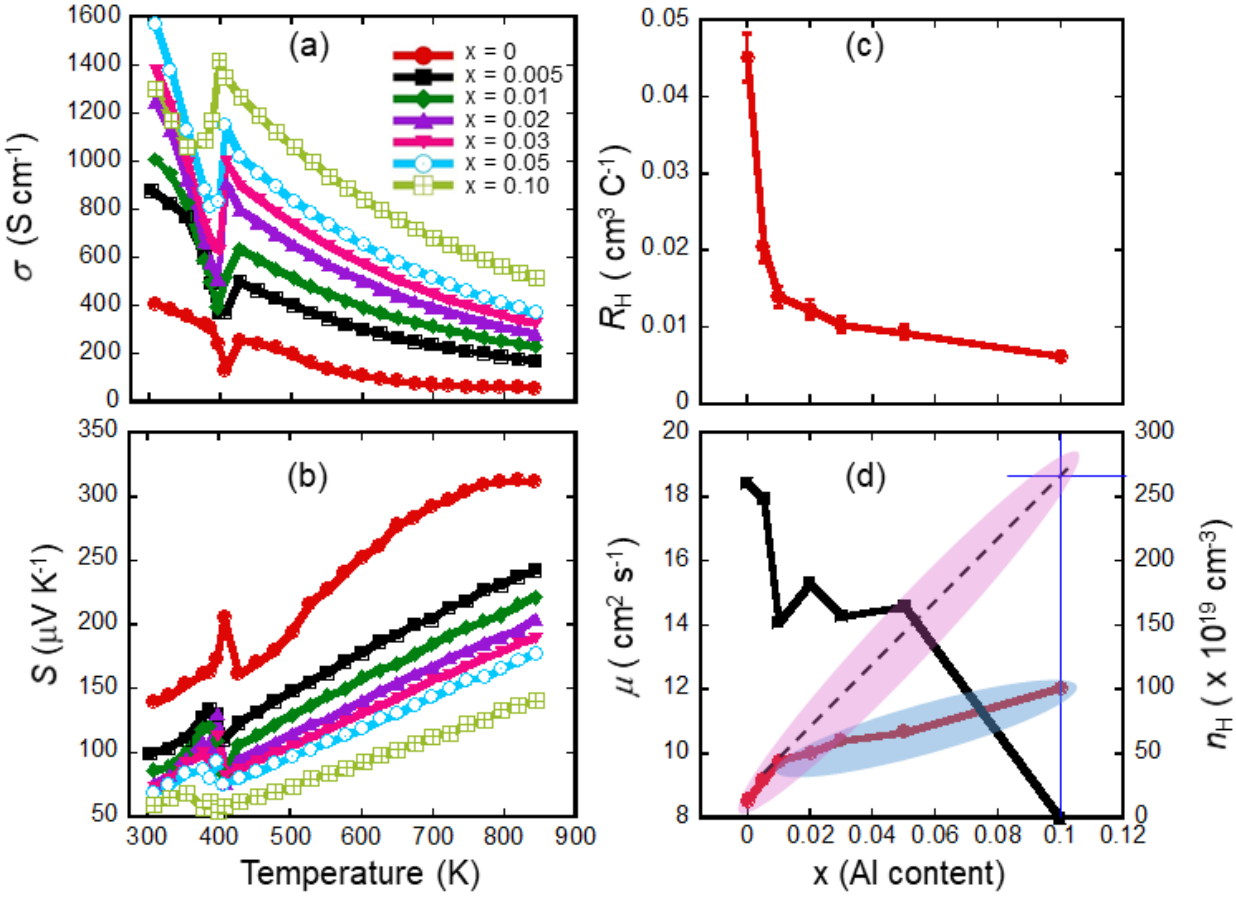

Figure 6-4. Electronic transport properties in (1-x)Cu_2Se/(x)$CuAlSe_2$ composites: (a) temperature-dependent electrical conductivity; (b) temperature-dependent Seebeck coefficient; (c) room-temperature Hall coefficient with increasing Al content and (d) carrier concentration and carrier mobility at 300 K with increasing Al content.

The complete opposite trends of electrical conductivity and Seebeck coefficient hint at the change in carrier concentration with respect to both $CuAlSe_2$ concentration and temperature. To prove this, room-temperature Hall measurements were carried out for all samples and high-temperature Hall were done for selected samples. As shown in **Figure 6-4d**, the carrier concentration ramps up to > 4.0 x 10^{20} cm^{-3} for the sample with only 1 mol % $CuAlSe_2$ from ~1 x 10^{20} cm^{-3} for the pristine Cu_2Se. Further adding $CuAlSe_2$ lead to a continuous increase in carrier concentration at a much slower rate, with a maximum carrier concentration of 1 x 10^{21} cm^{-3} for the

sample with 10 mol % $CuAlSe_2$. The carrier mobility decreases with increasing carrier concentration at a corresponding rate. The significant difference in carrier density prevails over the whole temperature range where high-temperature Hall was conducted, as shown in **Figure A4-9**. With rising temperature, the carrier density increases very slightly for the pristine Cu_2Se and the sample with 1 mol % $CuAlSe_2$. In contrast, the carrier density increases slowly with rising temperature before 673 K, and thereafter increases significantly in the sample with 10 mol % $CuAlSe_2$.

To fully understand the electrical transport properties as well as the influence of $CuAlSe_2$ precipitates, knowing the properties of $CuAlSe_2$ is critically important. $CuAlSe_2$ was reported to be a wide-bandgap semiconductor with a bandgap ~2.7 eV.[236, 247] Usually, p-type $CuAlSe_2$ was observed and more easily achieved compared to its n-type counterpart, which is realized through extrinsic doping by elements like Zn and Cd or changing the Cu/Al ratio in $CuAlSe_2$.[248-249] Recently, Y. Reddy and V. Raja reported the effect of Cu/Al ratio on properties of $CuAlSe_2$ and found high hole concentration in Cu-rich $CuAlSe_2$.[248] However, the n-type conductivity was much lower than the p-type conductivity due to a significant difference in charge carrier density. Therefore, $CuAlSe_2$ itself, as a secondary phase, can be an effective hole dumper within Cu_2Se. Another factor to be considered is the interaction between the $CuAlSe_2$ precipitate with the Cu_2Se matrix. According to the observations from microstructure analysis (chemical composition and distribution of various phases), significant diffusions happened during the synthesis process, resulting in Cu-rich $CuAlSe_2$ and Cu-deficient Cu_2Se at the $Cu_2Se/CuAlSe_2$ interfaces. Cu-rich $CuAlSe_2$ and especially Cu-deficient Cu_2Se give rise to the significant increase in hole concentration. In other words, the hole concentration is proportional to the interface area, which is comprised of Cu-rich $CuAlSe_2$ and especially Cu-deficient Cu_2Se. The driving force of the

diffusion process is the concentration gradient of individual elements. With a low content of $CuAlSe_2$ (< 2 mol%), the resulted precipitates are generally as small as a few microns (**Figure A4-4**), which are comparable to the thickness of $CuAlSe_2/Cu_2Se$ interfaces and can barely be noticed at low magnification under SEM. Therefore, these small precipitates are fully penetrated by Cu ions. With increasing amount of $CuAlSe_2$, the precipitates grow in size and the large precipitates are partially penetrated and consequently the increase in interface area is slowed down, leading to a slowed-down increase in hole concentration as well (**Figure A4-9**). On the other hand, the depth of Cu ion penetration depends on the element concentration gradient and also the diffusion kinetics, which is strongly related to temperature. In other words, the diffusion process is reactivated at elevated temperature, causing thicker interfaces and a larger interface area when steady state achieved. This explains the temperature-dependent hole concentrations of $(1-x)Cu_2Se/(x)CuAlSe_2$ composites. At the low $CuAlSe_2$ content, the hole concentration increases marginally with no significant increase in the interface area since the precipitates are fully penetrated. On the contrary, a large enhancement in hole concentration is observed in the sample with 10 mol% $CuAlSe_2$ at elevated temperature. This is further supported by the following analysis. Assuming that the precipitates are fully penetrated regardless of the $CuAlSe_2$ content, the interfaces area will be strictly proportional to the $CuAlSe_2$ content, leading to a constant increasing rate for hole concentration. By extrapolating the initial increase in carrier density for samples with low $CuAlSe_2$ content to the sample with 10 mol% $CuAlSe_2$, a hole concentration > 2.5×10^{21} cm^{-3} would be expected, which is similar to the value observed in the same sample near 773 K.

As a result of compromising electrical conductivity and Seebeck coefficient, all composite samples above 573 K have improved power factors (**Figure 6-5a**) compared to the pristine Cu_2Se, due to a dramatic increase in carrier concentration. A maximum power factor was obtained in the

samples with 2 mol% and 3 mol% $CuAlSe_2$, suggesting an optimal carrier concentration being achieved.

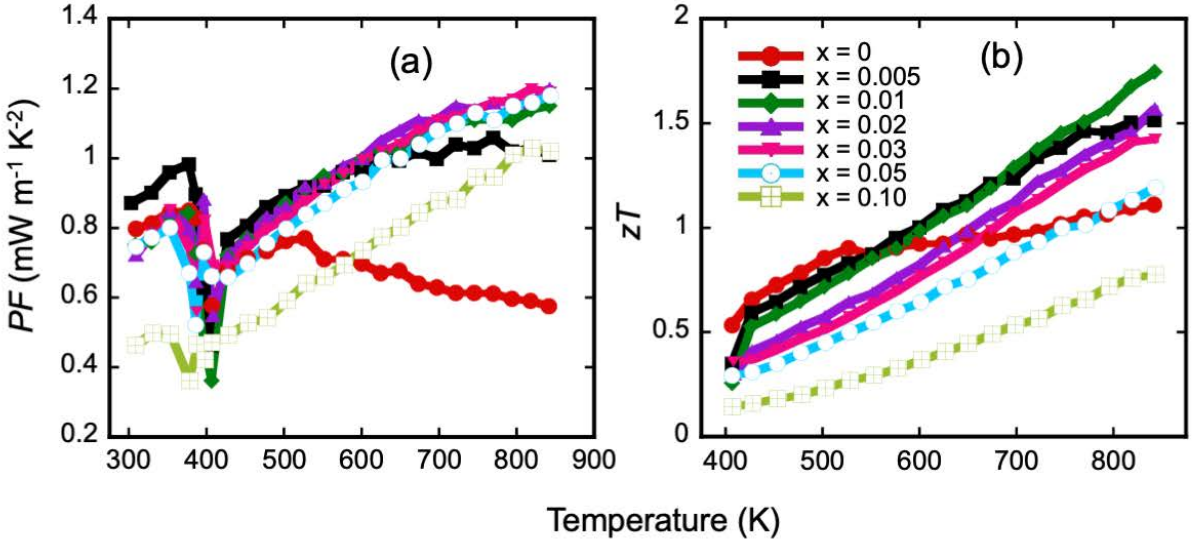

Figure 6-5. Temperature-dependent power factor, *PF*, (a) and figure of merit, *zT*, (b) of various (x)$CuAlSe_2$/(1-x)Cu_2Se composites.

Figure 6-6 presents the thermal transport properties of Cu_2Se-$CuAlSe_2$ samples with respect to temperature. The most dominant effect of $CuAlSe_2$ on thermal transport is the change in thermal diffusivity, compared to heat capacity. As shown in **Figure 6-6c**, all samples have similar heat capacities, which is around 0.2-0.3 J g^{-1} K^{-1}. A close examination (**Figure 6-6d**) suggests that the transition peak in heat capacity first grows stronger and shifts to higher temperature in the sample with 0.5 mol % $CuAlSe_2$, compared to pristine Cu_2Se. With more $CuAlSe_2$, it gradually decreases in intensity and shifts to lower temperature. On the other hand, adding $CuAlSe_2$ monotonically increase the thermal diffusivity, as shown in **Figure 6-6a**. For example, it increases from ~0.0028 cm^2 s^{-1} for the sample with 0.5 mol% $CuAlSe_2$ around 400 K (end of phase transition), to ~0.004 cm^2 s^{-1} for the sample with 2 mol% $CuAlSe_2$, later to ~0.005 cm^2 s^{-1} for the sample with 5 mol% $CuAlSe_2$ and finally to ~0.008 cm^2 $s^{-1}$for the sample with 10 mol% $CuAlSe_2$. As a result, the total thermal conductivity behaves in a similar manner as thermal diffusivity does, implying the change

in thermal diffusivity dominates the change in thermal conductivity. The pristine Cu_2Se bears a thermal conductivity ~0.5 W m^{-1} K^{-1} (**Figure 6-6b**), which is consistent with the value in our previous study of (1-x)Cu_2Se/(x)$CuFeSe_2$ composites. The increment in thermal conductivity seems to be proportional to the amount of $CuAlSe_2$. A marginal increase observed in the samples with 0.5 mol% and 1 mol% $CuAlSe_2$, then a much larger increase is found in the samples with 2 mol%, 3 mol% and 5 mol% $CuAlSe_2$ and finally a significant increase is observed in the sample with 10 mol% $CuAlSe_2$, compared to pristine Cu_2Se.

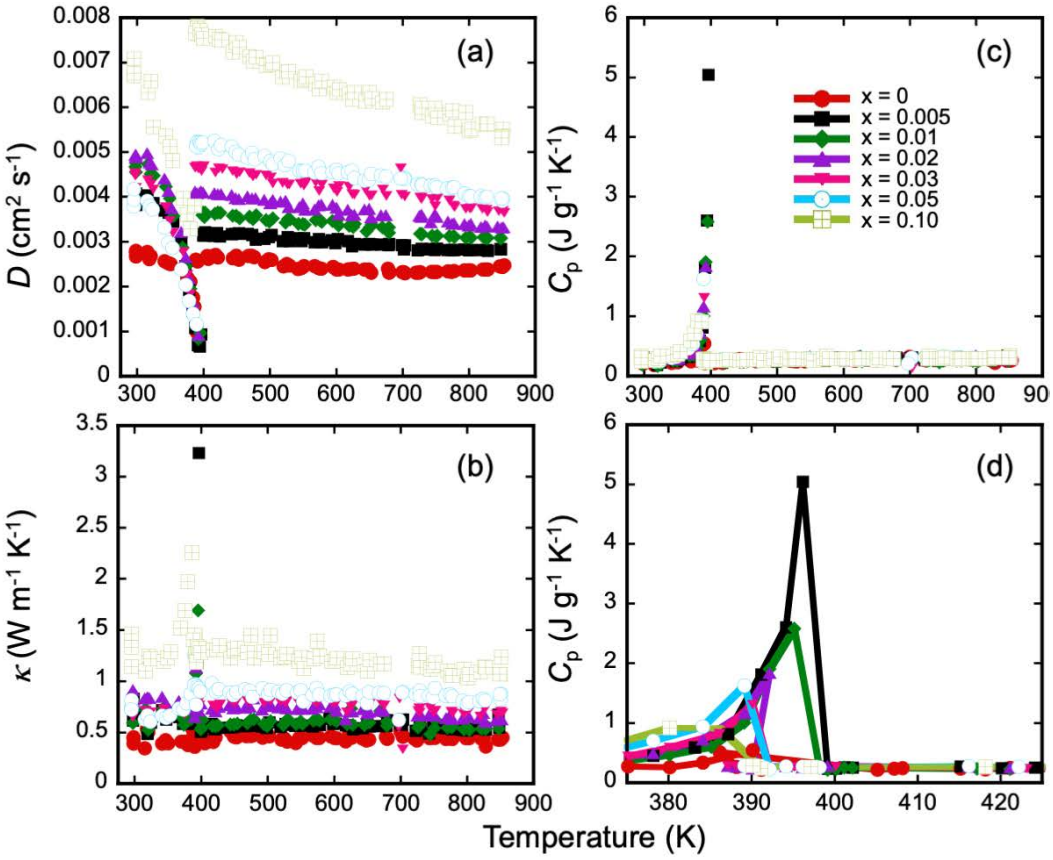

Figure 6-6. Thermal properties of (1-x)Cu_2Se/(x)$CuAlSe_2$ composites: (a) temperature-dependent thermal diffusivity; (b) temperature-dependent thermal conductivity and (c) temperature-dependent heat capacity with (d) a close-up view near the α-Cu_2Se to β-Cu_2Se phase transition.

It is interesting to see that the electrical conductivity and thermal conductivity show similar compositional dependency, hinting at the significant change in carrier concentration by introduced $CuAlSe_2$. In that case, the electronic thermal conductivity must account for a large portion of the

total thermal conductivity. Therefore, we calculated the electronic thermal conductivity based on the Wiedemann-Franz Law, i.e. $\kappa_e = L\sigma T$, where L, σ, T are Lorenz constant, the electrical conductivity of a material and absolute temperature. For a free electron system, L adopts the value of 2.44 x 10^{-8} W Ω K^{-2}. Clearly, the Lorenz constant has a strong dependency on electronic density of states and doping level.[175-176] To precisely estimate electronic thermal conductivity, we calculate the temperature-dependent Lorenz constant for each sample using the measured Seebeck coefficients, detail of which can be found in Chapter 2. Truly, the introduced $CuAlSe_2$ shows a great effect on Lorenz constant (**Figure A4-10a**). The pristine Cu_2Se has the lowest Lorenz constant with a value ~1.77 x 10^{-8} W Ω K^{-2} at room temperature. The Lorenz constant monotonically increases with the amount of $CuAlSe_2$. As a result, a room-temperature value of ~2.15 x 10^{-8} W Ω K^{-2} is obtained for the sample with 10 mol% $CuAlSe_2$. With this, electronic thermal conductivities were calculated (**Figure A4-10b**). The electronic thermal conductivity monotonically increases with the amount of $CuAlSe_2$ as well. The lattice thermal conductivity was calculated by subtracting the electronic thermal conductivity from the total thermal conductivity (**Figure A4-10c**). Surprisingly, the introduced $CuAlSe_2$ seems to be beneficial for the reduction of the lattice thermal conductivity. All composite samples have lower lattice thermal conductivity than the pristine Cu_2Se. Furthermore, increasing the $CuAlSe_2$ content leads to lower the lattice thermal conductivity over the entire temperature range, except the sample with 10 mol% $CuAlSe_2$, which shows increasing conductivity with rising temperature. At this point, we can get a general sense of the contribution from electron transport and lattice vibration to total thermal conductivity. For example, ~42% of total thermal conductivity at ~420 K is from electronic contribution for the pristine Cu_2Se. The electronic contribution ramps up to ~70% for the sample with 0.5 mol%

$CuAlSe_2$, ~88% for the sample with 1 mol%/ 2 mol% $CuAlSe_2$ and ~96% for the sample with 3 mol% and 5 mol% $CuAlSe_2$.

The beneficial decrease in the lattice thermal conductivity can be traced back to the microstructure and the composition near the $CuAlSe_2/Cu_2Se$ interfaces. A large density of nano structures is observed in both $CuAlSe_2$ precipitates and Cu_2Se matrix near the interfaces, which leads to enhanced phonon scattering. Additionally, the alloying of Cu in $CuAlSe_2$ and Al in Cu_2Se gives rise to an even stronger phonon scattering by mass and strain field fluctuations. Adding more $CuAlSe_2$ leads to increasing interface areas with large density of nano structures and improved degree of alloying. Therefore, the lattice thermal conductivity decreases monotonically with increasing $CuAlSe_2$ content. The "abnormal" lattice thermal conductivity for the sample with 10 mol% CuAlSe2 is probably related to the scaled-up precipitates, forming a network within the Cu_2Se matrix. The increased lattice thermal conductivity in the sample with 10 mol% $CuAlSe_2$ may be attributed to the relatively high thermal conductivity of $CuAlSe_2$ compared to Cu_2Se.

The figure of merit zT is presented in **Figure 6-5b**. Composites samples with small amount of $CuAlSe_2$ ($\leq$ 3 mol%) show improved figure of merit zTs, stemming from the enhanced power factors and low thermal conductivities or lowered lattice thermal conductivities. A maximum zT ~1.8 at ~850 K was achieved for the sample with 1 mol% $CuAlSe_2$, representing an enhancement of 80% compared to the pristine Cu_2Se. Furthermore, an even higher zT is expected at elevated temperature considering the continuously growing trend.

6.4 Conclusion

$CuAlSe_2$ as a secondary phase can be in-situ formed within the Cu_2Se matrix through a solid-state reaction. Due to the high tolerance of Cu ions in $CuAlSe_2$ and Al ions in Cu_2Se, ions exchange has been observed at the $CuAlSe_2/Cu_2Se$ interface. High Cu vacancies near the interface in Cu_2Se,

together with Cu-rich $CuAlSe_2$, give rise to a significant enhancement in carrier concentration and thus electrical conductivity. Consequently, the carrier concentration increases monotonically with the amount of $CuAlSe_2$. However, the increasing rate of hole concentration is slowed down in samples with higher $CuAlSe_2$ content, due to the partial penetration of Cu ions into scaled-up $CuAlSe_2$. Meanwhile, extensive alloying between Cu_2Se and $CuAlSe_2$ and a large density of nano structures significantly increase the phonon scattering, leading to the suppressed lattice thermal conductivities. A significantly improved zT has been achieved in the sample with 1 mol% $CuAlSe_2$ due to an enhanced power factor together with a low thermal conductivity. The simultaneous tuning effect on both electrical and thermal properties opens up the opportunity to push the TE performance to an even higher level, making this composite strategy by in-situ forming interactive secondary phase an alternative way to achieve future success in thermoelectrics.

Chapter 7 : Conclusion and Feature Work

7.1 Conclusion

Achieving high-performance materials is critical for practical applications of thermoelectric technology. Previously, high-performance TEs were mainly obtained by achieving low thermal conductivity, either by searching for materials with intrinsically low thermal conductivity or by suppressing the thermal conductivity through nano strategies. However, there are serious limitations for such strategies. For example, the thermal conductivities are already approaching their lower limits. Further improvement requires more focus on developing strategies to modulate the electronic transport. This thesis work is dedicated to exploring novel composite strategies for regulation of TE properties. Different from traditional composite strategy, the novel composite strategies aim at structural and compositional modulations through forming interactive interfaces, which leads to various effects on electronic and thermal transports. The major findings from this work are listed below:

1. By introducing magnetic full Heusler precipitates at nanoscale, a stronger regulation of electronic transport has been achieved due to (1) the energy filtering effect at the HH/FH interfaces because of misalignment of conduction bands for HH and FH phases, and (2) the localization of free electrons near magnetic impurities. In contrast to nonmagnetic FH precipitates, the application of magnetic FH precipitates enabled significant decrease in the carrier concentration even in a heavily doped HH matrix. High power factor was maintained due to the improved carrier mobility and Seebeck coefficient. A high power factor, in conjunction with a decreased thermal conductivity, resulted in a dramatic enhancement in the thermoelectric figure of merit.

2. Successful synthesis of (1-x)Cu_2Se/(x)$CuMSe_2$ composite materials was achieved through solid-state reactions by co-forming precipitate and matrix materials from a common precursor, Cu_2Se. The unique synthesis routes created highly interactive interfaces between $CuMSe_2$ precipitates and the Cu_2Se matrix. By choosing different precipitate materials, various interactions have been observed, leading to various modulations on the electronic and thermal transport. It is found that $CuGaSe_2$ has a very limited solubility ($\leq$ 1 mol%) in Cu_2Se. Below the solubility limit, all $CuGaSe_2$ will dissolve into Cu_2Se structure, stabilizing the α-Cu_2Se phase. Above the solubility limit, nanoscale $CuGaSe_2$ precipitates will serve as "crystal seeds" that guides the formation of β-Cu_2Se and stabilizes it at room temperature, due to excellent registry along certain orientations between $CuGaSe_2$ and β-Cu_2Se. The ratio of α-Cu_2Se to β-Cu_2Se in the material can be tuned by simply adjusting the $CuGaSe_2$ content and nearly pure β-Cu_2Se has been formed as the matrix with an introduction of 33 mol% $CuGaSe_2$. The strong correlations between electronic/ thermal transport properties and the ratio of β-Cu_2Se suggests an effective strategy to tune materials properties by selectively forming certain polymorph. When compositing Cu_2Se with $CuFeSe_2$, fascinating dendrite structures were observed within the composite materials, which is attributed to the temperature-dependent solubility of $CuFeSe_2$ in Cu_2Se. At high temperature, the solubility is higher than it is at low temperature. Therefore, when the materials are cooled down from high temperature during synthesis, the extrusion of $CuFeSe_2$ from the Cu_2Se matrix causes an extremely fine dendrite structure. When a small amount of $CuFeSe_2$ dissolves into Cu_2Se, an off stoichiometric Cu_2Se, i.e. $Cu_{2+m}Fe_mSe_{1+2m}$, forms and p-type doping arises from such a solid solution. At low concentration, $CuFeSe_2$ fully dissolves into Cu_2Se and dope the matrix at high efficiency. In contrast, $CuFeSe_2$ partially dissolves into Cu_2Se and dope the matrix at a much lower efficiency. The partial dissolving of $CuFeSe_2$ and its temperature-dependent solubility leads to an

interesting temperature-dependent doping effect as well. Different from $CuGaSe_2$ and $CuFeSe_2$ as precipitates, which both are well dispersed within Cu_2Se matrix, $CuAlSe_2$ precipitates seems to agglomerate severely, presumably due to high diffusion rate of Al^{3+} ions. However, the Cu ion extraction by $CuAlSe_2$ precipitates leads to a large density of nano structures and high Cu vacancies in Cu_2Se near the interfaces between $CuAlSe_2$ and Cu_2Se, thus simultaneously doping the materials and suppressing the lattice thermal conductivity. The penetration of Cu ions into $CuAlSe_2$ is further affected by temperature, making such a doping mechanism to be temperature dependent as well. A significantly improved power factor together with a low thermal conductivity resulted in a dramatic enhancement in thermoelectric figure merit.

7.2 Future Work

7.2.1 (1-x)Cu_2Se/(x)$CuCrSe_2$ for Thermoelectric Application

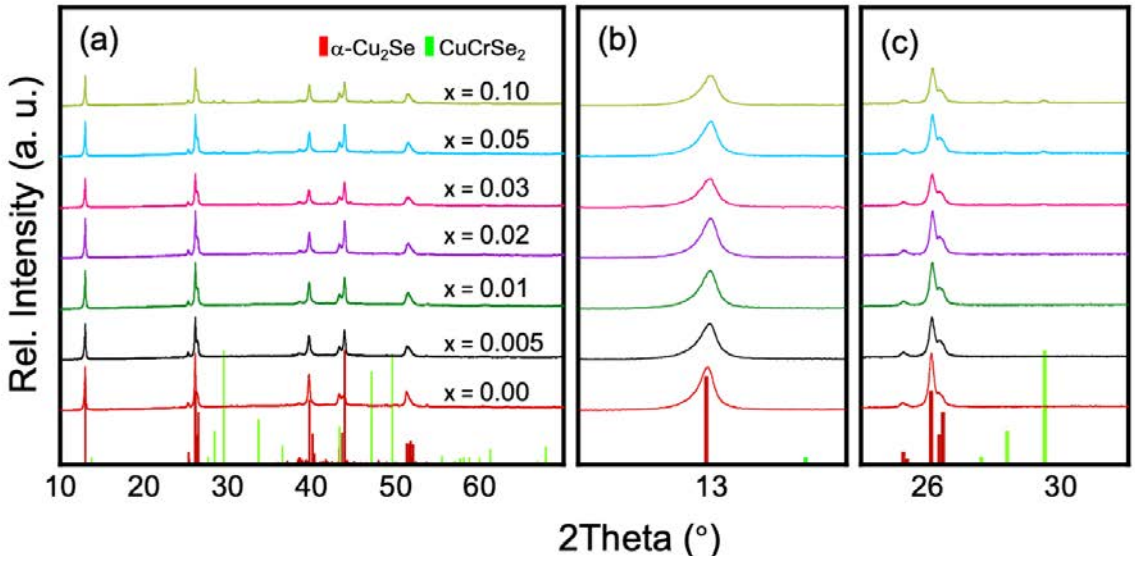

Figure 7-1. Bulk XRD of (1-x)Cu_2Se/x$CuCrSe_2$ composites after consolidation by hot pressing.

$CuCrSe_2$ is reported to be another phonon-glass-electron-crystal material with high TE performance.[250-254] $CuCrSe_2$ crystallizes in the R3m structure, in which $CrSe_2$ forms CsI_2 type layers with disordered Cu^+ cations distributed in-between. Therefore, $CuCrSe_2$ is also a superionic compound with an order-disorder transition around 365 K, above which a fast ion conducting state

prevails.[255-256] Additionally, a strong intralayer magnetic interaction was reported in $CuCrSe_2$ due to the competing magnetic exchanges: the antiferromagnetic direct exchange between nearest-neighbor Cr cations and the ferromagnetic Cr-Se-Cr super-exchange.[257-258] (1-x)Cu_2Se/(x)$CuCrSe_2$ composites with highly interactive interfaces will probably lead to complex effects on the TE transport properties.

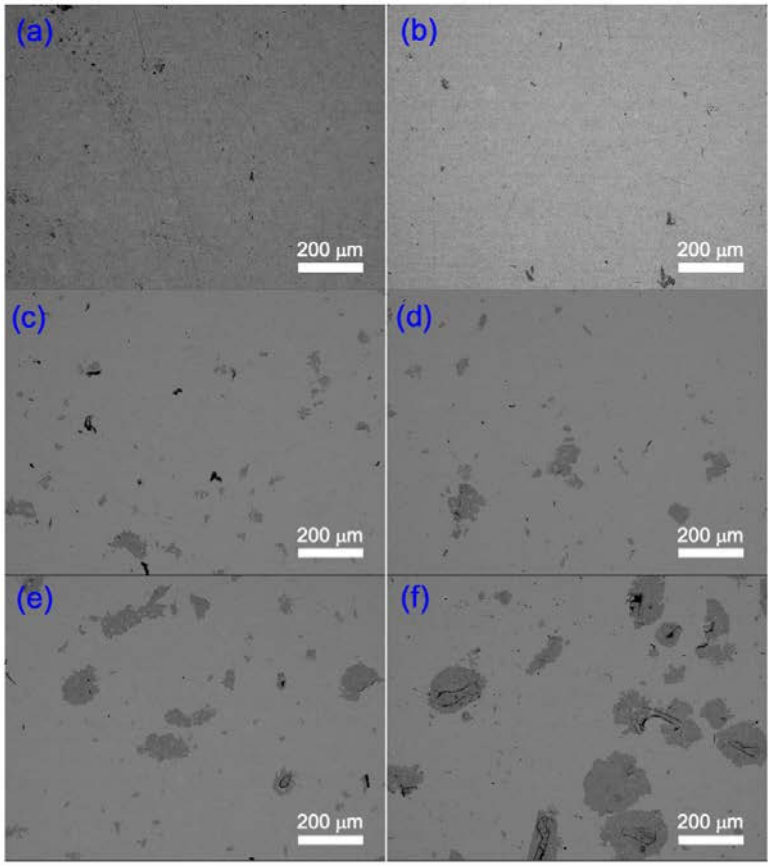

Figure 7-2. BSE images of (1-x)Cu_2Se/x$CuCrSe_2$ composites after consolidation by hot pressing: (a) x = 0; (b) x = 0.005; (c) x = 0.02; (d) x = 0.03; (e) x = 0.05 and (d) x = 0.10.

Preliminary studies have been conducted on (1-x)Cu_2Se/(x)$CuCrSe_2$ composites for thermoelectric applications. The synthesis of (1-x)Cu_2Se/x$CuCrSe_2$ composites was carried out in a similar manner as we did for making (1-x)Cu_2Se/(x)$CuFeSe_2$ and (1-x)Cu_2Se/(x)$CuAlSe_2$ composites. Composition and microstructure investigations suggest a successful synthesis of (1-x)Cu_2Se/(x)$CuCrSe_2$ composites with no impurity detected, as shown in **Figure 7-1**, **7-2** and

Figure A5-1 to **A5-6**. It is interesting to notice that the introduced $CuCrSe_2$ agglomerates to micron scale precipitates even at extremely low concentrations, such as 0.5 mol%, while the diffraction peaks for $CuCrSe_2$ are barely visible even at high concentrations, such as 10 mol%. Thermoelectric measurements have been conducted, including electrical conductivity, Seebeck coefficient, thermal conductivity and Hall carrier concentration, as shown in **Figure 7-3** to **7-5** and **Figure A5-7**, **A5-8**. Consistent with previous cases, all samples including the pristine Cu_2Se behave like a degenerated semiconductor, showing decreasing electrical conductivity and increasing Seebeck coefficient with rising temperature. The compositional dependency of TE properties seems to be less straightforward, suggesting a possible complex interaction between $CuCrSe_2$ precipitates and Cu_2Se matrix.

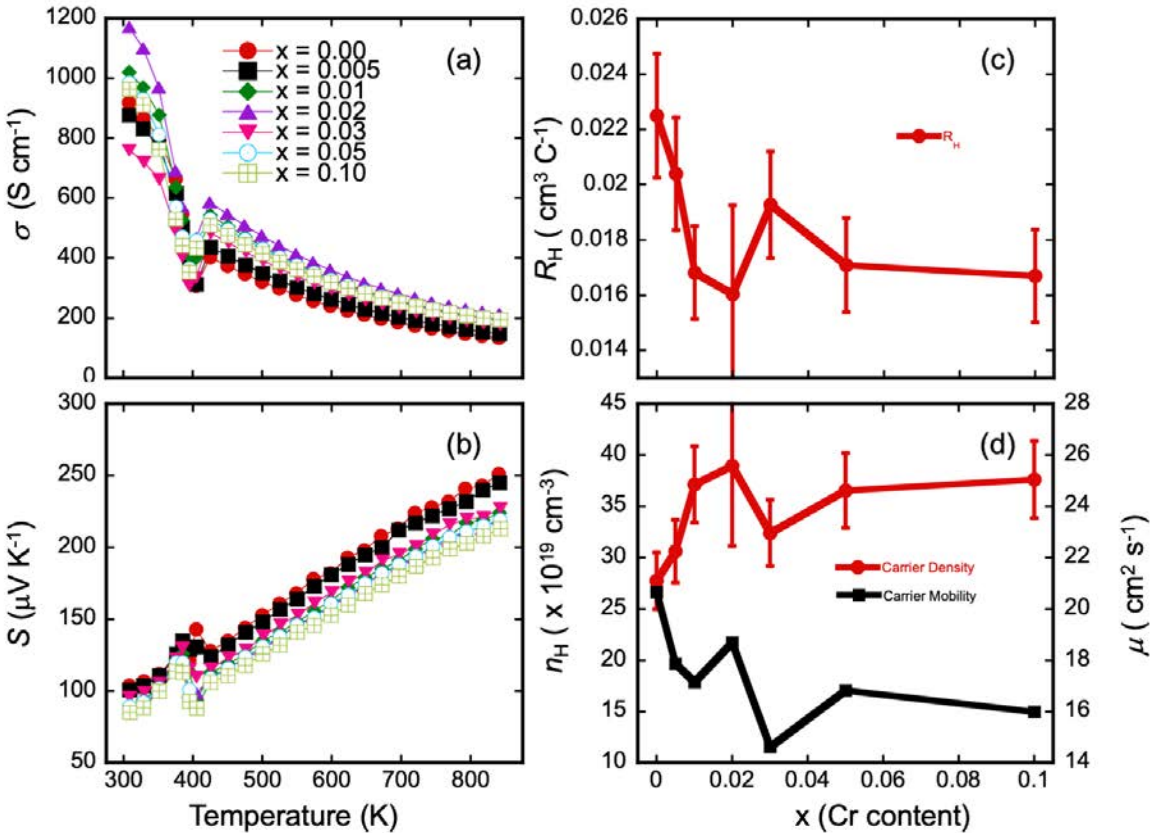

Figure 7-3. Electronic transport properties in $(1-x)Cu_2Se/(x)CuCrSe_2$ composites: (a) temperature-dependent electrical conductivity; (b) temperature-dependent Seebeck coefficient; (c) room-temperature Hall coefficient with increasing Cr content and (d) carrier concentration and carrier mobility at 300 K with increasing Cr content.

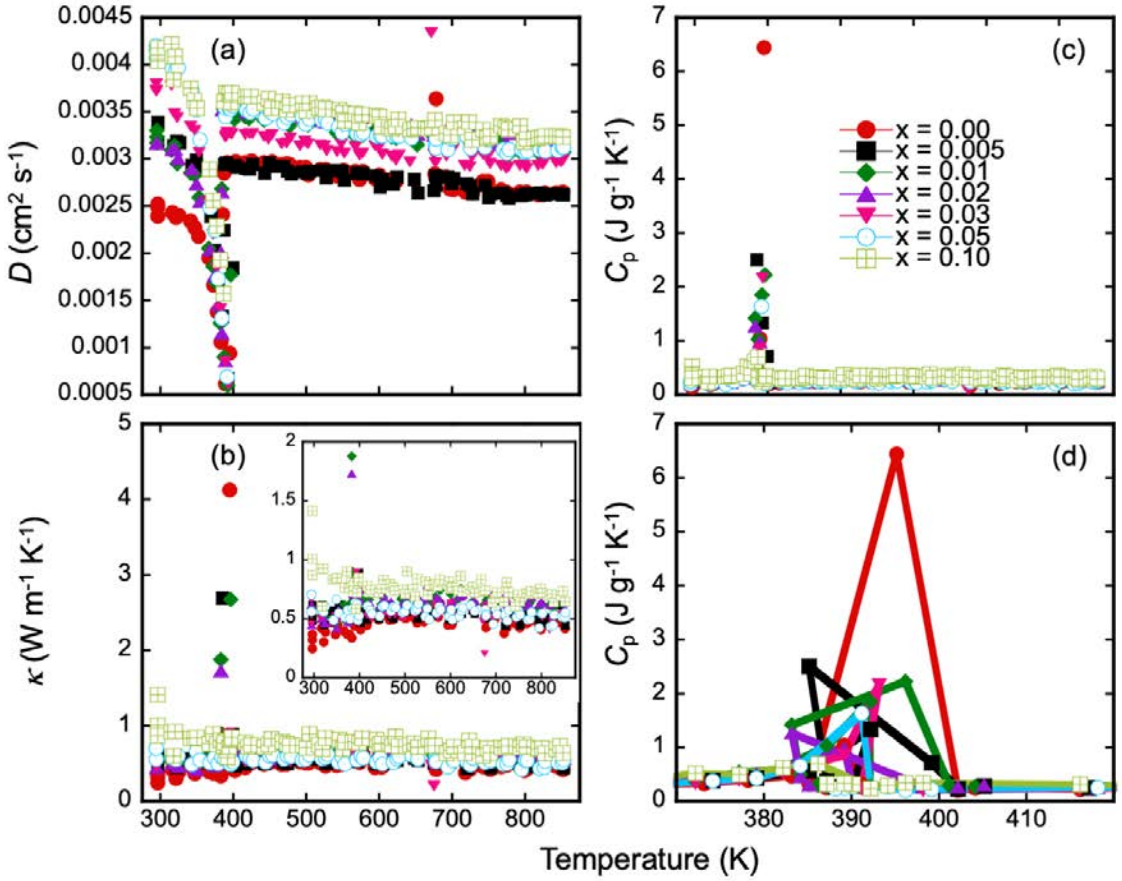

Figure 7-4. Thermal properties of (1-x)Cu_2Se/(x)$CuCrSe_2$ composites: (a) temperature-dependent thermal diffusivity; (b) temperature-dependent thermal conductivity and (c) temperature-dependent heat capacity with (d) a close-up view near the α-Cu_2Se to β-Cu_2Se phase transition.

To uncover the mysterious interaction between Cu_2Se and $CuCrSe_2$, systematic composition and microstructure studies should be conducted at even smaller scales, for example under TEM, focusing on the Cu_2Se/$CuCrSe_2$ interfaces. Further, the interaction between Cu_2Se and $CuCrSe_2$ may cause interesting magnetic behavior, which is different from what is observed in pure $CuCrSe_2$. With a thorough understanding of material's composition, microstructure, magnetic properties and TE transport properties, the correlation between them can be untangled to sort out the effect of $CuCrSe_2$ as precipitates in Cu_2Se on TE performance.

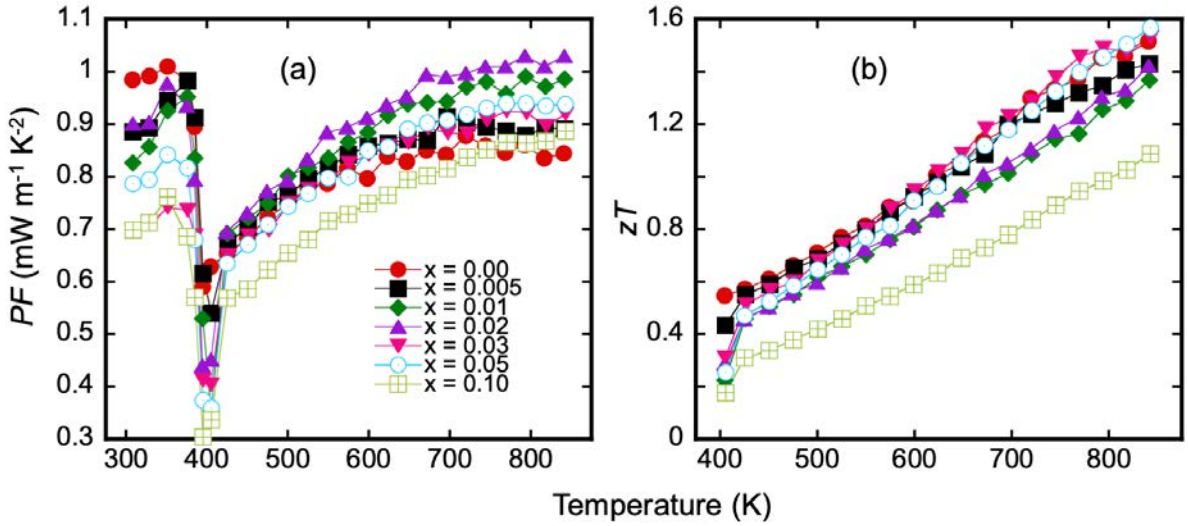

Figure 7-5. Temperature-dependent power factor, *PF*, (a) and figure of merit, *zT*, (b) of various (x)$CuCrSe_2$/(1-x)Cu_2Se composites.

7.2.2 (1-2x)Cu_2Se/(x)Cu_3SbSe_3 for Thermoelectric Application

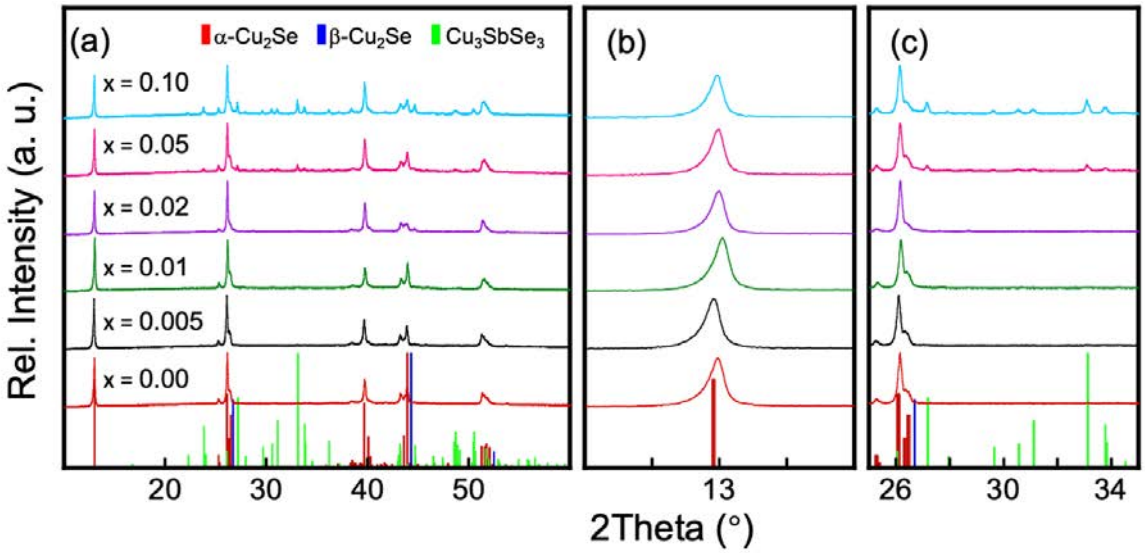

Figure 7-6. Bulk XRD of (1-2x)Cu_2Se/(x)Cu_3SbSe_3 composites after consolidation by hot pressing.

An attempt to develop (1-x)Cu_2Se/(x)$CuSbSe_2$ composites has been conducted in a similar manner as we did for making (1-x)Cu_2Se/(x)$CuFeSe_2$ and (1-x)Cu_2Se/(x)$CuAlSe_2$ composites. Preliminary studies have been conducted, including investigating phase composition and measuring TE properties. As shown in **Figure 7-6** and **Figure A5-9**, **A5-10**, (1-2x)Cu_2Se/(x)Cu_3SbSe_3 composites was formed instead of (1-x)Cu_2Se/(x)$CuSbSe_2$ composites as designed, with no other impurity phase detected. Previous studies suggests that $CuSbSe_2$ may be only stable at high temperature with the presence of Cu_2Se while Cu_3SbSe_3 is thermodynamically stable at room

temperature.[259] **Figure 7-7** and **7-8** show the TE properties, including electrical conductivity, Seebeck coefficient and thermal conductivity. Similarly, all samples show decreasing electrical conductivity and increasing Seebeck coefficient with rising temperature, typical behaviors of degenerated semiconductors. However, the compositional dependencies of TE properties of (1-2x)Cu_2Se/(x)Cu_3SbSe_3 composites seem very complicated. For example, the electrical conductivity decreases with 0.5 mol% Cu_3SbSe_3 compared to the pristine Cu_2Se, then increases significantly with increasing amount of Cu_3SbSe_3 until the sample with 2 mol% Cu_3SbSe_3 and thereafter decreases again with further increase in Cu_3SbSe_3 content. Similarly, the variation of Seebeck coefficient and thermal conductivity can be divided into three different stage with respect to the Cu_3SbSe_3 content.

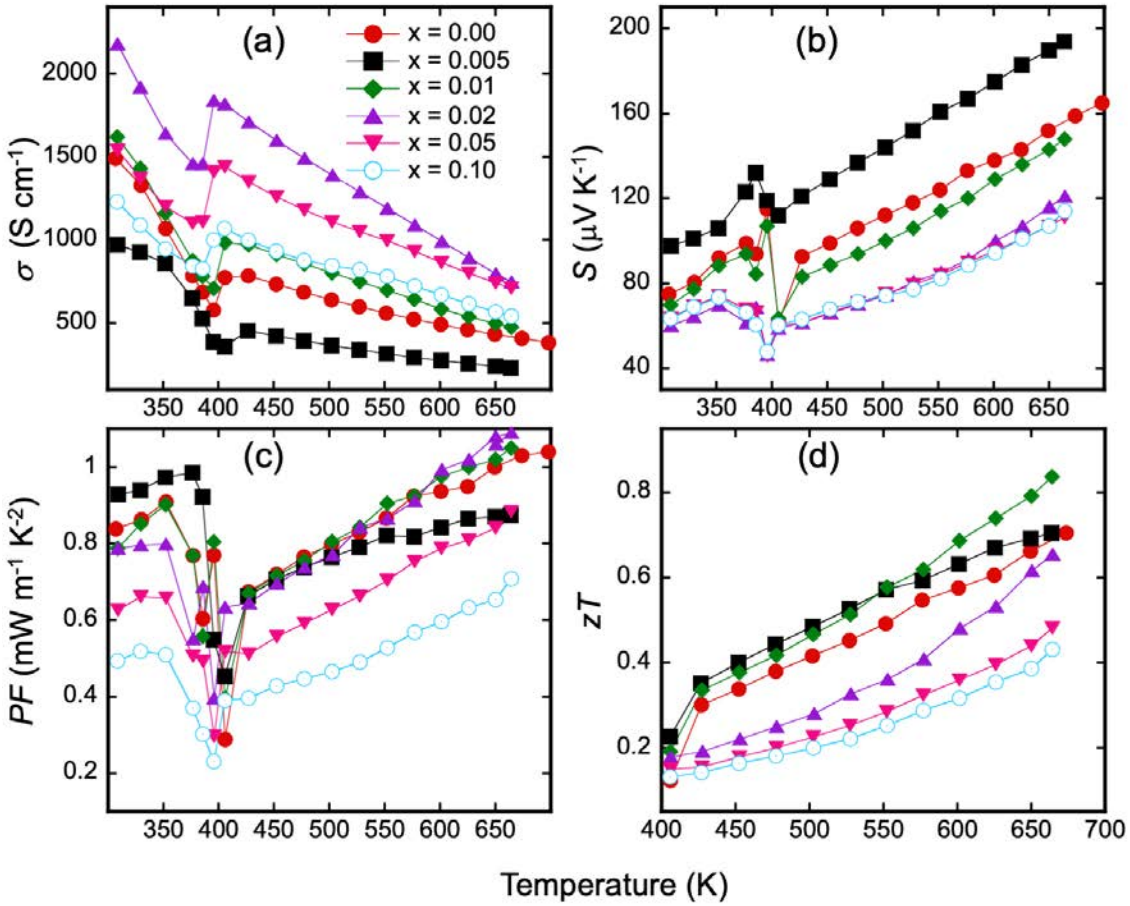

Figure 7-7. TE properties in (1-2x)Cu_2Se/(x)Cu_3SbSe_3 composites: (a) temperature-dependent electrical conductivity; (b) temperature-dependent Seebeck coefficient; (c) temperature-dependent power factor and (d) temperature-dependent figure of merit, *zT*.

All these suggest complicated interactions between the Cu_3SbSe_3 precipitates and the Cu_2Se matrix. To uncover the effects of introduced Cu_3SbSe_3 on TE properties at varied concentration,

systematic compositional and structural studies are needed at different scale under SEM and TEM. Simultaneously, Hall measurements are necessary to estimate the carrier concentration and calculate the carrier mobility for a better understanding of the electrical properties. With thorough understanding of material's composition, microstructure, magnetic properties and TE transport properties, the correlations between them can be untangled to sort out the effect of Cu_3Sbe_3 as precipitates in Cu_2Se on TE performance.

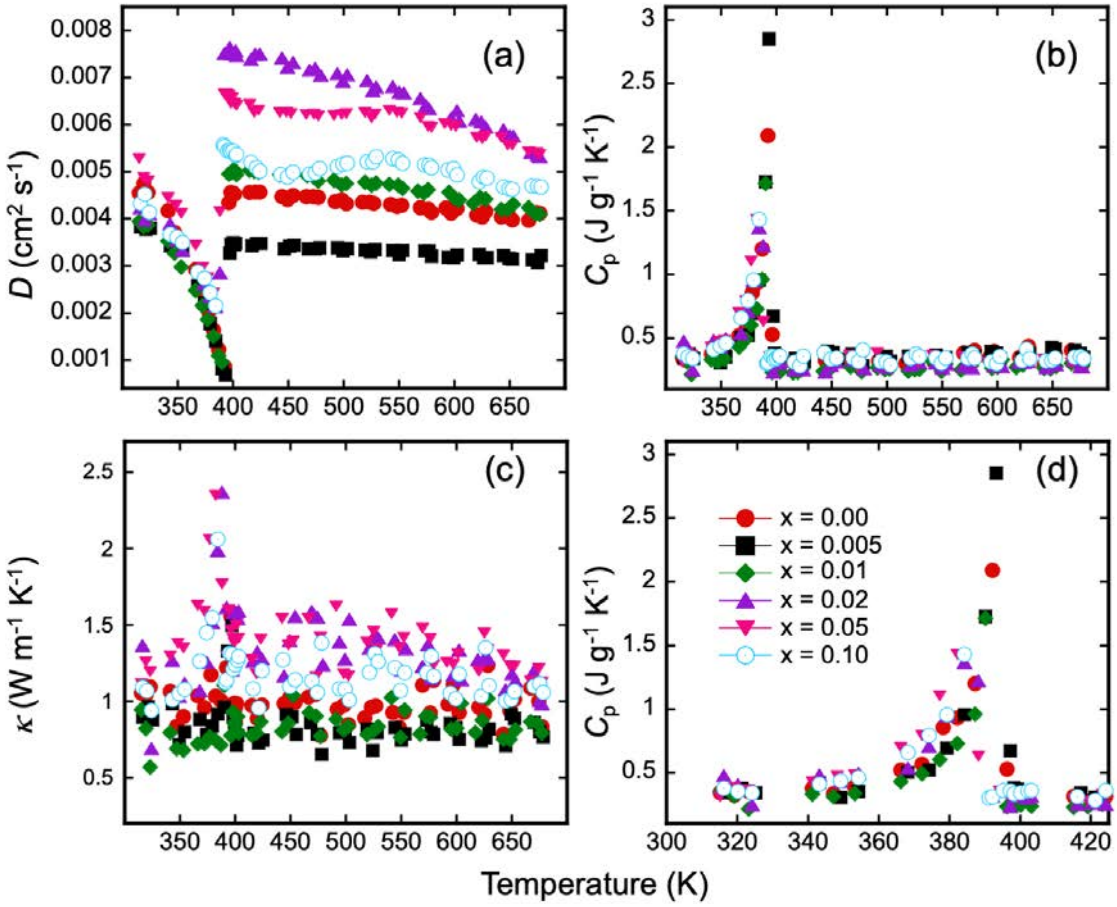

Figure 7-8. Thermal properties of $(1-2x)Cu_2Se/(x)Cu_3SbSe_3$ composites: (a) temperature-dependent thermal diffusivity; (b) temperature-dependent heat capacity with (d) a close-up view near the α-Cu_2Se to β-Cu_2Se phase transition and (c) temperature-dependent thermal conductivity.

7.2.3 Material Stability in (1-x)Cu_2Se/(x)$CuMSe_2$ Composites

Cu_2Se is a promising TE material with a beneficially low thermal conductivity. The challenges of putting Cu_2Se into practical applications include achieving even higher TE performance by co-optimizing electronic and thermal transport, which is the main focus in this work, and overcoming the instability issue due to the migration of Cu ions in these superionic compounds. Therefore,

studying the change in stability of Cu_2Se is also highly meaningful when introducing various precipitates. For example, it is suggested that partial solution of In in Cu_2Se can mitigate the migration of Cu ions and increase the stability of the material. It was found that a lot of the ternary precipitates show limited solubilities in Cu_2Se, for example, $CuGaSe_2$ with a solubility ≤ 1 mol%. A similar effect of improving stability can also be expected with the slight solution of a ternary compound other than $CuInSe_2$. Also, the extraction of Cu ions by $CuAlSe_2$ precipitates significantly drain the Cu ions in Cu_2Se, which may also affect the stability of Cu_2Se.

7.2.4 Developing A Composite Strategy with High Degree of Freedom

As mentioned in the introduction, the advantage of the novel composite strategy over traditional one for optimizing TE properties is the possibly high degree of freedom possible for properties tailoring. This includes the choice of a secondary phase, the distribution of the secondary phase and the interaction between the secondary phase and the matrix. This thesis work focuses more on the choice of the secondary phases, the unique distribution formed during the synthesis and the resulting interaction between the secondary phase and the matrix material. Undoubtedly, various distributions of a secondary phase and microstructures are possible when committing the material synthesis in different manners for a chosen composite materials system. For example, a very different microstructure was observed when $(1-x)Cu_2Se/(x)CuGaSe_2$ composites were synthesized through melting and quenching.[79] In contrast to the extremely fine distribution of $CuGaSe_2$ in our work, $CuGaSe_2$ agglomerates together and is not dispersed evenly within the Cu_2Se matrix. We believe that only by choosing various secondary phases, achieving different microstructures/ interfaces and so various interactions, can we make use of such strategy and achieve the best performance of TE materials out of it. Actually, the application of composite strategy is not limited to TE materials. There are many more applications for $(1-x)Cu_2Se/(x)CuMSe_2$ composites. For

example, the composite materials can be solar cell materials when making the $CuMSe_2$ phase, such as $CuAlSe_2$, $CuGaSe_2$ and $CuInSe_2$, as the matrix and the Cu_2Se as the secondary phase.

Appendix 1 : Supplementary Information for Chapter 3

Table A1-1. Chemical composition of various phases in $Ti_{0.25}Zr_{0.25}Hf_{0.5}(Ni,Fe_x)Sn_{0.975}Sb_{0.025}$ estimated from multiple points of electron microprobe analysis (EPMA), given in at %.

Sample Name*	Ti	Zr	Hf	Ni	Sn	Fe	Sb	Ti+Zr+Hf	Ni+Fe	Sn
Fe05_Dark	22.73	1.21	1.53	33.43	26.10	14.92	0.09	25.46	48.35	26.10
Fe05_Dark	22.65	0.77	1.67	29.88	26.06	18.81	0.17	25.09	48.68	26.06
Fe05_Dark	22.61	1.35	1.67	36.30	25.47	12.55	0.04	25.64	48.85	25.47
Fe05_Dark	21.94	0.62	1.92	26.11	25.94	23.29	0.18	24.48	49.40	25.94
Fe05_Dark	23.05	1.32	1.05	35.19	26.55	12.75	0.08	25.42	47.94	26.55
Fe05_Grey	5.07	19.31	8.15	33.67	32.73	0.13	0.95	32.53	33.79	32.73
Fe05_Grey	5.52	24.83	6.23	31.80	30.12	0.49	1.01	36.57	32.29	30.12
Fe05_Grey	11.19	6.23	15.23	32.89	32.50	0.84	1.12	32.66	33.73	32.50
Fe05_Grey	8.05	14.57	14.86	30.01	31.19	0.34	0.98	37.49	30.35	31.19
Fe05_Grey	7.78	9.76	16.06	32.68	32.26	0.35	1.10	33.60	33.03	32.26
Fe05_Light	2.12	1.90	29.86	33.29	32.46	0.06	0.31	33.88	33.36	32.46
Fe05_Light	0.37	0.55	46.56	44.89	0.27	7.39	BDL	47.48	52.28	0.27
Fe05_Light	0.95	1.66	30.59	33.44	32.63	0.29	0.43	33.21	33.73	32.63
Fe05_Light	0.27	1.81	41.52	34.48	18.12	3.57	0.23	43.60	38.05	18.12
Fe05_Light	8.20	13.45	15.09	29.41	29.81	3.20	0.85	36.73	32.61	29.81
Fe15_Dark	21.47	0.96	1.99	31.11	25.97	18.44	0.06	24.42	49.55	25.97
Fe15_Dark	21.21	1.19	2.46	31.15	25.67	18.26	0.06	24.87	49.41	25.67
Fe15_Dark	21.50	1.06	2.36	31.35	25.92	17.77	0.05	24.92	49.12	25.92
Fe15_Dark	21.33	1.09	2.41	31.28	25.94	17.91	0.05	24.82	49.18	25.94
Fe15_Dark	21.28	1.06	2.03	31.12	26.19	18.27	0.06	24.36	49.39	26.19
Fe15_Grey	1.04	29.69	2.27	33.00	31.82	0.42	1.76	33.01	33.41	31.82
Fe15_Grey	2.50	27.90	2.97	32.64	31.31	0.78	1.90	33.37	33.42	31.31
Fe15_Grey	2.01	28.40	2.44	32.81	31.71	1.11	1.52	32.85	33.92	31.71
Fe15_Light	0.66	2.32	30.36	33.11	32.09	0.24	1.23	33.34	33.35	32.09
Fe15_Light	1.34	3.17	28.79	33.09	32.90	0.19	0.52	33.29	33.28	32.90
Fe15_Light	3.80	6.50	22.85	33.05	32.22	0.74	0.82	33.16	33.79	32.22
Fe15_Light	2.55	5.04	25.93	32.71	32.29	0.39	1.09	33.51	33.10	32.29
Fe15_Light	3.28	5.91	23.70	33.04	31.63	1.09	1.35	32.89	34.13	31.63

*Number after Fe in sample name indicates the atomic percent of extra Fe; 'Dark' 'Grey' and 'Light' indicate the contrasts of phases in the back scatter image (BSE), which correspond to Ti-rich, Zr-rich and Hf-rich phases, respectively; 'BDL' means concentration below detection limit.

Table A1-2. Mole fraction, ν (%), of the (Ti,Fe)-rich phase in various $Ti_{0.25}Zr_{0.25}Hf_{0.5}(Ni,Fe_x)Sn_{0.975}Sb_{0.025}$ samples quantified using the Image J software compared to the mole fraction of the (Ti,Fe)-rich phase anticpated from the **Equation** (26), along with other (Ti,Fe)-rich phase characteristics collected by ImageJ.

Sample	Counts	Total Area [μm²]	Average Size [μm²]	Max Size [μm²]	ν_{obs}	ν_{calc}	$\lvert\Delta\nu\rvert/\nu_{calc}$
TZHNSS_0Fe	73	25887.6	354.6	2093.7	3.6	-	-
TZHNSS_5Fe	37	10830.5	292.7	1179.9	1.5	6.9	0.78
TZHNSS_10Fe	150	68794.5	458.6	3371.4	10.8	13	0.17
TZHNSS_15Fe	180	110540.2	614.1	8658.5	15.5	18.4	0.16

When processing the BSE images in Image J, a threshold value was set to be 50 μm² to select the Ti-rich phases, i.e. any dark phase larger than 50 μm² would be identified as a Ti-rich area.

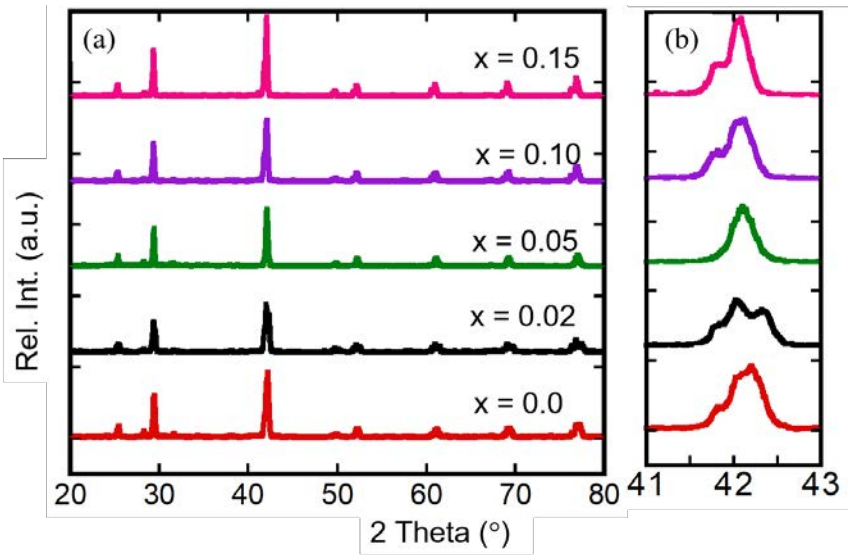

Figure A1-1. (a) Powder X-ray diffraction (PXRD) patterns of $Ti_{0.25}Zr_{0.25}Hf_{0.5}(Ni,Fe_x)Sn_{0.975}Sb_{0.025}$ samples and (b) a close-up view of the 220 diffraction peak revealing peak splitting that implies phase separation into multiple phases (Ti-rich and (Zr, Hf)-rich) with HH or FH structures.

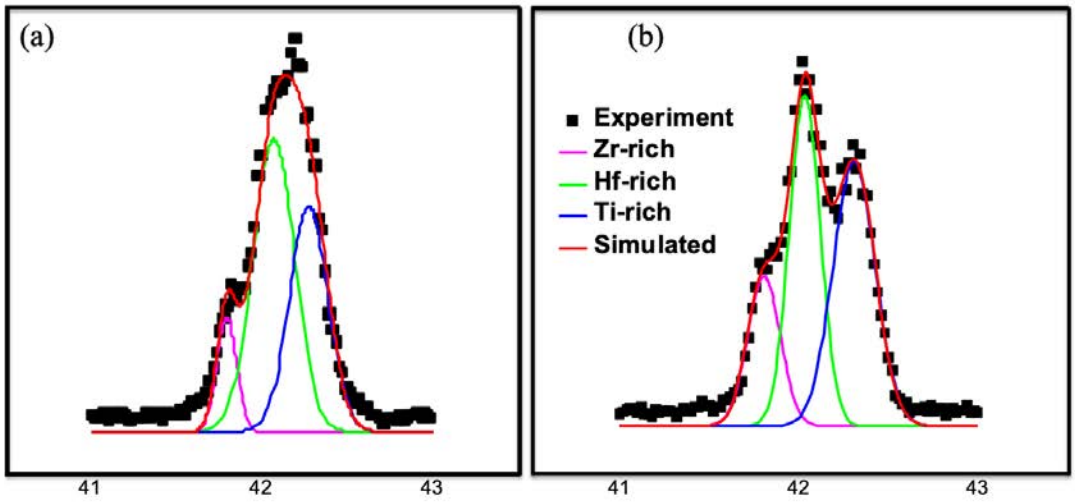

Figure A1-2. (a) Fitting of the 220 peak for the Fe-free $Ti_{0.25}Zr_{0.25}Hf_{0.5}NiSn_{0.975}Sb_{0.025}$ sample, indicating coexistence of Ti-rich, Hf-rich and Zr-rich phases and (b) Fitting of the 220 peak for the $Ti_{0.25}Zr_{0.25}Hf_{0.5}(Ni,Fe_{0.02})Sn_{0.975}Sb_{0.025}$ sample, indicating the coexistence of Ti-rich, Hf-rich and Zr-rich phases.

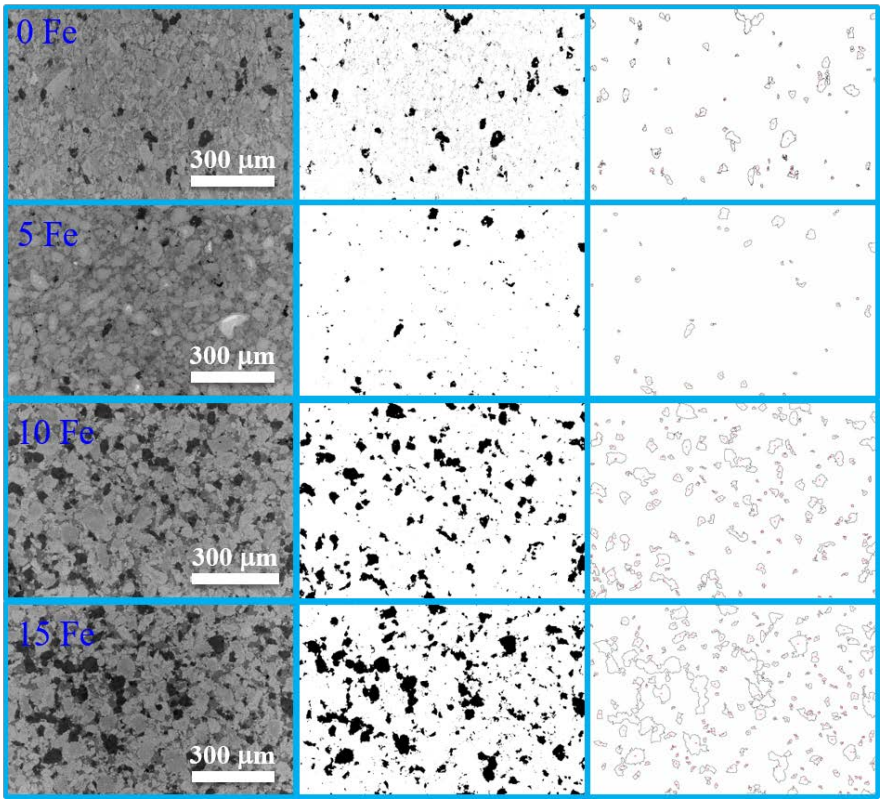

Figure A1-3. BSE images of $Ti_{0.25}Zr_{0.25}Hf_{0.5}(Ni,Fe_x)Sn_{0.975}Sb_{0.025}$ samples showing the distribution of (Ti,Fe)-rich (black) and (Zr,Hf)-rich (grey) domains in various composites. The processing of the BSE images with Image-J software enables semiquantitative determination of the fraction of (Ti,Fe)-rich phases within various samples.

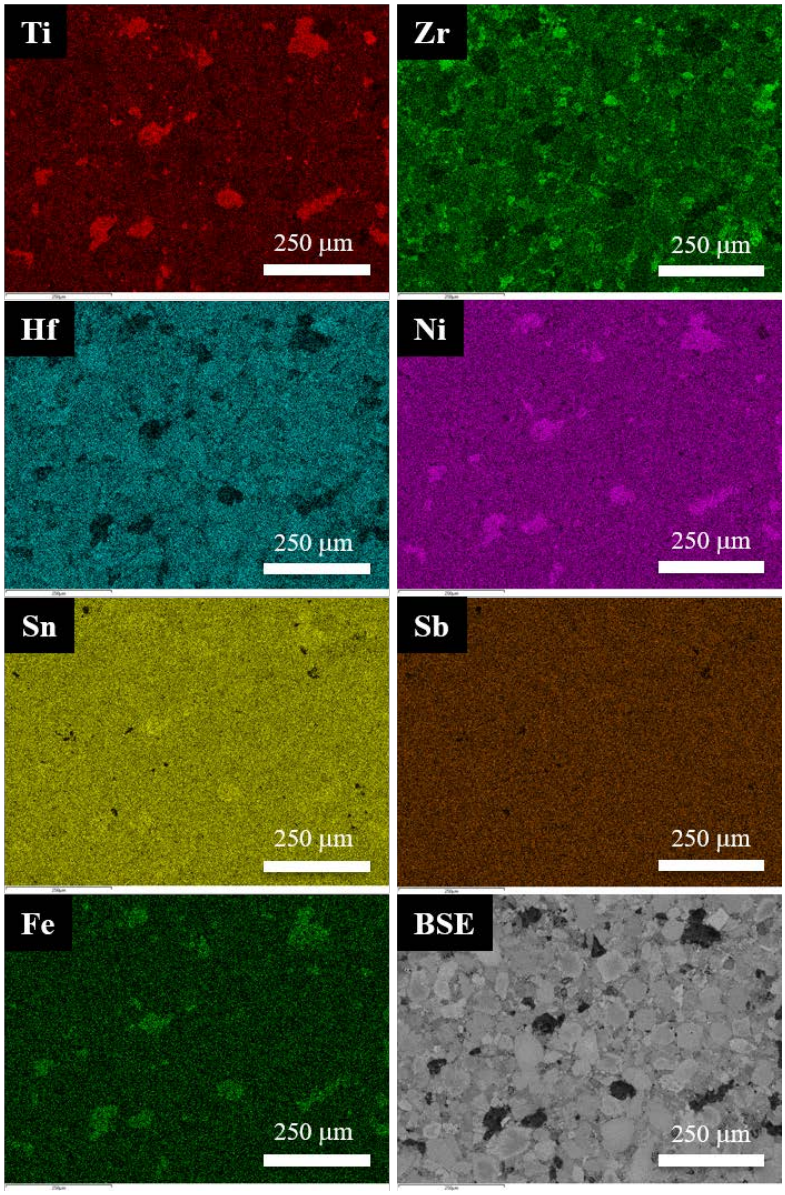

Figure A1-4. EDS mapping of the $Ti_{0.25}Zr_{0.25}Hf_{0.5}(Ni,Fe_{0.02})Sn_{0.975}Sb_{0.025}$ sample showing phase separation into (Ti,Fe)-rich, Hf-rich and Zr-rich phases with uniform distribution of Ni, Sn and Sb. Note the preferential incorporation of the added Fe into the Ti-rich phase to form the magnetic inclusions.

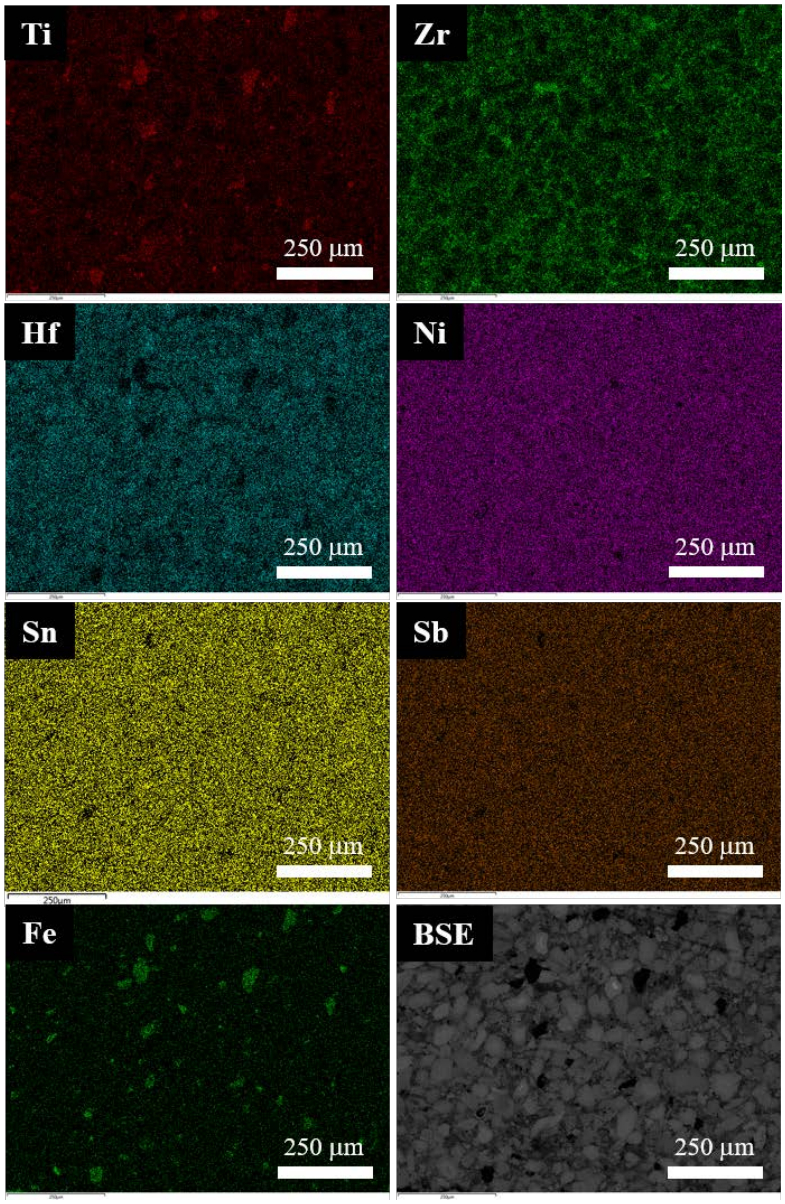

Figure A1-5. EDS mapping of the $Ti_{0.25}Zr_{0.25}Hf_{0.5}(Ni,Fe_{0.05})Sn_{0.975}Sb_{0.025}$ sample showing phase separation into (Ti,Fe)-rich, Hf-rich and Zr-rich phases with uniform distribution of Ni, Sn and Sb. Note the preferential incorporation of the added Fe into the Ti-rich phase to form the magnetic inclusions.

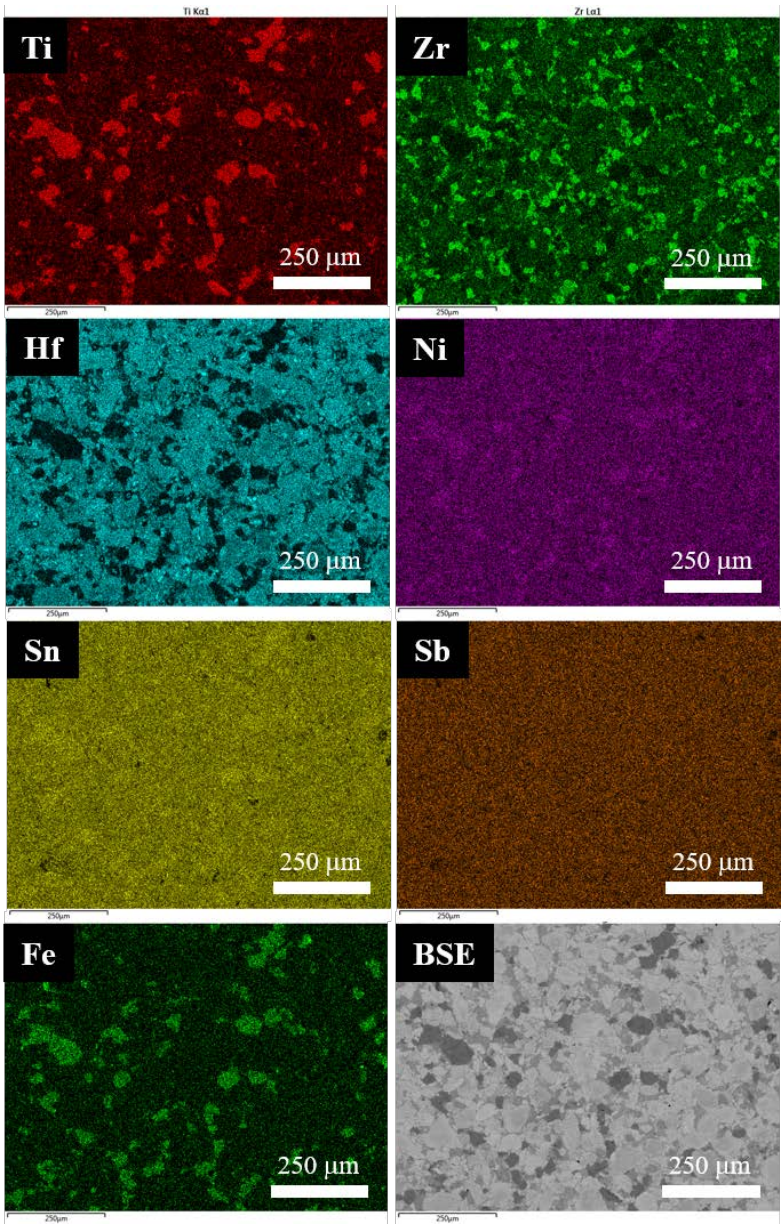

Figure A1-6. EDS mapping of the $Ti_{0.25}Zr_{0.25}Hf_{0.5}(Ni,Fe_{0.10})Sn_{0.975}Sb_{0.025}$ sample showing phase separation into (Ti,Fe)-rich, Hf-rich and Zr-rich phases with uniform distribution of Ni, Sn and Sb. Note the preferential incorporation of the added Fe into the Ti-rich phase to form the magnetic inclusions.

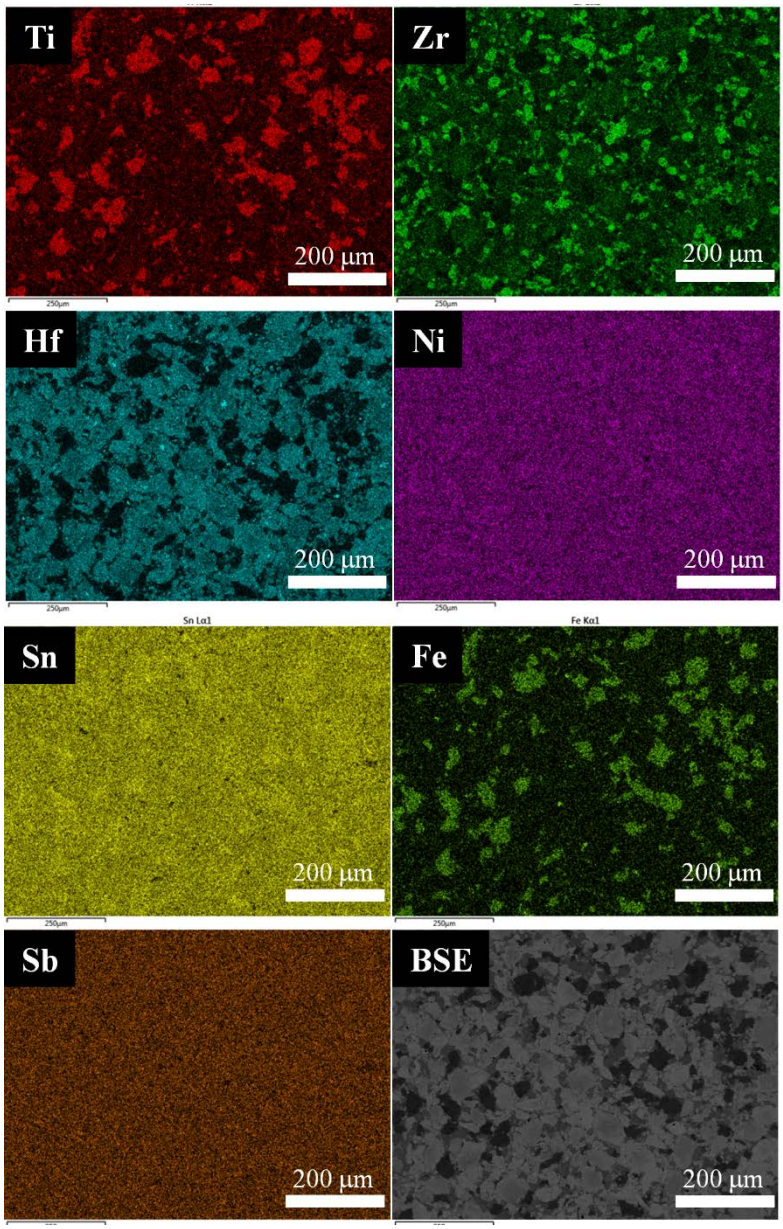

Figure A1-7. EDS mapping of the $Ti_{0.25}Zr_{0.25}Hf_{0.5}(Ni,Fe_{0.15})Sn_{0.975}Sb_{0.025}$ sample showing phase separation into (Ti,Fe)-rich, Hf-rich and Zr-rich phases with uniform distribution of Ni, Sn and Sb. Note the preferential incorporation of the added Fe into the Ti-rich phase to form the magnetic inclusions.

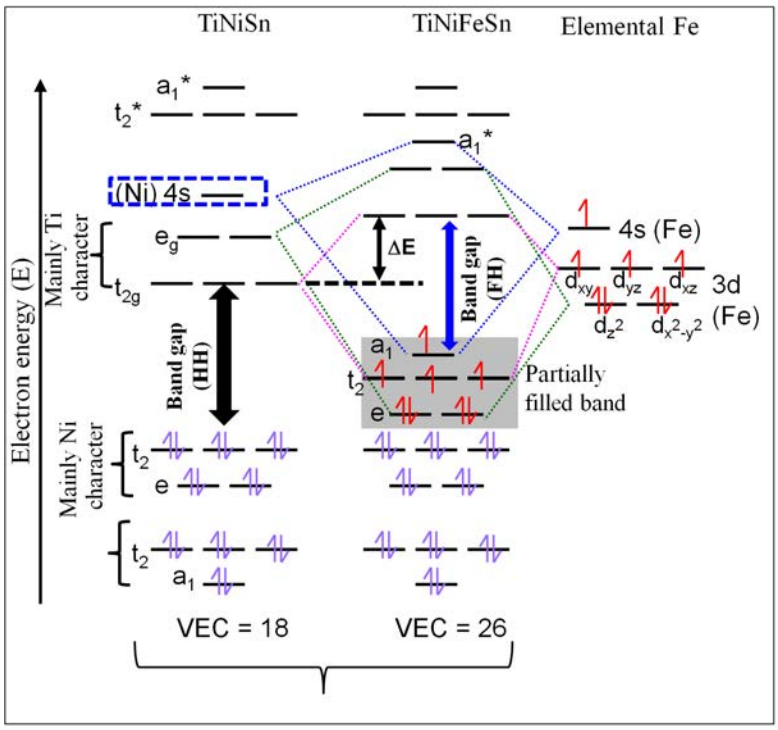

Figure A1-8. Schematic illustration of the molecular orbital diagrams of TiNiSn half-Heusler phase and selected TiNiFeSn full-Heusler inclusions. Δ*E* represents the energy offset between the conduction band minima of neighboring HH and FH phases.

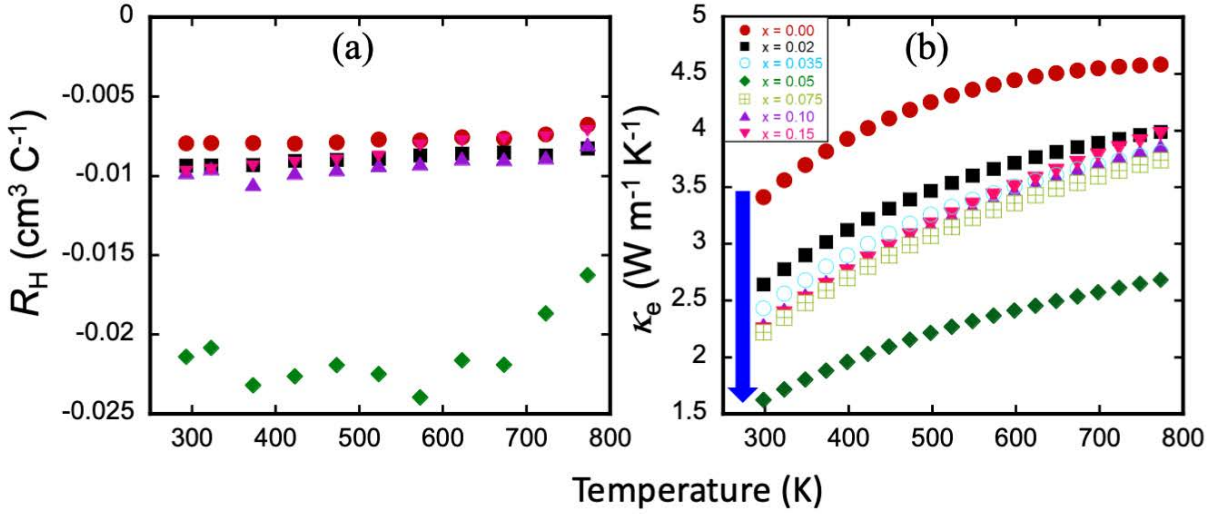

Figure A1-9. Transport properties of $Ti_{0.25}Zr_{0.25}Hf_{0.5}(Ni,Fe_x)Sn_{0.975}Sb_{0.025}$ composites: (a) Hall coefficient and (b) electronic thermal conductivity.

Appendix 2 : Supplementary Information for Chapter 4

Table A2-1. Lattice parameters from Rietveld refinement and phase quantification (*f*) based on RIR method of α-Cu_2Se, β-Cu_2Se and $CuGaSe_2$ phases in the synthesized (x)$CuGaSe_2$/(1-x)Cu_2Se composites at 300 K.

	α-Cu_2Se						β-Cu_2Se			$CuGaSe_2$			
Ga (x)	*a*(Å)	*b*(Å)	*c*(Å)	β(°)	V(Å^3)	*f* (mol%)	*a*(Å)	V(Å^3)	*f* (mol%)	*a*(Å)	*c*(Å)	V(Å^3)	*f* (mol%)
0	7.125	12.359	27.339	94.3	2400.6	33.3	5.768	191.9	66.7	-	-	-	0.0
0.005	7.136	12.379	27.382	94.3	2411.8	99.8	5.762	191.3	0.2	-	-	-	0.0
0.01	7.150	12.403	27.436	94.3	2426.2	99.8	5.849	200.1	0.2	-	-	-	0.0
0.015	7.132	12.373	27.369	94.3	2408.4	71.3	5.770	192.1	28.7	-	-	-	0.0
0.02	7.123	12.357	27.334	94.3	2399.2	11.9	5.767	191.8	88.1	-	-	-	0.0
0.025	7.126	12.362	27.344	94.3	2401.9	11.6	5.770	192.1	88.4	-	-	-	0.0
0.05	7.110	12.334	27.283	94.3	2385.7	11.8	5.764	191.5	85.2	5.616	11.009	347.2	3.1
0.17	7.120	12.351	27.321	94.3	2395.7	3.1	5.772	192.3	83.1	5.625	11.036	349.2	13.8
0.33	7.064	12.254	27.107	94.3	2339.7	0.5	5.777	192.8	67.1	5.630	11.045	350.1	32.4

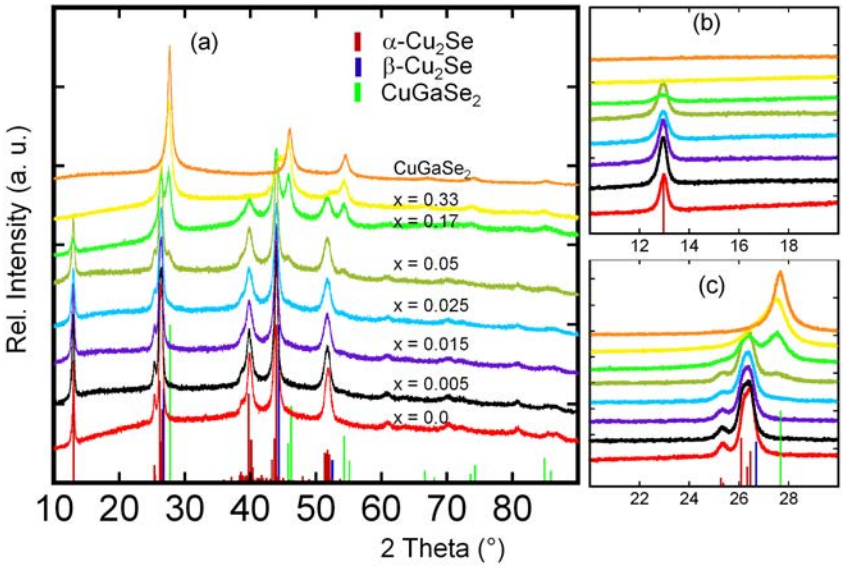

Figure A2-1. (a) PXRD of the as-synthesized (x)$CuGaSe_2$/(1-x)Cu_2Se composites. Enlarged views of the diffraction peaks around 13° (b) and around 27° (c), showing the depression in peak intensity from α-Cu_2Se and the growth in peak intensity from $CuGaSe_2$ with increasing Ga content.

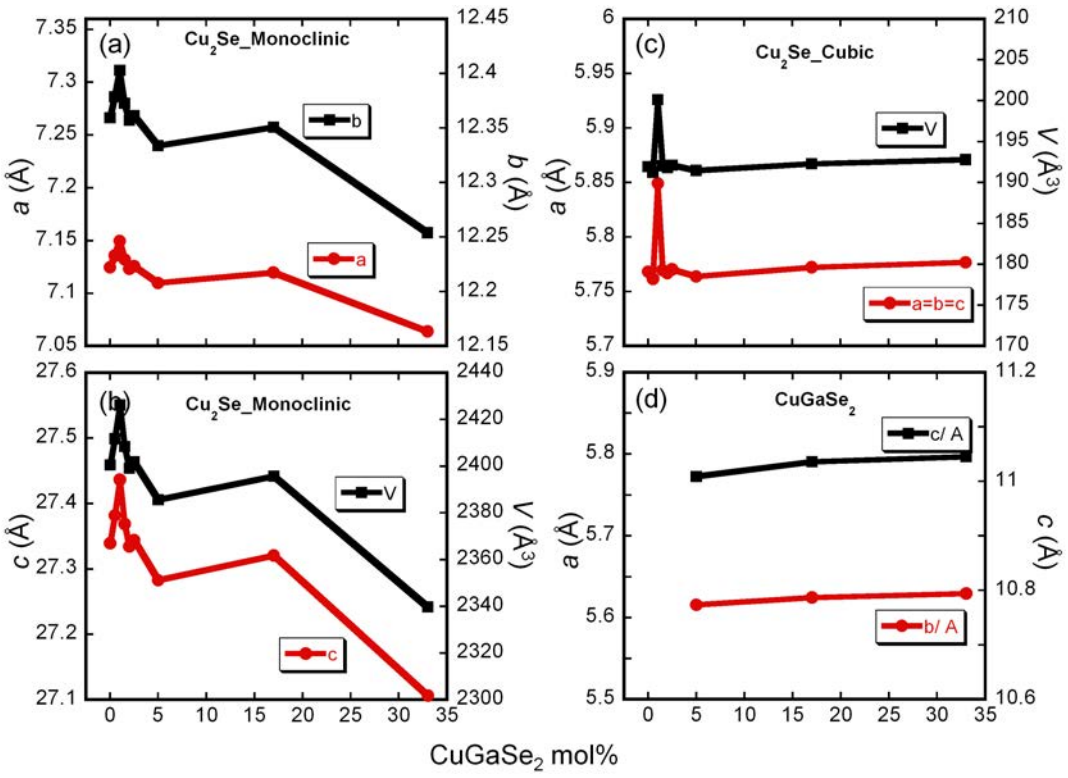

Figure A2-2. Lattice parameters of α-Cu_2Se (a-b), β-Cu_2Se (c) and $CuGaSe_2$ (d) obtained from Rietveld refinement using XRD patterns from bulk (x)$CuGaSe_2$/(1-x)Cu_2Se samples with increasing Ga content. The high lattice constants for cubic Cu_2Se in sample x = 0.01 is probably due to extremely low concentration of this phase, leading to an inaccurate estimation.

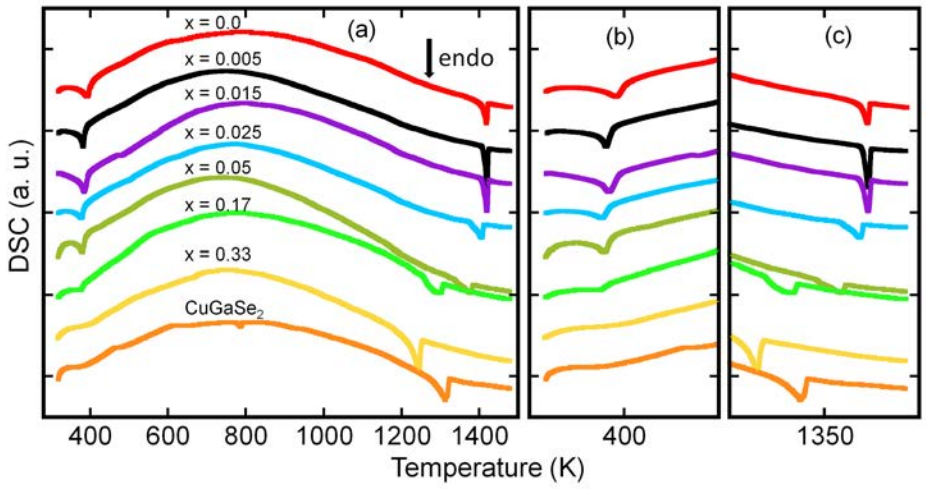

Figure A2-3. DSC of (x)$CuGaSe_2$/(1-x)Cu_2Se composites after mechanical milling (a). The phase transition peak from α-Cu_2Se to β-Cu_2Se (b) shifts towards lower temperature with increasing $CuGaSe_2$ content. Likewise, the melting peak of (x)$CuGaSe_2$/(1-x)Cu_2Se composites (c) gradually decreases with increasing $CuGaSe_2$ content, which is consistent with the Cu_2Se-$CuGaSe_2$ pseudo-binary phase diagram.

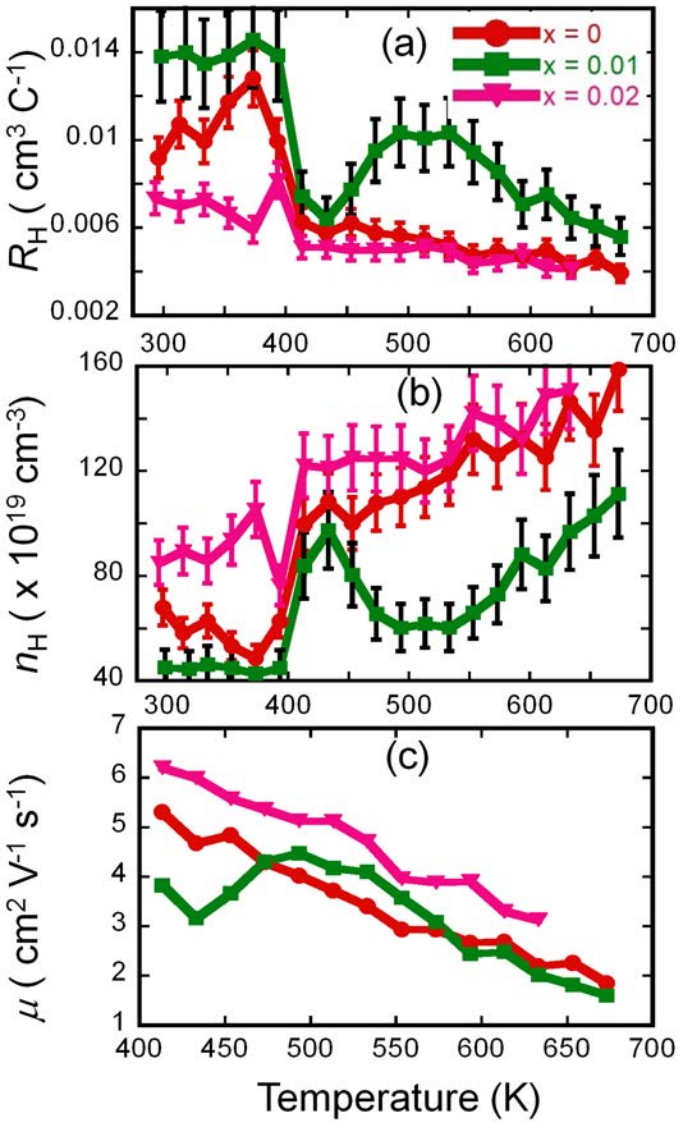

Figure A2-4. Temperature-dependent Hall coefficient (a), calculated carrier density (b) and charge carrier mobility (c) for selected (x)$CuGaSe_2$/(1-x)Cu_2Se composites.

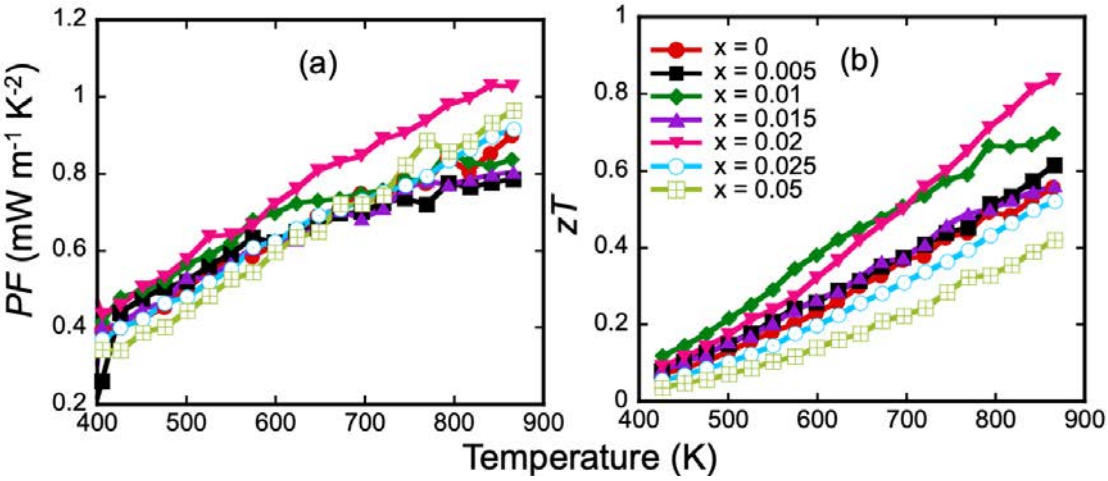

Figure A2-5. Temperature-dependent power factor, *PF*, (a) and figure of merit, z*T*, (b) of various (x)$CuGaSe_2$/(1-x)Cu_2Se composites.

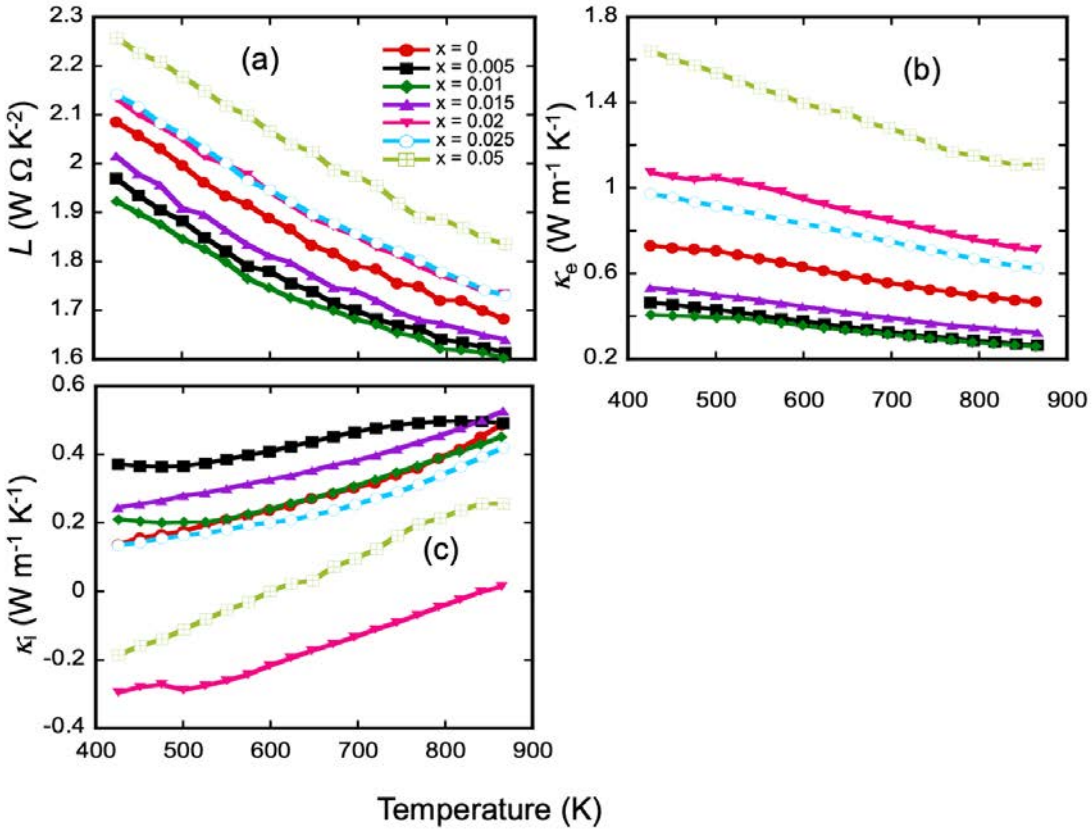

Figure A2-6. Temperature-dependent Lorenz constant (a), the electronic thermal conductivity calculated from the Wiedemann-Franz law (b), and the estimated lattice thermal conductivity (c) of (x)$CuGaSe_2$/(1-x)Cu_2Se composites. The analysis assumes a strong coupling between electronic and thermal transport properties.

Appendix 3 : Supplementary Information for Chapter 5

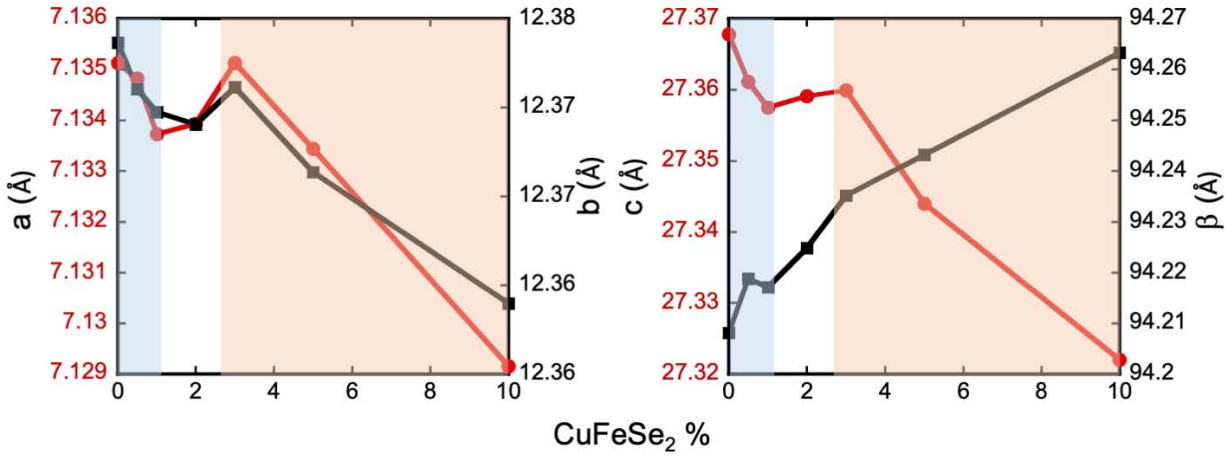

Figure A3-1. Lattice Parameter of monoclinic Cu_2Se with respect to $CuFeSe_2$ content based on Rietveld refinement of PXRD.

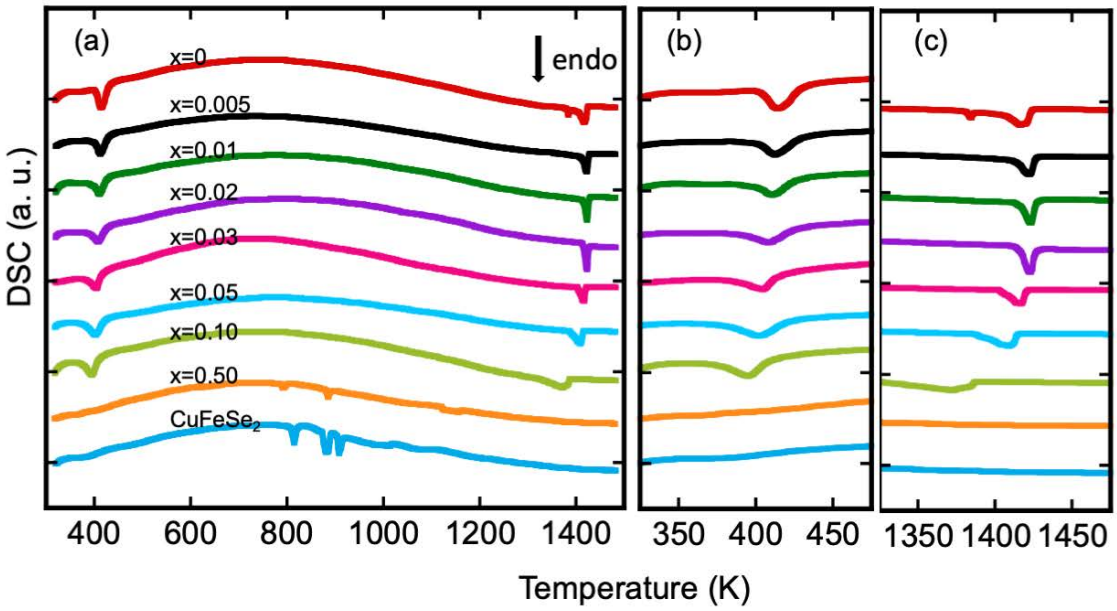

Figure A3-2. DSC of (1-x)Cu_2Se/(x)$CuFeSe_2$ composites (a), with two highlighted peaks attributed to the phase transition from α-Cu_2Se to β-Cu_2Se (b) and melting of the composites (c) respectively.

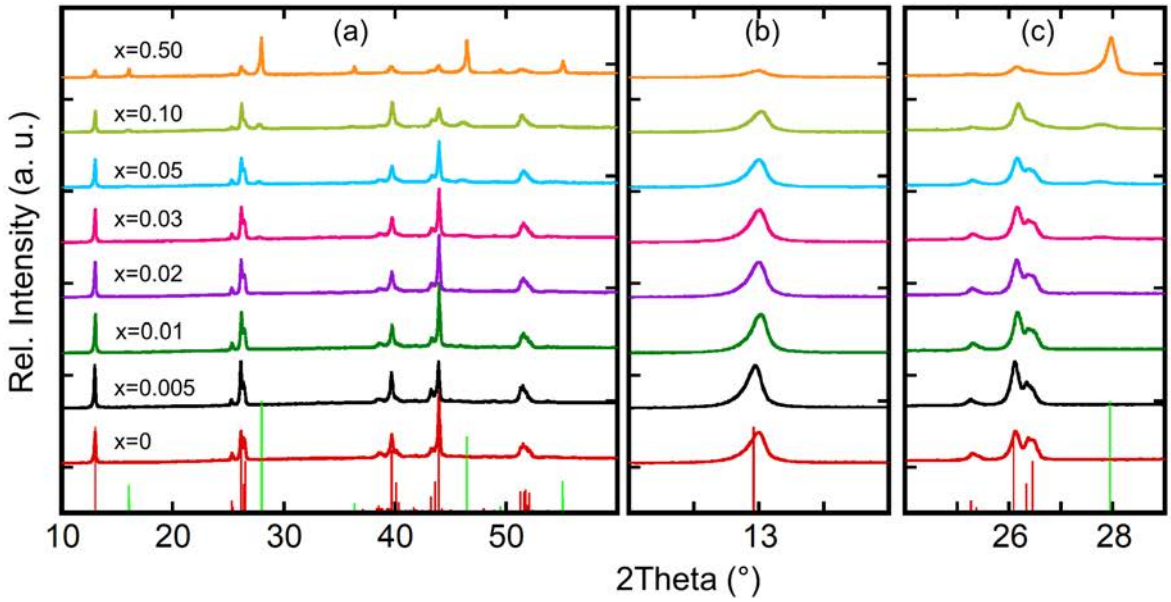

Figure A3-3. Bulk XRD of (1-x)Cu_2Se/(x)$CuFeSe_2$ composites after consolidation via hot press. Enlarged views of the diffraction peaks around 13° (b) and 27° (c) imply excellent purity was maintained after hot press.

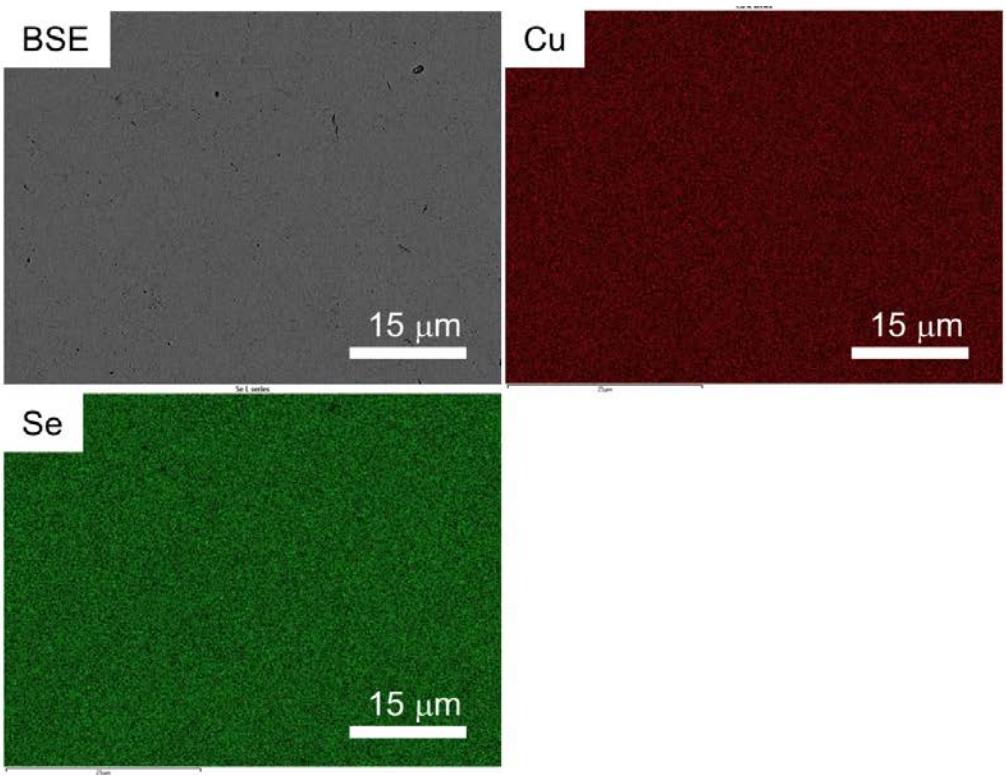

Figure A3-4. EDS mapping of the pristine Cu_2Se.

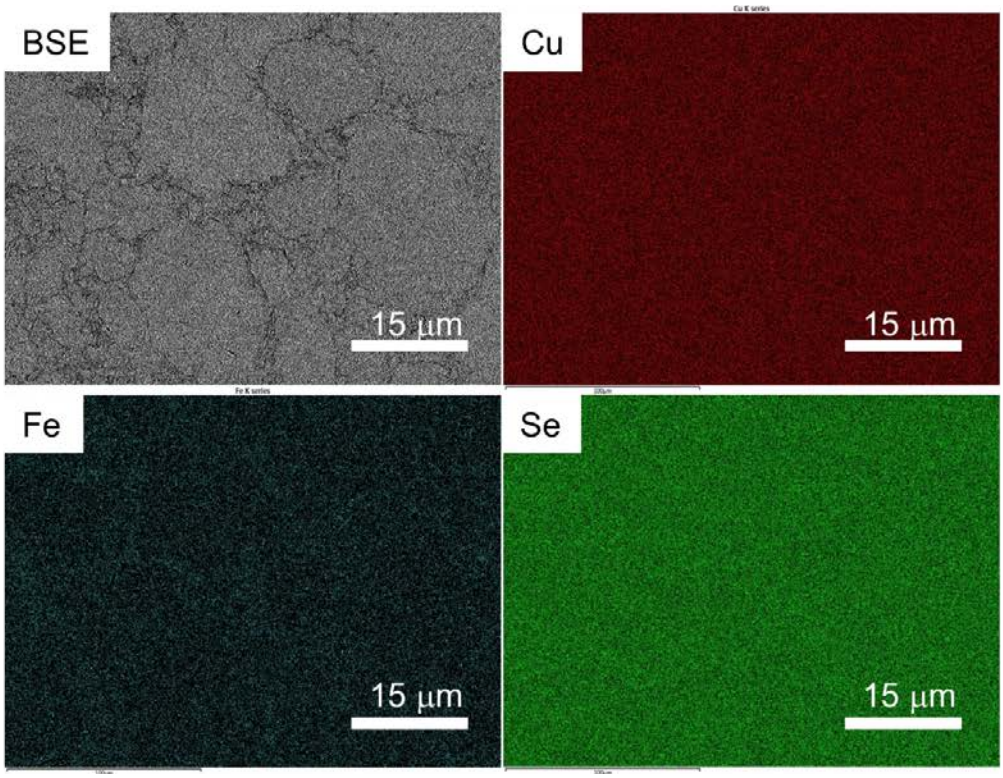

Figure A3-5. EDS mapping of $0.9Cu_2Se/0.1CuFeSe_2$.

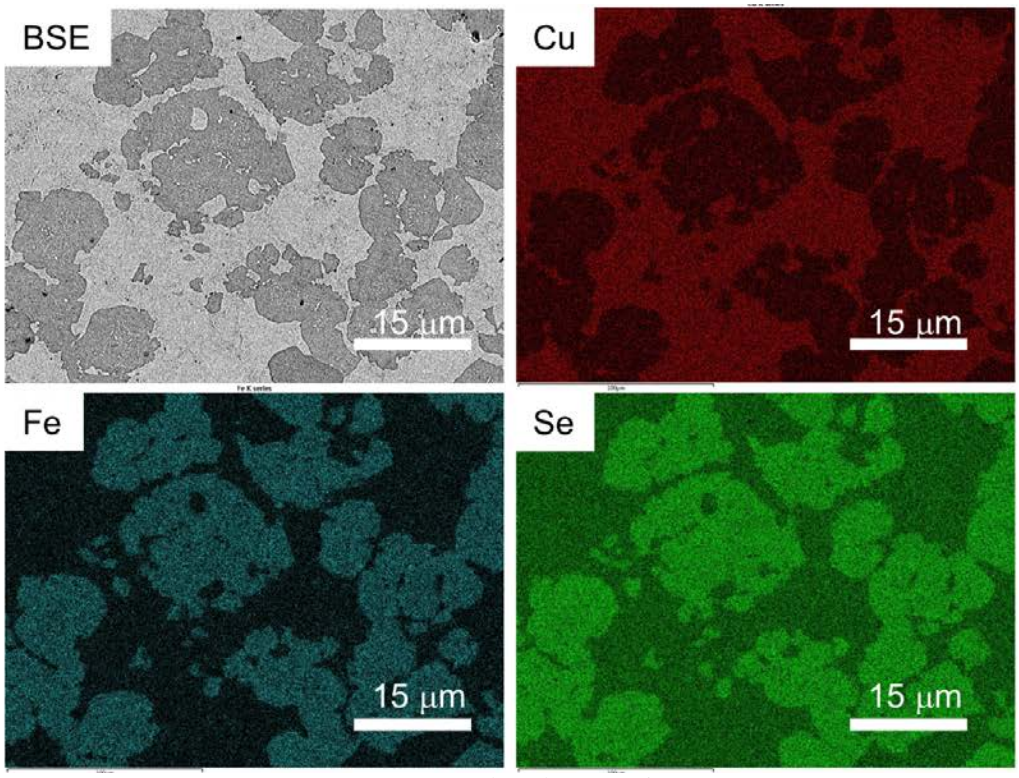

Figure A3-6. EDS mapping of $0.5Cu_2Se/0.5CuFeSe_2$.

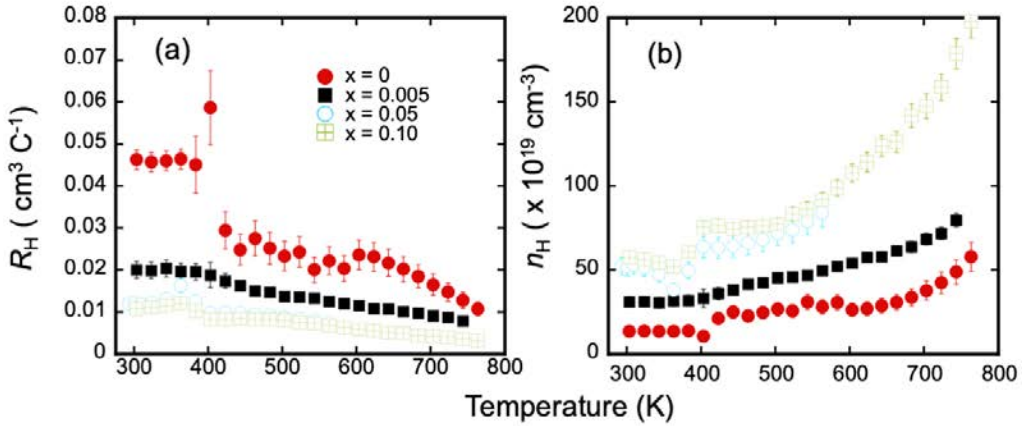

Figure A3-7. High-temperature Hall measurement: (a) hall coefficient and (b) carrier concentration.

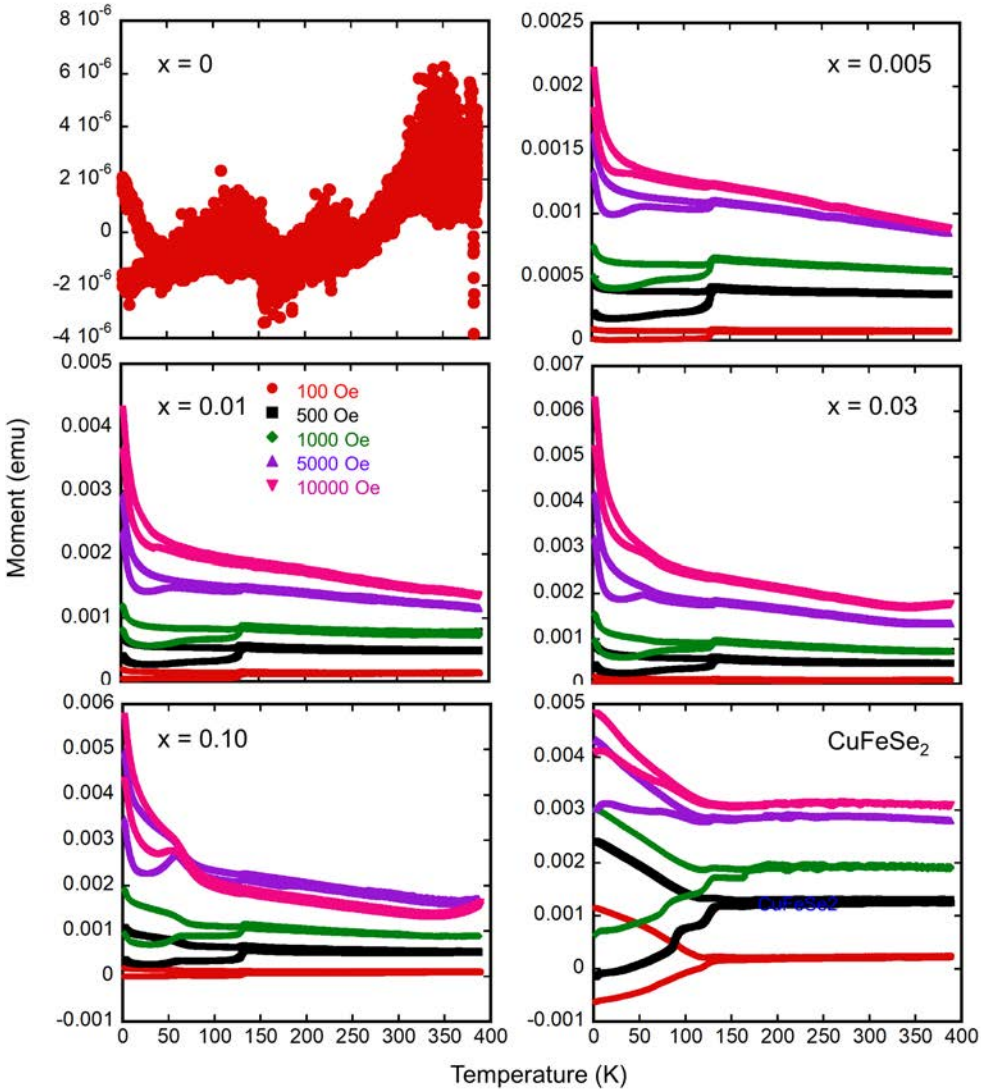

Figure A3-8. Temperature-dependent magnetic moment of (1-x)Cu_2Se/(x)$CuFeSe_2$ composites, where each sample is measured under ZFC (lower curve) and FC (upper curve) conditions at each selected field.

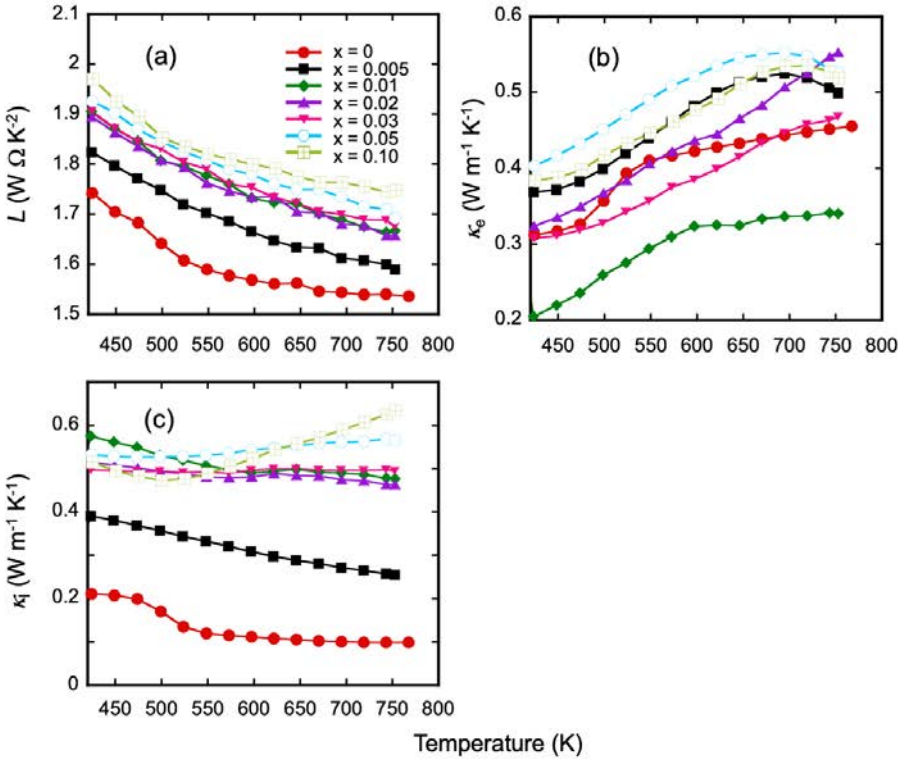

Figure A3-9. Lattice thermal conductivity of (1-x)Cu_2Se/(x)$CuFeSe_2$: (a) calculated Lorenz constant from measured Seebeck coefficient; (b) electronic thermal conductivity; and (c) lattice thermal conductivity.

Appendix 4 : Supplementary Information for Chapter 6

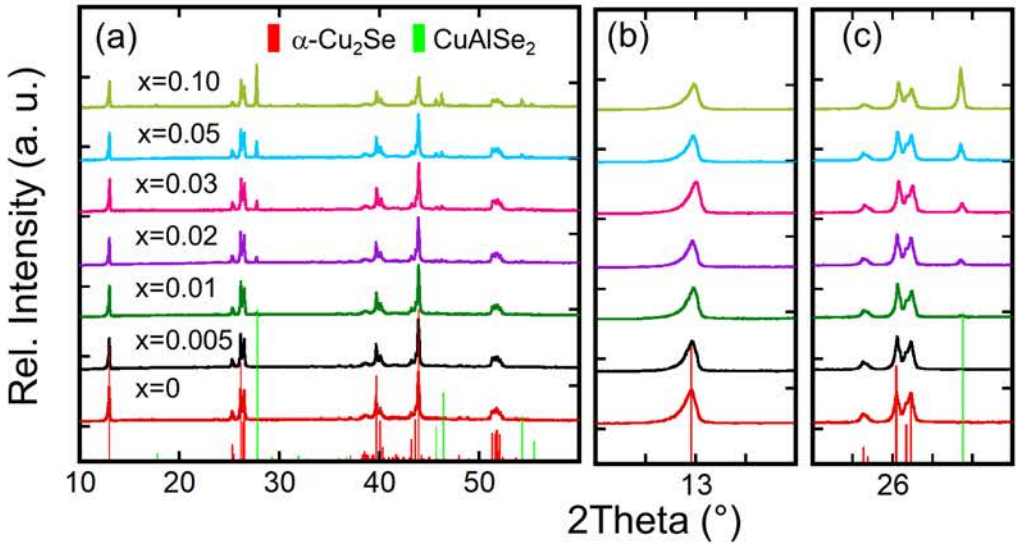

Figure A4-1. (a) PXRD of the as-synthesized (1-x)Cu_2Se/(x)$CuAlSe_2$ composites. Enlarged views of the diffraction peaks around 13° (b) and 27° (c), showing an obvious growth in peak intensity from $CuAlSe_2$ with increasing Al content.

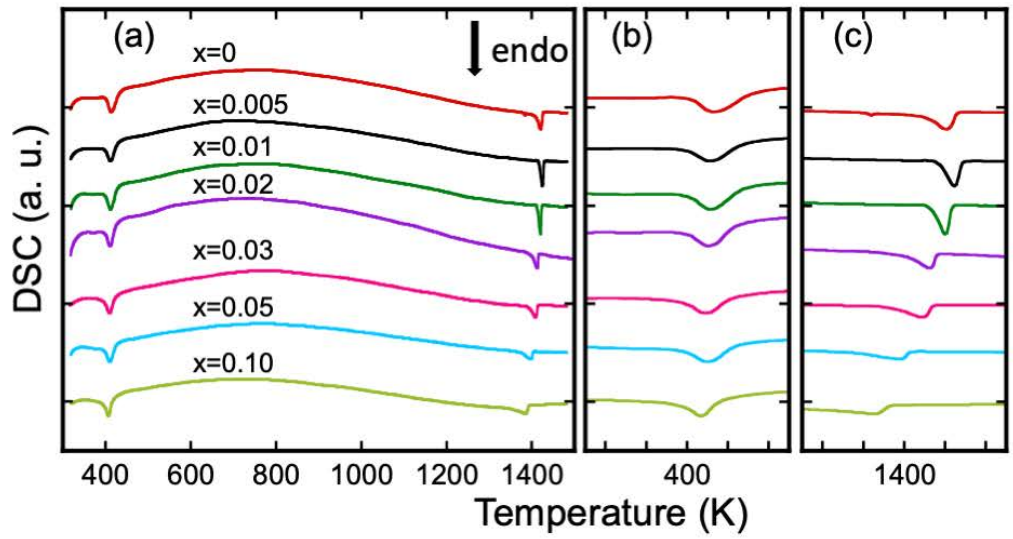

Figure A4-2. DSC of (x)$CuAlSe_2$/(1-x)Cu_2Se composites after the solid-state reaction (a). The phase transition peak from α-Cu_2Se to β-Cu_2Se (b) shifts towards lower temperature with increasing $CuAlSe_2$ content. Likewise, the melting peak of (x)$CuAlSe_2$/(1-x)Cu_2Se composites (c) gradually decreases with increasing $CuAlSe_2$ content, which is consistent with the Cu_2Se-$CuAlSe_2$ pseudo-binary phase diagram.

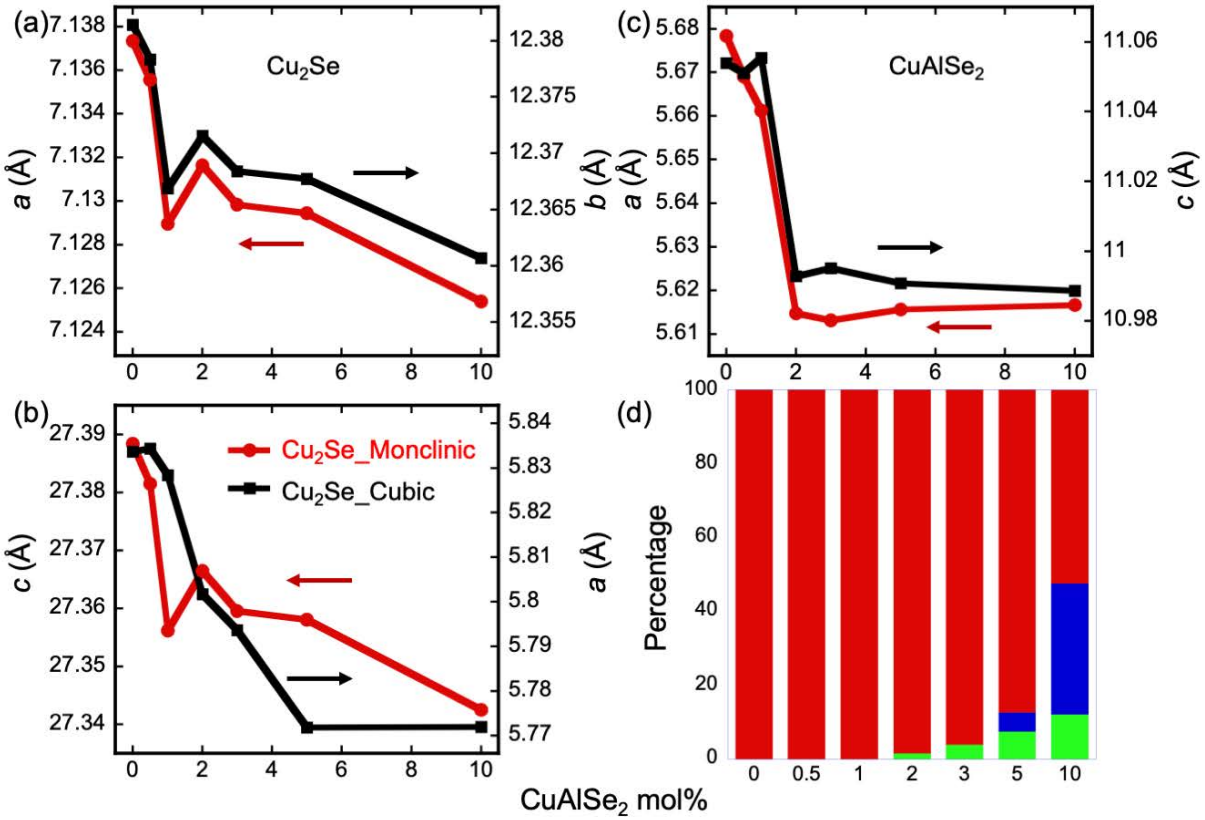

Figure A4-3. Lattice parameters of α-Cu_2Se (a-b), β-Cu_2Se(b), $CuAlSe_2$ (c) obtained from Rietveld refinement and phase quantification (d) based on RIR method using XRD patterns from bulk (x)$CuAlSe_2$/(1-x)Cu_2Se samples with increasing Al content. The strangely high lattice parameter for cubic Cu_2Se in sample x = 0.01 is probably due to extremely low concentration of this phase, leading to an inaccurate estimation.

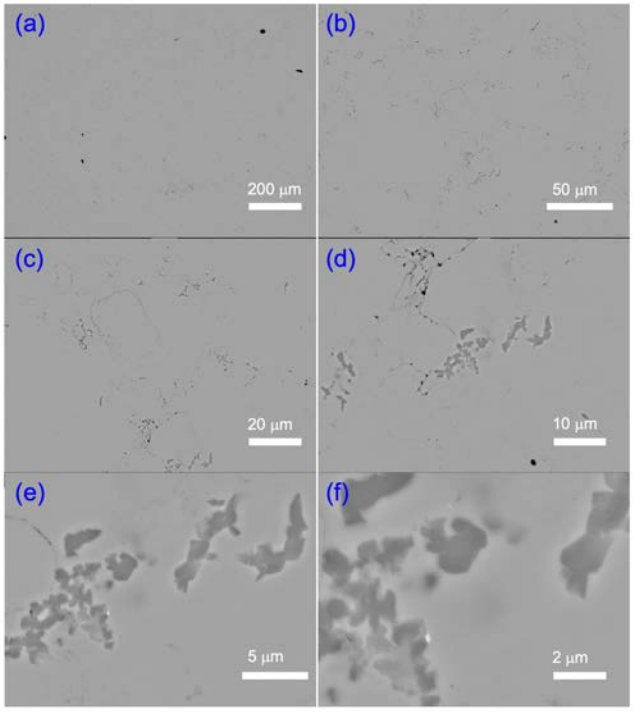

Figure A4-4. BSE images of $0.99Cu_2Se/0.01CuAlSe_2$ composite.

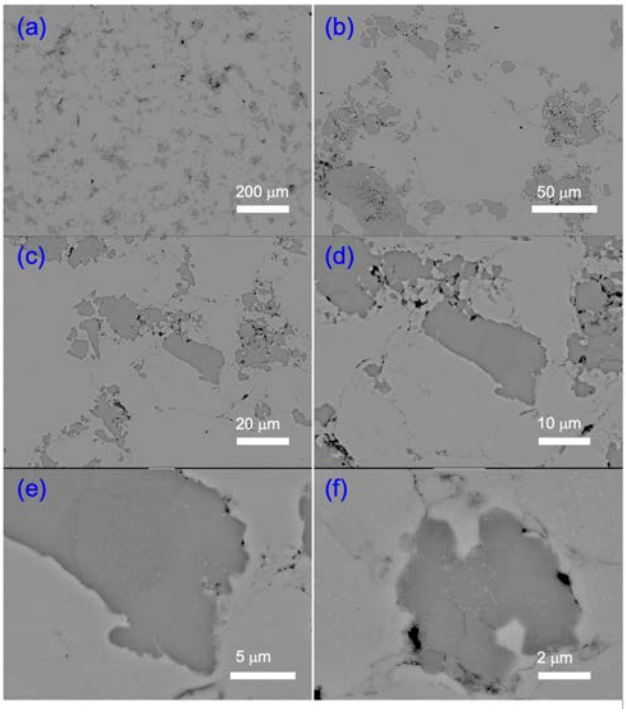

Figure A4-5. BSE images of $0.90Cu_2Se/0.10CuAlSe_2$ composite.

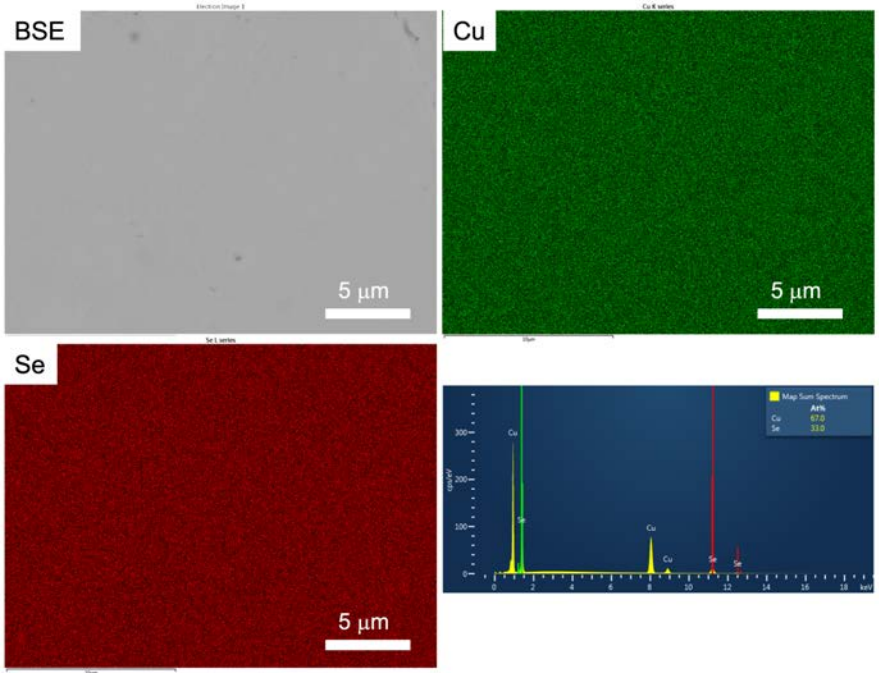

Figure A4-6. EDS mapping of the pristine Cu_2Se.

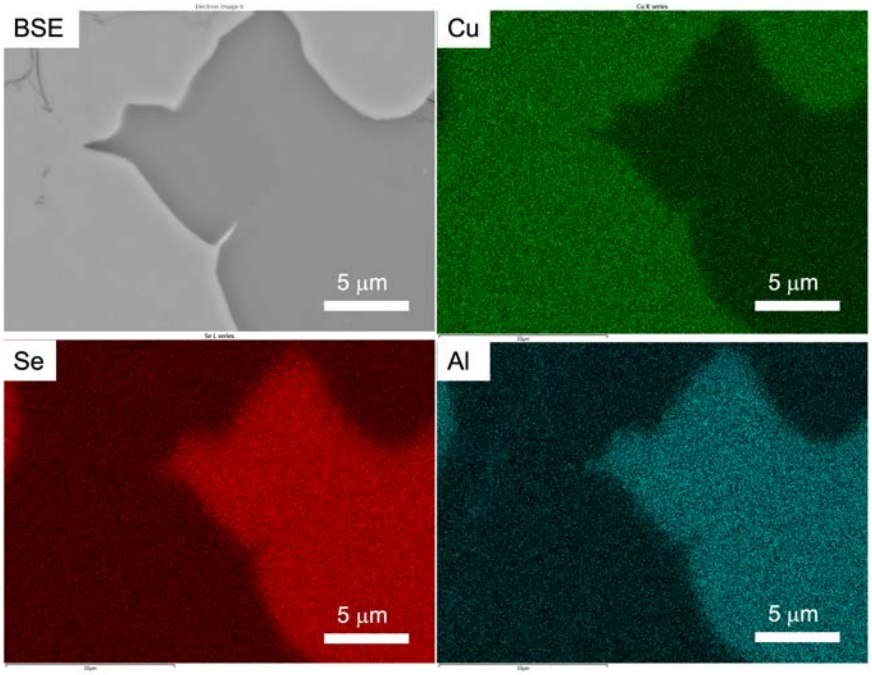

Figure A4-7. EDS mapping of $0.98Cu_2Se/0.02CuAlSe_2$ composite.

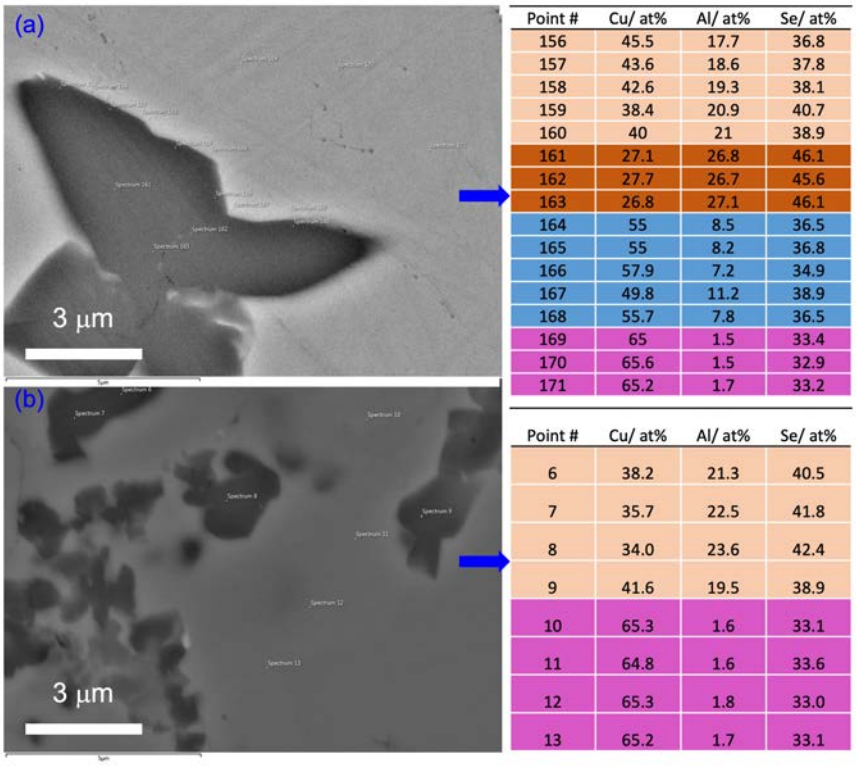

Point #	Cu/ at%	Al/ at%	Se/ at%
156	45.5	17.7	36.8
157	43.6	18.6	37.8
158	42.6	19.3	38.1
159	38.4	20.9	40.7
160	40	21	38.9
161	27.1	26.8	46.1
162	27.7	26.7	45.6
163	26.8	27.1	46.1
164	55	8.5	36.5
165	55	8.2	36.8
166	57.9	7.2	34.9
167	49.8	11.2	38.9
168	55.7	7.8	36.5
169	65	1.5	33.4
170	65.6	1.5	32.9
171	65.2	1.7	33.2

Point #	Cu/ at%	Al/ at%	Se/ at%
6	38.2	21.3	40.5
7	35.7	22.5	41.8
8	34.0	23.6	42.4
9	41.6	19.5	38.9
10	65.3	1.6	33.1
11	64.8	1.6	33.6
12	65.3	1.8	33.0
13	65.2	1.7	33.1

Figure A4-8. Point analysis via EDS for sample x = 0.01: (a) a large precipitate partially penetrated by Cu ions and (b) a small precipitate fully penetrated by Cu ions.

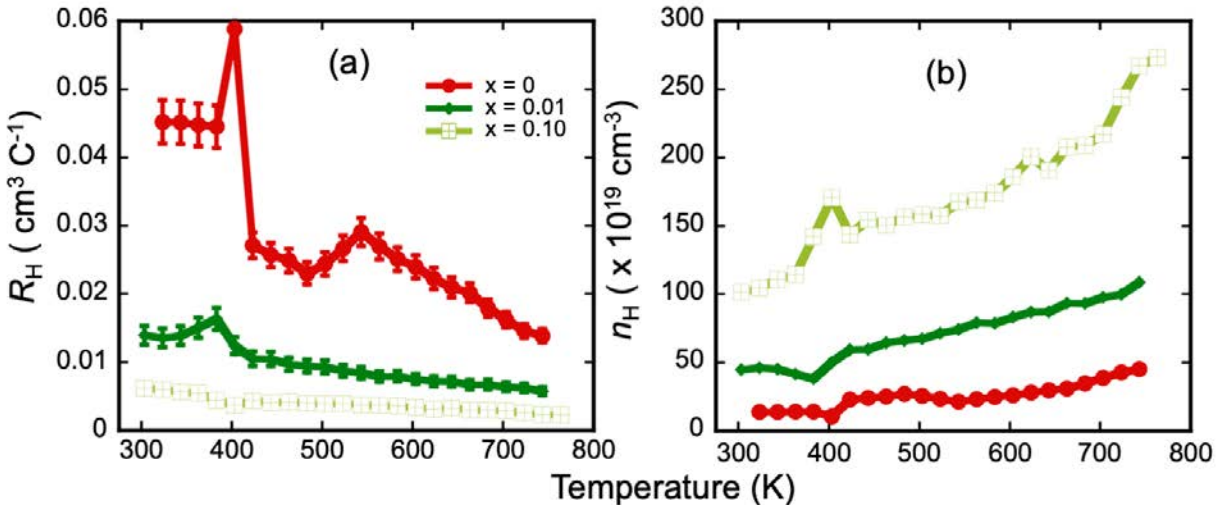

Figure A4-9. Temperature-dependent Hall coefficient (a) and calculated carrier density (b) for selected (x)$CuAlSe_2$/(1-x)Cu_2Se composites.

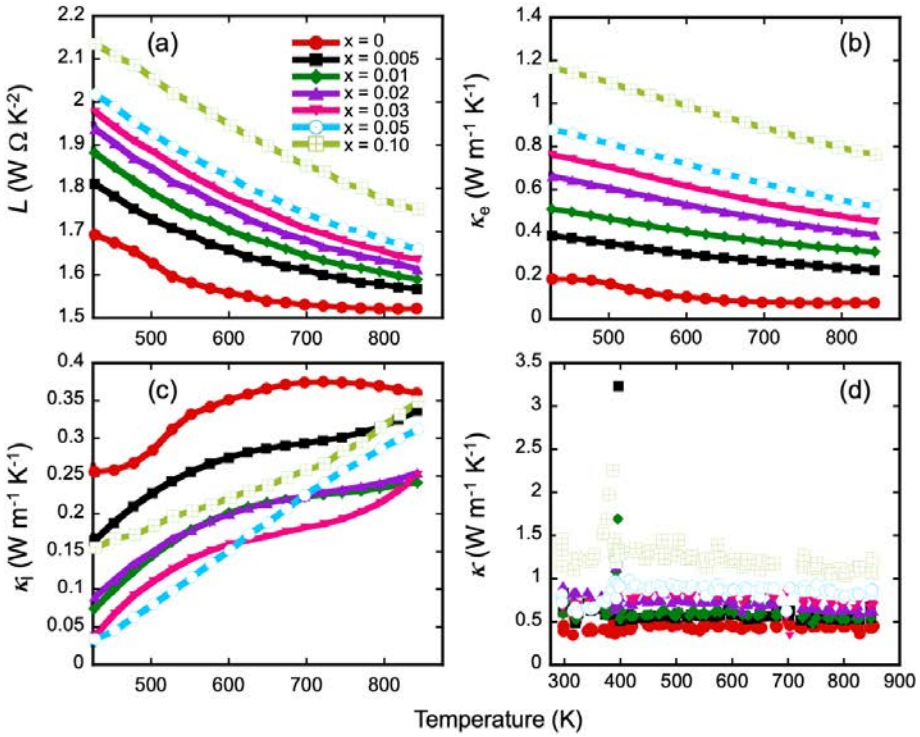

Figure A4-10. Temperature-dependent Lorenz constant (a), the electronic thermal conductivity calculated from the Wiedemann-Franz law (b), the estimated lattice thermal conductivity (c) and total thermal conductivity (d) of (x)$CuAlSe_2$/(1-x)Cu_2Se composites. This analysis assumes a strong coupling between electronic and thermal transport properties.

Appendix 5 : Supplementary Information for Chapter 7

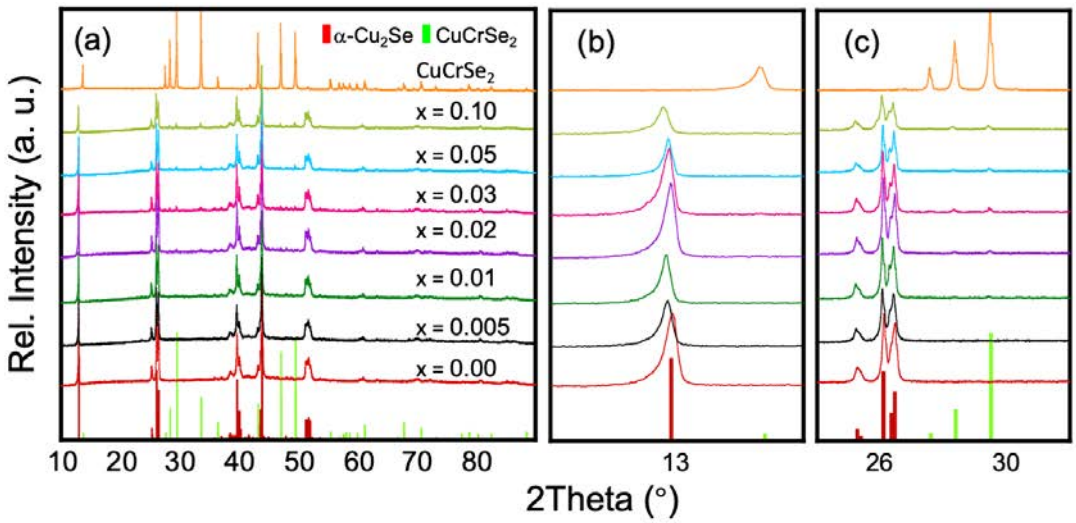

Figure A5-1. (a) PXRD of the as-synthesized (x)$CuCrSe_2$/(1-x)Cu_2Se composites. Enlarged views of the diffraction peaks around 13° (b) and 27° (c), showing the diffraction peaks for $CuCrSe_2$ appear when $x \geq 0.01$.

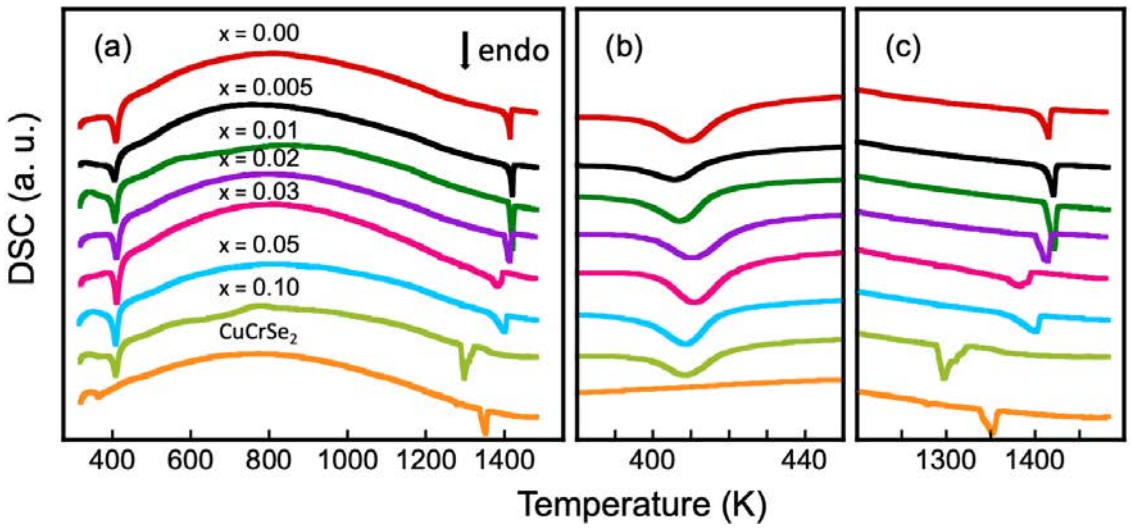

Figure A5-2. DSC of (x)$CuCrSe_2$/(1-x)Cu_2Se composites after the solid-state reaction (a). The phase transition peak from α-Cu_2Se to β-Cu_2Se (b) shifts towards lower temperature with increasing $CuCrSe_2$ content. Likewise, the melting peak of (x)$CuCrSe_2$/(1-x)Cu_2Se composites (c) gradually decreases with increasing $CuCrSe_2$ content and sample 0.1$CuCrSe_2$/0.9Cu_2Se has a melting temperature even lower than pure $CuCrSe_2$.

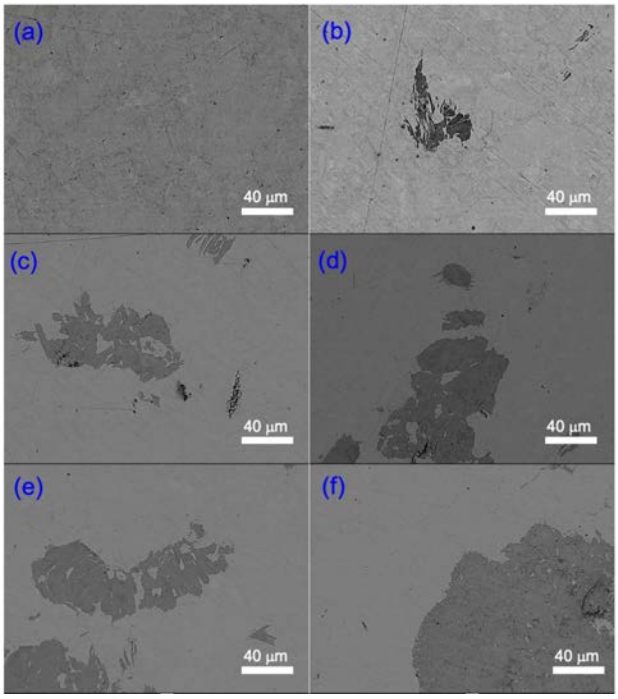

Figure A5-3. BSE images of (1-x)Cu_2Se/(x)$CuCrSe_2$ composites: (a) x = 0; (b) x = 0.005; (c) x = 0.02; (d) x = 0.03; (e) x = 0.05 and (d) x = 0.10.

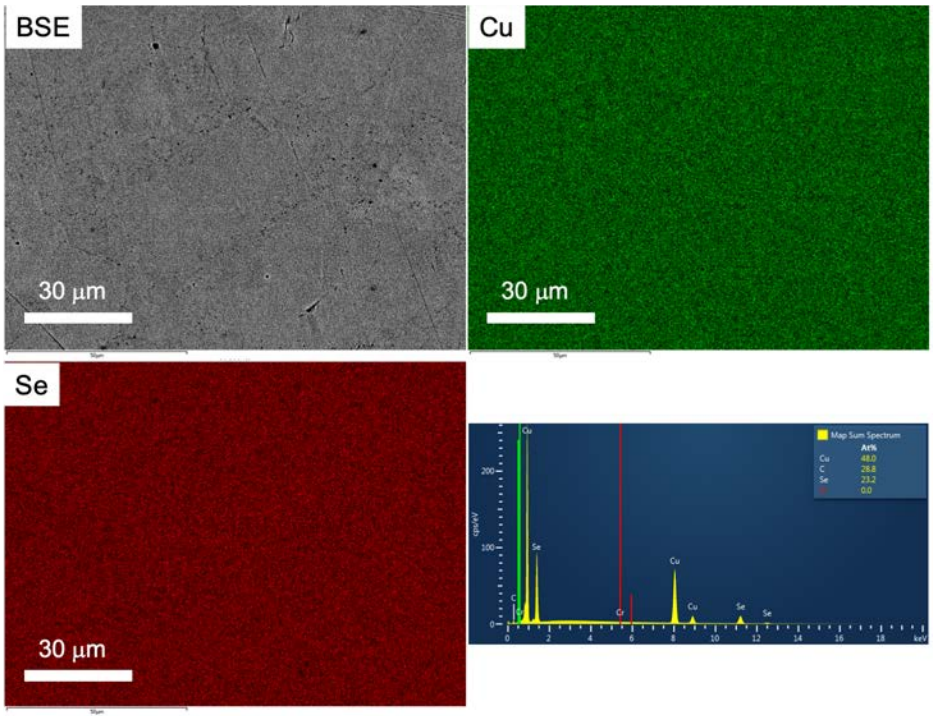

Figure A5-4. EDS mapping of the pristine Cu_2Se.

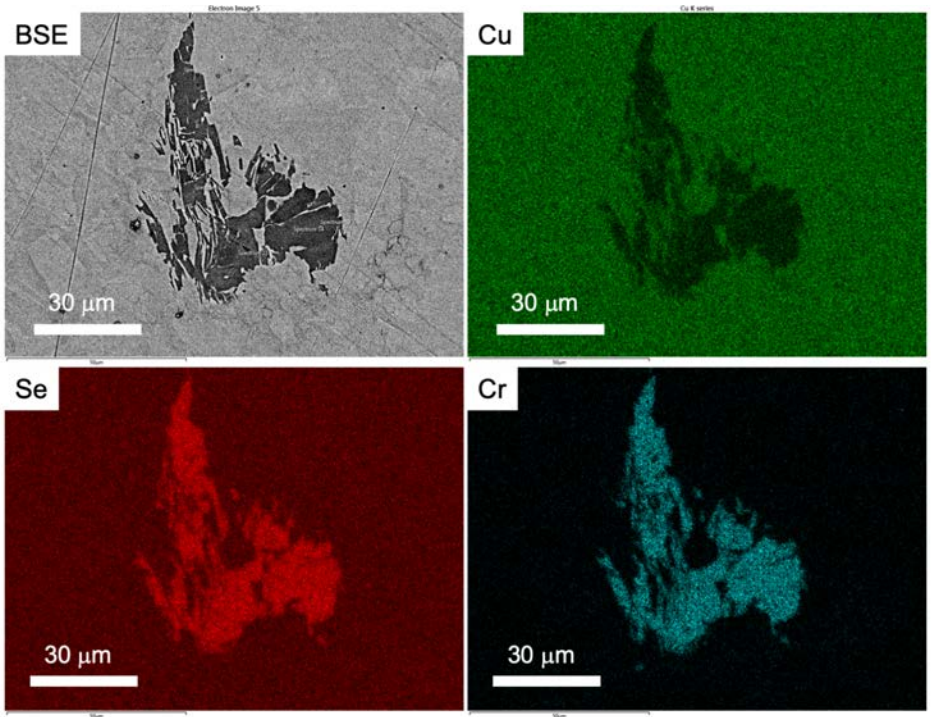

Figure A5-5. EDS mapping of $0.995Cu_2Se/0.005CuCrSe_2$ composite.

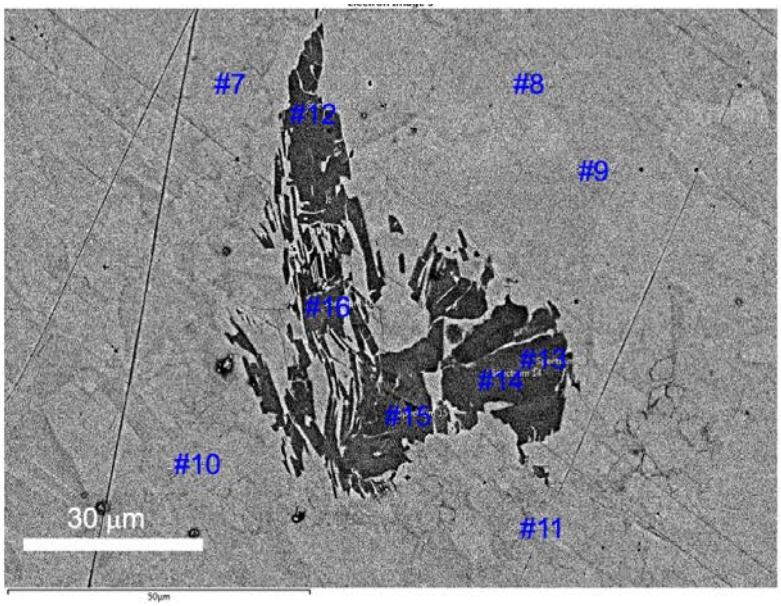

Point #	Cu/ at%	Cr/ at%	Se/ at%
7	66.8	0.3	32.9
8	67.0	0.1	33.0
9	67.0	0.0	33.0
10	67.5	0.1	32.4
11	67.1	0.4	32.6
12	27.7	24.0	48.3
13	27.2	24.5	48.3
14	27.2	24.6	48.1
15	27.3	24.5	48.2
16	27.2	24.3	48.5

Figure A5-6. Point composition analysis via EDS for $0.995Cu_2Se/0.005CuCrSe_2$ composite.

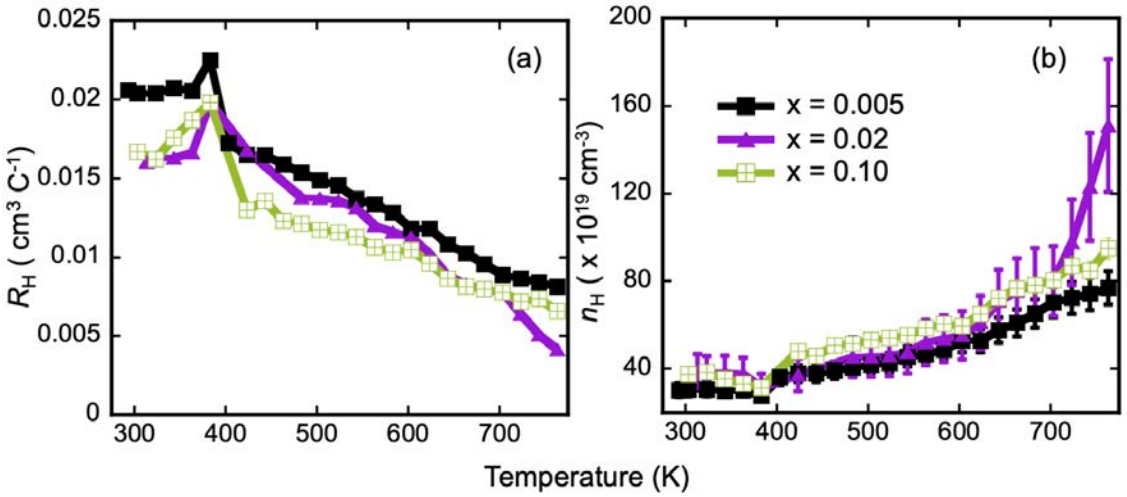

Figure A5-7. Temperature-dependent Hall coefficient (a) and calculated carrier density (b) for selected (x)$CuCrSe_2$/(1-x)Cu_2Se composites.

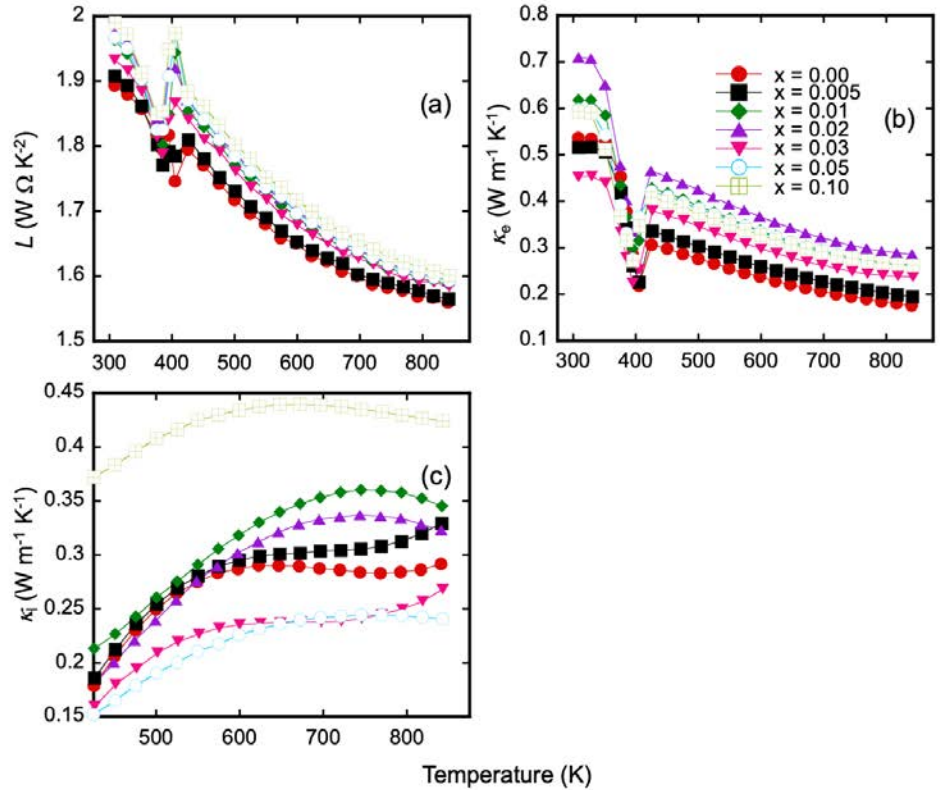

Figure A5-8. Temperature-dependence of the Lorenz constant (a), the electronic thermal conductivity calculated from the Wiedemann-Franz law (b), and the estimated lattice thermal conductivity (c) of (x)$CuCrSe_2$/(1-x)Cu_2Se composites.

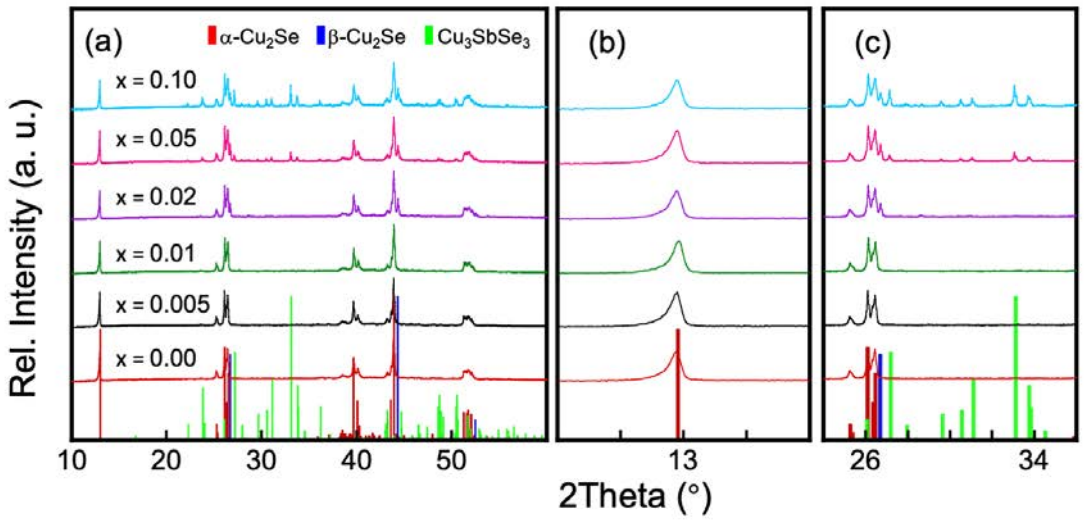

Figure A5-9. (a) PXRD of the as-synthesized (x)Cu_3SbSe_3/(1-2x)Cu_2Se composites. Enlarged views of the diffraction peak around 13° (b) and between 25-35° (c), showing the diffraction peaks for Cu_3SbSe_3 only appear when $x \geq 0.05$.

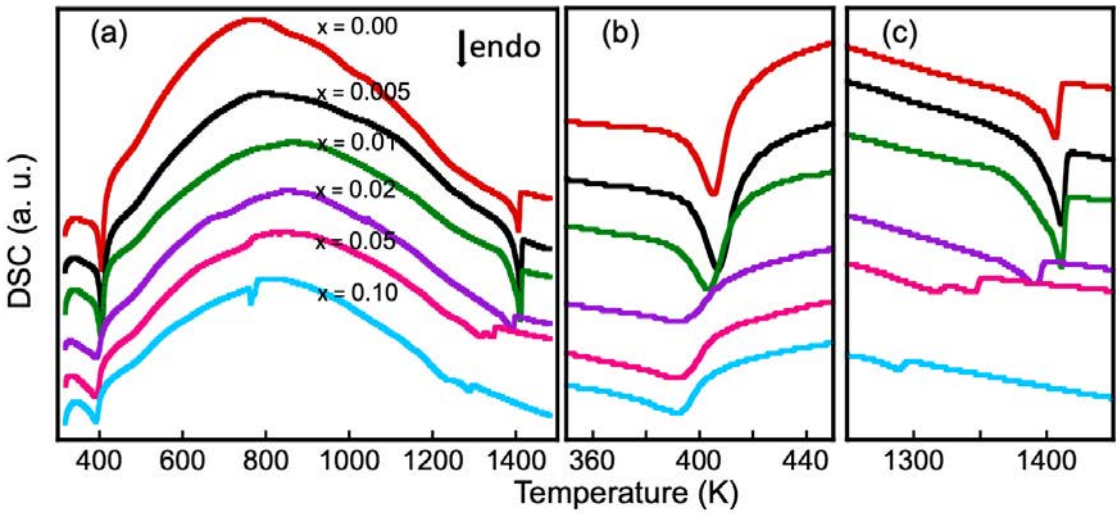

Figure A5-10. DSC of (x)Cu_3SbSe_3/(1-2x)Cu_2Se composites after the solid-state reaction (a). The phase transition peak from α-Cu_2Se to β-Cu_2Se (b) shifts towards lower temperature with increasing Cu_3SbSe_3 content. Likewise, the melting peak of (x)Cu_3SbSe_3/(1-2x)Cu_2Se composites (c) gradually decreases with increasing Cu_3SbSe_3 content.

Bibliography

1. International-Energy-Agency, Key World Energy Statistics 2015. IEA: Paris, France, 2015.
2. International-Energy-Agency, Key World Energy Statistics 2019. IEA: Paris, France, 2019.
3. Yang, J.; Stabler, F. R., Automotive applications of thermoelectric materials. *Journal of Electronic Materials* **2009,** *38* (7), 1245-1251.
4. Slack, G. A.; Rowe, D., CRC handbook of thermoelectrics. CRC press Boca Raton, FL: 1995.
5. Kittel, C.; McEuen, P.; McEuen, P., *Introduction to solid state physics*. Wiley New York: 1996; Vol. 8.
6. Snyder, G. J.; Toberer, E. S., Complex thermoelectric materials. In *Materials For Sustainable Energy: A Collection of Peer-Reviewed Research and Review Articles from Nature Publishing Group*, World Scientific: 2011; pp 101-110.
7. Heller, M.; Nasby, R.; Johnson Jr, R., Electrical transpoet properties of SiGe thermoelectric alloys doped with As, P, and As+P. *Journal of Applied Physics* **1976,** *47* (9), 4113-4121.
8. Wang, X.; Lee, H.; Lan, Y.; Zhu, G.; Joshi, G.; Wang, D.; Yang, J.; Muto, A.; Tang, M.; Klatsky, J., Enhanced thermoelectric figure of merit in nanostructured n-type silicon germanium bulk alloy. *Applied Physics Letters* **2008,** *93* (19), 193121.
9. Yu, B.; Zebarjadi, M.; Wang, H.; Lukas, K.; Wang, H.; Wang, D.; Opeil, C.; Dresselhaus, M.; Chen, G.; Ren, Z., Enhancement of thermoelectric properties by modulation-doping in silicon germanium alloy nanocomposites. *Nano letters* **2012,** *12* (4), 2077-2082.
10. Joshi, G.; Lee, H.; Lan, Y.; Wang, X.; Zhu, G.; Wang, D.; Gould, R. W.; Cuff, D. C.; Tang, M. Y.; Dresselhaus, M. S., Enhanced thermoelectric figure-of-merit in nanostructured p-type silicon germanium bulk alloys. *Nano letters* **2008,** *8* (12), 4670-4674.
11. Wei, W.; Chang, C.; Yang, T.; Liu, J.; Tang, H.; Zhang, J.; Li, Y.; Xu, F.; Zhang, Z.; Li, J.-F., Achieving high thermoelectric figure of merit in polycrystalline SnSe via introducing Sn vacancies. *Journal of the American Chemical Society* **2018,** *140* (1), 499-505.
12. Yang, L.; Chen, Z.-G.; Han, G.; Hong, M.; Zou, J., Impacts of Cu deficiency on the thermoelectric properties of $Cu_{2-x}Se$ nanoplates. *Acta Materialia* **2016,** *113*, 140-146.
13. Xiao, X.-X.; Xie, W.-J.; Tang, X.-F.; Zhang, Q.-J., Phase transition and high temperature thermoelectric properties of copper selenide $Cu_{2-x}Se$ ($0 \leqslant x \leqslant 0.25$). *Chinese Physics B* **2011,** *20* (8), 087201.
14. Peng, P.; Gong, Z.; Liu, F.; Huang, M.; Ao, W.; Li, Y.; Li, J., Structure and thermoelectric performance of β-Cu_2Se doped with Fe, Ni, Mn, In, Zn or Sm. *Intermetallics* **2016,** *75*, 72-78.

15. Liu, H.; Yuan, X.; Lu, P.; Shi, X.; Xu, F.; He, Y.; Tang, Y.; Bai, S.; Zhang, W.; Chen, L., Ultrahigh thermoelectric performance by electron and phonon critical scattering in $Cu_2Se_{1-x}I_x$. *Advanced Materials* **2013,** *25* (45), 6607-6612.
16. Kim, M. J.; Lee, G.-G.; Kim, W.; Kim, K.; Tak, J.-Y.; Shin, W. H.; Seo, W.-S.; Hong, J.; Lim, Y. S., Effects of Cl-Doping on Thermoelectric Transport Properties of Cu_2Se Prepared by Spark Plasma Sintering. *Journal of Electronic Materials* **2019,** *48* (4), 1958-1964.
17. Day, T. W.; Weldert, K. S.; Zeier, W. G.; Chen, B.-R.; Moffitt, S. L.; Weis, U.; Jochum, K. P.; Panthöfer, M.; Bedzyk, M. J.; Snyder, G. J., Influence of Compensating Defect Formation on the Doping Efficiency and Thermoelectric Properties of $Cu_{2-y}Se_{1-x}Br_x$. *Chemistry of Materials* **2015,** *27* (20), 7018-7027.
18. Zhong, B.; Zhang, Y.; Li, W.; Chen, Z.; Cui, J.; Li, W.; Xie, Y.; Hao, Q.; He, Q., High superionic conduction arising from aligned large lamellae and large figure of merit in bulk $Cu_{1.94}Al_{0.02}Se$. *Applied Physics Letters* **2014,** *105* (12), 123902.
19. Pei, Y.-L.; Wu, H.; Wu, D.; Zheng, F.; He, J., High thermoelectric performance realized in a BiCuSeO system by improving carrier mobility through 3D modulation doping. *Journal of the American Chemical Society* **2014,** *136* (39), 13902-13908.
20. Berry, T.; Fu, C.; Auffermann, G.; Fecher, G. H.; Schnelle, W.; Serrano-Sanchez, F.; Yue, Y.; Liang, H.; Felser, C., Enhancing thermoelectric performance of TiNiSn half-Heusler compounds via modulation doping. *Chemistry of Materials* **2017,** *29* (16), 7042-7048.
21. Mahan, G.; Sofo, J. O., The best thermoelectric. *Proceedings of the National Academy of Sciences* **1996,** *93* (15), 7436-7439.
22. Cutler, M.; Mott, N. F., Observation of Anderson localization in an electron gas. *Physical Review* **1969,** *181* (3), 1336.
23. Heremans, J. P.; Jovovic, V.; Toberer, E. S.; Saramat, A.; Kurosaki, K.; Charoenphakdee, A.; Yamanaka, S.; Snyder, G. J., Enhancement of thermoelectric efficiency in PbTe by distortion of the electronic density of states. *Science* **2008,** *321* (5888), 554-557.
24. Pei, Y.; Wang, H.; Snyder, G. J., Band engineering of thermoelectric materials. *Advanced Materials* **2012,** *24* (46), 6125-6135.
25. Pei, Y.; LaLonde, A. D.; Wang, H.; Snyder, G. J., Low effective mass leading to high thermoelectric performance. *Energy & Environmental Science* **2012,** *5* (7), 7963-7969.
26. Pei, Y.; LaLonde, A.; Iwanaga, S.; Snyder, G. J., High thermoelectric figure of merit in heavy hole dominated PbTe. *Energy & Environmental Science* **2011,** *4* (6), 2085-2089.
27. Fu, C.; Zhu, T.; Liu, Y.; Xie, H.; Zhao, X., Band engineering of high performance p-type FeNbSb based half-Heusler thermoelectric materials for figure of merit $zT > 1$. *Energy & environmental science* **2015,** *8* (1), 216-220.
28. Shen, J.; Fan, L.; Hu, C.; Zhu, T.; Xin, J.; Fu, T.; Zhao, D.; Zhao, X., Enhanced thermoelectric performance in the n-type NbFeSb half-Heusler compound with heavy element Ir doping. *Materials Today Physics* **2019,** *8*, 62-70.
29. Zhang, J.; Song, L.; Borup, K. A.; Jørgensen, M. R. V.; Iversen, B. B., New Insight on Tuning Electrical Transport Properties via Chalcogen Doping in n-type Mg_3Sb_2-Based Thermoelectric Materials. *Advanced Energy Materials* **2018,** *8* (16), 1702776.
30. Ren, G.-K.; Wang, S.-Y.; Zhu, Y.-C.; Ventura, K. J.; Tan, X.; Xu, W.; Lin, Y.-H.; Yang, J.; Nan, C.-W., Enhancing thermoelectric performance in hierarchically structured BiCuSeO by increasing bond covalency and weakening carrier-phonon coupling. *Energy & Environmental Science* **2017,** *10* (7), 1590-1599.

31. Braunstein, R.; Moore, A. R.; Herman, F., Intrinsic optical absorption in germanium-silicon alloys. *Physical Review* **1958,** *109* (3), 695.
32. Kenjo, T.; Kimura, Y.; Mishima, Y., Phase stability and thermoelectric properties of half-Heusler compounds (Ti,M)NiSn (M= Zr, Hf). *MRS Online Proceedings Library Archive* **2009,** *1218*.
33. Kimura, Y.; Chai, Y.-W., Ordered structures and thermoelectric properties of MNiSn (M= Ti, Zr, Hf)-based half-Heusler compounds affected by close relationship with Heusler compounds. *JOM* **2015,** *67* (1), 233-245.
34. Korkosz, R. J.; Chasapis, T. C.; Lo, S.-h.; Doak, J. W.; Kim, Y. J.; Wu, C.-I.; Hatzikraniotis, E.; Hogan, T. P.; Seidman, D. N.; Wolverton, C., High *ZT* in p-Type $(PbTe)_{1-2x}(PbSe)_x(PbS)_x$ Thermoelectric Materials. *Journal of the American Chemical Society* **2014,** *136* (8), 3225-3237.
35. Gelbstein, Y.; Dashevsky, Z.; Dariel, M., Powder metallurgical processing of functionally graded p-$Pb_{1-x}Sn_xTe$ materials for thermoelectric applications. *Physica B: Condensed Matter* **2007,** *391* (2), 256-265.
36. Callaway, J.; von Baeyer, H. C., Effect of point imperfections on lattice thermal conductivity. *Physical Review* **1960,** *120* (4), 1149.
37. Ren, T.; Ying, P.; Cai, G.; Li, X.; Han, Z.; Min, L.; Cui, J., Improvement of thermoelectric performance of copper-deficient compounds $Cu_{2.5+\delta}In_{4.5}Te_8$ (δ= 0−0.15) due to a degenerate impurity band and ultralow lattice thermal conductivity. *RSC Advances* **2018,** *8* (48), 27163-27170.
38. Wan, C.; Qu, Z.; Du, A.; Pan, W., Influence of B site substituent Ti on the structure and thermophysical properties of A2B2O7-type pyrochlore $Gd_2Zr_2O_7$. *Acta materialia* **2009,** *57* (16), 4782-4789.
39. Maycock, P., Thermal conductivity of silicon, germanium, III-V compounds and III-V alloys. *Solid-state electronics* **1967,** *10* (3), 161-168.
40. Mei, S.; Foss, C.; Maurer, L.; Jonasson, O.; Aksamija, Z.; Knezevic, I. In *Boundaries, interfaces, point defects, and strain as impediments to thermal transport in nanostructures*, 2017 IEEE International Reliability Physics Symposium (IRPS), IEEE: 2017; pp 6A-1.1-6A-1.10.
41. Pei, Y.; Shi, X.; LaLonde, A.; Wang, H.; Chen, L.; Snyder, G. J., Convergence of electronic bands for high performance bulk thermoelectrics. *Nature* **2011,** *473* (7345), 66.
42. Zhao, L.-D.; He, J.; Hao, S.; Wu, C.-I.; Hogan, T. P.; Wolverton, C.; Dravid, V. P.; Kanatzidis, M. G., Raising the thermoelectric performance of p-type PbS with endotaxial nanostructuring and valence-band offset engineering using CdS and ZnS. *Journal of the American Chemical Society* **2012,** *134* (39), 16327-16336.
43. Liu, W.; Tan, X.; Yin, K.; Liu, H.; Tang, X.; Shi, J.; Zhang, Q.; Uher, C., Convergence of conduction bands as a means of enhancing thermoelectric performance of n-type $Mg_2Si_{1-x}Sn_x$ solid solutions. *Physical review letters* **2012,** *108* (16), 166601.
44. Liu, X.; Zhu, T.; Wang, H.; Hu, L.; Xie, H.; Jiang, G.; Snyder, G. J.; Zhao, X., Low electron scattering potentials in high performance $Mg_2Si_{0.45}Sn_{0.55}$ based thermoelectric solid solutions with band convergence. *Advanced Energy Materials* **2013,** *3* (9), 1238-1244.
45. Tan, G.; Shi, F.; Hao, S.; Chi, H.; Bailey, T. P.; Zhao, L.-D.; Uher, C.; Wolverton, C.; Dravid, V. P.; Kanatzidis, M. G., Valence band modification and high thermoelectric performance in SnTe heavily alloyed with MnTe. *Journal of the American Chemical Society* **2015,** *137* (35), 11507-11516.

46. Tan, X.; Shao, H.; He, J.; Liu, G.; Xu, J.; Jiang, J.; Jiang, H., Band engineering and improved thermoelectric performance in M-doped SnTe (M= Mg, Mn, Cd, and Hg). *Physical Chemistry Chemical Physics* **2016,** *18* (10), 7141-7147.
47. Li, W.; Chen, Z.; Lin, S.; Chang, Y.; Ge, B.; Chen, Y.; Pei, Y., Band and scattering tuning for high performance thermoelectric $Sn_{1-x}Mn_xTe$ alloys. *Journal of Materiomics* **2015,** *1* (4), 307-315.
48. Al Rahal Al Orabi, R.; Mecholsky, N. A.; Hwang, J.; Kim, W.; Rhyee, J.-S.; Wee, D.; Fornari, M., Band degeneracy, low thermal conductivity, and high thermoelectric figure of merit in SnTe-CaTe alloys. *Chemistry of Materials* **2016,** *28* (1), 376-384.
49. Imasato, K.; Kang, S. D.; Ohno, S.; Snyder, G. J., Band engineering in Mg_3Sb_2 by alloying with Mg_3Bi_2 for enhanced thermoelectric performance. *Materials Horizons* **2018,** *5* (1), 59-64.
50. Fu, C.; Zhu, T.; Pei, Y.; Xie, H.; Wang, H.; Snyder, G. J.; Liu, Y.; Liu, Y.; Zhao, X., High band degeneracy contributes to high thermoelectric performance in p-type half-Heusler compounds. *Advanced Energy Materials* **2014,** *4* (18), 1400600.
51. Zheng, Z.; Su, X.; Deng, R.; Stoumpos, C.; Xie, H.; Liu, W.; Yan, Y.; Hao, S.; Uher, C.; Wolverton, C., Rhombohedral to cubic conversion of GeTe via MnTe alloying leads to ultralow thermal conductivity, electronic band convergence, and high thermoelectric performance. *Journal of the American Chemical Society* **2018,** *140* (7), 2673-2686.
52. Poudel, B.; Hao, Q.; Ma, Y.; Lan, Y.; Minnich, A.; Yu, B.; Yan, X.; Wang, D.; Muto, A.; Vashaee, D., High-thermoelectric performance of nanostructured bismuth antimony telluride bulk alloys. *Science* **2008,** *320* (5876), 634-638.
53. Zhang, Q.; Liao, B.; Lan, Y.; Lukas, K.; Liu, W.; Esfarjani, K.; Opeil, C.; Broido, D.; Chen, G.; Ren, Z., High thermoelectric performance by resonant dopant indium in nanostructured SnTe. *Proceedings of the National Academy of Sciences* **2013,** *110* (33), 13261-13266.
54. Zhou, M.; Li, J.-F.; Kita, T., Nanostructured $AgPb_mSbTe_{m+2}$ system bulk materials with enhanced thermoelectric performance. *Journal of the American Chemical Society* **2008,** *130* (13), 4527-4532.
55. Shuai, J.; Kim, H. S.; Lan, Y.; Chen, S.; Liu, Y.; Zhao, H.; Sui, J.; Ren, Z., Study on thermoelectric performance by Na doping in nanostructured $Mg_{1-x}Na_xAg_{0.97}Sb_{0.99}$. *Nano Energy* **2015,** *11*, 640-646.
56. Xie, W.; Tang, X.; Yan, Y.; Zhang, Q.; Tritt, T. M., Unique nanostructures and enhanced thermoelectric performance of melt-spun BiSbTe alloys. *Applied Physics Letters* **2009,** *94* (10), 102111.
57. Zheng, Y.; Zhang, Q.; Su, X.; Xie, H.; Shu, S.; Chen, T.; Tan, G.; Yan, Y.; Tang, X.; Uher, C., Mechanically robust BiSbTe alloys with superior thermoelectric performance: a case study of stable hierarchical nanostructured thermoelectric materials. *Advanced Energy Materials* **2015,** *5* (5), 1401391.
58. Tang, X.; Xie, W.; Li, H.; Zhao, W.; Zhang, Q.; Niino, M., Preparation and thermoelectric transport properties of high-performance p-type Bi_2Te_3 with layered nanostructure. *Applied physics letters* **2007,** *90* (1), 012102.
59. Li, H.; Tang, X.; Su, X.; Zhang, Q., Preparation and thermoelectric properties of high-performance Sb additional $Yb_{0.2}Co_4Sb_{12+y}$ bulk materials with nanostructure. *Applied Physics Letters* **2008,** *92* (20), 202114.

60. Li, H.; Tang, X.; Zhang, Q.; Uher, C., Rapid preparation method of bulk nanostructured $Yb_{0.3}Co_4Sb_{12+y}$ compounds and their improved thermoelectric performance. *Applied Physics Letters* **2008,** *93* (25), 252109.
61. Wang, S.; Li, H.; Qi, D.; Xie, W.; Tang, X., Enhancement of the thermoelectric performance of β-Zn_4Sb_3 by in situ nanostructures and minute Cd-doping. *Acta materialia* **2011,** *59* (12), 4805-4817.
62. Du, B.; Li, H.; Xu, J.; Tang, X.; Uher, C., Enhanced thermoelectric performance and novel nanopores in $AgSbTe_2$ prepared by melt spinning. *Journal of Solid State Chemistry* **2011,** *184* (1), 109-114.
63. Zhang, G.; Kirk, B.; Jauregui, L. A.; Yang, H.; Xu, X.; Chen, Y. P.; Wu, Y., Rational synthesis of ultrathin n-type Bi_2Te_3 nanowires with enhanced thermoelectric properties. *Nano letters* **2012,** *12* (1), 56-60.
64. Pei, Y.; May, A. F.; Snyder, G. J., Self-Tuning the Carrier Concentration of PbTe/Ag_2Te Composites with Excess Ag for High Thermoelectric Performance. *Advanced Energy Materials* **2011,** *1* (2), 291-296.
65. Pei, Y.; LaLonde, A. D.; Heinz, N. A.; Snyder, G. J., High thermoelectric figure of merit in PbTe alloys demonstrated in PbTe-CdTe. *Advanced Energy Materials* **2012,** *2* (6), 670-675.
66. Ohta, M.; Biswas, K.; Lo, S. H.; He, J.; Chung, D. Y.; Dravid, V. P.; Kanatzidis, M. G., Enhancement of thermoelectric figure of merit by the insertion of MgTe nanostructures in p-type PbTe doped with Na_2Te. *Advanced Energy Materials* **2012,** *2* (9), 1117-1123.
67. Makongo, J. P.; Misra, D. K.; Zhou, X.; Pant, A.; Shabetai, M. R.; Su, X.; Uher, C.; Stokes, K. L.; Poudeu, P. F., Simultaneous large enhancements in thermopower and electrical conductivity of bulk nanostructured half-Heusler alloys. *Journal of the American Chemical Society* **2011,** *133* (46), 18843-18852.
68. Liu, Y.; Sahoo, P.; Makongo, J. P.; Zhou, X.; Kim, S.-J.; Chi, H.; Uher, C.; Pan, X.; Poudeu, P. F., Large enhancements of thermopower and carrier mobility in quantum dot engineered bulk semiconductors. *Journal of the American Chemical Society* **2013,** *135* (20), 7486-7495.
69. Xie, W. J.; He, J.; Zhu, S.; Su, X. L.; Wang, S. Y.; Holgate, T.; Graff, J. W.; Ponnambalam, V.; Poon, S. J.; Tang, X. F.; Zhang, Q. J.; Tritt, T. M., Simultaneously optimizing the independent thermoelectric properties in (Ti,Zr,Hf)(Co,Ni)Sb alloy by in situ forming InSb nanoinclusions. *Acta Materialia* **2010,** *58* (14), 4705-4713.
70. Huang, X.; Xu, Z.; Chen, L., The thermoelectric performance of ZrNiSn/ZrO_2 composites. *Solid State Communications* **2004,** *130* (3-4), 181-185.
71. Misra, D. K.; Makongo, J. P. A.; Sahoo, P.; Shabetai, M. R.; Paudel, P.; Stokes, K. L.; Poudeu, P. F. P., Microstructure and Thermoelectric Properties of Mechanically Alloyed $Zr_{0.5}Hf_{0.5}Ni_{0.8}Pd_{0.2}Sn_{0.99}Sb_{0.01}$/$WO_3$ Half-Heusler Composites. *Sci Adv Mater* **2011,** *3* (4), 607-614.
72. Zhao, L.; Islam, S. M. K. N.; Wang, J.; Cortie, D. L.; Wang, X.; Cheng, Z.; Wang, J.; Ye, N.; Dou, S.; Shi, X., Significant enhancement of figure-of-merit in carbon-reinforced Cu_2Se nanocrystalline solids. *Nano Energy* **2017,** *41*, 164-171.
73. Nunna, R.; Qiu, P.; Yin, M.; Chen, H.; Hanus, R.; Song, Q.; Zhang, T.; Chou, M.-Y.; Agne, M. T.; He, J., Ultrahigh thermoelectric performance in Cu_2Se-based hybrid materials with highly dispersed molecular CNTs. *Energy & Environmental Science* **2017,** *10* (9), 1928-1935.

74. Islam, S. M. K. N.; Li, M.; Aydemir, U.; Shi, X.; Chen, L.; Snyder, G. J.; Wang, X., Giant enhancement of the figure-of-merit over a broad temperature range in nano-boron incorporated Cu_2Se. *Journal of Materials Chemistry A* **2018,** *6* (38), 18409-18416.
75. Kong, F.; Bai, J.; Zhao, Y.; Liu, Y.; Shi, J.; Wang, Z.; Xiong, R., Ultralow thermal conductivity and high thermoelectric performance of Cu_2Se/TiO_2 nanocomposite. *Applied Physics Letters* **2019,** *115* (20), 203901.
76. Liu, F.; Huang, M.; Gong, Z.; Ao, W.; Li, Y.; Li, J., Enhancing the thermoelectric performance of β-Cu_2Se by incorporating SnSe. *Journal of Alloys and Compounds* **2015,** *651*, 648-654.
77. Ballikaya, S.; Oner, Y.; Temel, T.; Ozkal, B.; Bailey, T. P.; Toprak, M. S.; Uher, C., Thermoelectric and thermal stability improvements in Nano-Cu_2Se included Ag_2Se. *Journal of Solid State Chemistry* **2019,** *273*, 122-127.
78. Farooq, M. U.; Butt, S.; Gao, K.; Sun, X.; Pang, X.; Khan, S. U.; Xu, W.; Mohmed, F.; Mahmood, A.; Mahmood, N., Enhanced thermoelectric efficiency of $Cu_{2-x}Se$-Cu_2S composite by incorporating Cu_2S nanoparticles. *Ceramics International* **2016,** *42* (7), 8395-8401.
79. Liu, F.; Gong, Z.; Huang, M.; Ao, W.; Li, Y.; Li, J., Enhanced thermoelectric properties of β-Cu_2Se by incorporating $CuGaSe_2$. *Journal of Alloys and Compounds* **2016,** *688*, 521-526.
80. Kim, W.; Zide, J.; Gossard, A.; Klenov, D.; Stemmer, S.; Shakouri, A.; Majumdar, A., Thermal conductivity reduction and thermoelectric figure of merit increase by embedding nanoparticles in crystalline semiconductors. *Physical review letters* **2006,** *96* (4), 045901.
81. Biswas, K.; He, J.; Blum, I. D.; Wu, C.-I.; Hogan, T. P.; Seidman, D. N.; Dravid, V. P.; Kanatzidis, M. G., High-performance bulk thermoelectrics with all-scale hierarchical architectures. *Nature* **2012,** *489* (7416), 414.
82. Quarez, E.; Hsu, K. F.; Pcionek, R.; Frangis, N.; Polychroniadis, E. K.; Kanatzidis, M. G., Nanostructuring, compositional fluctuations, and atomic ordering in the thermoelectric materials AgPbmSbTe2+m. The myth of solid solutions. *Journal of the American Chemical Society* **2005,** *127* (25), 9177-9190.
83. Androulakis, J.; Hsu, K. F.; Pcionek, R.; Kong, H.; Uher, C.; DAngelo, J. J.; Downey, A.; Hogan, T.; Kanatzidis, M. G., Nanostructuring and high thermoelectric efficiency in p-type $Ag(Pb_{1-y}Sn_y)_{(m)}SbTe_{2+m}$. *Advanced Materials* **2006,** *18* (9), 1170.
84. Poudeu, P. F. P.; D'Angelo, J.; Kong, H. J.; Downey, A.; Short, J. L.; Pcionek, R.; Hogan, T. P.; Uher, C.; Kanatzidis, M. G., Nanostructures versus solid solutions: Low lattice thermal conductivity and enhanced thermoelectric figure of merit in $Pb_{9.6}Sb_{0.2}Te_{10-x}Se_x$ bulk materials. *Journal of the American Chemical Society* **2006,** *128* (44), 14347-14355.
85. Androulakis, J.; Lin, C. H.; Kong, H. J.; Uher, C.; Wu, C. I.; Hogan, T.; Cook, B. A.; Caillat, T.; Paraskevopoulos, K. M.; Kanatzidis, M. G., Spinodal decomposition and nucleation and growth as a means to bulk nanostructured thermoelectrics: Enhanced performance in $Pb_{1-x}Sn_xTe$-PbS. *Journal of the American Chemical Society* **2007,** *129* (31), 9780-9788.
86. Poudeu, P. F. P.; Gueguen, A.; Wu, C. I.; Hogan, T.; Kanatzidis, M. G., High Figure of Merit in Nanostructured n-Type KPb_mSbTe_{m+2} Thermoelectric Materials. *Chemistry of Materials* **2010,** *22* (3), 1046-1053.
87. Sootsman, J. R.; He, J. Q.; Dravid, V. P.; Ballikaya, S.; Vermeulen, D.; Uher, C.; Kanatzidis, M. G., Microstructure and Thermoelectric Properties of Mechanically Robust PbTe-Si Eutectic Composites. *Chemistry of Materials* **2010,** *22* (3), 869-875.

88. Sootsman, J. R.; Pcionek, R. J.; Kong, H. J.; Uher, C.; Kanatzidis, M. G., Strong reduction of thermal conductivity in nanostructured PbTe prepared by matrix encapsulation. *Chemistry of Materials* **2006,** *18* (21), 4993-4995.
89. Chen, Z.-G.; Shi, X.; Zhao, L.-D.; Zou, J., High-performance SnSe thermoelectric materials: Progress and future challenge. *Progress in Materials Science* **2018,** *97*, 283-346.
90. McCarthy, T. J.; Ngeyi, S. P.; Liao, J. H.; DeGroot, D. C.; Hogan, T.; Kannewurf, C. R.; Kanatzidis, M. G., Molten salt synthesis and properties of three new solid-state ternary bismuth chalcogenides,. β-$CsBiS_2$,. γ-$CsBiS_2$, and $K_2Bi_8Se_{13}$. *Chemistry of materials* **1993,** *5* (3), 331-340.
91. Chung, D.-Y.; Choi, K.-S.; Iordanidis, L.; Schindler, J. L.; Brazis, P. W.; Kannewurf, C. R.; Chen, B.; Hu, S.; Uher, C.; Kanatzidis, M. G., High thermopower and low thermal conductivity in semiconducting ternary K-Bi-Se compounds. synthesis and properties of β-$K_2Bi_8Se_{13}$ and $K_{2.5}Bi_{8.5}Se_{14}$ and their Sb analogues. *Chemistry of materials* **1997,** *9* (12), 3060-3071.
92. Chung, D.-Y.; Hogan, T.; Brazis, P.; Rocci-Lane, M.; Kannewurf, C.; Bastea, M.; Uher, C.; Kanatzidis, M. G., $CsBi_4Te_6$: A high-performance thermoelectric material for low-temperature applications. *Science* **2000,** *287* (5455), 1024-1027.
93. Chung, D.-Y.; Hogan, T. P.; Rocci-Lane, M.; Brazis, P.; Ireland, J. R.; Kannewurf, C. R.; Bastea, M.; Uher, C.; Kanatzidis, M. G., A new thermoelectric material: $CsBi_4Te_6$. *Journal of the American Chemical Society* **2004,** *126* (20), 6414-6428.
94. Fleurial, J. P.; Vandersande, J.; Scoville, N.; Bajgar, C.; Beaty, J. In *Progress in the optimization of n-type and p-type SiGe thermoelectric materials*, AIP Conference Proceedings, American Institute of Physics: 1993; pp 759-764.
95. Fleurial, J. P.; Borshchevsky, A.; Vandersande, J. W. In *Improved n-type SiGe/GaP thermoelectric materials*, AIP Conference Proceedings, American Institute of Physics: 1991; pp 451-457.
96. Borshchevsky, A.; Fleurial, J. P.; Vandersande, J., Experimental approaches for improving SiGe thermoelectric efficiency at JPL. *iece* **1990,** *Vols 2*, 397-401.
97. Vandersande, J. W.; Wood, C.; Draper, S., Effect of high temperature annealing on the thermoelectric properties of GaP doped SiGe. *MRS Online Proceedings Library Archive* **1987,** *97*.
98. Brown, S. R.; Kauzlarich, S. M.; Gascoin, F.; Snyder, G. J., $Yb_{14}MnSb_{11}$: New high efficiency thermoelectric material for power generation. *Chemistry of materials* **2006,** *18* (7), 1873-1877.
99. Zhao, L.-D.; Lo, S.-H.; Zhang, Y.; Sun, H.; Tan, G.; Uher, C.; Wolverton, C.; Dravid, V. P.; Kanatzidis, M. G., Ultralow thermal conductivity and high thermoelectric figure of merit in SnSe crystals. *Nature* **2014,** *508* (7496), 373-377.
100. Zhao, L.-D.; Tan, G.; Hao, S.; He, J.; Pei, Y.; Chi, H.; Wang, H.; Gong, S.; Xu, H.; Dravid, V. P., Ultrahigh power factor and thermoelectric performance in hole-doped single-crystal SnSe. *Science* **2016,** *351* (6269), 141-144.
101. Jeitschko, W., Transition metal stannides with MgAgAs and $MnCu_2Al$ type structure. *Metallurgical Transactions* **1970,** *1* (11), 3159-3162.
102. Webster, P. J.; Ziebeck, K. R. A., *Landolt-Börnstein-group III condensed matter*. Berlin: Springer: 1988; Vol. 19C.

103. Aliev, F. G.; Brandt, N. B.; Moshchalkov, V. V.; Kozyrkov, V. V.; Skolozdra, R. V.; Belogorokhov, A. I., Gap at the Fermi Level in the Intermetallic Vacancy System Tinisn, Zrnisn, Hfnisn. *Z Phys B Con Mat* **1989,** *75* (2), 167-171.
104. Aliev, F. G.; Kozyrkov, V. V.; Moshchalkov, V. V.; Scolozdra, R. V.; Durczewski, K., Narrow-Band in the Intermetallic Compounds Tinisn, Zrnisn, Hfnisn. *Z Phys B Con Mat* **1990,** *80* (3), 353-357.
105. Poon, S. J., Electronic and Thermoelectric Properties of Half Heusler Alloys. In *Semiconductor and Semimetals*, Tritt, T. M., Ed. Academic: New York, 2001; Vol. 70, pp 37-76.
106. Simonson, J. W.; Poon, S. J., Electronic structure of transition metal-doped XNiSn and XCoSb (X = Hf,Zr) phases in the vicinity of the band gap *J. Phys.: Condens. Matter* **2008,** *20*, 255220.
107. Yu, C.; Zhu, T. J.; Shi, R. Z.; Zhang, Y.; Zhao, X. B.; He, J., High-performance half-Heusler thermoelectric materials $Hf_{1-x}Zr_xNiSn_{1-y}Sb_y$ prepared by levitation melting and spark plasma sintering. *Acta Materialia* **2009,** *57* (9), 2757-2764.
108. Yaqub, R.; Sahoo, P.; Makongo, J. P. A.; Takas, N.; Poudeu, P. F. P.; Stokes, K. L., Investigation of the Effect of NiO Nanoparticles on the Transport Properties of $Zr_{0.5}Hf_{0.5}Ni_{1-x}Pd_xSn_{0.99}Sb_{0.01}$ (x=0 and 0.2). *Sci Adv Mater* **2011,** *3* (4), 633-638.
109. Maji, P.; Takas, N. J.; Misra, D. K.; Gabrisch, H.; Stokes, K.; Poudeu, P. F. P., Effects of Rh on the thermoelectric performance of the p-type $Zr_{0.5}Hf_{0.5}Co_{1-x}Rh_xSb_{0.99}Sn_{0.01}$ half-Heusler alloys. *Journal of Solid State Chemistry* **2010,** *183* (5), 1120-1126.
110. Maji, P.; Makongo, J. P. A.; Zhou, X. Y.; Chi, H.; Uher, C.; Poudeu, P. F. P., Thermoelectric performance of nanostructured p-type $Zr_{0.5}Hf_{0.5}Co_{0.4}Rh_{0.6}Sb_{1-x}Sn_x$ half-Heusler alloys. *Journal of Solid State Chemistry* **2013,** *202*, 70-76.
111. Makongo, J. P.; Misra, D. K.; Salvador, J. R.; Takas, N. J.; Wang, G.; Shabetai, M. R.; Pant, A.; Paudel, P.; Uher, C.; Stokes, K. L., Thermal and electronic charge transport in bulk nanostructured $Zr_{0.25}Hf_{0.75}NiSn$ composites with full-Heusler inclusions. *Journal of Solid State Chemistry* **2011,** *184* (11), 2948-2960.
112. Culp, S. R.; Simonson, J. W.; Poon, S. J.; Ponnambalam, V.; Edwards, J.; Tritt, T. M., (Zr,Hf)Co(Sb,Sn) half-Heusler phases as high-temperature (> 700 degrees C) p-type thermoelectric materials. *Applied Physics Letters* **2008,** *93* (2), 022105.
113. Joshi, G.; Yan, X.; Wang, H.; Liu, W.; Chen, G.; Ren, Z., Enhancement in Thermoelectric Figure-Of-Merit of an N-Type Half-Heusler Compound by the Nanocomposite Approach. *Advanced Energy Materials* **2011,** *1*, 643.
114. Lan, Y. C.; Minnich, A. J.; Chen, G.; Ren, Z. F., Enhancement of Thermoelectric Figure-of-Merit by a Bulk Nanostructuring Approach. *Adv Funct Mater* **2010,** *20* (3), 357-376.
115. Simonson, J. W.; Wu, D.; Xie, W. J.; Tritt, T. M.; Poon, S. J., Introduction of resonant states and enhancement of thermoelectric properties in half-Heusler alloys. *Phys Rev B* **2011,** *83* (23), 235211.
116. Poudeu, P. F.; Salvador, J.; Sakamoto, J., A Special Issue on Advanced Thermoelectric Materials and Devices. *Sci Adv Mater* **2011,** *3* (4), 515-516.
117. Barth, J.; Balke, B.; Fecher, G. H.; Stryhanyuk, H.; Gloskovskii, A.; Naghavi, S.; Felser, C., Thermoelectric properties of CoTiSb based compounds. *J Phys D Appl Phys* **2009,** *42* (18), 308–311.
118. Chaput, L.; Tobola, J.; Pecheur, P.; Scherrer, H., Electronic structure and thermopower of $Ni(Ti_{0.5}Hf_{0.5})Sn$ and related half-Heusler phases. *Phys Rev B* **2006,** *73* (4), 045121.

119. Sakurada, S.; Shutoh, N., Effect of Ti substitution on the thermoelectric properties of (Zr,Hf)NiSn half-Heusler compounds. *Applied Physics Letters* **2005,** *86* (8), 082105.
120. Uher, C.; Yang, J.; Hu, S.; Morelli, D. T.; Meisner, G. P., Transport properties of pure and doped MNiSn (M=Zr, Hf). *Physical Review B* **1999,** *59*, 8615-8621.
121. Nanda, B. R. K.; Dasgupta, I., Electronic structure and magnetism in doped semiconducting half-Heusler compounds. *J Phys-Condens Mat* **2005,** *17* (33), 5037-5048.
122. Kroth, K.; Balke, B.; Fecher, G. H.; Ksenofontov, V.; Felser, C.; Lin, H. J., Diluted magnetic semiconductors with high Curie temperature based on C1(b) compounds: $CoTi_{1-x}Fe_xSb$. *Applied Physics Letters* **2006,** *89* (20), 202509.
123. Ouardi, S.; Fecher, G. H.; Balke, B.; Kozina, X.; Stryganyuk, G.; Felser, C.; Lowitzer, S.; Kodderitzsch, D.; Ebert, H.; Ikenaga, E., Electronic transport properties of electron- and hole-doped semiconducting C1b Heusler compounds: $NiTi_{1-x}M_xSn$ (M=Sc, V). *Phys Rev B* **2010,** *82* (8), 085108.
124. Sanyal, B.; Eriksson, O.; Suresh, K. G.; Dasgupta, I.; Nigam, A. K.; Nordblad, P., Ferromagnetism in Mn doped half-heusler NiTiSn: Theory and experiment. *Applied Physics Letters* **2006,** *89* (21), 212502.
125. Lin, H.; Wray, L. A.; Xia, Y. Q.; Xu, S. Y.; Jia, S. A.; Cava, R. J.; Bansil, A.; Hasan, M. Z., Half-Heusler ternary compounds as new multifunctional experimental platforms for topological quantum phenomena. *Nat Mater* **2010,** *9* (7), 546-549.
126. Chadov, S.; Qi, X. L.; Kubler, J.; Fecher, G. H.; Felser, C.; Zhang, S. C., Tunable multifunctional topological insulators in ternary Heusler compounds. *Nat Mater* **2010,** *9* (7), 541-545.
127. Xiao, D.; Yao, Y. G.; Feng, W. X.; Wen, J.; Zhu, W. G.; Chen, X. Q.; Stocks, G. M.; Zhang, Z. Y., Half-Heusler Compounds as a New Class of Three-Dimensional Topological Insulators. *Physical Review Letters* **2010,** *105* (9), 096404.
128. Culp, S. R.; Poon, S. J.; Hickman, N.; Tritt, T. M.; Blumm, J., Effect of substitutions on the thermoelectric figure of merit of half-Heusler phases at 800 degrees C. *Applied Physics Letters* **2006,** *88* (4), 042106
129. Shen, Q.; Chen, L.; Goto, T.; Hirai, T.; Yang, J.; Meisner, G. P.; Uher, C., Effects of partial substitution of Ni by Pd on the thermoelectric properties of ZrNiSn-based half-Heusler compounds. *Applied Physics Letters* **2001,** *79* (25), 4165-4167.
130. Yang, J.; Meisner, G. P.; Chen, L., Strain field fluctuation effects on lattice thermal conductivity of ZrNiSn-based thermoelectric compounds. *Applied Physics Letters* **2004,** *85* (7), 1140-1142.
131. Liu, Y. F.; Poudeu, P. F. P., Thermoelectric properties of Ge doped n-type $Ti_xZr_{1-x}NiSn_{0.975}Ge_{0.025}$ half-Heusler alloys. *Journal of Materials Chemistry A* **2015,** *3* (23), 12507-12514.
132. Shutoh, N.; Sakurada, S., Thermoelectric properties of the $Ti_x(Zr_{0.5}Hf_{0.5})_{1-x}NiSn$ half-Heusler compounds. *Journal of alloys and compounds* **2005,** *389* (1-2), 204-208.
133. Chen, L. D.; Huang, X. Y.; Zhou, M.; Shi, X.; Zhang, W. B., The high temperature thermoelectric performances of $Zr_{0.5}Hf_{0.5}Ni_{0.8}Pd_{0.2}Sn_{0.99}Sb_{0.01}$ alloy with nanophase inclusions. *J. Appl. Phys.* **2006,** *99* (6), 064305/1-064305/6.
134. Yu, C.; Zhu, T.-J.; Xiao, K.; Shen, J.-J.; Yang, S.-H.; Zhao, X.-B., Reduced Grain Size and Improved Thermoelectric Properties of Melt Spun (Hf,Zr)NiSn Half-Heusler Alloys. *Journal of Electronic Materials* **2010,** *39* (9), 2008-2012.

135. Poon, S. J.; Wu, D.; Zhu, S.; Xie, W.; Tritt, T. M.; Thomas, P.; Venkatasubramanian, R., Half-Heusler phases and nanocomposites as emerging high-*ZT* thermoelectric materials. *Journal of Materials Research* **2011,** *26* (22), 2795-2802.
136. Visconti, A.; Navone, C.; Leforestier, J.; Mingo, N.; Bernard-Granger, G., Influence of the addition of HfO_2 particles on the thermoelectric properties of an n-type half-Heusler alloy sintered by spark plasma sintering. *Journal of Alloys and Compounds* **2017,** *709*, 36-41.
137. Huang, X. Y.; Xu, Z.; Chen, L. D.; Tang, X. F. In *Effect of γ-Al_2O_3 content on the thermoelectric performance of ZrNiSn/γ-Al_2O_3 composites*, Key Engineering Materials, Trans Tech Publ: 2003; pp 79-82.
138. Chauhan, N. S.; Bathula, S.; Vishwakarma, A.; Bhardwaj, R.; Gahtori, B.; Srivastava, A. K.; Saravanan, M.; Dhar, A., A nanocomposite approach for enhancement of thermoelectric performance in Hafnium-free Half-Heuslers. *Materialia* **2018,** *1*, 168-174.
139. Huang, X. Y.; Chen, L. D.; Shi, X.; Zhou, M.; Xu, Z. In *Thermoelectric Performances of ZrNiSn/C60 Composite*, Key Engineering Materials, Trans Tech Publ: 2005; pp 385-388.
140. Wang Chai, Y.; Kimura, Y., Nanosized precipitates in half-Heusler TiNiSn alloy. *Applied Physics Letters* **2012,** *100* (3), 033114.
141. Liu, Y.; Makongo, J. P.; Page, A.; Sahoo, P.; Uher, C.; Stokes, K.; Poudeu, P. F., Distribution of impurity states and charge transport in $Zr_{0.25}Hf_{0.75}Ni_{1+x}Sn_{1-y}Sb_y$ nanocomposites. *Journal of Solid State Chemistry* **2016,** *234*, 72-86.
142. Xie, W.; Weidenkaff, A.; Tang, X.; Zhang, Q.; Poon, J.; Tritt, T. M., Recent advances in nanostructured thermoelectric half-Heusler compounds. *Nanomaterials* **2012,** *2* (4), 379-412.
143. Liu, H.; Shi, X.; Xu, F.; Zhang, L.; Zhang, W.; Chen, L.; Li, Q.; Uher, C.; Day, T.; Snyder, G. J., Copper ion liquid-like thermoelectrics. *Nat Mater* **2012,** *11* (5), 422.
144. Skomorokhov, A.; Trots, D.; Knapp, M.; Bickulova, N.; Fuess, H., Structural behaviour of β-$Cu_{2-\delta}Se$ (δ= 0, 0.15, 0.25) in dependence on temperature studied by synchrotron powder diffraction. *Journal of alloys and compounds* **2006,** *421* (1-2), 64-71.
145. Heyding, R. D.; Murray, R. M., The crystal structures of $Cu_{1.8}Se$, Cu_3Se_2, α-and γCuSe, $CuSe_2$, and $CuSe_2$II. *Canadian Journal of Chemistry* **1976,** *54* (6), 841-848.
146. Oliveria, M.; McMullan, R.; Wuensch, B., Single crystal neutron diffraction analysis of the cation distribution in the high-temperature phases α-$Cu_{2-x}S$, α-$Cu_{2-x}Se$, and α-Ag_2Se. *Solid State Ionics* **1988,** *28*, 1332-1337.
147. Danilkin, S.; Avdeev, M.; Sale, M.; Sakuma, T., Neutron scattering study of ionic diffusion in Cu-Se superionic compounds. *Solid State Ionics* **2012,** *225*, 190-193.
148. Chatov, V., Ionic conduction and diffusion of copper in copper selenide. *Sov. Phys. Semicond.* **1980,** *14* (4), 474-475.
149. Kashida, S.; Akai, J., X-ray diffraction and electron microscopy studies of the room-temperature structure of Cu_2Se. *Journal of Physics C: Solid State Physics* **1988,** *21* (31), 5329.
150. Murray, R. M.; Heyding, R. D., The copper-selenium system at temperatures to 850 K and pressures to 50 kbar. *Canadian Journal of Chemistry* **1975,** *53* (6), 878-887.
151. Vučić, Z.; Milat, O.; Horvatić, V.; Ogorelec, Z., Composition-induced phase-transition splitting in cuprous selenide. *Phys Rev B* **1981,** *24* (9), 5398.
152. Nguyen, M. C.; Choi, J.-H.; Zhao, X.; Wang, C.-Z.; Zhang, Z.; Ho, K.-M., New layered structures of cuprous chalcogenides as thin film solar cell materials: Cu_2Te and Cu_2Se. *Physical review letters* **2013,** *111* (16), 165502.

153. Lu, P.; Liu, H.; Yuan, X.; Xu, F.; Shi, X.; Zhao, K.; Qiu, W.; Zhang, W.; Chen, L., Multiformity and fluctuation of Cu ordering in Cu_2Se thermoelectric materials. *Journal of Materials Chemistry A* **2015,** *3* (13), 6901-6908.
154. Sorokin, G.; Papshev, Y. M.; Oush, P., Photoconductivity of Cu_2S Cu_2Se and Cu_2Te. 1966; Vol. 7, pp 1810-+.
155. Hampl, E., Thermoelectric composition. Google Patents: 1974.
156. Ohtani, T.; Tachibana, Y.; Ogura, J.; Miyake, T.; Okada, Y.; Yokota, Y., Physical properties and phase transitions of β $Cu_{2-x}Se$ ($0.20 \leqslant x \leqslant 0.25$). *Journal of alloys and compounds* **1998,** *279* (2), 136-141.
157. Zhao, K.; Duan, H.; Raghavendra, N.; Qiu, P.; Zeng, Y.; Zhang, W.; Yang, J.; Shi, X.; Chen, L., Solid-State Explosive Reaction for Nanoporous Bulk Thermoelectric Materials. *Advanced Materials* **2017,** *29* (42), 1701148.
158. Qiu, P.; Shi, X.; Chen, L., Cu-based thermoelectric materials. *Energy Storage Materials* **2016,** *3*, 85-97.
159. Zhao, K.; Guan, M.; Qiu, P.; Blichfeld, A. B.; Eikeland, E.; Zhu, C.; Ren, D.; Xu, F.; Iversen, B. B.; Shi, X., Thermoelectric properties of $Cu_2Se_{1-x}Te_x$ solid solutions. *Journal of Materials Chemistry A* **2018,** *6* (16), 6977-6986.
160. Bhardwaj, R.; Bhattacharya, A.; Tyagi, K.; Gahtori, B.; Chauhan, N. S.; Vishwakarma, A.; Johari, K. K.; Bathula, S.; Auluck, S.; Dhar, A., Enhancement in thermoelectric performance of single step synthesized Mg doped Cu_2Se: An experimental and theoretical study. *Intermetallics* **2019,** *112*, 106541.
161. Bailey, T. P.; Hui, S.; Xie, H.; Olvera, A.; Poudeu, P. F.; Tang, X.; Uher, C., Enhanced *ZT* and attempts to chemically stabilize Cu_2Se via Sn doping. *Journal of Materials Chemistry A* **2016,** *4* (43), 17225-17235.
162. Yao, M.; Liu, W.; Chen, X.; Ren, Z.; Wilson, S.; Ren, Z.; Opeil, C., Low temperature thermoelectric properties of p-type copper selenide with Ni, Te and Zn dopants. *Journal of Alloys and Compounds* **2017,** *699*, 718-721.
163. Liao, W.-W.; Yang, L.; Chen, J.; Zhou, D.-L.; Qu, X.-l.; Zheng, K.; Han, G.; Zhou, J.-B.; Hong, M.; Chen, Z.-G., Realizing Bi-doped α-Cu_2Se as a promising near-room-temperature thermoelectric material. *Chemical Engineering Journal* **2019,** *371*, 593-599.
164. Zhu, Z.; Zhang, Y.; Song, H.; Li, X.-J., Enhancement of thermoelectric performance of Cu_2Se by K doping. *Applied Physics A* **2018,** *124* (12), 871.
165. Kang, S. D.; Pöhls, J.-H.; Aydemir, U.; Qiu, P.; Stoumpos, C. C.; Hanus, R.; White, M. A.; Shi, X.; Chen, L.; Kanatzidis, M. G., Enhanced stability and thermoelectric figure-of-merit in copper selenide by lithium doping. *Materials Today Physics* **2017,** *1*, 7-13.
166. Zhu, Z.; Zhang, Y.; Song, H.; Li, X.-J., High thermoelectric performance and low thermal conductivity in $Cu_{2-x}Na_xSe$ bulk materials with micro-pores. *Applied Physics A* **2019,** *125* (8), 572.
167. Ballikaya, S.; Chi, H.; Salvador, J. R.; Uher, C., Thermoelectric properties of Ag-doped Cu_2Se and Cu_2Te. *Journal of Materials Chemistry A* **2013,** *1* (40), 12478-12484.
168. Liu, W.; Shi, X.; Hong, M.; Yang, L.; Moshwan, R.; Chen, Z.-G.; Zou, J., Ag doping induced abnormal lattice thermal conductivity in Cu_2Se. *Journal of Materials Chemistry C* **2018,** *6* (48), 13225-13231.
169. Yang, L.; Chen, Z.-G.; Han, G.; Hong, M.; Huang, L.; Zou, J., Te-Doped Cu_2Se nanoplates with a high average thermoelectric figure of merit. *Journal of Materials Chemistry A* **2016,** *4* (23), 9213-9219.

170. Zhao, K.; Qiu, P.; Song, Q.; Blichfeld, A. B.; Eikeland, E.; Ren, D.; Ge, B.; Iversen, B. B.; Shi, X.; Chen, L., Ultrahigh thermoelectric performance in $Cu_{2-y}Se_{0.5}S_{0.5}$ liquid-like materials. *Materials Today Physics* **2017,** *1*, 14-23.
171. Olvera, A.; Moroz, N.; Sahoo, P.; Ren, P.; Bailey, T.; Page, A.; Uher, C.; Poudeu, P., Partial indium solubility induces chemical stability and colossal thermoelectric figure of merit in Cu_2Se. *Energy & Environmental Science* **2017,** *10* (7), 1668-1676.
172. Lei, J.; Ma, Z.; Zhang, D.; Chen, Y.; Wang, C.; Yang, X.; Cheng, Z.; Wang, Y., High thermoelectric performance in Cu_2Se superionic conductor with enhanced liquid-like behaviour by dispersing SiC. *Journal of materials chemistry A* **2019,** *7* (12), 7006-7014.
173. Borup, K. A.; De Boor, J.; Wang, H.; Drymiotis, F.; Gascoin, F.; Shi, X.; Chen, L.; Fedorov, M. I.; Müller, E.; Iversen, B. B., Measuring thermoelectric transport properties of materials. *Energy & Environmental Science* **2015,** *8* (2), 423-435.
174. Hsu, K. F.; Loo, S.; Guo, F.; Chen, W.; Dyck, J. S.; Uher, C.; Hogan, T.; Polychroniadis, E. K.; Kanatzidis, M. G., Cubic $AgPb_mSbTe_{2+m}$: Bulk thermoelectric materials with high figure of merit. *Science* **2004,** *303* (5659), 818-821.
175. Pichanusakorn, P.; Bandaru, P., Nanostructured thermoelectrics. *Materials Science and Engineering: R: Reports* **2010,** *67* (2-4), 19-63.
176. Minnich, A.; Dresselhaus, M.; Ren, Z.; Chen, G., Bulk nanostructured thermoelectric materials: current research and future prospects. *Energy & Environmental Science* **2009,** *2* (5), 466-479.
177. Wood, C., Materials for thermoelectric energy conversion. *Reports on progress in physics* **1988,** *51* (4), 459.
178. Snyder, G. J.; Christensen, M.; Nishibori, E.; Caillat, T.; Iversen, B. B., Disordered zinc in Zn_4Sb_3 with phonon-glass and electron-crystal thermoelectric properties. *Nat Mater* **2004,** *3* (7), 458.
179. Nolas, G.; Morelli, D.; Tritt, T. M., Skutterudites: A phonon-glass-electron crystal approach to advanced thermoelectric energy conversion applications. *Annual Review of Materials Science* **1999,** *29* (1), 89-116.
180. Cahill, D. G.; Watson, S. K.; Pohl, R. O., Lower limit to the thermal conductivity of disordered crystals. *Phys Rev B* **1992,** *46* (10), 6131.
181. Kurosaki, K.; Kosuga, A.; Muta, H.; Uno, M.; Yamanaka, S., Ag_9TlTe_5: A high-performance thermoelectric bulk material with extremely low thermal conductivity. *Applied Physics Letters* **2005,** *87* (6), 061919.
182. Bux, S. K.; Zevalkink, A.; Janka, O.; Uhl, D.; Kauzlarich, S.; Snyder, J. G.; Fleurial, J.-P., Glass-like lattice thermal conductivity and high thermoelectric efficiency in $Yb_9Mn_{4.2}Sb_9$. *Journal of Materials Chemistry A* **2014,** *2* (1), 215-220.
183. Morelli, D.; Jovovic, V.; Heremans, J., Intrinsically minimal thermal conductivity in cubic I-V-VI_2 semiconductors. *Physical Review Letters* **2008,** *101* (3), 035901.
184. Shi, X.; Yang, J.; Salvador, J. R.; Chi, M.; Cho, J. Y.; Wang, H.; Bai, S.; Yang, J.; Zhang, W.; Chen, L., Multiple-filled skutterudites: high thermoelectric figure of merit through separately optimizing electrical and thermal transports. *Journal of the American Chemical Society* **2011,** *133* (20), 7837-7846.
185. Schmitt, D. C.; Haldolaarachchige, N.; Xiong, Y.; Young, D. P.; Jin, R.; Chan, J. Y., Probing the lower limit of lattice thermal conductivity in an ordered extended solid: $Gd_{117}Co_{56}Sn_{112}$, a phonon glass-electron crystal system. *Journal of the American Chemical Society* **2012,** *134* (13), 5965-5973.

186. Wu, D.; Zhao, L.-D.; Tong, X.; Li, W.; Wu, L.; Tan, Q.; Pei, Y.; Huang, L.; Li, J.-F.; Zhu, Y., Superior thermoelectric performance in PbTe-PbS pseudo-binary: extremely low thermal conductivity and modulated carrier concentration. *Energy & Environmental Science* **2015,** *8* (7), 2056-2068.
187. Sharp, J. W.; Sales, B. C.; Mandrus, D. G.; Chakoumakos, B. C., Thermoelectric properties of Tl_2SnTe_5 and Tl_2GeTe_5. *Applied Physics Letters* **1999,** *74* (25), 3794-3796.
188. Polman, A.; Atwater, H. A., Photonic design principles for ultrahigh-efficiency photovoltaics. *Nat Mater* **2012,** *11* (3), 174.
189. Green, M. A., Third generation photovoltaics: Ultra‐high conversion efficiency at low cost. *Progress in Photovoltaics: Research and Applications* **2001,** *9* (2), 123-135.
190. Biswas, K.; He, J.; Zhang, Q.; Wang, G.; Uher, C.; Dravid, V. P.; Kanatzidis, M. G., Strained endotaxial nanostructures with high thermoelectric figure of merit. *Nature Chemistry* **2011,** *3* (2), 160.
191. Li, J.-F.; Liu, W.-S.; Zhao, L.-D.; Zhou, M., High-performance nanostructured thermoelectric materials. *NPG Asia Materials* **2010,** *2* (4), 152.
192. Tan, G.; Zhao, L.-D.; Shi, F.; Doak, J. W.; Lo, S.-H.; Sun, H.; Wolverton, C.; Dravid, V. P.; Uher, C.; Kanatzidis, M. G., High thermoelectric performance of p-type SnTe via a synergistic band engineering and nanostructuring approach. *Journal of the American Chemical Society* **2014,** *136* (19), 7006-7017.
193. Hicks, L.; Dresselhaus, M. S., Thermoelectric figure of merit of a one-dimensional conductor. *Phys Rev B* **1993,** *47* (24), 16631.
194. Zebarjadi, M.; Joshi, G.; Zhu, G.; Yu, B.; Minnich, A.; Lan, Y.; Wang, X.; Dresselhaus, M.; Ren, Z.; Chen, G., Power factor enhancement by modulation doping in bulk nanocomposites. *Nano Letters* **2011,** *11* (6), 2225-2230.
195. Vashaee, D.; Shakouri, A., Improved thermoelectric power factor in metal-based superlattices. *Physical Review Letters* **2004,** *92* (10), 106103.
196. Heremans, J. P.; Thrush, C. M.; Morelli, D. T., Thermopower enhancement in lead telluride nanostructures. *Phys Rev B* **2004,** *70* (11), 115334.
197. Kimura, Y.; Tanoguchi, T.; Sakai, Y.; Chai, Y.-W.; Mishima, Y., Effect of vacancy-site occupation in half-Heusler compound ZrNiSn on phase stability and thermoelectric properties. *MRS Online Proceedings Library Archive* **2011,** *1295*.
198. Chai, Y. W.; Yoshioka, K.; Kimura, Y., Intrinsic point defects in thermoelectric half-Heusler alloys. *Scripta Materialia* **2014,** *83*, 13-16.
199. Culp, S.; Poon, S.; Sorloaica, N.; Tritt, T. In *Complex MNiSn phases as stable high-temperature thermoelectric materials*, Thermoelectrics, 2005. ICT 2005. 24th International Conference on, IEEE: 2005; pp 384-387.
200. Joshi, G.; Dahal, T.; Chen, S.; Wang, H.; Shiomi, J.; Chen, G.; Ren, Z., Enhancement of thermoelectric figure-of-merit at low temperatures by titanium substitution for hafnium in n-type half-Heuslers $Hf_{0.75-x}Ti_xZr_{0.25}NiSn_{0.99}Sb_{0.01}$. *Nano Energy* **2013,** *2* (1), 82-87.
201. Sahoo, P.; Liu, Y.; Makongo, J. P.; Su, X.-L.; Kim, S. J.; Takas, N.; Chi, H.; Uher, C.; Pan, X.; Poudeu, P. F., Enhancing thermopower and hole mobility in bulk p-type half-Heuslers using full-Heusler nanostructures. *Nanoscale* **2013,** *5* (19), 9419-9427.
202. Tsujii, N.; Mori, T., High thermoelectric power factor in a carrier-doped magnetic semiconductor $CuFeS_2$. *Applied Physics Express* **2013,** *6* (4), 043001.
203. Tsujii, N.; Mori, T.; Isoda, Y., Phase stability and thermoelectric properties of $CuFeS_2$-based magnetic semiconductor. *Journal of Electronic Materials* **2014,** *43* (6), 2371-2375.

204. Zhao, W.; Liu, Z.; Sun, Z.; Zhang, Q.; Wei, P.; Mu, X.; Zhou, H.; Li, C.; Ma, S.; He, D., Superparamagnetic enhancement of thermoelectric performance. *Nature* **2017,** *549* (7671), 247.
205. Page, A.; Van der Ven, A.; Poudeu, P.; Uher, C., Origins of phase separation in thermoelectric (Ti,Zr,Hf)NiSn half-Heusler alloys from first principles. *Journal of Materials Chemistry A* **2016,** *4* (36), 13949-13956.
206. Berche, A.; Tédenac, J.; Jund, P., Phase separation in the half-Heusler thermoelectric materials (Hf,Ti,Zr)NiSn. *Scripta Materialia* **2017,** *139*, 122-125.
207. Gałązka, K.; Populoh, S.; Sagarna, L.; Karvonen, L.; Xie, W.; Beni, A.; Schmutz, P.; Hulliger, J.; Weidenkaff, A., Phase formation, stability, and oxidation in (Ti,Zr,Hf)NiSn half-Heusler compounds. *Physica Status Solidi (a)* **2014,** *211* (6), 1259-1266.
208. Geng, H.; Zhang, H., Effects of phase separation on the thermoelectric properties of (Ti,Zr,Hf)NiSn half-Heusler alloys. *Journal of Applied Physics* **2014,** *116* (3), 033708.
209. Downie, R. A.; Smith, R. I.; MacLaren, D. A.; Bos, J.-W. G., Metal distributions, efficient n-type doping, and evidence for in-gap states in $TiNiM_ySn$ (M= Co, Ni, Cu) half-Heusler nanocomposites. *Chemistry of Materials* **2015,** *27* (7), 2449-2459.
210. Fujita, Y.; Endo, K.; Terada, M.; Kimura, R., Magnetic properties of heusler type alloys M_2XSn (M= Fe, Co or Ni, X= Ti or V). *Journal of Physics and Chemistry of Solids* **1972,** *33* (7-9), 1443-1446.
211. Van Engen, P.; Buschow, K.; Erman, M., Magnetic properties and magneto-optical spectroscopy of Heusler alloys based on transition metals and Sn. *Journal of Magnetism and Magnetic Materials* **1983,** *30* (3), 374-382.
212. Miyazaki, H.; Nakano, T.; Inukai, M.; Soda, K.; Izumi, Y.; Muro, T.; Kim, J.; Takata, M.; Matsunami, M.; Kimura, S.-i., Electronic and local crystal structures of the ZrNiSn half-Heusler thermoelectric material. *Materials Transactions* **2014,** *55* (8), 1209-1214.
213. Romaka, V.; Rogl, P.; Romaka, L.; Stadnyk, Y.; Grytsiv, A.; Lakh, O.; Krayovskii, V., Peculiarities of structural disorder in Zr- and Hf-containing Heusler and half-Heusler stannides. *Intermetallics* **2013,** *35*, 45-52.
214. Goodenough, J. B., An interpretation of the magnetic properties of the perovskite-type mixed crystals $La_{1-x}Sr_xCoO_{3-\lambda}$. *Journal of Physics and Chemistry of Solids* **1958,** *6* (2-3), 287-297.
215. Djieutedjeu, H.; Poudeu, P. F.; Takas, N. J.; Makongo, J. P.; Rotaru, A.; Ranmohotti, K. G.; Anglin, C. J.; Spinu, L.; Wiley, J. B., Structural-Distortion-Driven Cooperative Magnetic and Semiconductor-to-Insulator Transitions in Ferromagnetic $FeSb_2Se_4$. *Angewandte Chemie International Edition* **2010,** *49* (51), 9977-9981.
216. Ranmohotti, K. G.; Djieutedjeu, H.; Lopez, J.; Page, A.; Haldolaarachchige, N.; Chi, H.; Sahoo, P.; Uher, C.; Young, D.; Poudeu, P. F., Coexistence of High-T_c Ferromagnetism and n-Type Electrical Conductivity in $FeBi_2Se_4$. *Journal of the American Chemical Society* **2015,** *137* (2), 691-698.
217. Yamamoto, S.; Fukui, T.; Maisinger, K.; Schollwöck, U., Combination of ferromagnetic and antiferromagnetic features in Heisenberg ferrimagnets. *Journal of Physics: Condensed Matter* **1998,** *10* (48), 11033.
218. Terashita, H.; Neumeier, J., Bulk magnetic properties of $La_{1-x}Ca_xMnO_3$ ($0 \leqslant x \leqslant 0.14$): Signatures of local ferromagnetic order. *Phys Rev B* **2005,** *71* (13), 134402.
219. Pillai, S. S.; Rangarajan, G.; Raju, N.; Epstein, A.; Santhosh, P., Coexistence of ferromagnetic and antiferromagnetic phases in $Nd_{0.5}Ca_xSr_{0.5-x}MnO_3$ manganites. *Journal of Physics: Condensed Matter* **2007,** *19* (49), 496221.

220. Torrance, J.; Shafer, M.; McGuire, T., Bound magnetic polarons and the insulator-metal transition in EuO. *Physical Review Letters* **1972,** *29* (17), 1168.
221. Lascaray, J.; Desfours, J.; Averous, M., Bound magnetic polaron evidence in EuO. *Solid State Communications* **1976,** *19* (7), 677-679.
222. Sawicki, M.; Dietl, T.; Kossut, J.; Igalson, J.; Wojtowicz, T.; Plesiewicz, W., Influence of s-d exchange interaction on the conductivity of $Cd_{1-x}Mn_xSe$: In in the weakly localized regime. *Physical Review Letters* **1986,** *56* (5), 508.
223. Berciu, M.; Bhatt, R., Effects of disorder on ferromagnetism in diluted magnetic semiconductors. *Physical Review Letters* **2001,** *87* (10), 107203.
224. Kaminski, A.; Sarma, S. D., Polaron percolation in diluted magnetic semiconductors. *Physical Review Letters* **2002,** *88* (24), 247202.
225. Sarma, S. D.; Hwang, E.; Kaminski, A., Temperature-dependent magnetization in diluted magnetic semiconductors. *Phys Rev B* **2003,** *67* (15), 155201.
226. Coey, J.; Venkatesan, M.; Fitzgerald, C., Donor impurity band exchange in dilute ferromagnetic oxides. *Nat Mater* **2005,** *4* (2), 173.
227. Moroz, N. A.; Lopez, J. S.; Djieutedjeu, H.; Ranmohotti, K. G.; Olvera, A.; Ren, P.; Page, A.; Takas, N. J.; Uher, C.; Poudeu, P. F., Indium Preferential Distribution Enables Electronic Engineering of Magnetism in $FeSb_{2-x}In_xSe_4$ p-Type High-T_c Ferromagnetic Semiconductors. *Chemistry of Materials* **2016,** *28* (23), 8570-8579.
228. Liu, Y.; Makongo, J. P.; Page, A.; Sahoo, P.; Uher, C.; Stokes, K.; Poudeu, P. F., Distribution of impurity states and charge transport in $Zr_{0.25}Hf_{0.75}Ni_{1+x}Sn_{1-y}Sb_y$ nanocomposites. *Journal of Solid State Chemistry* **2016,** *234*, 72-86.
229. Nolas, G. S.; Slack, G. A.; Schujman, S. B., Semiconductor clathrates: A phonon glass electron crystal material with potential for thermoelectric applications. In *Semiconductors and semimetals*, Elsevier: 2001; Vol. 69, pp 255-300.
230. Ramanathan, K.; Contreras, M. A.; Perkins, C. L.; Asher, S.; Hasoon, F. S.; Keane, J.; Young, D.; Romero, M.; Metzger, W.; Noufi, R., Properties of 19.2% efficiency $ZnO/CdS/CuInGaSe_2$ thin-film solar cells. *Progress in Photovoltaics: research and applications* **2003,** *11* (4), 225-230.
231. Cohen, K.; Rivet, J.; Dugué, J., Description of the Cu-As-Se ternary system. *Journal of alloys and compounds* **1995,** *224* (2), 316-329.
232. Jitsukawa, H.; Matsushita, H.; Takizawa, T., Phase diagrams of the (Cu_2Se,CuSe)-$CuGaSe_2$ system and the crystal growth of $CuGaSe_2$ by the solution method. *Journal of crystal growth* **1998,** *186* (4), 587-593.
233. Yang, L.; Chen, Z.-G.; Han, G.; Hong, M.; Zou, Y.; Zou, J., High-performance thermoelectric Cu_2Se nanoplates through nanostructure engineering. *Nano Energy* **2015,** *16*, 367-374.
234. El Akkad, F.; Mansour, B.; Hendeya, T., Electrical and thermoelectric properties of Cu_2Se and Cu_2S. *Materials Research Bulletin* **1981,** *16* (5), 535-539.
235. Yu, B.; Liu, W.; Chen, S.; Wang, H.; Wang, H.; Chen, G.; Ren, Z., Thermoelectric properties of copper selenide with ordered selenium layer and disordered copper layer. *Nano Energy* **2012,** *1* (3), 472-478.
236. Tell, B.; Shay, J.; Kasper, H., Room‐temperature electrical properties of ten I‐III‐VI2 semiconductors. *Journal of Applied Physics* **1972,** *43* (5), 2469-2470.
237. DeAngelis, A. D.; Horsley, K.; Gaillard, N., Wide Band Gap $CuGa(S,Se)_2$ Thin Films on Transparent Conductive Fluorinated Tin Oxide Substrates as Photocathode Candidates for

Tandem Water Splitting Devices. *The Journal of Physical Chemistry C* **2018,** *122* (26), 14304-14312.
238. Carr, W. D., *Electronic and thermal transport in copper-based chalcopyrite semiconductors for thermoelectric applications*. Michigan State University: 2016.
239. Woolley, J.; Lamarche, A.-M.; Lamarche, G.; del Re, R. B.; Quintero, M.; Gonzalez-Jimenez, F.; Swainson, I.; Holden, T., Low temperature magnetic behaviour of $CuFeSe_2$ from neutron diffraction data. *Journal of magnetism and magnetic materials* **1996,** *164* (1-2), 154-162.
240. Lamazares, J.; Gonzalez-Jimenez, F.; Jaimes, E.; D'Onofrio, L.; Iraldi, R.; Sanchez-Porras, G.; Quintero, M.; Gonzalez, J.; Woolley, J.; Lamarche, G., Magnetic, transport, X-ray diffraction and Mössbauer measurements on $CuFeSe_2$. *Journal of Magnetism and Magnetic Materials* **1992,** *104*, 997-998.
241. Berthebaud, D.; Lebedev, O.; Maignan, A., Thermoelectric properties of n-type cobalt doped chalcopyrite $Cu_{1-x}Co_xFeS_2$ and p-type eskebornite $CuFeSe_2$. *Journal of Materiomics* **2015,** *1* (1), 68-74.
242. Zhang, B.-Q.; Liu, Y.; Zuo, Y.; Chen, J.-S.; Song, J.-M.; Niu, H.-L.; Mao, C.-J., Colloidal synthesis and thermoelectric properties of $CuFeSe_2$ nanocrystals. *Nanomaterials* **2018,** *8* (1), 8.
243. Shannon, R. D., Revised effective ionic radii and systematic studies of interatomic distances in halides and chalcogenides. *Acta crystallographica section A: crystal physics, diffraction, theoretical and general crystallography* **1976,** *32* (5), 751-767.
244. Bernardini, G. P.; Mazzetti, G.; Trosti-Ferroni, R., The system Cu-Fe-Se; reconnaissance phase relations between 500 and 700 degrees C. *The Canadian Mineralogist* **1981,** *19* (3), 451-460.
245. Bernardini, G.; Mazzetti, G., Phase relations in the Cu-Fe-Se system at 900 and 700. *C.«Rend. Soc. Ital. Minerai. Petrol* **1979,** *35*, 71-90.
246. Korzoun, B.; Makovetskaya, L.; Savchuk, V.; Rubtsov, V.; Popelnyuk, G.; Chernyakova, A., T(x) phase diagram of the Cu_2Se-Al_2Se_3 system. *Journal of electronic materials* **1995,** *24* (7), 903-906.
247. Madelung, O., I-III-VI2 compounds. In *Semiconductors: Data Handbook*, Springer: 2004; pp 289-328.
248. Reddy, Y. B. K.; Raja, V. S., Effect of Cu/Al ratio on the properties of $CuAlSe_2$ thin films prepared by co-evaporation. *Materials chemistry and physics* **2006,** *100* (1), 152-157.
249. Barkat, L.; Morsli, M.; Amory, C.; Marsillac, S.; Khelil, A.; Bernede, J.; El Moctar, C., Study on the fabrication of n-type $CuAlSe_2$ thin films. *Thin solid films* **2003,** *431*, 99-104.
250. Yan, Y.; Guo, L.; Zhang, Z.; Lu, X.; Peng, K.; Yao, W.; Dai, J.; Wang, G.; Zhou, X., Sintering temperature dependence of thermoelectric performance in $CuCrSe_2$ prepared via mechanical alloying. *Scripta Materialia* **2017,** *127*, 127-131.
251. Bhattacharya, S.; Bohra, A.; Basu, R.; Bhatt, R.; Ahmad, S.; Meshram, K.; Debnath, A.; Singh, A.; Sarkar, S. K.; Navneethan, M., High thermoelectric performance of $(AgCrSe_2)_{0.5}(CuCrSe_2)_{0.5}$ nano-composites having all-scale natural hierarchical architectures. *Journal of Materials Chemistry A* **2014,** *2* (40), 17122-17129.
252. Tewari, G. C.; Tripathi, T.; Yamauchi, H.; Karppinen, M., Thermoelectric properties of layered antiferromagnetic $CuCrSe_2$. *Materials Chemistry and Physics* **2014,** *145* (1-2), 156-161.
253. Bhattacharya, S.; Basu, R.; Bhatt, R.; Pitale, S.; Singh, A.; Aswal, D.; Gupta, S.; Navaneethan, M.; Hayakawa, Y., $CuCrSe_2$: a high performance phonon glass and electron crystal thermoelectric material. *Journal of Materials Chemistry A* **2013,** *1* (37), 11289-11294.

254. Cheng, Y.; Yang, J.; Jiang, Q.; Fu, L.; Xiao, Y.; Luo, Y.; Zhang, D.; Zhang, M., $CuCrSe_2$ ternary chromium chalcogenide: facile fabrication, doping and thermoelectric properties. *Journal of the American Ceramic Society* **2015,** *98* (12), 3975-3980.
255. Gagor, A.; Gnida, D.; Pietraszko, A., Order-disorder phenomena in layered $CuCrSe_2$ crystals. *Materials Chemistry and Physics* **2014,** *146* (3), 283-288.
256. Niedziela, J. L.; Bansal, D.; May, A. F.; Ding, J.; Lanigan-Atkins, T.; Ehlers, G.; Abernathy, D. L.; Said, A.; Delaire, O., Selective breakdown of phonon quasiparticles across superionic transition in $CuCrSe_2$. *Nature Physics* **2019,** *15* (1), 73-78.
257. Tewari, G. C.; Karppinen, M.; Rastogi, A. K., Effects of competing magnetic interactions on the electronic transport properties of $CuCrSe_2$. *Journal of Solid State Chemistry* **2013,** *198*, 108-113.
258. Srivastava, D.; Tewari, G. C.; Karppinen, M.; Nieminen, R., First-principles study of layered antiferromagnetic $CuCrX_2$ (X= S, Se and Te). *Journal of Physics: Condensed Matter* **2013,** *25* (10), 105504.
259. Liu, R.; Ren, G.; Tan, X.; Lin, Y.; Nan, C., Enhanced thermoelectric properties of Cu_3SbSe_3-based composites with inclusion phases. *Energies* **2016,** *9* (10), 816.